

Ministry of Science and Higher Education of the Russian Federation  
ITMO University

ISSN 2220-8054

***NANOSYSTEMS:***  
***PHYSICS, CHEMISTRY, MATHEMATICS***

**2023, volume 14(1)**

**Наносистемы: физика, химия, математика**

**2023, том 14, № 1**



# **NANOSYSTEMS:**

## **PHYSICS, CHEMISTRY, MATHEMATICS**

### **ADVISORY BOARD MEMBERS**

**Chairman:** V.N. Vasiliev (*St. Petersburg, Russia*),  
V.M. Buznik (*Moscow, Russia*); V.M. Ievlev (*Voronezh, Russia*), P.S. Kop'ev (*St. Petersburg, Russia*), N.F. Morozov (*St. Petersburg, Russia*), V.N. Parmon (*Novosibirsk, Russia*),  
A.I. Rusanov (*St. Petersburg, Russia*),

### **EDITORIAL BOARD**

**Editor-in-Chief:** I.Yu. Popov (*St. Petersburg, Russia*)

#### **Section Co-Editors:**

Physics – V.M. Uzdin (*St. Petersburg, Russia*),

Material science – V.V. Gusarov (*St. Petersburg, Russia*); O.V. Al'myasheva (*St. Petersburg, Russia*);

Chemistry – V.K. Ivanov (*Moscow, Russia*),

Mathematics – I.Yu. Popov (*St. Petersburg, Russia*).

#### **Editorial Board Members:**

V.M. Adamyan (*Odessa, Ukraine*); A.P. Alodjants (*St. Petersburg, Russia*); S. Bechta (*Stockholm, Sweden*); J. Behrndt (*Graz, Austria*); M.B. Belonenko (*Volgograd, Russia*); A. Chatterjee (*Hyderabad, India*); A.V. Chizhov (*Dubna, Russia*); A.N. Enyashin (*Ekaterinburg, Russia*), P.P. Fedorov (*Moscow, Russia*); E.A. Gudilin (*Moscow, Russia*); H. Jónsson (*Reykjavik, Iceland*); A.A. Kiselev (*Durham, USA*); Yu.S. Kivshar (*Canberra, Australia*); S.A. Kozlov (*St. Petersburg, Russia*); P.A. Kurasov (*Stockholm, Sweden*); A.V. Lukashin (*Moscow, Russia*); I.V. Melikhov (*Moscow, Russia*); G.P. Miroshnichenko (*St. Petersburg, Russia*); I.Ya. Mittova (*Voronezh, Russia*); Nguyen Anh Tien (*Ho Chi Minh, Vietnam*); V.V. Pankov (*Minsk, Belarus*); K. Pankrashkin (*Orsay, France*); A.V. Ragulya (*Kiev, Ukraine*); V. Rajendran (*Tamil Nadu, India*); A.A. Rempel (*Ekaterinburg, Russia*); V.Ya. Rudyak (*Novosibirsk, Russia*); H.M. Sedighi (*Ahvaz, Iran*); D Shoikhet (*Karmiel, Israel*); P Stovicek (*Prague, Czech Republic*); V.M. Talanov (*Novocherkassk, Russia*); A.Ya. Vul' (*St. Petersburg, Russia*); A.V. Yakimansky (*St. Petersburg, Russia*), V.A. Zagrebnov (*Marseille, France*).

#### **Editors:**

I.V. Blinova; A.I. Popov; A.I. Trifanov; E.S. Trifanova (*St. Petersburg, Russia*),  
R. Simoneaux (*Philadelphia, Pennsylvania, USA*).

**Address:** ITMO University, Kronverkskiy pr., 49, St. Petersburg 197101, Russia.

**Phone:** +7(812)607-02-54, **Journal site:** <http://nanojournal.ifmo.ru/>,

**E-mail:** [nanojournal.ifmo@gmail.com](mailto:nanojournal.ifmo@gmail.com)

### **AIM AND SCOPE**

The scope of the journal includes all areas of nano-sciences. Papers devoted to basic problems of physics, chemistry, material science and mathematics inspired by nanosystems investigations are welcomed. Both theoretical and experimental works concerning the properties and behavior of nanosystems, problems of its creation and application, mathematical methods of nanosystem studies are considered.

The journal publishes scientific reviews (up to 30 journal pages), research papers (up to 15 pages) and letters (up to 5 pages). All manuscripts are peer-reviewed. Authors are informed about the referee opinion and the Editorial decision.

# CONTENT

## MATHEMATICS

H. Deka, J. Sarma

**A numerical investigation of modified Burgers' equation in dusty plasmas with non-thermal ions and trapped electrons** 5

T.K. Yuldashev, A.K. Fayziyev

**Inverse problem for a second order impulsive system of integro-differential equations with two redefinition vectors and mixed maxima** 13

M.I. Muminov, Z.Kh. Ochilov

**An inversion formula for the weighted Radon transform along family of cones** 22

C. Parkash, W.C. Parke, P. Singh

**Exact irregular solutions to radial Schrödinger equation for the case of hydrogen-like atoms** 28

## PHYSICS

R. Chaurasiya, S. Dahiya, R. Sharma

**A study of confined Stark effect, hydrostatic pressure and temperature on nonlinear optical properties in 1-D Ga<sub>x</sub>Al<sub>1-x</sub>As/GaAs/Ga<sub>x</sub>Al<sub>1-x</sub>As quantum dots under a finite square well potential** 44

N.N. Konobeeva, M.B. Belonenko

**Tunneling current of contact of fractal object with metal and superlattice** 54

F.M. Goncharov, B.E. Pervushin, B.A. Nasedkin, R.K. Goncharov, D.A. Yashin, M.E. Gellert, D.V. Sulimov, P.A. Morozova, I.M. Filipov, I.A. Adam, V.V. Chistiakov, E.O. Samsonov, V.I. Egorov

**Increase of signal to reference ratio for phase compensation in continuous-variable quantum key distribution systems** 59

Rohit Phogaat, Venkatesh Yepuri

**Performance enhancement of triboelectric nanogenerator using iodine doped PVDF** 69

E.V. Aksenova, A.A. Karetnikov, N.A. Karetnikov, A.P. Kovshik, A.V. Svanidze, S.V. Ul'yanov

**Electric field effect on the light penetration depth and switching times in liquid crystal cells with nonuniform director orientation** 74

R.V. Shalayev, A.I. Izotov, V.V. Syrotkin  
**Electrical properties of “metal-carbon film” contact** 86

## **CHEMISTRY AND MATERIAL SCIENCE**

A.D. Shirokikh, V.A. Anikina, E.A. Zamyatina, E.V. Mishchenko,  
M.Y. Koroleva, V.K. Ivanov, N.R. Popova  
**Bioavailability of nanoemulsions modified with curcumin  
and cerium dioxide nanoparticles** 89

Y.D. Kaldante, M.G. Chaskar  
**A comparative study of photocatalytic degradation of Xylenol  
Orange dye under natural sunlight over ZnO nanoparticles  
synthesized via mechanochemical and hydrothermal  
assistance routes** 98

A.A. Valeeva, I.B. Dorosheva, A.A. Sushnikova  
**Influence of high energy milling on titanium oxide  $Ti_3O_5$   
crystal structure** 107

T.O. Kozlova, D.N. Vasilyeva, D.A. Kozlov, M.A. Teplonogova,  
A.E. Baranchikov, N.P. Simonenko, V.K. Ivanov  
**Synthesis and thermal behavior of  $KCe_2(PO_4)_3$ , a new full-member  
in the  $A^I M^{IV}_2(PO_4)_3$  family** 112

O.V. Proskurina, R.Sh. Abiev, V.N. Nevedomsky  
**Influence of using different types of microreactors on the formation  
of nanocrystalline  $BiFeO_3$**  120

R.R. Kabulov, F.A. Akbarov, A.A. Alimov  
**Time of transition processes in a CdS-CIGS structural solar cells  
in the short-wave part of the absorption spectrum at different  
loading resistances** 127

Yu.A. Avdeeva, I.V. Luzhkova, A.M. Murzakaev, A.N. Ermakov  
**Plasma-chemical synthesis of nanocrystalline “core-shell” structures  
 $TiN-Mo-Co$**  132

## **ERRATUM**

B.V. Vasil'ev, R.Yu. Smyslov, D.A. Kirilenko, A.N. Bugrov  
**Correction to the paper "Synthesis and magnetic properties  
of cobalt ferrite nanoparticles formed under hydro  
and solvothermal condition"** 142

**Information for authors** 144

## A numerical investigation of modified Burgers' equation in dusty plasmas with non-thermal ions and trapped electrons

Harekrishna Deka<sup>1,a</sup>, Jnanjyoti Sarma<sup>2,b</sup><sup>1</sup>K. K. Handiqui State Open University, Department of Mathematics, Khanapara, Guwahati, 781022, India<sup>2</sup>R. G. Baruah College, Fatasil Ambari, Guwahati, 781025, India<sup>a</sup>harekrishnadeka11@gmail.com, <sup>b</sup>sjnanjyoti@gmail.com

Corresponding author: Harekrishna Deka, harekrishnadeka11@gmail.com

PACS 02.70Bf, 52.27Lw, 52.35Fp, 52.35Tc

**ABSTRACT** In this paper, one-dimensional lower order modified Burgers' equation (MBE) in dusty plasmas having non-thermal ions and trapped electrons is investigated numerically by finite difference explicit method. The numerical results obtained by the finite difference explicit method for various values of the nonlinear and dissipative coefficients have been compared with the analytical solutions. The obtained numerical results are found to have good agreement with the analytical solutions. It is found that the nonlinear and dissipative coefficients have very important effect on the dust acoustic waves in the system. The absolute error between the analytical and the numerical solutions of the MBE is demonstrated. The stability condition is derived in terms of the equation parameters and the discretization using the von Neumann stability analysis. It has been observed that the waves become flatten and steeper when the dissipative coefficient decreases. It can be concluded that the finite difference explicit method is suitable and efficient method for solving the modified Burgers' equation.

**KEYWORDS** plasma, dusty plasmas, non-thermal ions, reductive perturbation method, modified Burgers' equation, finite difference explicit method, von Neumann stability analysis

**FOR CITATION** Deka H., Sarma J. A numerical investigation of modified Burgers' equation in dusty plasmas with non-thermal ions and trapped electrons. *Nanosystems: Phys. Chem. Math.*, 2023, **14** (1), 5–12.

### 1. Introduction

In the last few decades, many researchers studied the electrostatic and electromagnetic waves propagation in dusty plasmas in various environments such as in the upper part of the Earth atmosphere, planetary rings, comet tails, interstellar space, the solar atmosphere and low temperature plasmas in laboratory [1–3]. Many authors [4, 5] investigated the effect of higher order nonlinearity for dusty plasma considering the negative ions and hot isothermal as well as non-isothermal electrons. Asgari et al. [6] derived the nonlinear Burgers' equation with a non-thermal ion in dusty plasma environment. Many authors [7–9] also investigated the nonlinear behaviors of electrostatic waves in a dusty plasma with trapped particles as well as in unmagnetized and magnetized plasmas. Dev et al. [10] have investigated the wave propagation in a non-magnetized and warm dusty plasma containing trapped electrons as well as non-thermal positive and negative ions under the influence of lower order nonlinearity. In this paper, we deal with the nonlinear modified Burgers' equation in dusty plasmas having negative and positive non-thermal ions with trapped electrons. The finite difference method was first developed by Thomas in 1920 to solve nonlinear hydrodynamic equations [11]. Finite difference methods are the first techniques for numerical solving of nonlinear partial differential equations [12]. The most commonly used finite difference methods for the solution of partial differential equations are as follows: Explicit method, Implicit method and Crank Nicolson method. Many authors applied finite difference explicit method to obtain numerical solutions of nonlinear partial differential equations. The modified Burgers' equation is a nonlinear expansion of the Burgers' equation. There are several methods proposed for solving the modified Burgers' equation that can be briefly presented as follows.

Bratsos et al. [13] applied a finite difference scheme for calculating the numerical solution of the modified Burgers' equation. A collocation method based on quantic splines was proposed by Ramadan and El-Danaf [14]. Irk [15] also proposed the sextic B-spline collocation method for numerical solution of the modified Burgers' equation. Aswin and Awasthi [16] have solved the modified Burgers' equation using iterative differential quadrature algorithms. Roshan and Sharma [17] solved the modified Burgers' equation by the Petrov–Galerkin method. Grienwank and El-Danaf [18] have employed a non-polynomial spline based method to obtain numerical solutions of the modified Burgers' equation. Duan et al. [19] proposed Lattice Boltzmann method to obtain numerical solution of modified Burgers' equation. Bashan et al. [20] used quintic B-spline Differential Quadrature method to solve modified Burgers' equation. Ucar et al. [21] proposed the finite difference method for numerical solution of the modified Burgers' equation. Karakoc et al. [22] have proposed the

quartic B-spline subdomain finite element method (SFEM) for finding the numerical solution of the Burgers' equation and modified Burgers' equation. In the paper, we have used the finite difference explicit method to obtain the numerical solution of the modified Burgers' equation in dusty plasmas having non-thermal ions and trapped electrons. The finite difference approximation to partial derivatives can be obtained from Taylor series expansion using either the backward, forward or central difference approximations. The paper is organized in the following manner. In section 2, we discuss the basic equations governing the proposed dusty plasma system, modified Burgers' equation with trapped electrons and reductive perturbation technique. In section 3, the stability analysis of the finite difference explicit method is presented. We include the solutions and discussion of numerical results in section 4. Conclusion is given in section 5.

## 2. Basic equations and Modified Burgers' Equation

The basic equations, governing the dynamical system, of the dust particles in a one-dimensional dust acoustic wave for the dusty plasma is as follows [10]:

$$\frac{\partial n_d}{\partial t} + \frac{\partial}{\partial x} (n_d v_d) = 0, \quad (1)$$

$$\frac{\partial v_d}{\partial t} + v_d \frac{\partial v_d}{\partial x} + \frac{1}{m_d n_d} \frac{\partial p_d}{\partial x} = -\frac{q_d}{m_d} \frac{\partial \psi}{\partial x} + \mu \frac{\partial^2 v_d}{\partial x^2}, \quad (2)$$

$$\frac{\partial p_d}{\partial t} + v_d \frac{\partial p_d}{\partial x} + \gamma p_d \frac{\partial v_d}{\partial x} = 0, \quad (3)$$

$$\frac{\partial^2 \psi}{\partial x^2} = 4\pi e (n_e + n_n - n_p + z_d n_d), \quad (4)$$

where  $n_d$  is the number density of the negatively charged dust particles in the plasma,  $v_d$  is the dust fluid velocity,  $\psi$  is the electrostatic potential,  $z_d$  is the number of electrons residing on the dust surface at equilibrium,  $p_d$  is the pressure of the dust fluid,  $e$  is the electron charge and  $m_d$  is the mass of the dust particle and  $\gamma = 3$  is the adiabatic index. The non-thermal number densities of positive ions  $n_p$  and negative ions  $n_n$  can be expressed by the using the following relations [23]:

$$n_p = n_{p0} (1 + \alpha\phi + \alpha\phi^2) \exp(-\phi), \quad (5)$$

$$n_n = n_{n0} \left\{ 1 + \alpha\sigma_p\phi + \alpha(\sigma_p)^2 \right\} \exp(z_n\sigma_p\phi) \quad (6)$$

with  $\alpha = \frac{4\gamma_1}{1 + 3\gamma_1}$ , where  $\gamma_1$  represents the population of the non-thermal ions, and  $\sigma_p = \frac{T_p}{T_n}$ . Also,  $z_p(z_n)$  is the positive (negative) ion's charge state,  $T_e$  is the electron temperature and  $T_p(T_n)$  is the positive ion (negative ion) temperatures.

The electron density in the presence of trapped electron can be expressed by using the following relations [7, 24]:

$$n_e = n_{e0} \left\{ 1 + (\beta\phi) - b(\beta\phi)^{3/2} + \frac{1}{2}(\beta\phi)^2 - \dots \right\}, \quad (7)$$

where  $\beta = \frac{T_p}{T_e}$ ,  $b = \frac{4(1 - \gamma_2)}{3\sqrt{\pi}}$  and the parameter  $\gamma_2$  is as follows  $\gamma_2 = \frac{T_{ef}}{T_{et}}$ , with  $T_{ef}$  and  $T_{et}$  being the temperatures of free electrons and trapped electrons in plasma, respectively.

The parameter  $\gamma_2$  determines the nature of the distribution function, giving a plateau if  $\gamma_2 = 0$  and a dip if  $\gamma_2 < 0$  and a hump shape if  $\gamma_2 > 0$ . However,  $\gamma_2 = 1$  corresponds to the Maxwellian distribution of the electrons. In the present plasma system, the range of  $\gamma_2$  will be considered as  $0 < \gamma_2 < 1$  for non-isothermal (trapped) electrons.

Now,  $N_d$  dust number density is normalized to its equilibrium value  $n_{d0}$ ,  $V_d$  dust-fluid velocity is normalized to  $C_{sd} = \left( \frac{Z_d k_B T_p}{m_d} \right)^{1/2}$ ,  $\phi$  is the DA wave's potential normalized to  $\frac{k_B T_p}{e}$ , where  $k_B$  is the Boltzmann constant, the time

variable  $T$  is normalized to  $\omega_{pd}^{-1} = \left( \frac{m_d}{4\pi n_{d0} z_d^2 e^2} \right)^{1/2}$ , the space variable  $X$  is normalized to  $\lambda_{Dd}^{-1} = \left( \frac{4\pi n_{d0} z_d^2 e^2}{k_B T_p} \right)^{1/2}$ , and pressure  $p_d$  is normalized to  $p_d = n_{d0} k_B T_d$ .

The normalized forms of the basic equations (1 – 4) are as follows

$$\frac{\partial N_d}{\partial T} + \frac{\partial}{\partial X} (N_d V_d) = 0, \quad (8)$$

$$N_d \frac{\partial V_d}{\partial T} + N_d V_d \frac{\partial V_d}{\partial X} + \sigma_d \frac{\partial P_d}{\partial X} = N_d \frac{\partial \phi}{\partial X} + \eta \frac{\partial^2 V_d}{\partial X^2}, \quad (9)$$

$$\frac{\partial P_d}{\partial T} + V_d \frac{\partial P_d}{\partial X} + 3P_d \frac{\partial V_d}{\partial X} = 0, \quad (10)$$

$$\frac{\partial^2 \phi}{\partial X^2} = p_1 \phi - p_2 \phi^{3/2} + p_3 \phi^2 - p_4 \phi^{5/2} + (N_d - 1) \quad (11)$$

with the overall charge neutrality condition

$$n_{e0} = n_{p0} - Z_d n_{d0} - n_{n0} \quad (12)$$

and

$$\begin{aligned}\mu_p &= \frac{n_{p0}}{Z_d n_{d0}}, \quad \sigma_d = \frac{T_d}{Z_d T_p}, \quad \mu_n = \frac{n_{n0}}{Z_d n_{d0}}, \quad \frac{n_{e0}}{Z_d n_{d0}} = \mu_p - \mu_n - 1, \quad \eta = \frac{\mu}{\omega_p d \lambda_D^2}, \\ p_1 &= \{(\mu_p - \mu_n - 1)\beta + \mu_n(z_n + \alpha\sigma) - \mu_n(\alpha - z_p)\}, \\ p_2 &= b(\mu_p - \mu_n - 1)\beta^{3/2}, \\ p_3 &= \left\{(\mu_p - \mu_n - 1)\frac{\beta}{2} + \mu_n\left(\frac{(z_n)^2}{2} + \alpha\sigma z_n + \alpha(\sigma)^2\right) - \mu_p\left(\frac{(z_p)^2}{2} - \alpha z_p + \alpha\right)\right\}\end{aligned}$$

and

$$p_4 = (\mu_p - \mu_n - 1)b\beta^{5/2}.$$

The modified Burgers' equation for the propagation of small and finite amplitude dust-acoustic shock waves (DASWs) is derived. Here the independent variables  $\xi$  and  $\tau$  are the new stretched variables given by  $\xi = \epsilon^{1/2}(x - V_0 t)$  and  $\tau = \epsilon t$ , where  $V_0$  is the phase speed (normalized to  $C_{sd}$ ) and  $\epsilon$  is a small parameter ( $0 < \epsilon < 1$ ) which measures the weakness of the dispersion. The dependent variables  $N_d, V_d, P_d$  and  $\phi$  can be expanded in the power series as follows [10]:

$$N_d = 1 + \epsilon N_d^{(1)} + \epsilon^{3/2} N_d^{(2)} + \dots, \quad (13)$$

$$V_d = \epsilon V_d^{(1)} + \epsilon^{3/2} V_d^{(2)} + \dots, \quad (14)$$

$$P_d = 1 + \epsilon P_d^{(1)} + \epsilon^{3/2} P_d^{(2)} + \dots, \quad (15)$$

$$\phi = \epsilon \phi^{(1)} + \epsilon^{3/2} \phi^{(2)} + \epsilon^2 \phi^{(3)} + \dots \quad (16)$$

Substituting the stretched coordinates and the expression for  $N_d, V_d, P_d$  and  $\phi$  into the normalized basic equations (8–11) and equating the coefficients of lower order in  $\epsilon$ , the required lower order modified Burgers' equation is obtained

$$\frac{\partial \phi^{(1)}}{\partial \tau} + A(\phi^{(1)})^{1/2} \frac{\partial \phi^{(1)}}{\partial \xi} = B \frac{\partial^2 \phi^{(1)}}{\partial \xi^2}, \quad (17)$$

where the nonlinear coefficient  $A$  and dissipative coefficient  $B$  are given by the following expressions

$$A = \frac{3p_2(V_0^2 - 3\sigma_d)}{4p_1 V_0}, \quad B = \frac{\eta}{2}. \quad (18)$$

Equation (17) represents the well-known lower order modified Burgers' equation describing the nonlinear propagation of dust-acoustic shock waves in electronegative dusty plasma with non-thermal ions and trapped electrons.

The stationary shock wave solution of the modified Burgers' equation (17) is obtained by transforming independent variables  $\xi$  and  $\tau$  to  $\xi = \zeta - U_0 \tau'$  and  $\tau = \tau'$  where  $U_0$  is the speed of the shock waves.

Now, the analytical solution of the modified Burgers' equation is given by the formula

$$\phi^{(1)} = \left\{ \phi_{m1} \left\{ 1 - \tanh\left(\frac{\xi}{\delta_1}\right) \right\} \right\}^2, \quad (19)$$

where  $\phi_{m1} = \frac{3M}{4A}$  and  $\delta_1 = \frac{4B}{M}$  are the amplitude and the width of the shock waves, respectively, and  $M$  is the Mach number.

### 3. Stability analysis of the explicit finite difference method

In this section, the stability of the finite difference explicit method is investigated by using von Neumann stability analysis. The von Neumann stability theory in which the growth factor of a Fourier mode is defined as  $u_{i,j} = \xi^j e^{I k h i} = \xi^j e^{I \theta i}$  where  $I = \sqrt{-1}$ ,  $\xi^j$  is the amplitude at time level  $k$  is the wave number and  $h = \Delta x$ .

To investigate the stability of the numerical scheme, the non-linear term  $u^{1/2}u$  of the modified Burgers' equation has been linearized by putting  $u^{1/2} = L$ , where  $L$  is constant.

From (29):

$$\begin{aligned}u_{i,j+1} &= u_{i,j} + \frac{kAL}{2h} [u_{i-1,j} - u_{i+1,j}] + \frac{kB}{h^2} [u_{i+1,j} - 2u_{i,j} + u_{i-1,j}], \\ u_{i,j+1} &= \left(1 - \frac{2kB}{h^2}\right) u_{i,j} + \left(\frac{kAL}{2h} + \frac{kB}{h^2}\right) u_{i-1,j} + \left(\frac{kB}{h^2} - \frac{kAL}{2h}\right) u_{i+1,j}.\end{aligned}$$

Substitute  $u^{1/2} = L$  in the above equation, we get

$$\begin{aligned}\xi^j e^{I \theta i} \xi &= \xi^j e^{I \theta i} \left[ \left(1 - \frac{2kB}{h^2}\right) + \left(\frac{kAL}{2h} + \frac{kB}{h^2}\right) e^{-I \theta} + \left(\frac{kB}{h^2} - \frac{kAL}{2h}\right) e^{I \theta} \right], \\ \xi &= \left(1 - \frac{2kB}{h^2}\right) + \left(\frac{kAL}{2h} + \frac{kB}{h^2}\right) e^{-I \theta} + \left(\frac{kB}{h^2} - \frac{kAM}{2h}\right) e^{I \theta},\end{aligned}$$

$$\begin{aligned}\xi &= \left(1 - \frac{2kB}{h^2}\right) + \frac{kAL}{2h} (e^{-I\theta} - e^{I\theta}) + \frac{kB}{h^2} (e^{I\theta} + e^{-I\theta}), \\ \xi &= \left(1 - \frac{2kB}{h^2}\right) + \frac{kAL}{2h} (-2I \sin \theta) + \frac{kB}{h^2} 2 \cos \theta, \\ \xi &= \left(1 - \frac{2kB}{h^2}\right) - \frac{kAL}{h} \sin \theta + \frac{2kB}{h^2} \cos \theta.\end{aligned}$$

The stability condition for the numerical scheme is as follows

$$\begin{aligned}|\xi| &\leq 1, \\ |\xi| &= \left| \left(1 - \frac{2kB}{h^2}\right) - \frac{kAL}{h} \sin \theta + \frac{2kB}{h^2} \cos \theta \right| \leq 1.\end{aligned}$$

So the stability condition is  $\frac{2kB}{h^2} \leq 1$  or  $k \leq \frac{h^2}{2B}$ . And thus restricts the allowable temporal step size. Since not all choices of spatial and temporal steps lead to convergent, the explicit scheme (29) is called conditionally stable.

#### 4. Numerical results and discussion

It has been shown in Section 2 that the modified Burgers' equation has an analytical solution in the form (19). In this paper, the modified Burgers' equation (17) in dusty plasmas with non-thermal ions and trapped electrons is solved by the explicit finite difference method and the numerical results are compared with the analytical solutions.

For simplicity, we consider  $\phi^{(1)}(\zeta, \tau) = u(x, t) \cong u(i\Delta x, j\Delta t) \cong u_{i,j}$ .

Equation (17) can be expressed as

$$\frac{\partial u}{\partial t} + Au^{1/2} \frac{\partial u}{\partial x} = B \frac{\partial^2 u}{\partial x^2}. \quad (20)$$

For convenience, we put  $M = \frac{1}{2}$ ,  $U_0 = \frac{1}{2}$ ,  $\phi_{m1} = \frac{3}{8A}$  and  $\delta_1 = \frac{4B}{M} = 8B$  in (19).

The analytical solution of the modified Burgers' equation is given by the following expression

$$u(x, t) = \left\{ \frac{3}{8A} \left\{ 1 - \tanh \frac{1}{8B} \left( x - \frac{t}{2} \right) \right\} \right\}^2. \quad (21)$$

The boundary and the initial conditions are taken from the exact solution. In this paper, the numerical solutions of (20) will be sought for the following initial and boundary conditions. In the interval  $0 \leq x \leq 1$ ,  $t \geq 0$ , and with the initial condition

$$u(x, 0) = \left\{ \frac{3}{8A} \left\{ 1 - \tanh \frac{x}{8B} \right\} \right\}^2 \quad (22)$$

and the boundary conditions

$$u(0, t) = \left\{ \frac{3}{8A} \left\{ 1 + \tanh \frac{t}{16B} \right\} \right\}^2, \quad (23)$$

$$u(1, t) = \left\{ \frac{3}{8A} \left\{ 1 - \tanh \frac{1}{8B} \left( 1 - \frac{t}{2} \right) \right\} \right\}^2. \quad (24)$$

We discretize the modified Burgers' equation by replacing  $\frac{\partial u}{\partial t}$  by the forward difference and  $\frac{\partial u}{\partial x}$  and  $\frac{\partial^2 u}{\partial x^2}$  by the central difference approximation, i.e. as follows

$$\frac{\partial u}{\partial t} \approx \frac{u_{i,j+1} - u_{i,j}}{k}, \quad (25)$$

$$\frac{\partial^2 u}{\partial x^2} \approx \frac{u_{i-1,j} - 2u_{i,j} + u_{i+1,j}}{h^2}, \quad (26)$$

$$\frac{\partial u}{\partial x} \approx \frac{u_{i+1,j} - u_{i-1,j}}{2h}. \quad (27)$$

Thus, (20) becomes as follows

$$\frac{u_{i,j+1} - u_{i,j}}{k} + Au_{i,j}^{1/2} \left[ \frac{u_{i+1,j} - u_{i-1,j}}{2h} \right] = B \left[ \frac{u_{i+1,j} - 2u_{i,j} + u_{i-1,j}}{h^2} \right], \quad (28)$$

which can be simplified

$$u_{i,j+1} = u_{i,j} + \frac{kA}{2h} u_{i,j}^{1/2} [u_{i-1,j} - u_{i+1,j}] + \frac{kB}{h^2} [u_{i+1,j} - 2u_{i,j} + u_{i-1,j}]. \quad (29)$$

By the von Neumann stability condition, we consider the space steps  $h = 0.01$ , the time steps  $k = 0.005, 0.001$  and  $0.0005$  and  $B = 0.01, 0.05$  and  $0.1$ . The nonlinear coefficient  $A$  is a function of  $p_1, p_2, \sigma_d$  and  $V_0$ . During the solution process, we consider  $A = 1, 1.5$  and  $2$ . Numerical solutions are obtained for different values of  $B$  and  $A$ . The obtained figures of the numerical results are compared with the figures obtained from the analytical solutions which are displayed in Figs. 1–3.

The accuracy of the present method is measured using the absolute error which is defined as  $|u_i^{\text{Analytical}} - u_i^{\text{Numerical}}|$ .

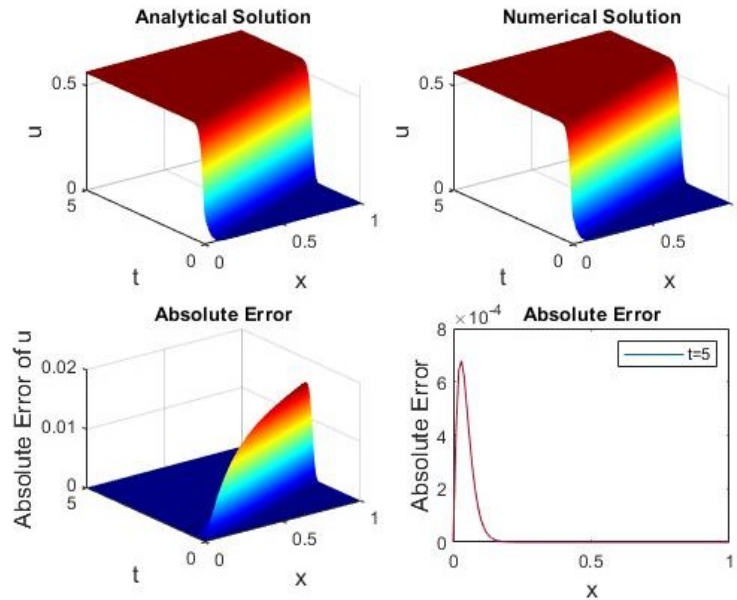


FIG. 1. Graph of analytical and numerical solutions with absolute error at  $A = 1, B = 0.01, h = 0.01, k = 0.005$

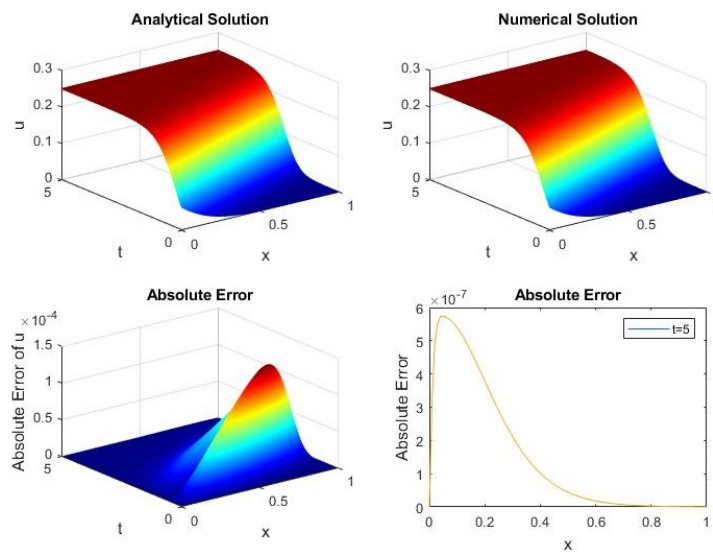


FIG. 2. Graph of analytical and numerical solutions with absolute error at  $A = 1.5, B = 0.05, h = 0.01, k = 0.001$

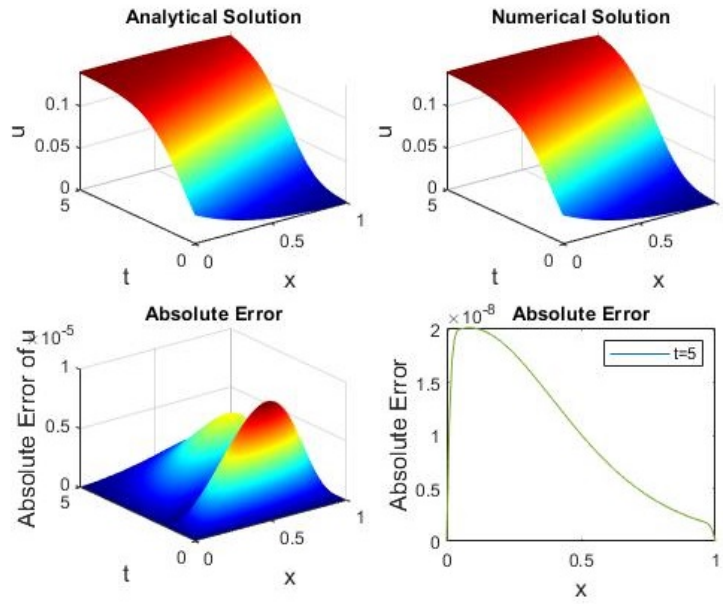


FIG. 3. Graph of analytical and numerical solutions with absolute error at  $A = 2, B = 0.1, h = 0.01, k = 0.0005$

The analytical solutions and the computed numerical results together with their errors are plotted in Figs. 1 to 3 for various values of the nonlinear coefficient and the dissipative coefficient. But the graphs of the errors have been drawn at time  $t = 5$ . It can be seen that the maximal error occurs at the left hand boundary when the greater value of the dissipative coefficient  $B = 0.1$  is considered and the maximal error is found around the location where the shock wave has the highest amplitude with the smaller value of the dissipative coefficient  $B = 0.01$ . It can be concluded that as the value of  $x$  increases, the errors gradually decreases and it is also seen that as the value of the dissipation coefficient increase, the error will increase.

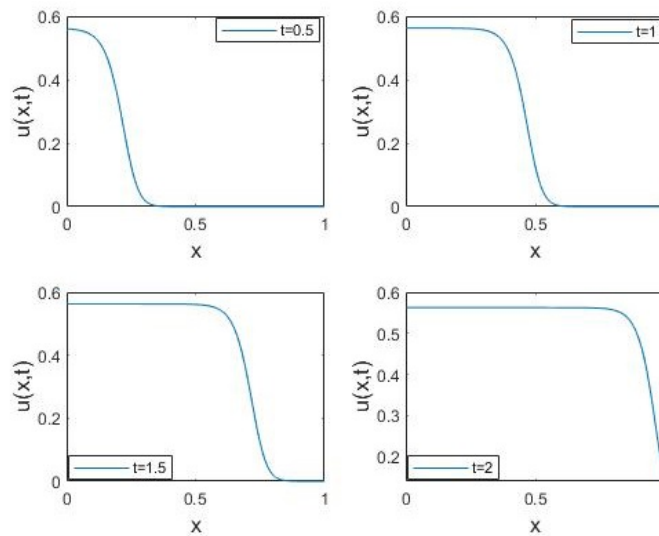


FIG. 4. The numerical solutions with  $A = 1, B = 0.01, h = 0.01, k = 0.0005$  at  $t = 0.5, 1, 1.5, 2$

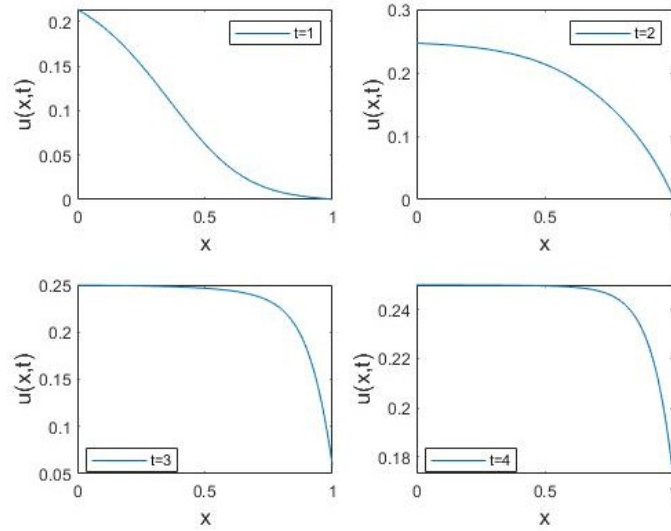


FIG. 5. The numerical solutions with  $A = 1.5, B = 0.05, h = 0.01, k = 0.001$  at  $t = 1, 2, 3, 4$

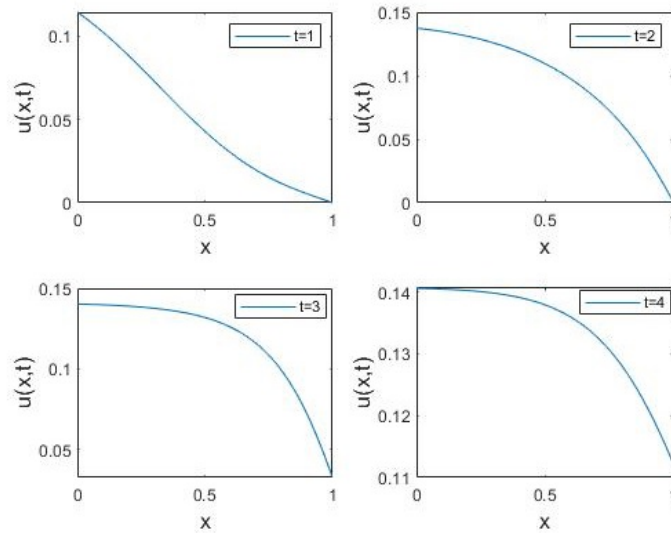


FIG. 6. The numerical solutions with  $A = 2, B = 0.1, h = 0.01, k = 0.0005$  at  $t = 1, 2, 3, 4$

The computed numerical results for various values of the nonlinear coefficient and the dissipative coefficient at different times are plotted in Figs. 4 to 6. From the figures, it has been observed that as the time increases, the curve of the numerical solution decays.

### 5. Conclusion

In this paper, the finite difference explicit method has been successfully used for obtaining the numerical solution of the modified Burgers' equation in dusty plasmas having non-thermal ions with trapped electrons. It is obtained using finite difference explicit method. Graphs have been plotted to show a comparison between the analytical and the numerical solutions for various values of the dissipative coefficient. The obtained numerical results show good accuracy when comparing it with the analytical results for various values of the dissipative coefficient. The absolute error has been computed and presented in graphical form. The effects of the nonlinear coefficient and the dissipative coefficient on the shock strength and steepness are investigated. It is found that the shock wave steepness depends more on the dissipative coefficient than on the nonlinear coefficient. In this study, it has been seen that when the dissipative coefficient decreases, the shock waves become flatten and the propagation front becomes steeper. In conclusion, it has been observed that the dissipative coefficient in dusty plasmas having non-thermal ions and trapped electrons plays an important role to dissipate the acoustic shock wave while propagating through the system.

## References

- [1] Goertz C. Dusty plasmas in the solar system. *Reviews of Geophysics*, 1989, **27** (2), P. 271–292.
- [2] Adhikary N.C., Deka M.K., Bailung H. Observation of rarefactive ion acoustic solitary waves in dusty plasma containing negative ions. *Physics of Plasmas*, 2009, **16** (6), 063701.
- [3] Deka M., Adhikary A., Misra A., Bailung H., Nakamura Y. Characteristics of ion-acoustic solitary wave in a laboratory dusty plasma under the influence of ion-beam. *Physics of Plasmas*, 2012, **19** (10), 103704.
- [4] Tagare S., Reddy R.V. Effect of higher-order nonlinearity on propagation of nonlinear ion-acoustic waves in a collisionless plasma consisting of negative ions. *J. of Plasma Physics*, 1986, **35** (2), P. 219–237.
- [5] El-Labany S. Contribution of higher-order nonlinearity to nonlinear ion-acoustic waves in a weakly relativistic warm plasma. Part I. Isothermal case. *J. of Plasma Physics*, 1993, **50** (3), P. 495–504.
- [6] Asgari H., Muniandy S., Wong C. Dust-acoustic shock formation in adiabatic hot dusty plasmas with variable charge. *Physics of Plasmas*, 2011, **18** (1), 013702.
- [7] Schamel H. A modified Korteweg-de Vries equation for ion acoustic waves due to resonant electrons. *J. of Plasma Physics*, 1973, **9** (3), P. 377–387.
- [8] Mamun A., Cairns R., Shukla P. Effects of vortex-like and nonthermal ion distributions on non-linear dust-acoustic waves. *Physics of Plasmas*, 1996, **3** (7), P. 2610–2614.
- [9] Javidan K., Pakzad H. Obliquely propagating electron acoustic solitons in a magnetized plasma with superthermal electrons. *Indian J. of Physics*, 2013, **87** (1), P. 83–87.
- [10] Dev A.N., Deka M.K., Sarma J., Adhikary N.C. Shock wave solution in a hot adiabatic dusty plasma having negative and positive non-thermal ions with trapped electrons. *J. of the Korean Physical Society*, 2015, **67** (2), P. 339–345.
- [11] Smith G.D., Smith G.D., Smith G.D.S. *Numerical solution of partial differential equations: finite difference methods*. Oxford University Press, 1985.
- [12] Dehghan M. Parameter determination in a partial differential equation from the overspecified data. *Mathematical and Computer Modelling*, 2005, **41** (2–3), P. 196–213.
- [13] Bratsos A., Petrakis L. An explicit numerical scheme for the modified burgers' equation. *Int. J. for Numerical Methods in Biomedical Engineering*, 2011, **27** (2), P. 232–237.
- [14] Ramadan M.A., El-Danaf T.S. Numerical treatment for the modified burgers equation. *Mathematics and Computers in Simulation*, 2005, **70** (2), P. 90–98.
- [15] Irk D. Sextic B-spline collocation method for the modified Burgers' equation. *Kybernetes*, 2009, **38** (9), P. 1599–1620.
- [16] Aswin V., Awasthi A. Iterative differential quadrature algorithms for modified burgers equation. *Engineering Computations*, 2018, **35** (1), P. 235–250.
- [17] Roshan T., Bhamra K. Numerical solutions of the modified Burgers' equation by Petrov-Galerkin method. *Applied Mathematics and Computation*, 2011, **218** (7), P. 3673–3679.
- [18] Griewank A., El-Danaf T.S. Efficient accurate numerical treatment of the modified Burgers' equation. *Applicable Analysis*, 2009, **88** (1), P. 75–87.
- [19] Duan Y., Liu R., Jiang Y. Lattice Boltzmann model for the modified Burgers' equation. *Applied Mathematics and Computation*, 2008, **202** (2), P. 489–497.
- [20] Bashan A., Karakoc S.B.G., Geyikli T. B-spline differential quadrature method for the modified Burgers' equation. *Cankaya University J. of Science and Engineering*, 2015, **12** (1), P. 1–13.
- [21] Ucar A., Yagmurcu N.M., Tasbozan O. Numerical solutions of the modified Burgers' equation by finite difference methods. *J. of Applied Mathematics, Statistics and Informatics*, 2017, **13** (1), P. 19–30.
- [22] Karakoc S.B.G., Bashan A., Geyikli T. Two different methods for numerical solution of the modified Burgers' equation. *The Scientific World J.*, 2014, **2014**, 780269.
- [23] Adhikary A., Deka M., Dev A., Sarmah J. Modified Korteweg-de Vries equation in a negative ion rich hot adiabatic dusty plasma with non-thermal ion and trapped electron. *Physics of Plasmas*, 2014, **21** (8), 083703.
- [24] Schamel H. Stationary solitary, snoidal and sinusoidal ion acoustic waves. *Plasma Physics*, 1972, **14** (10), 905.

---

*Submitted 13 September 2022; revised 10 December 2022; accepted 13 December 2022*

### *Information about the authors:*

*Harekrishna Deka* – K. K. Handiqui State Open University, Department of Mathematics, Khanapara, Guwahati, 781022, India; ORCID 0000-0003-4280-3728; harekrishnadeka11@gmail.com

*Jnanjyoti Sarma* – R. G. Baruah College, Fatasil Ambari, Guwahati, 781025, India; ORCID 0000-0002-0793-5680; sjnanjyoti@gmail.com

*Conflict of interest:* There is no conflict of interest in this research paper.

## Inverse problem for a second order impulsive system of integro-differential equations with two redefinition vectors and mixed maxima

Tursun K. Yuldashev<sup>1,a</sup>, Aziz K. Fayziyev<sup>1,b</sup>

<sup>1</sup>Tashkent State University of Economics, Tashkent, Uzbekistan

<sup>a</sup>tursun.k.yuldashev@gmail.com, <sup>b</sup>fayziyev.a@inbox.ru

Corresponding author: T. K. Yuldashev, tursun.k.yuldashev@gmail.com

**ABSTRACT** An inverse problem for a second order system of ordinary integro-differential equations with impulsive effects, mixed maxima and two redefinition vectors is investigated. A system of nonlinear functional integral equations is obtained by applying some transformations. The existence and uniqueness of the solution of the nonlinear inverse problem is reduced to the unique solvability of the system of nonlinear functional integral equations in Banach space  $PC([0, T], \mathbb{R}^n)$ . The method of successive approximations in combination with the method of compressing mapping is used in the proof of unique solvability of the nonlinear functional integral equations. Then values of redefinition vectors are founded.

**KEYWORDS** inverse problem, second order system, impulsive integro-differential equations, two-point nonlinear boundary value conditions, two redefinition vectors, mixed maxima, existence and uniqueness of solution.

**FOR CITATION** Yuldashev T.K., Fayziyev A.K. Inverse problem for a second order impulsive system of integro-differential equations with two redefinition vectors and mixed maxima. *Nanosystems: Phys. Chem. Math.*, 2023, **14** (1), 13–21.

### 1. Introduction

It is known that the dynamics of evolving processes undergoes sometimes abrupt changes, for example, upheavals, natural disasters and shocks. Such short-term, but very painful, perturbations are often interpreted as impulses. That is, we actually have a dynamic system with impulsive actions. Dynamic systems with mixed maxima naturally describe processes with impulsive actions. It is presented by differential equations having solutions with first kind "discontinuities" at fixed or non-fixed time moments. This type of differential and integro-differential equations have applications in biological, chemical and physical sciences, ecology, biotechnology, industrial robotic, pharmacokinetics, optimal control, etc. [1–5]. In particular, such kind of problems appear in biophysics at micro- and nano-scales [6–10]. Such differential equations with "discontinuities" at fixed or non-fixed time moments are called differential equations with impulsive effects. There are a lot of publications devoted to differential equations with impulsive effects, which describe many natural and technical processes [11–25].

Two-point and multi-point boundary value problems for the differential and integro-differential equations are studied by many authors (see, for example [26–29]). However, second-order differential equations with nonlocal boundary value conditions and impulsive effects are almost not studied. It is related to the fact that the reduction of such problem to equivalent functional integral equation faces difficulties. In this paper, we investigate an inverse problem for a system of second order integro-differential equations with impulsive effects, two-point nonlinear boundary value conditions and mixed maxima. The questions of existence and uniqueness of the solution to the nonlinear inverse problem are investigated. We note that when studying the solvability problem for the differential and integro-differential equations with mixed maxima one should deal with singularity. Moreover, the jumps of solutions are a natural things for differential equations with mixed maxima [30].

We consider the existence problem and constructive method for calculating the unique solutions of the second order system of nonlinear ordinary integro-differential equations on the interval  $[0, T]$  for  $t \neq t_i$ ,  $i = 1, 2, \dots, p$

$$x''(t) = f\left(t, x(t), \int_0^T \Theta(t, s, \max\{x(\tau) | \tau \in [\lambda_1(s) : \lambda_2(s)]\}) ds\right), \quad (1)$$

where  $t \neq t_i$ ,  $i = 1, 2, \dots, p$ ,  $0 = t_0 < t_1 < \dots < t_p < t_{p+1} = T$ ,  $x \in X$ ,  $X$  is the closed bounded domain in the space  $\mathbb{R}^n$ ,  $f(t, x, y) \in C([0, T] \times X \times Y, \mathbb{R}^n)$ ,  $Y$  is the closed bounded domain in  $\mathbb{R}^n$ ,  $0 < \lambda_j(t) < T$ ,  $j = 1, 2$ ,  $[\lambda_1(t) : \lambda_2(t)] = [\min\{\lambda_1(t), \lambda_2(t)\} ; \max\{\lambda_1(t), \lambda_2(t)\}]$ ,  $\lambda_j(t) = \lambda_j(t, x(t)) \in C([0, T] \times X, \mathbb{R})$ ,  $j = 1, 2$ ,

$$\max_{0 \leq t \leq T} \int_0^T |\Theta(t, s, x)| ds < \infty.$$

We study equation (1) with two nonlinear two-point conditions

$$A_1(t)x(0^+) + B_1(t)x(T^-) = C_1 + D_1(t, x(t)), \quad (2)$$

$$A_2(t)x'(0^+) + B_2(t)x'(T^-) = C_2 + D_2(t, x(t)) \quad (3)$$

and two nonlinear impulsive conditions

$$x(t_i^+) - x(t_i^-) = F_i(x(t_i)), \quad i = 1, 2, \dots, p, \quad (4)$$

$$x'(t_i^+) - x'(t_i^-) = G_i(x(t_i)), \quad i = 1, 2, \dots, p, \quad (5)$$

where  $A_i(t)$ ,  $B_i(t)$  are  $n \times n$ -dimensional matrix-functions,  $C_1 \in \mathbb{R}^n$  and  $C_2 \in \mathbb{R}^n$  are redefinition vectors,  $D_i(t, x(t)) \in C([0, T] \times X, \mathbb{R}^n)$  is nonlinear vector-function,  $i = 1, 2$ ,  $F_i, G_i \in C(X, \mathbb{R}^n)$ ,  $x(t_i^+) = \lim_{\nu \rightarrow 0^+} x(t_i + \nu)$ ,  $x(t_i^-) = \lim_{\nu \rightarrow 0^-} x(t_i - \nu)$  are right-hand side and left-hand side limits of function  $x(t)$  at the point  $t = t_i$ , respectively.

In order to find redefinition vectors, we use the following two intermediate conditions

$$x(\bar{t}) = E_1, \quad E_1 \in \mathbb{R}^n, \quad 0 < \bar{t} < T, \quad \bar{t} \neq t_i, \quad i = 1, 2, \dots, p, \quad (6)$$

$$x'(\bar{t}) = E_2, \quad E_2 \in \mathbb{R}^n, \quad 0 < \bar{t} < T, \quad \bar{t} \neq t_i, \quad i = 1, 2, \dots, p. \quad (7)$$

We use the Banach space  $C([0, T], \mathbb{R}^n)$ , which consists of continuous vector-functions  $x(t)$  on the segment  $[0, T]$  with the norm

$$\|x\| = \sqrt{\sum_{j=1}^n \max_{0 \leq t \leq T} |x_j(t)|}.$$

$PC([0, T], \mathbb{R}^n)$  is the linear vector space:

$$PC([0, T], \mathbb{R}^n) = \{x : [0, T] \rightarrow \mathbb{R}^n; x(t) \in C((t_i, t_{i+1}], \mathbb{R}^n), i = 1, \dots, p\},$$

where  $x(t_i^+)$  and  $x(t_i^-)$  ( $i = 0, 1, \dots, p$ ) exist and they are bounded;  $x(t_i^-) = x(t_i)$ . Note, that the linear vector space  $PC([0, T], \mathbb{R}^n)$  is the Banach space with the following norm

$$\|x\|_{PC} = \max \left\{ \|x\|_{C((t_i, t_{i+1}])}, i = 1, 2, \dots, p \right\}.$$

**Formulation of the problem.** Find a triple of unknown quantities

$$\left\{ x(t) \in PC([0, T], \mathbb{R}^n), C_j \in \mathbb{R}^n, j = 1, 2 \right\},$$

that the function  $x(t)$  satisfies the second-order integro-differential equation (1) for all  $t \in [0, T]$ ,  $t \neq t_i$ ,  $i = 1, 2, \dots, p$ , nonlinear two-point conditions (2), (3) and for  $t = t_i$ ,  $i = 1, 2, \dots, p$ ,  $0 < t_1 < t_2 < \dots < t_p < T$  satisfies the nonlinear limit conditions (4), (5) and intermediate conditions (6), (7).

## 2. Reduction of the direct problem (1)–(5) to nonlinear system of functional integral equations

Let function  $x(t) \in PC([0, T], \mathbb{R}^n)$  be a solution of the second order two-point boundary value problem (1)–(5). Then, integrating the integro-differential equation (1) one time over intervals:  $(0, t_1]$ ,  $(t_1, t_2]$ ,  $\dots$ ,  $(t_p, t_{p+1}] \in [0, T]$ ,  $t_{p+1} = t$ , we obtain:

$$\begin{aligned} \int_0^{t_1} f(x) ds &= \int_0^{t_1} x''(s) ds = x'(t_1^-) - x'(0^+), \\ \int_{t_1}^{t_2} f(s) ds &= \int_{t_1}^{t_2} x''(s) ds = x'(t_2^-) - x'(t_1^+), \\ &\dots \\ \int_{t_p}^{t_{p+1}} f(s) ds &= \int_{t_p}^{t_{p+1}} x''(s) ds = x'(t_{p+1}^-) - x'(t_p^+), \end{aligned}$$

where, for convenience, we put

$$f(t) = f\left(t, x(t), \int_0^T \Theta(t, s, \max\{x(\tau) | \tau \in [\lambda_1(s) : \lambda_2(s)]\}) ds\right).$$

Hence, taking  $x'(0^+) = x'(0)$ ,  $x'(t_{p+1}^-) = x'(t)$  into account, we have on the interval  $(0, T]$

$$\int_0^t f(s) ds = [x'(t_1) - x'(0^+)] + [x'(t_2) - x'(t_1^+)] + \dots + [x'(t) - x'(t_p^+)] =$$

$$= -x'(0) - [x'(t_1^+) - x'(t_1)] - [x'(t_2^+) - x'(t_2)] - \dots - [x'(t_p^+) - x'(t_p)] + x'(t).$$

Taking into account the impulsive condition (5), we rewrite the last equality as follows

$$x'(t) = x'(0) + \int_0^t f(s) ds + \sum_{0 < t_i < t} G_i(x(t_i)). \quad (8)$$

Subordinate the function  $x'(t) \in PC([0, T], \mathbb{R}^n)$  in presentation (8) to satisfy the nonlinear two-point boundary condition (3):

$$x'(T) = x'(0) + \int_0^T f(s) ds + \sum_{0 < t_i < T} G_i(x(t_i)). \quad (9)$$

Substituting (9) into condition (3), we find  $x'(0)$  as follows:

$$x'(0) = Q_2^{-1}(t) \left[ C_2 + D_2(t, x(t)) - B_2(t) \int_0^T f(s) ds - B_2(t) \sum_{0 < t_i < T} G_i(x(t_i)) \right], \quad (10)$$

where  $\det Q_2(t) \neq 0$ ,  $Q_2(t) = A_2(t) + B_2(t)$ .

Substituting (10) into presentation (8), we obtain:

$$x'(t) = Q_2^{-1}(t) \left[ C_2 + D_2(t, x(t)) - B_2(t) \int_0^T f(s) ds - B_2(t) \sum_{0 < t_i < T} G_i(x(t_i)) \right] + \int_0^t f(s) ds + \sum_{0 < t_i < t} G_i(x(t_i)). \quad (11)$$

Then, integrating integro-differential equation (11) one time over the intervals  $(0, t_1]$ ,  $(t_1, t_2]$ ,  $\dots$ ,  $(t_p, t_{p+1}]$  and taking  $x'(0^+) = x'(0)$ ,  $x'(t_{p+1}^-) = x'(t)$  into account, we have on the interval  $(0, T]$ :

$$\begin{aligned} & \int_0^t Q_2^{-1}(s) \left[ C_2 + D_2(s, x(s)) - B_2(s) \int_0^T f(\theta) d\theta - B_2(s) \sum_{0 < t_i < T} G_i(x(t_i)) \right] ds + \\ & + \int_0^t \left[ \int_0^s f(\theta) d\theta + \sum_{0 < t_i < s} G_i(x(t_i)) \right] ds = \\ & = [x(t_1) - x(0^+)] + [x(t_2) - x(t_1^+)] + \dots + [x(t) - x(t_p^+)] = \\ & = -x(0) - [x(t_1^+) - x(t_1)] - [x(t_2^+) - x(t_2)] - \dots - [x(t_p^+) - x(t_p)] + x(t). \end{aligned} \quad (12)$$

Taking into account the nonlinear impulsive condition (4), we derive the following formula from the equality (12)

$$\begin{aligned} x(t) = x(0) + \int_0^t Q_2^{-1}(s) \left[ C_2 + D_2(s, x(s)) - B_2(s) \int_0^T f(\theta) d\theta - B_2(s) \sum_{0 < t_i < T} G_i(x(t_i)) \right] ds + \\ + \int_0^t \left[ \int_0^s f(\theta) d\theta + \sum_{0 < t_i < s} G_i(x(t_i)) \right] ds + \sum_{0 < t_i < t} F_i(x(t_i)). \end{aligned} \quad (13)$$

Applying the two-point nonlinear condition (2) to equation (13), we find the value of  $x(0)$  as follows:

$$\begin{aligned} x(0) = Q_1^{-1}(t) [C_1 + D_1(t, x(t))] - \int_0^T Q_1^{-1}(t) B_1(t) Q_2^{-1}(s) [C_2 + D_2(s, x(s))] ds + \\ + \int_0^T Q_1^{-1}(t) B_1(t) Q_2^{-1}(s) B_2(s) \int_0^T f(\theta) d\theta ds + \\ + \int_0^T Q_1^{-1}(t) B_1(t) Q_2^{-1}(s) B_2(s) \sum_{0 < t_i < t} G_i(x(t_i)) ds - Q_1^{-1}(t) B_1(t) \int_0^T \int_0^s f(\theta) d\theta ds - \\ - Q_1^{-1}(t) B_1(t) \int_0^T \sum_{0 < t_i < t} G_i(x(t_i)) ds - Q_1^{-1}(t) B_1(t) \sum_{0 < t_i < t} F_i(x(t_i)). \end{aligned} \quad (14)$$

When obtaining (14), we used the well known formulas suggested by Dirichlet:

$$\int_0^T g(t, s) \int_0^s f(\theta) d\theta ds = \int_0^T f(s) \int_s^T g(t, \theta) d\theta ds,$$

$$\int_0^T g(t, s) \sum_{0 < t_i < t} I_i(x(t_i)) ds = \sum_{0 < t_i < T} \int_{t_i}^T g(t, s) ds I_i(x(t_i)).$$

Then, we rewrite (14) as follows

$$x(0) = Q_1^{-1}(t) [C_1 + D_1(t, x(t))] - \int_0^T V_0(t, s) [C_2 + D_2(s, x(s))] ds +$$

$$+ \int_0^T V_1(t, s) f(s) ds + \sum_{0 < t_i < T} V_1(t, t_i) G_i(x(t_i)) - Q_1^{-1}(t) B_1(t) \sum_{0 < t_i < T} F_i(x(t_i)), \quad (15)$$

where  $V_0(t, s) = Q_1^{-1}(t) B_1(t) Q_2^{-1}(s)$ ,  $\det Q_1(t) \neq 0$ ,  $Q_1(t) = A_1(t) + B_1(t)$ ,

$$V_1(t, s) = Q_1^{-1}(t) B_1(t) \int_s^T Q_2^{-1}(\theta) [A_2(\theta) + 2B_2(\theta)] d\theta.$$

Substituting (15) into presentation (13), we obtain nonlinear system of functional integral equations:

$$x(t) = Q_1^{-1}(t) [C_1 + D_1(t, x(t))] + \int_0^T W_0(t, s) [C_2 + D_2(s, x(s))] ds +$$

$$+ \int_0^T W_1(t, s) f\left(s, x(s), \int_0^T \Theta\left(s, \theta, \max\{x(\tau) | \tau \in [\lambda_1(\theta) : \lambda_2(\theta)]\}\right) d\theta\right) ds +$$

$$+ \sum_{0 < t_i < T} W_1(t, t_i) G_i(x(t_i)) + \sum_{0 < t_i < T} W_2(t_i) F_i(x(t_i)), \quad (16)$$

where

$$W_0(t, s) = \begin{cases} -V_0(t, s), & t < s \leq T, \\ -V_0(t, s) + Q_2^{-1}(s), & 0 \leq s < t, \end{cases}$$

$$W_1(t, s) = \begin{cases} V_1(t, s), & t < s \leq T, \\ V_1(t, s) - \int_0^t Q_2^{-1}(\theta) B_2(\theta) d\theta + \int_s^t Q_2^{-1}(\theta) [A_2(\theta) + B_2(\theta)] d\theta, & 0 \leq s < t, \end{cases}$$

$$W_2(s) = \begin{cases} -Q_1^{-1}(s) B_1(s), & t < s \leq T, \\ Q_1^{-1}(s) A_1(s), & 0 \leq s < t. \end{cases}$$

In the nonlinear system of functional integral equations (16), the vectors  $C_1$  and  $C_2$  are redefinition vectors. We will redefine these constant vectors  $C_1$  and  $C_2$ .

### 3. Inverse problem (1)–(7)

By virtue of intermediate condition (6), we obtain from presentation (16)

$$C_1 = Q_1(t) E_1 - D_1(t, x(t)) - P(t) C_2 - \int_0^T W_0(t, s) D_2(s, x(s)) ds -$$

$$- \int_0^T W_1(t, s) f\left(s, x(s), \int_0^T \Theta\left(s, \theta, \max\{x(\tau) | \tau \in [\lambda_1(\theta) : \lambda_2(\theta)]\}\right) d\theta\right) ds -$$

$$- \sum_{0 < t_i < T} W_1(t, t_i) G_i(x(t_i)) - \sum_{0 < t_i < T} W_2(t_i) F_i(x(t_i)), \quad (17)$$

where  $P(t) = \int_0^T W_0(t, s) ds$ .

As we see in (17), there is unknown constant vector  $C_2$ . To find  $C_2$ , we use intermediate condition (7). Then, from presentation (11), we have

$$C_2 = Q_2(t)E_2 - D_2(t, x(t)) + \sum_{0 < t_i < T} K_0(t)G_i(x(t_i)) + \int_0^T K_0(t)f\left(s, x(s), \int_0^T \Theta(s, \theta, \max\{x(\tau) | \tau \in [\lambda_1(\theta) : \lambda_2(\theta)]\}) d\theta\right) ds, \quad (18)$$

where

$$K_0(t) = \begin{cases} B_2(t), & t < s \leq T, \\ B_2(t) - Q_2(t), & 0 \leq s < t. \end{cases}$$

Substituting (18) into presentation (17), we obtain

$$C_1 = Q_1(t)E_1 - P(t)Q_2(t)E_2 - D_1(t, x(t)) + P(t)D_2(t, x(t)) - \int_0^T W_0(t, s)D_2(s, x(s)) ds + \int_0^T K_1(t, s)f\left(s, x(s), \int_0^T \Theta(s, \theta, \max\{x(\tau) | \tau \in [\lambda_1(\theta) : \lambda_2(\theta)]\}) d\theta\right) ds + \sum_{0 < t_i < T} K_1(t, t_i)G_i(x(t_i)) - \sum_{0 < t_i < T} W_2(t_i)F_i(x(t_i)), \quad (19)$$

where

$$K_1(t, s) = \begin{cases} -W_1(t, s) - P(t)B_2(t), & t < s \leq T, \\ -W_1(t, s) - P(t)[B_2(t) - Q_2(t)], & 0 \leq s < t. \end{cases}$$

Formulas (18) and (19) allow one to determine constant vectors  $C_1$  and  $C_2$ . However, there is unknown function  $x(t)$  in these expressions. We substitute expressions (18) and (19) into equation (16) and obtain the following nonlinear system of functional integral equations

$$x(t) = J(t; x) \equiv \Phi_0(t) + Q_1^{-1}(t)[D_1(t, x(t)) - D_1(\bar{t}, x(\bar{t}))] + \Phi_1(t)D_2(\bar{t}, x(\bar{t})) + \int_0^T \Phi_2(t, s)D_2(s, x(s)) ds + \int_0^T \Phi_3(t, s)f\left(s, x(s), \int_0^T \Theta(s, \theta, \max\{x(\tau) | \tau \in [\lambda_1(\theta, x(\theta)) : \lambda_2(\theta, x(\theta))]\}) d\theta\right) ds + \sum_{0 < t_i < T} \Phi_3(t, t_i)G_i(x(t_i)) + \sum_{0 < t_i < T} \Phi_4(t, t_i)F_i(x(t_i)), \quad (20)$$

where  $\Phi_0(t) = Q_1^{-1}(t)Q_1^{-1}(\bar{t})E_1 + Q_2(\bar{t})[Q_1^{-1}(t)P(\bar{t}) + P(t)]E_2$ ,  $\Phi_1(t) = Q_1^{-1}(t)P(\bar{t}) - P(t)$ ,

$$\Phi_2(t, s) = Q_1^{-1}(t)W_0(\bar{t}, s) + W_0(t, s), \quad \Phi_3(t, s) = Q_1^{-1}(t)K_1(\bar{t}, s) + P(t)K_0(\bar{t}) + W_1(t, s),$$

$$\Phi_4(t, s) = [1 - Q_1^{-1}(t)]W_2(s).$$

#### 4. Unique solvability

**Theorem.** Suppose that the following conditions are fulfilled:

1).  $M_f = \max_{0 \leq t \leq T} \left| f\left(t, 0, \int_0^T \Theta(t, s, 0) ds\right) \right| < \infty$ ;  $M_{D_j} = \max_{0 \leq t \leq T} |D_j(t, 0)| < \infty$ ,  $j = 1, 2$ ;

2).  $m_F = \max_{i \in \{1, 2, \dots, p\}} |F_i(0)| < \infty$ ,  $m_G = \max_{i \in \{1, 2, \dots, p\}} |G_i(0)| < \infty$ ;

3). For all  $t \in [0, T]$ ,  $x, y \in \mathbb{R}^n$ , the following inequality holds

$$|f(t, x_1, y_1) - f(t, x_2, y_2)| \leq M_1(t) |x_1 - x_2| + M_2(t) |y_1 - y_2|;$$

4). For all  $t, s \in [0, T]^2$ ,  $x \in \mathbb{R}^n$ , the following inequality holds

$$|\Theta(t, s, x_1) - \Theta(t, s, x_2)| \leq M_3(t, s) |x_1 - x_2|;$$

5). For all  $t \in [0, T]$ ,  $x \in \mathbb{R}^n$ , the following inequality holds

$$|\lambda_j(t, x_1) - \lambda_j(t, x_2)| \leq M_{4j}(t) |x_1 - x_2|, \quad j = 1, 2;$$

6). For all  $t \in [0, T]$ ,  $x \in \mathbb{R}^n$ , the following inequality holds

$$|D_j(t, x_1) - D_j(t, x_2)| \leq M_{5j}(t) |x_1 - x_2|, \quad j = 1, 2;$$

7). For all  $x \in \mathbb{R}^n$ ,  $i = 0, 1, \dots, p$ , the following inequality hold

$$|F_i(x_1) - F_i(x_2)| \leq m_{1i} |x_1 - x_2|, \quad |G_i(x_1) - G_i(x_2)| \leq m_{2i} |x_1 - x_2|;$$

8).  $\rho = \chi_1 + \dots + \chi_5 < 1$ , where  $\chi_1, \dots, \chi_5$  are defined by formulas (25)–(27) below.

Then equation (20) has unique solution  $x(t) \in PC([0, T], \mathbb{R}^n)$ . This solution can be found by the following iterative process:

$$\begin{cases} x^k(t) = J(t; x^{k-1}), \quad k = 1, 2, 3, \dots \\ x^0(t) = \Phi_0(t), \quad t \in (t_i, t_{i+1}), \quad i = 0, 1, 2, \dots, p. \end{cases} \quad (21)$$

*Proof.* We consider the following operator

$$J : PC([0, T]; \mathbb{R}^n) \rightarrow PC([0, T] \times \mathbb{R}^n; \mathbb{R}^n),$$

defined by the right-hand side of equation (20). Applying the principle of contracting operators to (20), we show that the operator  $J$  has unique fixed point.

Taking the first and the second conditions of the theorem, we obtain the following estimates for zero approximations and the first difference of the approximations (21):

$$\begin{aligned} \|x^0(t)\| &\leq \max_{0 \leq t \leq T} |\Phi_0(t)| = \delta_1 < \infty, \\ \|x^1(t) - x^0(t)\| &\leq 2 \max_{0 \leq t \leq T} |Q_1^{-1}(t)| \cdot |D_1(t, 0)| + \max_{0 \leq t \leq T} |\Phi_1(t)| \cdot |D_2(\bar{t}, 0)| + \\ &+ \max_{0 \leq t \leq T} \int_0^T |\Phi_2(t, s)| \cdot |D_2(s, 0)| ds + \max_{0 \leq t \leq T} \int_0^T |\Phi_3(t, s)| \left| f\left(s, 0, \int_0^T \Theta(s, \theta, 0) d\theta\right) \right| ds + \\ &+ \max_{0 \leq t \leq T} \sum_{i=1}^p |\Phi_3(t, t_i)| \cdot |G_i(0)| + \sum_{i=1}^p |\Phi_4(t_i)| \cdot |F_i(0)| \leq \\ &\leq 2 \|Q_1^{-1}(t)\| M_{D_1} + \sigma_0 M_{D_2} + \sigma_{11} M_f + \sigma_{12} m_G + \sigma_2 m_F = \delta_2 < \infty, \end{aligned} \quad (22)$$

where

$$\begin{aligned} \sigma_0 &= \max_{0 \leq t \leq T} |\Phi_2(t)| + \max_{0 \leq t \leq T} \int_0^T |\Phi_2(t, s)| ds, \quad \sigma_{11} = \max_{0 \leq t \leq T} \int_0^T |\Phi_3(t, s)| ds, \\ \sigma_{12} &= \max_{0 \leq t \leq T} \sum_{i=1}^p |\Phi_3(t, t_i)|, \quad \sigma_2 = \sum_{i=1}^p |\Phi_4(t_i)|. \end{aligned}$$

Then, by the third–seventh conditions of the theorem, for difference of arbitrary consecutive approximations and arbitrary  $t \in (t_i, t_{i+1}]$ , we have

$$\begin{aligned} \|x^{k+1}(t) - x^k(t)\| &\leq 2 \max_{0 \leq t \leq T} |Q_1^{-1}(t)| M_{51}(t) |x^k(t) - x^{k-1}(t)| + \\ &+ \max_{0 \leq t \leq T} |\Phi_1(t)| \cdot M_{52}(\bar{t}) |x^k(\bar{t}) - x^{k-1}(\bar{t})| + \end{aligned}$$

$$\begin{aligned}
& + \max_{0 \leq t \leq T} \int_0^T |\Phi_2(t, s)| M_{52}(s) |x^k(s) - x^{k-1}(s)| ds + \\
& + \max_{0 \leq t \leq T} \int_0^T |\Phi_3(t, s)| [M_1(s) |x^k(s) - x^{k-1}(s)| + \\
& + M_2(s) \int_0^T M_3(s, \theta) |\max \{x^k(\tau) | \tau \in [\lambda_1(\theta, x^k(\theta)) : \lambda_2(\theta, x^k(\theta))]\} - \\
& - \max \{x^{k-1}(\tau) | \tau \in [\lambda_1(\theta, x^{k-1}(\theta)) : \lambda_2(\theta, x^{k-1}(\theta))]\}| d\theta] ds + \\
& + \max_{0 \leq t \leq T} \sum_{i=1}^p |\Phi_3(t, t_i)| m_{2i} |x^k(t_i) - x^{k-1}(t_i)| + \sum_{i=1}^p |\Phi_4(t_i)| m_{1i} |x^k(t_i) - x^{k-1}(t_i)|.
\end{aligned}$$

Hence, by virtue of the following estimate

$$\begin{aligned}
& M_2(s) \int_0^T M_3(s, \theta) |\max \{x^k(\tau) | \tau \in [\lambda_1(\theta, x^k(\theta)) : \lambda_2(\theta, x^k(\theta))]\} - \\
& - \max \{x^{k-1}(\tau) | \tau \in [\lambda_1(\theta, x^{k-1}(\theta)) : \lambda_2(\theta, x^{k-1}(\theta))]\}| d\theta \leq \\
& \leq M_2(s) \int_0^T M_3(s, \theta) \left[ \left\| \max \{x^k(\tau) | \tau \in [\lambda_1(\theta, x^k(\theta)) : \lambda_2(\theta, x^k(\theta))]\} - \right. \right. \\
& \quad \left. \left. - \max \{x^{k-1}(\tau) | \tau \in [\lambda_1(\theta, x^k(\theta)) : \lambda_2(\theta, x^k(\theta))]\} \right\| + \right. \\
& \quad \left. \left\| \max \{x^{k-1}(\tau) | \tau \in [\lambda_1(\theta, x^k(\theta)) : \lambda_2(\theta, x^k(\theta))]\} - \right. \right. \\
& \quad \left. \left. - \max \{x^{k-1}(\tau) | \tau \in [\lambda_1(\theta, x^{k-1}(\theta)) : \lambda_2(\theta, x^{k-1}(\theta))]\} \right\| \right] d\theta \leq \\
& \leq M_2(s) \int_0^T M_3(s, \theta) \left\{ \|x^k(\theta) - x^{k-1}(\theta)\| + \right. \\
& \left. + (\delta_1 + \delta_2) \left[ |\lambda_1(\theta, x^k(\theta)) - \lambda_1(\theta, x^{k-1}(\theta))| + |\lambda_2(\theta, x^k(\theta)) - \lambda_2(\theta, x^{k-1}(\theta))| \right] \right\} d\theta \leq \\
& \leq \max_{0 \leq t \leq T} M_2(t) \int_0^T M_3(t, s) \left\{ \|x^k(s) - x^{k-1}(s)\| + \right. \\
& \left. + (\delta_1 + \delta_2)(M_{41}(s) + M_{42}(s)) \|x^k(s) - x^{k-1}(s)\| \right\} ds,
\end{aligned}$$

and by the introduced norm in the space  $PC([0, T], \mathbb{R}^n)$ , we obtain

$$\|x^k(t) - x^{k-1}(t)\|_{PC} \leq \rho \cdot \|x^{k-1}(t) - x^{k-2}(t)\|_{PC}, \quad (24)$$

where  $\rho = \chi_1 + \dots + \chi_5$ ,

$$\chi_1 = 2 \max_{0 \leq t \leq T} |Q_1^{-1}(t)| M_{51}(t), \quad \chi_2 = \max_{0 \leq t \leq T} \left[ |\Phi_1(t)| M_{52}(t) + \int_0^T |\Phi_2(t, s)| M_{52}(s) ds \right], \quad (25)$$

$$\chi_3 = \int_0^T \|\Phi_3(t, s)\| \left[ M_1(s) + M_2(s) \int_0^T M_3(s, \theta) [1 + (\delta_1 + \delta_2)(M_{41}(\theta) + M_{42}(\theta))] d\theta \right] ds, \quad (26)$$

$$\chi_4 = \max_{0 \leq t \leq T} \sum_{i=1}^p |\Phi_3(t, t_i)| m_{2i}, \quad \chi_5 = \sum_{i=1}^p |\Phi_4(t_i)| m_{1i}. \quad (27)$$

According to the last condition of the theorem, we have  $\rho < 1$ . Therefore, from the estimate (24), it follows that

$$\|x^k(t) - x^{k-1}(t)\|_{PC} < \|x^{k-1}(t) - x^{k-2}(t)\|_{PC}. \quad (28)$$

It implies from (28), that the operator  $J$  on the right-hand side of equation (20) is contracting. According to fixed point principle in the Banach space  $PC([0, T], \mathbb{R}^n)$  and taking into account estimates (22), (23) and (28), we conclude that the operator  $J$  has unique fixed point. Consequently, equation (20) has unique solution  $x(t) \in PC([0, T], \mathbb{R}^n)$ .  $\square$

Substituting this solution  $x(t) \in PC([0, T], \mathbb{R}^n)$  into presentations (18) and (19), we obtain the redefinition vectors  $C_1$  and  $C_2$ .

## 5. Conclusion

The theory of differential equations plays an important role in solving applied problems of sciences and technology. Especially, nonlocal boundary value problems for differential equations with impulsive actions have many applications in mathematical physics, mechanics and technology, in particular in nanotechnology.

In this paper, we investigated the questions of unique solvability of the system of second order integro-differential equations (1) with nonlinear two-point boundary value conditions (2) and (3), with nonlinear conditions (4) and (5) of impulsive effects for  $t = t_i$ ,  $i = 1, 2, \dots, p$ ,  $0 < t_1 < t_2 < \dots < t_p < T$  and intermediate conditions (6) and (7). The nonlinear right-hand side of this equation consists of the construction of mixed maxima. The problems of existence and uniqueness of the solution of the inverse problem (1)–(7) are studied. If the system (1) has a solution for all  $t \in [0, T]$ ,  $t \neq t_i$ ,  $i = 1, 2, \dots, p$ , then it is proved that this solution can be found by the system of nonlinear functional integral equations (20).

The results obtained in this work will allow us to investigate another kind of inverse problems for the equations of mathematical physics with impulsive actions. We hope that our work will stimulate the study of various kind of inverse boundary value problems for impulsive partial differential and integro-differential equations with many redefinition functions and results of investigations find the applications in mechanics, technology and nanotechnology.

## References

- [1] Benchohra M., Henderson J., Ntouyas S.K. *Impulsive differential equations and inclusions. Contemporary mathematics and its application*. Hindawi Publishing Corporation, New York, 2006.
- [2] Halanay A., Veksler D. *Qualitative theory of impulsive systems*. Mir, Moscow, 1971, 309 p. (in Russian).
- [3] Lakshmikantham V., Bainov D.D., Simeonov P.S. *Theory of impulsive differential equations*. World Scientific, Singapore, 1989, 434 p.
- [4] Perestyk N.A., Plotnikov V.A., Samoilenko A.M., Skripnik N.V. *Differential equations with impulse effect: multivalued right-hand sides with discontinuities*. DeGruyter Stud. 40, Math. Walter de Gruyter Co., Berlin, 2011.
- [5] Samoilenko A.M., Perestyk N.A. *Impulsive differential equations*. World Sci., Singapore, 1995.
- [6] Stamova I., Stamov, G. *Impulsive biological models. In: Applied impulsive mathematical models*. CMS Books in Mathematics. Springer, Cham., 2016.
- [7] Catlla J., Schaeffer D.G., Witelski Th.P., Monson E.E., Lin A.L. On spiking models for synaptic activity and impulsive differential equations. *SIAM Review*, 2008, **50**(3), P. 553–569.
- [8] Fedorov E.G., Popov I.Yu. Analysis of the limiting behavior of a biological neurons system with delay. *J. Phys.: Conf. Ser.*, 2021, **2086**, P. 012109.
- [9] Fedorov E.G., Popov I.Yu. Hopf bifurcations in a network of Fitzhigh-Nagumo biological neurons. *International Journal of Nonlinear Sciences and Numerical Simulation*, 2021.
- [10] Fedorov E.G. Properties of an oriented ring of neurons with the FitzHugh-Nagumo model. *Nanosystems: Phys. Chem. Math.*, 2021, **12**(5), P. 553–562.
- [11] Anguraj A., Arjunan M.M. Existence and uniqueness of mild and classical solutions of impulsive evolution equations. *Elect. J. of Differential Equations*, 2005, **2005**(111), P. 1–8.
- [12] Ashyralyev A., Sharifov Ya.A. Existence and uniqueness of solutions for nonlinear impulsive differential equations with two-point and integral boundary conditions. *Advances in Difference Equations*, 2013, **2013**, P. 173.
- [13] Ashyralyev A., Sharifov Ya.A. Optimal control problems for impulsive systems with integral boundary conditions. *Elect. J. of Differential Equations*, 2013, **2013**(80), P. 1–11.
- [14] Bai Ch., Yang D. Existence of solutions for second-order nonlinear impulsive differential equations with periodic boundary value conditions. *Boundary Value Problems (Hindawi Publishing Corporation)*, 2007, **2007**(41589), P. 1–13.
- [15] Bin L., Xinzhi L., Xiaoxin L. Robust global exponential stability of uncertain impulsive systems. *Acta Mathematica Scientia*, 2005, **25**(1), P. 161–169.
- [16] Chen J., Tisdell Ch.C., Yuan R. On the solvability of periodic boundary value problems with impulse. *J. of Math. Anal. and Appl.*, 2007, **331**, P. 902–912.
- [17] Mardanov M.J., Sharifov Ya.A., Habib M.H. Existence and uniqueness of solutions for first-order nonlinear differential equations with two-point and integral boundary conditions. *Electr. J. of Differential Equations*, 2014, **2014**(259), P. 1–8.
- [18] Sharifov Ya.A. Optimal control problem for systems with impulsive actions under nonlocal boundary conditions. *Vestnik samarskogo gosudarstvennogo tekhnicheskogo universiteta. Seria: Fiziko-matematicheskie nauki*, 2013, **33**(4), P. 34–45 (Russian).
- [19] Sharifov Ya.A. Optimal control for systems with impulsive actions under nonlocal boundary conditions. *Russian Mathematics (Izv. VUZ)*, 2013, **57**(2), P. 65–72.
- [20] Sharifov Ya.A., Mammadova N.B. Optimal control problem described by impulsive differential equations with nonlocal boundary conditions. *Differential equations*, 2014, **50**(3), P. 403–411.
- [21] Sharifov Ya.A. Conditions optimality in problems control with systems impulsive differential equations with nonlocal boundary conditions. *Ukrainian Math. Journ.*, 2012, **64**(6), P. 836–847.
- [22] Yuldashev T.K. Periodic solutions for an impulsive system of nonlinear differential equations with maxima. *Nanosystems: Phys. Chem. Math.*, 2022, **13**(2), P. 135–141.
- [23] Yuldashev T.K., Fayziyev A.K. On a nonlinear impulsive system of integro-differential equations with degenerate kernel and maxima. *Nanosystems: Phys. Chem. Math.*, 2022, **13**(1), P. 36–44.
- [24] Yuldashev T.K., Fayziyev A.K. Integral condition with nonlinear kernel for an impulsive system of differential equations with maxima and redefinition vector. *Lobachevskii Journ. Math.*, 2022, **43**(8), P. 2332–2340.
- [25] Yuldashev T.K., Ergashev T.G., Abduvahobov T.A. Nonlinear system of impulsive integro-differential equations with Hilfer fractional operator and mixed maxima. *Chelyabinsk Physical and Mathematical Journal*, 2022, **7**(3), P. 312–325.

- [26] Abildayeva A., Assanova A., Imanchiyev A. A multi-point problem for a system of differential equations with piecewise-constant argument of generalized type as a neural network model. *Eurasian Math. Journ.*, 2022, **13**(2), P. 8–17.
- [27] Assanova A.T., Dzhobulaeva Z.K., Imanchiyev A.E. A multi-point initial problem for a non-classical system of a partial differential equations. *Lobachevskii Journ. Math.*, 2020, **41**(6), P. 1031–1042.
- [28] Minglibayeva B.B., Assanova A.T. An existence of an isolated solution to nonlinear twopoint boundary value problem with parameter. *Lobachevskii Journ. Math.*, 2021, **42**(3). P. 587–597.
- [29] Usmanov K.I., Turmetov B.Kh., Nazarova K.Zh. On unique solvability of a multipoint boundary value problem for systems of integro-differential equations with involution. *Symmetry*, 2022, **14**(8), ID 1262, P. 1–15.
- [30] Yuldashev T.K. On a nonlocal problem for impulsive differential equations with mixed maxima. *Vestnik KRAUNTS. Seria: Fiziko-matematicheskie nauki*, 2022, **38**(1), P. 40–53.

---

*Submitted 6 November 2022; revised 24 December 2022; accepted 25 December 2022*

*Information about the authors:*

*T. K. Yuldashev* – Tashkent State University of Economics, Karimov street, 49, TSUE, Tashkent, 100066, Uzbekistan; ORCID 0000-0002-9346-5362; tursun.k.yuldashev@gmail.com

*A. K. Fayziyev* – Tashkent State University of Economics, Karimov street, 49, TSUE, Tashkent, 100066, Uzbekistan; ORCID 0000-0001-6798-3265; fayziyev.a@inbox.ru

*Conflict of interest:* the authors declare no conflict of interest.

## An inversion formula for the weighted Radon transform along family of cones

Mukhiddin I. Muminov<sup>1,2,a</sup>, Zarifjon Kh. Ochilov<sup>1,b</sup>

<sup>1</sup>Samarkand State University, Samarkand, Uzbekistan

<sup>2</sup>V. I. Romanovskiy Institute of Mathematics, Uzbekistan Academy of Sciences, Tashkent, Uzbekistan

<sup>a</sup>mmuminov@mail.ru, <sup>b</sup>zarifjonochilov@mail.ru

Corresponding author: M. I. Muminov, mmuminov@mail.ru

**ABSTRACT** In this paper, an inversion problem for the weighted Radon transform along family of cones in three-dimensional space is considered. An inversion formula for the weighted Radon transform is obtained for the case when the range is a space of infinitely smooth functions.

**KEYWORDS** integral geometry problem, weighted Radon transform, inversion formula

**ACKNOWLEDGEMENTS** Authors partially supported by the grant FZ-20200929224 of Fundamental Science Foundation of Uzbekistan. Authors thank the referee for valuable comments and gratefully acknowledge.

**FOR CITATION** Muminov M.I., Ochilov Z.Kh. An inversion formula for the weighted Radon transform along family of cones. *Nanosystems: Phys. Chem. Math.*, 2023, **14** (1), 22–27.

### 1. Introduction

The standard X-ray transform consists of recovering a function supported in a bounded domain from its integrals along straight lines through this domain. In dimension two ( $n = 2$ ), it coincides with the Radon transform [1], which provides the theoretical underpinning for several medical imaging techniques such as Computed Tomography (CT) and Positron Emission Tomography (PET). The X-ray tomography method for three-dimensional object reconstruction is offered in [2] which is based on the 3D Radon transform and is compatible with anisotropic beam conditions.

Weighted and limited data Radon transforms ( $d = n - 1$ ) have been studied in [3]. The Coherent X-ray Diffraction Imaging (CXDI) with its application to nanostructures are given in [4]. In [5] examples are constructed for non injectivity weighted ray and Radon transforms along hyperplanes in  $R^d$ ,  $d \geq 3$  with a non-trivial kernel in the space of finite infinitely smooth functions. The weighted Radon transforms in multidimensions are studied in [6]. Authors introduced an analog of Chang approximate inversion formula for such transforms and describe all weights for which this formula is exact. They indicated possible tomographic applications of inversion methods for weighted Radon transforms in 3D. In paper [7], the reconstruction approach proposed in [6] for weighted ray transforms (weighted Radon transforms along oriented straight lines) in 3D is investigated numerically.

Some problems of integral geometry as restoring a function on some linear space from the set of values of this function on a given family of manifolds embedded in this space are studied in [8, 9]. In [10–12] a problem of reconstruction of a function in a strip from their given integrals with known weight function along polygonal and parabolic lines is considered. The uniqueness theorems are proved and the stability estimates for solutions in Sobolev spaces are obtained.

In this paper, we consider an inversion problem for the weighted Radon transform along family of cones in three-dimensional space. The problem is reduced to study of Volterra integral equation. Under some natural conditions, an inversion formula for the weighted Radon transform is obtained for the case when the range is a space of infinitely smooth functions.

### 2. Problem statement and the Main results

We introduce the following notations

$$(x, y, z), (\xi, \eta, \zeta) \in \mathbb{R}^3, \lambda, \mu \in \mathbb{R}^1, \\ \Omega = \{(x, y, z) : x, y \in \mathbb{R}, z \in [0, h] \quad h < \infty\}.$$

A family of cones  $S(x, y, z)$  is considered on  $\Omega$ , which are uniquely parameterized using the coordinates of their vertices  $(x, y, z) \in \Omega$ :

$$S(x, y, z) = \{(\xi, \eta, \zeta) : (x - \xi)^2 + (y - \eta)^2 = (z - \zeta)^2, \quad \xi \in \mathbb{R}, \quad 0 \leq \zeta \leq z\}.$$

We denote by  $\mathcal{J}(\mathbb{R}^2, C[0, h])$  the set of infinitely differentiable functions  $\varphi(x, y, z)$  in  $x, y \in \mathbb{R}^2$  and continuous in  $z \in [0, h]$  for which

$$\sup \left| x^{\alpha_1} y^{\alpha_2} \frac{\partial^{\beta+\gamma} \varphi(x, y, z)}{\partial^\beta x \partial^\gamma y} \right| < \infty$$

for all nonnegative integer numbers  $\alpha_1, \alpha_2, \beta$  and  $\gamma$ .

**Problem A.** Determine a function of three variables  $u(x, y, z)$ , if the integrals of the function  $u(x, y, z)$  over a family of cones  $S(x, y, z)$  are known for all  $(x, y, z)$  of the layer  $\Omega$  as

$$\int \int_{S(x,y,z)} g(x - \xi, y - \eta) u(\xi, \eta, \zeta) ds = f(x, y, z), \quad (1)$$

where  $g$  is the weight function on  $\mathbb{R}^2$  and  $f \in \mathcal{J}(\mathbb{R}^2, C[0, h])$ .

Let us mark that the left hand side of equation (1) can be considered as the generalized Radon transform  $\mathbf{R}$  over a family of cones  $S$  (See [13] and [14]), i.e.  $\mathbf{R}u = f$ .

Denote by  $\hat{f}(\cdot, \cdot, z)$  the Fourier transform of  $f(x, y, z) \in \mathcal{J}(\mathbb{R}^2, C[0, h])$  with respect to  $(x, y) \in \mathbb{R}^2$ , i.e.

$$\hat{f}(\lambda, \mu, z) = \frac{1}{2\pi} \int_{-\infty}^{+\infty} \int_{-\infty}^{+\infty} e^{i(\lambda x + \mu y)} f(x, y, z) dx dy.$$

The following theorem describes the uniqueness conditions and the exact solution for the Problem A. Moreover, the solution expresses the inversion formula for the generalized Radon transform i.e.  $u = \mathbf{R}^{-1}f$ .

**Theorem 2.1.** Let  $g(x, y) = ax + by$ ,  $|a| + |b| \neq 0$  and  $f \in \mathcal{J}(\mathbb{R}^2, C[0, h])$  have continuous partial derivatives up to the third order with respect to variable  $z$ . We suppose that  $\frac{\partial^i}{\partial z^i} f \in \mathcal{J}(\mathbb{R}^2, C[0, h])$ ,  $i = 1, 2, 3$ ,  $f(x, y, 0) = \frac{\partial}{\partial z} f(x, y, 0) = \frac{\partial^2}{\partial z^2} f(x, y, 0) = \frac{\partial^3}{\partial z^3} f(x, y, 0) = 0$  for all  $x, y \in \mathbb{R}$  and  $\hat{f}(\lambda, \mu, z) = 0$  for all  $(\lambda, \mu) \in \{\lambda, \mu \in \mathbb{R} : a\lambda + b\mu = 0\}$  and  $z \in [0, h]$ . Then the Problem A has unique solution  $u(x, y, z)$  which is continuous on  $\Omega$ .

Additionally, if  $f \in \mathcal{J}(\mathbb{R}^2, C[0, h])$  has continuous partial derivatives up to the ninth order with respect to variable  $z$  and  $\frac{\partial^i}{\partial z^i} f \in \mathcal{J}(\mathbb{R}^2, C[0, h])$ ,  $i = 1, \dots, 9$ , then the function  $u(x, y, z)$  has the following form

$$u(x, y, z) = \frac{1}{18\sqrt{2}\pi i} \int_{-\infty}^{+\infty} \int_{-\infty}^{+\infty} e^{-i(\lambda x + \mu y)} \frac{(\frac{d^2}{dt^2} + \lambda^2 + \mu^2)^5}{(a\lambda + b\mu)(\lambda^2 + \mu^2)} \int_0^z \int_0^t (t - \tau)^2 J_2((t - \tau)\sqrt{\lambda^2 + \mu^2}) \hat{f}(\lambda, \mu, \tau) d\tau dt d\mu d\lambda, \quad (2)$$

where  $J_n(\cdot)$  is the Bessel function of the first kind of order  $n$  i.e.

$$J_n(t) = \sum_{k=0}^{\infty} \frac{(-1)^k t^{2k+n}}{2^{2k+n} k! \Gamma(n+k+1)}.$$

### 3. Proof of the Main result

In the integral on the left hand side of (1), we provide the following changing of variable

$$\zeta = z - \sqrt{(x - \xi)^2 + (y - \eta)^2}.$$

Then

$$\zeta'_\xi = -\frac{x - \xi}{\sqrt{(x - \xi)^2 + (y - \eta)^2}}, \quad \zeta'_\eta = -\frac{y - \eta}{\sqrt{(x - \xi)^2 + (y - \eta)^2}}, \quad ds = \sqrt{1 + (\zeta'_\xi)^2 + (\zeta'_\eta)^2} d\xi d\eta.$$

Hence, equation (1) is represented as follows

$$\sqrt{2} \int \int_{D(x,y,z)} g(x - \xi, y - \eta) u(\xi, \eta, z - \sqrt{(x - \xi)^2 + (y - \eta)^2}) d\xi d\eta = f(x, y, z). \quad (3)$$

Making the following substitutions in (3)

$$\xi = x - \rho \cos \phi, \quad \eta = y - \rho \sin \phi,$$

we get

$$\sqrt{2} \int_0^{2\pi} \int_0^z g(\rho \cos \phi, \rho \sin \phi) u(x - \rho \cos \phi, y - \rho \sin \phi, z - \rho) \rho d\rho d\phi = f(x, y, z). \quad (4)$$

We apply the Fourier transform to the both sides of equation (4) with respect to variables  $x$  and  $y$

$$\hat{f}(\lambda, \mu, z) = \sqrt{2} \int_0^{2\pi} \int_0^z e^{i\rho(\lambda \cos \phi + \mu \sin \phi)} g(\rho \cos \phi, \rho \sin \phi) \hat{u}(\lambda, \mu, z - \rho) \rho d\rho d\phi. \quad (5)$$

where

$$\hat{u}(\lambda, \mu, z) = \frac{1}{2\pi} \int_{-\infty}^{+\infty} \int_{-\infty}^{+\infty} e^{i(\lambda x + \mu y)} u(x, y, z) dx dy.$$

Remark that  $\hat{f} \in \mathcal{J}(\mathbb{R}^2, C[0, h])$ , since  $f \in \mathcal{J}(\mathbb{R}^2, C[0, h])$ .

Making the change of variable  $t = z - \rho$  in equation (5), we obtain

$$\hat{f}(\lambda, \mu, z) = \sqrt{2} \int_0^{2\pi} \int_0^z e^{i(z-t)(\lambda \cos \phi + \mu \sin \phi)} g((z-t) \cos \phi, (z-t) \sin \phi) \hat{u}(\lambda, \mu, t) (z-t) dt d\phi. \quad (6)$$

Thus, equation (1) is equivalent to equation (6). Since  $g(x, y) = ax + by$ , equation (6) yields

$$\hat{f}(\lambda, \mu, z) = \int_0^z G(\lambda, \mu, z-t) \hat{u}(\lambda, \mu, t) dt, \quad (7)$$

where

$$G(\lambda, \mu, z-t) = \sqrt{2}(z-t)^2 \int_0^{2\pi} e^{i(z-t)(\lambda \cos \phi + \mu \sin \phi)} (a \cos \phi + b \sin \phi) d\phi.$$

According to the equality

$$\lambda \cos \phi + \mu \sin \phi = \sqrt{\lambda^2 + \mu^2} \cos(\phi - \psi), \quad \cos \psi = \frac{\lambda}{\sqrt{\lambda^2 + \mu^2}},$$

changing variable  $\phi = \theta + \psi$  gives us

$$G(\lambda, \mu, z-t) = \sqrt{2}(z-t)^2 \int_0^{2\pi} e^{i\beta \cos \theta} (a \cos(\theta + \psi) + b \sin(\theta + \psi)) d\theta,$$

where

$$\beta = (z-t) \sqrt{\lambda^2 + \mu^2}.$$

Since

$$e^{i\beta \cos \theta} = \cos(\beta \cos \theta) + i \sin(\beta \cos \theta),$$

the function  $G(\lambda, \mu, z-t)$  is represented as

$$\begin{aligned} G(\lambda, \mu, z-t) &= \sqrt{2}a(z-t)^2 \int_0^{2\pi} \cos(\beta \cos \theta) \cos(\theta + \psi) d\theta + i\sqrt{2}a(z-t)^2 \int_0^{2\pi} \sin(\beta \cos \theta) \cos(\theta + \psi) d\theta + \\ &+ \sqrt{2}b(z-t)^2 \int_0^{2\pi} \cos(\beta \cos \theta) \sin(\theta + \psi) d\theta + i\sqrt{2}b(z-t)^2 \int_0^{2\pi} \sin(\beta \cos \theta) \sin(\theta + \psi) d\theta. \end{aligned}$$

Using the identities

$$\cos(\theta + \psi) = \cos \theta \cos \psi - \sin \theta \sin \psi,$$

$$\sin(\theta + \psi) = \sin \theta \cos \psi + \cos \theta \sin \psi,$$

we have

$$\begin{aligned} G(\lambda, \mu, z-t) &= \sqrt{2}a(z-t)^2 \cos \psi \int_0^{2\pi} \cos(\beta \cos \theta) \cos \theta d\theta - \sqrt{2}a(z-t)^2 \sin \psi \int_0^{2\pi} \cos(\beta \cos \theta) \sin \theta d\theta + \\ &+ i\sqrt{2}a(z-t)^2 \cos \psi \int_0^{2\pi} \sin(\beta \cos \theta) \cos \theta d\theta - i\sqrt{2}a(z-t)^2 \sin \psi \int_0^{2\pi} \sin(\beta \cos \theta) \sin \theta d\theta + \\ &+ \sqrt{2}b(z-t)^2 \cos \psi \int_0^{2\pi} \cos(\beta \cos \theta) \sin \theta d\theta + \sqrt{2}b(z-t)^2 \sin \psi \int_0^{2\pi} \cos(\beta \cos \theta) \cos \theta d\theta + \\ &+ i\sqrt{2}b(z-t)^2 \cos \psi \int_0^{2\pi} \sin(\beta \cos \theta) \sin \theta d\theta + i\sqrt{2}b(z-t)^2 \sin \psi \int_0^{2\pi} \sin(\beta \cos \theta) \cos \theta d\theta. \end{aligned}$$

Now, according to the integral equalities

$$\int_0^{2\pi} \cos(\beta \cos \theta) \cos \theta d\theta = 2 \int_0^{\pi} \cos(\beta \cos \theta) \cos \theta d\theta,$$

$$\int_0^{2\pi} \sin(\beta \cos \theta) \cos \theta d\theta = 2 \int_0^{\pi} \sin(\beta \cos \theta) \cos \theta d\theta$$

and

$$\int_0^{2\pi} \cos(\beta \cos \theta) \sin \theta d\theta = 0, \quad \int_0^{2\pi} \sin(\beta \cos \theta) \sin \theta d\theta = 0,$$

we obtain

$$G(\lambda, \mu, z - t) = 2\sqrt{2}(z - t)^2(a \cos \psi + b \sin \psi) \left\{ \int_0^{\pi} \cos(\beta \cos \theta) \cos \theta d\theta + i \int_0^{\pi} \sin(\beta \cos \theta) \cos \theta d\theta \right\}.$$

The equalities (see, pages 419-420 in [16])

$$\int_0^{\pi} \cos(\beta \cos \theta) \cos(n\theta) d\theta = \pi \cos \frac{n\pi}{2} J_n(\beta),$$

$$\int_0^{\pi} \sin(\beta \cos \theta) \cos(n\theta) d\theta = \pi \sin \frac{n\pi}{2} J_n(\beta),$$

give one

$$\int_0^{\pi} \cos(\beta \cos \theta) \cos \theta d\theta = 0, \quad \int_0^{\pi} \sin(\beta \cos \theta) \cos \theta d\theta = \pi J_1(\beta).$$

Then equation (7) is written as

$$\hat{f}(\lambda, \mu, z) = 2\sqrt{2}i\pi \frac{a\lambda + b\mu}{\sqrt{\lambda^2 + \mu^2}} \int_0^z (z - t)^2 J_1\{(z - t)\sqrt{\lambda^2 + \mu^2}\} \hat{u}(\lambda, \mu, t) dt, \quad (8)$$

Remark that if equation (8) has a solution then  $\hat{f}$  should be  $\hat{f}(\lambda, \mu, z) = 0$  for all  $(\lambda, \mu) \in \{\lambda, \mu \in \mathbb{R} : a\lambda + b\mu = 0\}$  and  $z \in [0, h]$ . This is provided by the condition of the theorem. To prove the existence of a solution of (8), we write

$$\hat{f}(z) = \int_0^z G(z, t) \hat{u}(t) dt, \quad (9)$$

where

$$G(z, t) := 2\sqrt{2}i\pi (z - t)^2 \frac{a\lambda + b\mu}{\sqrt{\lambda^2 + \mu^2}} J_1\{(z - t)\sqrt{\lambda^2 + \mu^2}\}, \quad \hat{u}(t) := \hat{u}(\lambda, \mu, t), \quad \hat{f}(t) := \hat{f}(\lambda, \mu, t).$$

Note that the smoothness of the first kind Bessel function  $J_1(\cdot)$  and  $J_1(0) = 0$  yield the smoothness of the function  $G(\cdot)$  for any fixed  $\lambda, \mu \in \mathbb{R}$ . The conditions  $f(x, y, 0) = \frac{\partial}{\partial z} f(x, y, 0) = \frac{\partial^2}{\partial z^2} f(x, y, 0) = \frac{\partial^3}{\partial z^3} f(x, y, 0) = 0$  yield  $\hat{f}(\lambda, \mu, 0) = \frac{\partial}{\partial z} \hat{f}(\lambda, \mu, 0) = \frac{\partial^2}{\partial z^2} \hat{f}(\lambda, \mu, 0) = \frac{\partial^3}{\partial z^3} \hat{f}(\lambda, \mu, 0) = 0$ . Since  $G(z, z) = G'_z(z, z) = G''_z(z, z) = 0, G'''_z(z, z) \neq 0$ , equation (9) has unique solution  $\hat{u}(\lambda, \mu, t)$  for any fixed  $\lambda, \mu \in \mathbb{R}$ . The function  $u(t) := \hat{u}(\lambda, \mu, t)$  is a solution of the equation

$$K''_z(z, z)u(z) + \int_0^z K'''_z(z, t)u(t) dt = \hat{f}'''(z),$$

where  $\hat{f}(t) := \hat{f}(\lambda, \mu, t)$ . Note that  $\frac{\partial^3}{\partial z^3} \hat{f} \in \mathcal{J}(\mathbb{R}^2, C[0, h])$  since  $\frac{\partial^3}{\partial z^3} f \in \mathcal{J}(\mathbb{R}^2, C[0, h])$ . Therefore, the function  $\hat{u}(\lambda, \mu, t)$  is continuous on  $\Omega$  and, hence,  $u(x, y, t)$  is continuous on  $\Omega$ .

Next, we present the explicit formula for  $u(x, y, t)$ . The equality  $\hat{f}(\lambda, \mu, z) = 0$  for all  $(\lambda, \mu) \in \{\lambda, \mu \in \mathbb{R} : a\lambda + b\mu = 0\}$  and  $z \in [0, h]$  yields continuity of the ratio function  $\frac{\sqrt{\lambda^2 + \mu^2}}{2\sqrt{2}\pi i(a\lambda + b\mu)} \hat{f}(\lambda, \mu, z)$  on  $\Omega$ .

We rewrite equation (7) as

$$F(z) = \int_0^z K(z, t)U(t)dt. \quad (10)$$

where

$$F(z) = \frac{\sqrt{\lambda^2 + \mu^2}}{2\sqrt{2}\pi i(a\lambda + b\mu)} \hat{f}(\lambda, \mu, z),$$

$$K(z, t) = (z - t)^2 J_1\{(z - t)\sqrt{\lambda^2 + \mu^2}\} \hat{u}(\lambda, \mu, t), \quad U(t) = \hat{u}(\lambda, \mu, t).$$

Since the function  $f \in \mathcal{J}(\mathbb{R}^2, C[0, h])$  has continuous partial derivatives up to the ninth order with respect to variable  $z \in (0, h)$ , the same is valid for  $\hat{f}(\lambda, \mu, z)$ . The solution of equation (10) has the form (see, section 1.8-1 of [15])

$$U(z) = \int_0^z V(t)dt, \quad (11)$$

where

$$V(t) = \frac{1}{9\sqrt{\lambda^2 + \mu^2}^3} \left( \frac{d^2}{dt^2} + \lambda^2 + \mu^2 \right)^5 \int_0^t (t - \tau)^2 J_2\{(t - \tau)\sqrt{\lambda^2 + \mu^2}\} F(\tau) d\tau.$$

Thus, from (11), we obtain

$$\hat{u}(\lambda, \mu, z) = \frac{\left( \frac{d^2}{dt^2} + \lambda^2 + \mu^2 \right)^5}{18\sqrt{2}\pi i(a\lambda + b\mu)(\lambda^2 + \mu^2)} \int_0^z \int_0^t (t - \tau)^2 J_2\{(t - \tau)\sqrt{\lambda^2 + \mu^2}\} \hat{f}(\lambda, \mu, \tau) d\tau dt. \quad (12)$$

Hence, applying the inverse Fourier transform with respect to variables  $\mu$  and  $\lambda$  to equation (12), we obtain equation (2). The Theorem 2.1 is proved.

#### 4. Conclusion

Consider equation (1) as the generalized Radon transform  $\mathbf{R}$  over a family of cones  $S$ , i.e.  $\mathbf{R}u = f$ . Let  $\mathbf{R}$  consist of functions  $f \in \mathcal{J}(\mathbb{R}^2, C[0, h])$  satisfying the following conditions  $\frac{\partial^i}{\partial z^i} f \in \mathcal{J}(\mathbb{R}^2, C[0, h]), i = 1, 2, 3, f(x, y, 0) = \frac{\partial}{\partial z} f(x, y, 0) = \frac{\partial^2}{\partial z^2} f(x, y, 0) = \frac{\partial^3}{\partial z^3} f(x, y, 0) = 0$  for all  $x, y \in \mathbb{R}$  and  $\hat{f}(\lambda, \mu, z) = 0$  for all  $(\lambda, \mu) \in \{\lambda, \mu \in \mathbb{R} : a\lambda + b\mu = 0\}$  and  $z \in [0, h]$ . Then  $\mathbf{R}$  is invertible for the case when the rang of  $\mathbf{R}$  is  $\mathcal{R}$ , where  $u = \mathbf{R}^{-1}f$  is continuous on  $\Omega$ . Additionally, if  $f \in \mathcal{R}$  has continuous partial derivatives up to the ninth order with respect to variable  $z$  and  $\frac{\partial^i}{\partial z^i} f \in \mathcal{J}(\mathbb{R}^2, C[0, h]), i = 1, \dots, 9$ , then  $\mathbf{R}^{-1}f$  is expressed by (2).

#### References

- [1] Radon J. Über die bestimmung von funktionen durch ihre integralwerte lngs gewisser mannigfaltigkeiten. Berichte über die Verhandlungen der Königlich-Sächsischen Akademie der Wissenschaften zu Leipzig, Mathematisch-Physische Klasse, 1917, **69**, P. 262–277.
- [2] Vassholz M., Koberstein-Schwarz B., Ruhlandt A., Krenkel M. and Salditt T. New X-ray tomography method based on the 3d Radon transform compatible with anisotropic sources. *Physical Review Letters*, 2016, **116**(8), P. 088101.
- [3] Friel J., Quinto E.T. Limited data problems for the generalized Radon transform in  $R_n$ , *SIAM J. Math. Anal.*, 2016, **48**(4), P. 2301–2318.
- [4] Seeck O.H., Murphy B. (Eds.) *X-Ray Diffraction: Modern Experimental Techniques* (1st ed.). Jenny Stanford Publishing, 2014.
- [5] Goncharov F.O., Novikov R.G. An example of non-uniqueness for the weighted Radon transforms along hyperplanes in multidimensions. *Inverse Problem*, 2018, **34**, P. 054001.
- [6] Goncharov F.O., Novikov R.G. An analog of Chang inversion formula for weighted Radon transforms in multidimensions. *Eurasian Journal of Mathematical and Computer Applications*, 2016, **4**(2), P. 23–32.
- [7] Goncharov F.O. A geometric based preprocessing for weighted ray transforms with applications in SPECT, *Journal of Inverse and Ill-posed Problems*, 2021, **29**(3), P. 435–457.
- [8] Lavrentyev M.M., Savelyev L.Ya. *Operator theory and ill-posed problems*. Publishing house of the Institute of Mathematics, Moscow, 2010.
- [9] Kabanikhin S.I. *Inverse and ill-posed problems*. Siberian Scientific Publishing House, 2009.
- [10] Begmatov A.Kh., Muminov M.E., Ochilov Z.H. The problem of integral geometry of Volterra type with a weight function of a special type. *Mathematics and Statistics*, 2015, **3**, P. 113–120.
- [11] Ochilov Z.X. The uniqueness of solution problems of integral geometry a family of parabolas with a weight function of a special type. *Uzbek Mathematical Journal*, 2020, **3**, P. 107–116.
- [12] Ochilov Z.Kh. Existence of solutions to problems of integral geometry by a family of parabolas with a weight function of a special form. *Bull. Inst. Math.*, 2021, **4**(4), P. 28–33.
- [13] Helgason S. *Integral Geometry and Radon Transform*. Springer, New York, 2011.

- [14] Natterer F. *The mathematics of computerized tomography, Classics in Mathematics*. Society for Industrial and Applied Mathematics, New York, 2001.
- [15] Polyaniin A.D., Manzhirov A.V. *Handbook of Integral Equations*. CRC Press LLC, N.W. Corporate Blvd., Boca Raton, Florida, 2000.
- [16] Gradsteyn I.S., Ryzhik I.M. *Table of Integrals. Series, and Products*, Academic Press, New York, 2007.

---

*Submitted 19 November 2022; revised 01 December 2022; accepted 02 December 2022*

*Information about the authors:*

*Mukhiddin I. Muminov* – Samarkand State University, 140100, Samarkand, Uzbekistan; V.I. Romanovskiy Institute of Mathematics, Uzbekistan Academy of Sciences, 100174, Tashkent, Uzbekistan; ORCID 0000-0003-0335-6558; mmuminov@mail.ru

*Zarifjon Kh. Ochilov* – Samarkand State University, 140100, Samarkand, Uzbekistan; ORCID 0000-0002-4803-538X; zarifjonochilov@mail.ru

*Conflict of interest:* the authors declare no conflict of interest.

## Exact irregular solutions to radial Schrödinger equation for the case of hydrogen-like atoms

Chander Parkash<sup>1</sup>, William C. Parke<sup>2</sup>, Parvinder Singh<sup>3</sup>

<sup>1</sup>Department Of Mathematics, Rayat Bahra University, Mohali, Punjab, 140104, India

<sup>2</sup>Department Of Physics, The George Washington University, Washington D.C., USA

<sup>3</sup>Department of Chemistry, Rayat Bahra University, Mohali, Punjab, 140104, India

Corresponding author: William C. Parke, [wparke@email.gwe.edu](mailto:wparke@email.gwe.edu)

**ABSTRACT** This study propounds a novel methodology for obtaining the explicit/closed representation of the two linearly independent solutions of a large class of second order ordinary linear differential equation with special polynomial coefficients. The proposed approach is applied for obtaining the closed forms of regular and irregular solutions of the Coulombic Schrödinger equation for an electron experiencing the Coulomb force, and examples are displayed. The methodology is totally distinguished from getting these solutions either by means of associated Laguerre polynomials or confluent hypergeometric functions. Analytically, both the regular and irregular solutions spread in their radial distributions as the system energy increases from strongly negative values to values closer to zero. The threshold and asymptotic behavior indicate that the regular solutions have an  $r^\ell$  dependence near the origin, while the irregular solutions diverge as  $r^{-\ell-1}$ . Also, the regular solutions drop exponentially in proportion to  $r^{n-1} \exp(-r/n)$ , in natural units, while the irregular solutions grow as  $r^{-n-1} \exp(r/n)$ . Knowing the closed form irregular solutions leads to study the analytic continuation of the complex energies, complex angular momentum, and solutions needed for studying bound state poles and Regge trajectories.

**KEYWORDS** second exact solutions, irregular exact solutions, Coulombic Schrödinger equation, Frobenius method, Coulombic interaction

**ACKNOWLEDGEMENTS** The authors are grateful to Prof. Nyengeri Hippolyte, Department of Physics, Faculty of Science, University of Burundi, Bujumbura, Burundi, for providing his contribution towards the finalization of this manuscript.

**FOR CITATION** Parkash C, Parke W.C., Singh P. Exact irregular solutions to radial Schrödinger equation for the case of hydrogen-like atoms. *Nanosystems: Phys. Chem. Math.*, 2023, **14** (1), 28–43.

### 1. Introduction

Finding the closed-form of the first (regular) and the second (irregular) solutions to the quantum Coulomb problem for negative energies have not been well elucidated by the literature. Although, the regular solutions to the Coulombic Schrödinger equation have been more elucidated by an infinite power series representation, but the irregular solutions to the Schrödinger equation in the case of a bound electron experiencing a Coulomb force are being ignored for several reasons. Some of them indicate that irregular solutions are ill-behaved at the origin (due to the irregular singularity) and unbounded at infinity. But ignoring irregular solutions based on fancy reasons is worthless as they can be of great interest in problems describing hydrogenic bound electronic waves. The independent irregular solutions to the Coulomb Schrödinger equation for hydrogen like atoms can be effectively deployed for studying the complex poles for the bound, resonance and virtual states, hydrogenic wave functions, Regge trajectories, Pade extrapolation, and so on. If the electron potential energy is Coulombic only within a shell region around a central region, then irregular solutions can be accomplished in deriving shell region solutions on the boundaries of the shell. Geilhufe et al. [1] effectively constructed a Green function by taking into consideration the first (regular) and the second (irregular) solutions of the scattering (single site) problem and thereafter discussed the asymptotic behavior of the resulting spherical wave functions. Newton [2] studied the two linearly independent solutions of one dimensional Schrödinger equation (SE) and noted that the regular solution (in the form of Whittaker functions) that lies in the right half plane experiences analyticity near the origin whereas the irregular solution lying in the left half plane experiences logarithmic singularity and infinite derivative in the vicinity of the origin. Cantelaube [3] ruled out the necessity of the usual boundary condition imposed in extracting the radial part of the Coulombic SE in spherical polar coordinates and concluded that the first solutions are regular, but the second solutions are either singular or pseudo functions, the latter arises when the second solutions are derived by taking the Laplacian of the radial part. Khelashvili and Nadareishvili [4] exploited the singular behavior of the Laplacian operator and found that the radial wave function is less regular than  $1/r$ , owing to the delta like singularity at the origin.

Seaten [5] studied the asymptotic behavior of both regular and irregular solutions of radial SE with the Coulomb potential and remarked that the two solutions for attractive potentials decay exponentially whereas, for repulsive potentials, the regular (irregular) solutions grow (decay) exponentially. Khalilov and Mamsurov [6] constituted an expression for the radial Green's function after converting the regular and irregular solutions of radial Dirac equation into the form of Whittaker functions and found that the first (regular) solutions are R-integrable in the vicinity of the origin whereas the second (irregular) solutions are integrable at the point of infinity. Michel [7] compared the analytical and numerical computations of the first (regular) and the second (irregular) solutions of zero dimensional SE with the Coulomb potential. The authors concluded that, along the real axis, the numerical computation of the radial wave functions is quite difficult as they can vary significantly by many orders for absolute values of principal quantum numbers. Nevertheless, the analytic computation becomes more problematic when these wave functions are continued analytically in the complex plane. After solving coupled radial SE having regular singularity in the vicinity of the origin and irregular singularity at infinity, Galilev and Polupanov [8] rehabilitated irregular (logarithmic) solutions into the forms of asymptotic expansions and regular solutions as an algebraic combination of logarithmic function, power function, and power series.

Axel Schulze-Halberg [9] derived a finite normal series (order zero) solution of 1D radial SE with a large class of singular potentials having irregular singularity in the vicinity of infinity and/or the origin and thereafter computed energy eigenvalues corresponding to the SE. Gersten [10] rehabilitated the regular and irregular (logarithmic) solutions of the SE into the forms of spherical Bessel's functions and thereafter deployed backward recurrence relations and the Cauchy integral formula to achieve a 5-digit numerical accuracy of the resulting special functions. Based upon the numerical solutions of the SE with nuclear plus Coulomb potential, Mukhaamedzhanov et al. [11] established a novel procedure for obtaining the scattering pole parameters corresponding to the resonance(narrow and broad), virtual (anti bound) and bound states and utilized them to study asymptotic behavior of the Coulomb wave functions.

Cattapan and Maglione [12] numerically evaluated characteristic roots (eigenvalues) and corresponding characteristic vectors( eigenfunctions) of the SE and exploited them, by means of Pade extrapolation (approximant), to analytically continue the bound-states Coulomb wave function into the scattering region and finally achieved a larger numerical accuracy of the resonance parameters.

To overcome the limitations of the Milne-Thompson method, Midy et al. [13] deployed the enduring LT ( Lanczes Tau) method to numerically approximate the regular and irregular solutions of 1D SE, intended to extract the complex poles for the bound states, resonance and virtual states and finally achieved a 12-digit numerical accuracy of the resulting solutions. Thompson and Barnnet [14] made analytic continuation of the hypergeometric series and obtained some continued fractions for the logarithmic derivatives of first(regular) and second(irregular) Coulomb wave functions of the 1D SE and rehabilitated the resulting solutions into the forms of Whittaker and Bessel's functions. The explicit representation of the independent irregular solutions at hand can help us in studying the analytic behavior of Coulomb scattered-wave amplitudes as the energy of the scattered electron is extended into the complex plane, and as the electron angular momentum quantum number  $\ell$  takes on complex values, such as in Regge pole analysis(See Gaspard [16]). Furthermore, the closed-form expressions for the irregular solutions, rather than the usual Laurent series representation, provide explicit answers to how the irregular solutions behave for the electron waves at large distances from the nucleus, useful in presentations of the quantum Coulomb problem.Toli and Zou [17] obtained a Taylor series expansion of the regular Coulomb wave functions and concluded that the exact solutions of the SE, having the Coulomb potential for molecules consisting of more than two particles, cannot be achieved. Simos [19] developed multiderivative methods for comparing the numerical solution of the 1D SE with the existing exponentially- fitted Raptis-Allison method and Ixaru-Rizea method. Parke and Maximon [20] deployed the extended version of the Cauchy integral formula for obtaining the closed- form second independent solutions of the confluent hypergeometric difference equation for the degenerate case. Liu and Mei [21] applied the Laplace transform method as well as the transcendental integral function method for obtaining the second independent infinite series solution of the time dependent SE for hydrogen like atoms.

Many times the Frobenius coefficients, required for the explicit power series representation of a solution to a  $2^{nd}$  order differential equation, obey a three-term recursion relation which cannot be easily utilized. The difficulty comes from the fact that three-term recursion relations have two linearly independent solutions. While attempting to compute the first solution from the recursion, numerical contamination from the second solution can grow, destroying the accuracy of the first solution. We here consider a large class of ordinary second-order differential equations which yield, via the Frobenius method, two-term recursion relations that have explicit solutions. We derive simplifying results for the Frobenius coefficients. These are applied to find the irregular solution of the radial Schrödinger equation for the case of hydrogen-like atoms. The irregular solution, having an  $1/r^{l+1}$  as well as a logarithmic singularity at the origin, is not ordinarily considered. However, it could be used, for instance, in a 'toy' problem wherein the nucleus is given a finite size, say radius  $r_a$ , and there is a different potential energy for the electron at a radius  $r_b > r_a$ , such as a screened electron potential energy proportional to  $e^{-r/b}/r$ . Between the radius  $r_a$  and  $r_b$ , both the first and the second Coulombic solutions would enter the steady bound-state wave function solution to match boundary conditions at  $r_a$  and  $r_b$ . (These boundary conditions are that the wave function, determining electron probabilities, and its derivative, determining the electron charge flux, must match on the boundaries.) However, under realistic conditions,  $r_a$  is more than 10,000 times

smaller than the RMS radius  $\sqrt{\int_0^\infty r^2 |R(r)|^2 r^2 dr}$ , so that the contribution of the second solution is also extremely small. Moreover, theoretical quantum chemists have developed far more sophisticated techniques for getting good wave functions for inner electrons in atoms. This is why we call the problem a ‘toy’.

The rest of this research paper is organized as follows: Section 2 addresses the concept of the Frobenius method required for the subsequent development of the proposed work. Section 3 discusses attempts to develop a novel procedure for obtaining the explicit representation of the two exact solutions of a large class of second order ordinary linear homogeneous differential equation with polynomial coefficients. Section 4 validates the applicability of the proposed procedure by solving the Coulombic Schrödinger equation. Some example expressions, plots and asymptotic behavior of both the regular and the irregular solutions to the Coulombic SE are given in Section 5. Finally, Section 6 summarizes the concrete conclusions and future scope of the work done in this paper.

## 2. Frobenius method

A large class of  $2^{nd}$  order homogeneous linear differential equations with polynomial coefficients and regular singularity at the origin can be expressed as:

$$LR \equiv r^2(\alpha_0 + \alpha_s r^s)R'' + r(\beta_0 + \beta_s r^s)R' + (\gamma_0 + \gamma_s r^s)R = 0, \quad (1)$$

where  $\alpha_i, \beta_i, \gamma_i$  ( $i = 0, s$ ) are real constants with the additional provision that  $\alpha_0 \neq 0$ , and  $s$  needs not be positive nor any negative integer. The most commonly utilized procedure for obtaining the power series solutions to (1), under the situations, when the polynomial  $r^2(\alpha_0 + \alpha_s r^s)$  and  $r(\beta_0 + \beta_s r^s)$  possess regular singularity in the vicinity of  $x = 0$ , was first exploited by Frobenius [15]. Thus, following the work of Frobenius [15], equation (1) will admit at least one infinite series solution of the form:

$$R(r, m) = r^m \sum_{k=0}^{\infty} b_{sk}(m) r^{sk}. \quad (2)$$

Here, the factor  $r^m$  reflects the threshold behavior of the resulting solutions to (1) and the exponent ‘ $m$ ’ is chosen so that the leading coefficient  $b_0(m)$  is a non-zero constant. The Frobenius series on the right of equation (2) can be differentiated term by term and converges on some interval  $(0, d)$  where  $d$  is the distance from the origin to the nearest zero of the polynomial  $(\alpha_0 r + \alpha_s r^s)$  of arbitrary degree in the complex plane and has no zeros on  $(0, d)$ . Further, the coefficients  $b_0(m), b_s(m), b_{2s}(m), \dots$  and the exponent ‘ $m$ ’ are independent of  $r$  and the term  $r^m$  may be complex for the negative powers of  $r$  or undefined at the regular singularity. Due to this reason, we shall consider only those solutions which are defined for positive values of  $r$  since solutions for negative powers of  $r$  can be similarly obtained by using the well-

known result which states that if  $r^m \sum_{k=0}^{\infty} b_{sk}(m) r^{sk}$  is a power series solution of  $LR \equiv 0$  on the interval  $(0, d)$ , then

$|r|^m \sum_{k=0}^{\infty} b_{sk}(m) r^{sk}$  is also a solution on the intervals  $(-d, 0)$  and  $(0, d)$ , respectively. Moreover, the coefficients  $b_{sk}(m_1)$

can be determined recursively for  $k > 0$  and for  $k = 0$ , an ‘‘indicial’’ equation must be satisfied. If the roots  $m_1, m_2$  with  $m_1 \geq m_2$ , of the indicial equation differ by an integer, that is, when  $(m_1 - m_2)/s = t, t \in \mathbb{Z}^+$ , then the two resulting solutions for  $y(x)$  will not be independent.

## 3. Procedure

Finding the closed-form of the first (regular) and the second (irregular) solutions to equation (1) have been well elucidated by developing a novel procedure. The proposed procedure is then applied for obtaining the explicit representation of the two independent solutions as well as some radial wave functions related to the Coulombic Schrödinger equation. The underlying procedure of getting these solutions is totally distinguished from getting them either by means of associated Laguerre polynomials or functions of hypergeometric nature. We observe that the series on the right of equation (2) is a positive term series and hence it is uniformly as well as absolutely convergent, which in turn, possesses first order partial derivatives with respect to the argument  $r$ . Thus, term by term partial differentiation of equation (2) w.r.t.  $r$  yields

$$R'(r, m) = \sum_{k=0}^{\infty} (sk + m) b_{sk}(m) r^{sk+m-1}, \quad (3)$$

$$R''(r, m) = \sum_{k=0}^{\infty} (sk + m)(sk + m - 1) b_{sk}(m) r^{sk+m-2}, \quad (4)$$

where the primes indicate partial derivatives of  $R$  with respect to  $r$ . Define

$$f_i(m) = \alpha_i m(m - 1) + \beta_i m + \gamma_i, \quad (5)$$

where  $i = 0$  or  $s$  and  $m$  is any number (real or complex) such that  $f_0(sk + m)$  is defined for all positive integer values of  $k$ . A practical way to compute the coefficients  $b_{sk}(m) \forall k \geq 1$ , is through the following theorem.

**Theorem 1.** If  $R = R(r, m) = r^m \sum_{k=0}^{\infty} b_{sk}(m) r^{sk}$  is a power series solution of  $LR \equiv 0$ . Then

$$LR \equiv f_0(m) b_0(m) r^m. \quad (6)$$

**Proof:** Insert expressions (3) and (4) into (1) to get

$$LR \equiv \sum_{k=0}^{\infty} \left[ \alpha_0(sk + m)(sk + m - 1) + \beta_0(sk + m) + \gamma_0 \right] b_{sk}(m) r^{sk+m} + \sum_{k=0}^{\infty} \left[ \alpha_s(sk + m)(sk + m - 1) + \beta_s(sk + m) + \gamma_s \right] b_{sk}(m) r^{s(k+1)+m}. \quad (7)$$

Plugging the notations defined by (5) in the forgoing equation (7) yields

$$LR \equiv \sum_{k=0}^{\infty} f_0(sk + m) b_{sk}(m) r^{sk+m} + \sum_{k=0}^{\infty} f_s(sk + m) b_{sk}(m) r^{s(k+1)+m}. \quad (8)$$

The index of the second summation in (8) is a dummy parameter and hence, without loss of generality, it can be shifted from  $k$  to  $k - 1$  to obtain

$$LR \equiv \sum_{k=0}^{\infty} f_0(sk + m) b_{sk}(m) r^{sk+m} + \sum_{k=1}^{\infty} f_s(s(k - 1) + m) b_{s(k-1)}(m) r^{sk+m}.$$

To obtain more clarity on the successive coefficients  $b_{sk}(m) \forall k \geq 1$ , extracting the first non zero term and combining the rest with the second summation yields

$$LR \equiv f_0(m) b_0(m) r^m + \sum_{k=1}^{\infty} \left[ f_0(sk + m) b_{sk}(m) + f_s(s(k - 1) + m) b_{s(k-1)}(m) \right] r^{sk+m}. \quad (9)$$

For  $LR = 0$  to be satisfied, the coefficient of  $r^m$  in the first term and of  $r^{sk+m}$  in the bracket of the summation must be vanished and hence it becomes necessary to define

$$b_{sk}(m) = - \frac{b_{s(k-1)}(m) f_s(s(k - 1) + m)}{f_0(sk + m)} \quad \forall k \geq 1, \quad (10)$$

which completes the proof.

The equation  $f_0(m) = 0$ , so-called indicial equation, is quadratic in  $m$  and determines possible values of ‘ $m$ ’ for a solution of the assumed Frobenius form to exist. The two-term recursion relation (10), with a given starting value for  $b_0(m)$ , will give one all the subsequent coefficients for larger values of  $k$ . We now see that the form of the original differential equation (1) allows for a two-term (rather than a three-term) recursion relation for the coefficients in a Frobenius series. Having this two-term recursion relation, it is straight forward to solve  $b_{sk}(m)$  in terms of  $b_0(m)$ .

Thus, giving  $k$  the values, 1, 2, 3, ... to the recurrence relation (10) yields

$$b_s(m) = \frac{b_0(m)(-1)^1 f_s(m)}{f_0(s + m)}, \quad b_{2s}(m) = \frac{b_0(m)(-1)^2 f_s(s + m) f_s(m)}{f_0(2s + m) f_0(s + m)},$$

$$b_{3s}(m) = \frac{b_0(m)(-1)^3 f_s(2s + m) f_s(s + m) f_s(m)}{f_0(3s + m) f_0(2s + m) f_0(s + m)}$$

and so on. Recursively, we have

$$b_{sk}(m) = \frac{b_0(m)(-1)^k \prod_{j=1}^k (f_s(s(j - 1) + m))}{\prod_{j=1}^k f_0(sj + m)} \quad \forall k \geq 1, \quad (11)$$

where  $1 \leq j \leq k$  and  $\prod_{j=k_1}^{k_2} b_j = 1$  if  $k_2 < k_1$  for any expression  $b_j$ . The result (11) has been furnished to compute the coefficient  $b_{sk}(m)$  in our procedure.

To understand our procedure, let us denote the two possible solutions for ‘ $m$ ’ of the indicial equation  $f_0(m) = 0$  as  $m_1, m_2$  with  $m_1 \geq m_2$ . Here, we briefly discuss the situation when the roots differ by an integer, that is, when  $(m_1 - m_2)/s = t, t \in \mathbb{Z}^+$ . Since

$$f_0(sk + m_1) = \alpha_0 sk(sk + st) = \alpha_0 s^2 k(k + t) \neq 0 \quad \forall \alpha_0 \neq 0, \quad s, m, t \in \mathbb{Z}^+,$$

it follows that  $b_{sk}(m_1)$  is defined for each  $k \geq 1$  and therefore, the method of Frobenius permits us to obtain the first power series solution of (1) as

$$R_1 = R(r, m_1) = \sum_{k=0}^{\infty} b_{sk}(m_1) r^{sk+m_1}.$$

But  $f_0(sk + m_2) = \alpha_0 s^2 k(k - t)$  vanishes for  $k = t$  and hence the coefficient  $b_{sk}(m_2)$  can not be computed for  $k \geq t$ . In such situation, we construct the second solution as a linear combination of  $w_1$  and  $w_2$  as discussed in the following theorems.

**Theorem 2.** Let

$$w_1 = \left. \frac{\partial R}{\partial m} \right|_{m=m_1} = R(r, m_1) \log r + \sum_{k=0}^{\infty} b'_{sk}(m_1) r^{sk+m_1}$$

with the additional provision that  $b_0(m_1) = 1$ . Then

$$L(w_1) = L \left( \left. \frac{\partial R}{\partial m} \right) \right|_{m=m_1} = \alpha_0 s t r^{m_1}. \quad (12)$$

**Proof:** The series on the right hand side of (2) can be differentiated partially with respect to the argument  $m$  to obtain

$$\begin{aligned} \frac{\partial R}{\partial m} &= \frac{\partial}{\partial m} \left( r^m \sum_{k=0}^{\infty} b_{sk}(m) r^{sk} \right) = r^m \log r \sum_{k=0}^{\infty} b_{sk}(m) r^{sk+m} + \sum_{k=0}^{\infty} b'_{sk}(m) r^{sk+m} = \\ &R(r, m) \log r + \sum_{k=0}^{\infty} b'_{sk}(m) r^{sk+m}. \end{aligned}$$

Let the primes indicate partial differentiation with respect to  $r$ , such that  $\frac{dR}{dr} = \frac{\partial R}{\partial r}$ ;  $\frac{d^2 R}{dr^2} = \frac{\partial^2 R}{\partial r^2}$ . The resulting Theorem 1 yields

$$r^2(\alpha_0 + \alpha_s r^s) \frac{\partial^2 R}{\partial r^2} + r(\beta_0 + \beta_s r^s) \frac{\partial R}{\partial r} + (\gamma_0 + \gamma_s r^s) R = f_0(m) b_0(m) r^m. \quad (13)$$

Both sides of equation (13) can be partially differentiated with respect to the argument  $m$ , which yields

$$\begin{aligned} r^2(\alpha_0 + \alpha_s r^s) \frac{\partial^2}{\partial r^2} \left( \frac{\partial R}{\partial m} \right) + r(\beta_0 + \beta_s r^s) \frac{\partial}{\partial r} \left( \frac{\partial R}{\partial m} \right) + (\gamma_0 + \gamma_s r^s) \frac{\partial R}{\partial m} = \\ L \left[ \frac{\partial R}{\partial m} \right] = f'_0(m) b_0(m) r^m + f_0(m) b'_0(m) r^m + f_0(m) b_0(m) r^m \log r. \end{aligned}$$

Setting  $m = m_1$  yields the desired result.

**Theorem 3.** Assume the coefficients  $b_s(m_2), b_{2s}(m_2), \dots, b_{s(t-1)}(m_2)$  are suitable chosen. Let  $w_2 = \sum_{k=0}^{t-1} b_{sk}(m_2) r^{sk+m_2}$  with the provision that  $b_0(m_2) = 1$ , then

$$L(w_2) = f_s(m_1 - s) b_{s(t-1)}(m_2) r^{m_1}. \quad (14)$$

**Proof:** Since  $w_2$  is a polynomial of degree  $t - 1$ , we can, suitably, choose  $b_{st}(m_2) = b_{s(t+1)}(m_2) = \dots = 0$ . Under these restricted conditions, we have

$$w_2 = \sum_{k=0}^{t-1} b_{sk}(m_2) r^{sk+m_2} = \sum_{k=0}^{t-1} b_{sk}(m_2) r^{sk+m_2} + \sum_{k=t}^{\infty} b_{sk}(m_2) r^{sk+m_2} = \sum_{k=0}^{\infty} b_{sk}(m_2) r^{sk+m_2}.$$

With the aid of equation (9), the foregoing equation yields

$$\begin{aligned} L(w_2) &= \sum_{k=1}^{\infty} (f_0(sk + m_2) b_{sk}(m_2) + f_s(s(k-1) + m_2) b_{s(k-1)}(m_2)) r^{sk+m_2} \\ &= \sum_{k=1}^{t-1} (f_0(sk + m_2) b_{sk}(m_2) + f_s(s(k-1) + m_2) b_{s(k-1)}(m_2)) r^{sk+m_2} \\ &+ (f_0(st + m_2) b_{st}(m_2) + f_s(s(t-1) + m_2) b_{s(t-1)}(m_2)) r^{st+m_2} \\ &+ \sum_{k=t+1}^{\infty} (f_0(sk + m_2) b_{sk}(m_2) + f_s(s(k-1) + m_2) b_{s(k-1)}(m_2)) r^{sk+m_2}. \end{aligned}$$

Since  $f_0(sk + m_2) = \alpha_0 s^2 k(k - t) \neq 0 \forall 1 \leq k \leq t - 1$ , we can use (10) to choose the coefficients  $b_s(m_2), b_{2s}(m_2), \dots, b_{s(t-1)}(m_2)$  to satisfy

$$b_{sk}(m_2) = -\frac{f_s(s(k-1) + m_2)b_{s(k-1)}(m_2)}{f_0(sk + m_2)} = (-1)^k \prod_{j=1}^k \frac{f_s(s(j-1) + m_2)}{f_0(sj + m_2)} \quad \forall 1 \leq k \leq t-1. \quad (15)$$

With the aid of newly introduced formula (15) and employing the conditions  $f_0(st + m_2) = f_0(m_1) = 0$  and  $b_{st}(m_2) = b_{s(t+1)}(m_2) = \dots = 0$ , we finally have

$$L(w_2) = (f_s(s(t-1) + m_2)b_{s(t-1)}(m_2)) r^{st+m_2} = f_s(m_1 - s)b_{s(t-1)}(m_2)r^{m_1}.$$

We next move to compute the coefficients  $b'_{sk}(m_1) \forall k \geq 1$ , which will strengthen the subsequent development of the proposed procedure.

### 3.1. Computation of $b'_{sk}(m_1)$

In finding the coefficient  $b'_{sk}(m_1)$ , it is legitimate to take logarithm of each member of equation (11) and write

$$\log |b_{sk}(m)| = \sum_{j=1}^k \log |f_s(s(j-1) + m)| - \sum_{j=1}^k \log |f_0(sj + m)| + \log |b_0(m)|.$$

Term by term logarithmic differentiation of each term of the foregoing series with respect to  $m$  yields

$$\frac{b'_{sk}(m)}{b_{sk}(m)} = \sum_{j=1}^k \frac{f'_s(s(j-1) + m)}{f_s(s(j-1) + m)} - \sum_{j=1}^k \frac{f'_0(sj + m)}{f_0(sj + m)} + \frac{b'_0(m)}{b_0(m)}.$$

The last term on the right in above vanishes, since  $b_0(m_1) = 1$ . Thus, setting  $m = m_1$ , we discover that

$$b'_{sk}(m_1) = b_{sk}(m_1)J_{sk}(m_1), \quad (16)$$

where

$$J_{sk}(m_1) = \sum_{j=1}^k \frac{f'_s(s(j-1) + m_1)}{f_s(s(j-1) + m_1)} - \sum_{j=1}^k \frac{f'_0(sj + m_1)}{f_0(sj + m_1)}. \quad (17)$$

The expression, formed by pair of equations (16) and (17), will act as an important formula for obtaining the second exact power series solution of (1). Next, we turn to establish one more important formula involved in obtaining the linear combination  $L(Cw_1 + w_2)$  which will put us in a better position to construct obtain the desired second exact solution to Coulombic Schrödinger equation. With the aid of equations (12) and (14), we finally have

$$L(Cw_1 + w_2) = CL(w_1) + L(w_2) = C\alpha_0 str^{m_1} + f_s(m_1 - s)b_{s(t-1)}(m_2)r^{m_1}.$$

Lastly, We choose  $C$  such that

$$C = -\frac{f_s(m_1 - s)b_{s(t-1)}(m_2)}{\alpha_0 st} \text{ so that } L(Cw_1 + w_2) = 0,$$

which shows that  $R_2 = R(r, m_2) = Cw_1 + w_2$  is the second exact power series solution of (1). However, if  $C = 0$ , then there is no need to compute  $w_1$  and hence, the second solution in this case becomes  $R_2 = R(r, m_2) = w_2$ .

## 4. Two exact solutions of the Coulombic Schrödinger equation

To exemplify the procedure, we consider the case when  $s = 1$ . (The resulting differential equation is then of hypergeometric type.) We apply the proposed procedure for obtaining two exact solutions to the Coulombic Schrödinger equation:

$$\frac{1}{r^2} \frac{d}{dr} \left( r^2 \frac{dR}{dr} \right) + \frac{2m}{\hbar^2} \left( E - V(r) - \frac{\hbar^2 \ell(\ell + 1)}{2m r^2} \right) R = 0, \quad (18)$$

where the non negative integer  $\ell$  represents the angular momentum quantum number,  $\hbar = h/(2\pi)$ ,  $h$  is Planck's constant,  $E$  represents the total energy of the system and  $V(r) = -\frac{Ze^2}{4\pi\epsilon_0 r}$  represents the potential energy. Incidentally, the Coulomb potential energy,  $V(r)$ , admits continuous states for  $E > 0$ , describing electron-nucleus scattering, and discrete bound states for  $E < 0$ . We shall confine our discussion to the latter. Therefore, the values of  $\kappa \equiv \left| \frac{\sqrt{-2mE}}{\hbar} \right|$  will be taken as a positive real number with the units of inverse length.

Under these restrictions, equation (18) reduces to the following form:

$$\frac{1}{r^2} \frac{d}{dr} \left( r^2 \frac{dR}{dr} \right) + \left( -\kappa^2 + 2 \left( \frac{Zme^2}{4\pi\epsilon_0 \hbar^2} \right) \cdot \frac{1}{r} - \frac{\ell(\ell + 1)}{r^2} \right) R = 0.$$

Dividing throughout by  $\kappa^2$  and defining  $\kappa_0 = \frac{Zme^2}{4\pi\epsilon_0\hbar^2}$  in the foregoing equation, we obtain

$$\frac{1}{(\kappa r)^2} \frac{d}{dr} \left( r^2 \frac{dR}{dr} \right) + \left( -1 + \frac{2\kappa_0}{\kappa} \frac{1}{(\kappa r)} - \frac{\ell(\ell+1)}{(\kappa r)^2} \right) R = 0, \quad (19)$$

which can be further simplified as

$$r^2 \frac{d^2 R}{dr^2} + 2r \frac{dR}{dr} + \left( -\kappa^2 r^2 + 2\kappa_0 r - \ell(\ell+1) \right) R = 0. \quad (20)$$

The parameter  $\kappa_0$  is the inverse of the Bohr radius  $a$ . We first examine the asymptotic behavior of the solutions of (20) for large value of  $r$ . For this, take  $\rho = \kappa r$  so that  $\frac{d\rho}{dr} = \kappa$ . Thus,

$$\frac{dR}{dr} = \frac{dR}{d\rho} \cdot \frac{d\rho}{dr} = \kappa \frac{dR}{d\rho}; \quad \frac{d}{dr} \left( r^2 \frac{dR}{dr} \right) = \rho^2 \frac{d^2 R}{d\rho^2} + 2\rho \frac{dR}{d\rho}.$$

Inserting these derivatives into (20) yields

$$\frac{d^2 R}{d\rho^2} + \frac{2}{\rho} \frac{dR}{d\rho} + \left( -1 + \frac{2\kappa_0}{\kappa} \frac{1}{\rho} - \frac{\ell(\ell+1)}{\rho^2} \right) R = 0. \quad (21)$$

For large values of  $\rho$ , the coefficient in parenthesis can be approximated by  $-1$ , so equation (21) reduces to

$$\frac{d^2 R}{d\rho^2} \cong R. \quad (22)$$

The general solution of (22) is given by  $R \cong c_1 e^\rho + c_2 e^{-\rho}$ , but  $e^\rho$  blows up for large value of  $\rho$ , which is an unbounded solution. Therefore, we must have  $c_1 = 0$ . That leaves  $R \cong c_2 e^{-\rho}$ . Matters are simplified if we extract the asymptotic behavior from  $R$ . Thus, we define a new function  $u(r)$  through

$$R(r) = e^{-\rho} u(r) = e^{-\kappa r} u(r). \quad (23)$$

Next, we have

$$\frac{dR}{dr} = e^{-\kappa r} \left( \frac{du}{dr} - \kappa u \right); \quad \frac{d^2 R}{dr^2} = e^{-\kappa r} \left( \frac{d^2 u}{dr^2} - 2\kappa \frac{du}{dr} + \kappa^2 u \right).$$

Inserting these derivatives and (23) into (20) yields

$$r^2 \frac{d^2 u}{dr^2} + 2r(1 - \kappa r) \frac{du}{dr} + (-\ell(\ell+1) + 2(\kappa_0 - \kappa)r) u = 0 \quad (24)$$

Here, we see that  $r = 0$  is a regular singular point. In our notations, we have

$$\begin{aligned} s &= 1, \\ \alpha_0 &= 1, \quad \alpha_1 = 0; \quad \beta_0 = 2, \quad \beta_1 = -2\kappa; \quad \gamma_0 = -\ell(\ell+1), \quad \gamma_1 = 2(\kappa_0 - \kappa). \\ f_0(m) &= (m - \ell)(m + \ell + 1), \quad f'_0(m) = 2m + 1; \\ f_1(m) &= -2\kappa(m - \eta + 1), \quad f'_1(m) = -2\kappa, \quad \text{where } \kappa_0 = \kappa\eta. \end{aligned}$$

#### 4.1. Comments and discussion

The roots of the indicial equation  $f_0(m) = 0$  are  $m = \ell, -\ell - 1$ . Take  $m_1 = \ell, m_2 = -\ell - 1$  so that  $m_1 - m_2 = 2\ell + 1 = t$  where  $t$  is a positive integer. Thus, by Frobenius method, equation (20) has at least one solution of the form

$$R(r, m) = e^{-\kappa r} \sum_{k=0}^{\infty} b_k(m) r^{k+m}. \quad (25)$$

Since  $e^{-\kappa r} = 1 - \kappa r + \frac{\kappa^2 r^2}{2} + \dots$ , the radial wave function  $R(r)$  behaves as  $b_0(m) r^m$  for small  $r$ . Therefore, for  $m = \ell$ ,  $R(r)$  is not singular at the origin. But for  $m = -\ell - 1$ ,  $R(r) \propto 1/r^{\ell+1}$  for small  $r$ . Since  $\ell = 0, 1, 2, 3, \dots$ , the root  $m = -\ell - 1$  makes the term  $1/r^{\ell+1}$  infinite at the origin. But, for the bound state eigenfunction to be normalized, we should have

$$\int_0^{\infty} R^2 r^2 dr \propto \int_0^a \frac{1}{r^{2\ell}} dr \propto \frac{1}{r^{2\ell-1}} \Big|_0^a, \quad (26)$$

where  $a$  is a small number. The  $m = -\ell - 1$  case gives states unnormalizable when  $\ell > 0$ . When  $\ell = 0$ , the divergence of the  $R(r)$  near the origin gives one a radial function which no longer satisfies the original SE, since the diverge at the origin is strong enough to make  $LR(r) = -(4\pi/r^2)\delta(r)$ , where  $\delta(r)$  is the Dirac delta function (see Messiah [18, p.352]). For this reason, standard references reject this root. Little effort is seen in the literature for obtaining the second exact solution of the Coulombic Schrödinger equation.

#### 4.2. First exact solution of Coulombic Schrödinger equation

By the Frobenius method, equation (24) has at least one solution of the form

$$u(r, m) = \sum_{k=0}^{\infty} b_k(m) r^{k+m}. \quad (27)$$

Calculating the coefficients by successive differentiating a differential equation may be excellent in theory, but it is usually not a practical computational procedure. Rather, one might try to evaluate  $b_k(m)$  recursively, one by one by writing the recurrence relation (10) first for  $k = 1$ , then  $k = 2$ , and so forth. Alternatively, we can convert the general formula for  $b_k(m)$  in terms of  $b_0(m)$ . Thus, equation (10) gives one

$$b_k(m) = -\frac{f_1(k-1+m)b_{k-1}(m)}{f_0(k+m)} = \frac{2\kappa(k+m-\eta)b_{k-1}(m)}{(k+m-\ell)(k+m+\ell+1)} \quad \forall k \geq 1.$$

Giving  $k$  the values 1, 2, 3, ...,

$$\begin{aligned} b_1(m) &= \frac{(2\kappa)^1 b_0(m) (1+m-\eta)}{(1+m-\ell)(1+m+\ell+1)}, \\ b_2(m) &= \frac{(2\kappa)^2 b_0(m) (2+m-\eta) (1+m-\eta)}{(2+m-\ell)(1+m-\ell)(2+m+\ell+1)(1+m+\ell+1)}, \\ &\dots \\ b_k(m) &= (2\kappa)^k b_0(m) \prod_{j=1}^k \frac{(j+m-\eta)}{(j+m-\ell)(j+m+\ell+1)} \quad \forall k \geq 1. \end{aligned} \quad (28)$$

Setting  $m = m_1 = \ell$  in equation (28) yields

$$b_k(\ell) = \frac{(2\kappa)^k b_0(\ell)}{k!} \prod_{j=1}^k \frac{j+\ell-\eta}{j+2\ell+1}. \quad (29)$$

Changing  $k$  to  $k+1$  in the resulting equation (29) to obtain

$$b_{k+1}(\ell) = \frac{(2\kappa)^{k+1} b_0(\ell)}{(k+1)!} \prod_{j=1}^{k+1} \frac{j+\ell-\eta}{j+2\ell+1} = \frac{2\kappa(k+1+\ell-\eta)}{(k+1)(k+2\ell+2)} b_k(\ell). \quad (30)$$

Suppose  $B_k(m)$  represents the  $k^{\text{th}}$  term of the series represented by (27). Using (30), the ratio of  $(k+1)^{\text{th}}$  term to  $k^{\text{th}}$  term of this series for the case  $m = m_1 = \ell$  is represented as

$$\frac{B_{k+1}(\ell)}{B_k(\ell)} = \frac{b_{k+1}(\ell)}{b_k(\ell)} r = \frac{2\kappa(k+1+\ell-\eta)}{(k+1)(k+2\ell+2)} r \cong \frac{2\kappa r}{k} \text{ for large } k.$$

This means that the first solution  $u_1(r) = u(r, \ell)$  is asymptotically equals to  $e^{2\kappa r}$ . This implies  $R_1(r) = R(r, \ell) = e^{-\kappa r} u_1(r) \cong e^{\kappa r}$  which blows up for large value of  $r$ . This means the series solution  $u_1(r) = u(r, \ell)$  must terminate. This implies there must exist some maximum integer  $k$  such that  $b_k \neq 0$ , and  $b_{k+1} = 0, b_{k+2} = 0$  and so on. This is possible only if we can choose  $k+\ell+1-\eta = 0$  so that  $\eta = k+\ell+1$  (so called principal quantum number) This suggests that  $R_1(r)$  is a polynomial of maximum degree  $\eta - \ell - 1$ . Setting  $b_0(m_1) = 1$ , and using  $\eta \equiv \kappa_0/\kappa$ , the first exact series solution represented by (25) is finally expressed as

$$R(r, m_1) = e^{-\kappa r} u(r) = e^{-\frac{Zr}{\eta a}} \sum_{k=0}^{\eta-\ell-1} b_k(\ell) r^{k+\ell} = e^{-\frac{Zr}{\eta a}} r^\ell \sum_{k=0}^{\eta-\ell-1} \frac{1}{k!} \prod_{j=1}^k \frac{(j+\ell-\eta)}{(j+2\ell+1)} \left(\frac{2Zr}{\eta a}\right)^k. \quad (31)$$

The sum factor is the associated Laguerre polynomial  $L_{\eta-\ell-1}^{2\ell+1}(2Zr/(\eta a))$ .

#### 4.3. Second exact solution of the Coulombic Schrödinger equation

We first establish the fact that two solutions of the indicial equation give a set of linearly dependent solutions to equation (25). For this, changing  $k$  to  $k+1$  in (28) to obtain

$$b_{k+1}(m) = \frac{(2\kappa)^{k+1} (k+1+m-\eta) b_0(m)}{(k+1+m-\ell)(k+1+m+\ell+1)} \cdot \prod_{j=1}^k \frac{(j+m-\eta)}{(j+m-\ell)(j+m+\ell+1)}. \quad (32)$$

Setting  $m = \ell$ ,  $b_0(\ell) = 1$ , the foregoing equation (32) yields

$$b_{k+1}(\ell) = \frac{(2\kappa)^{k+1} (k+1+\ell-\eta)}{(k+1)(k+2\ell+2)} \cdot \frac{1}{k!} \cdot \frac{\prod_{j=1}^k (j+\ell-\eta)}{\prod_{j=1}^k (j+2\ell+1)}.$$

But

$$\prod_{j=1}^k (j + 2\ell + 1) = \frac{(k + 2\ell + 1)!}{(2\ell + 1)!}$$

and

$$\prod_{j=1}^k (j + \ell - \eta) = (k + \ell - \eta)! \text{ and vanishes for } j \leq \eta - \ell.$$

Therefore

$$b_{k+1}(\ell) = \frac{(2\kappa)^{k+1} (k + 1 + \ell - \eta)!(2\ell + 1)!}{(k + 1)!(k + 2\ell + 2)!}. \quad (33)$$

Similarly, setting,  $m = -\ell - 1$ ,  $b_0(-\ell - 1) = \frac{(2\ell + 1)!}{(2\kappa)^{2\ell+1}}$  in equation (32) to get

$$b_{k+1}(-\ell - 1) = \frac{(2\kappa)^{k+1} (k - \ell - \eta) (2\ell + 1)!}{(k + 1)!(k - 2\ell) (2\kappa)^{2\ell+1}} \cdot \frac{\prod_{j=1}^k (j - \ell - \eta - 1)}{\prod_{j=1}^k (j - 2\ell - 1)}.$$

Changing  $k$  to  $k + 2\ell + 1$ , we get

$$b_{k+2\ell+1+1}(-\ell - 1) = \frac{(2\kappa)^{k+2\ell+2} (k + \ell + 1 - \eta) (2\ell + 1)!}{(k + 1)!(k + 2\ell + 2)! (2\kappa)^{2\ell+1}} \cdot \frac{\prod_{j=1}^{k+2\ell+1} (j - \ell - \eta - 1)}{\prod_{j=1}^{k+2\ell+1} (j - 2\ell - 1)}.$$

But

$$\prod_{j=1}^{k+2\ell+1} (j - 2\ell - 1) \text{ will vanish for } j \leq 2\ell + 1, \text{ and otherwise}$$

$$\prod_{j=2\ell+2}^{k+2\ell+1} (j - 2\ell - 1) = k!.$$

Also,  $\prod_{j=1}^{k+2\ell+1} (j - \ell - 1 - \eta)$  vanishes for  $j \leq \eta + \ell + 1$ , and otherwise

$$\prod_{j=\eta+\ell+2}^{k+2\ell+1} (j - \ell - 1 - \eta) = (k + \ell - \eta)(k + \ell - \eta - 1)\dots(1) = (k + \ell - \eta)!.$$

Therefore

$$b_{k+2\ell+1+1}(-\ell - 1) = \frac{(2\kappa)^{k+1} (k + \ell + 1 - \eta)!(2\ell + 1)!}{(k + 1)!(k + 2\ell + 2)!}, \quad (34)$$

which is exactly the same as (33). This suggests that the two solutions of the indicial equation yield a set of two linearly dependent solutions to the Coulombic Schrödinger equation (18). In other words, out of these two, only one of them is useful and the other one can be dropped. Interestingly, discarding one of the solution has nothing to do with the regular singularity at  $r = 0$ . Incidentally, we will construct another linearly independent solution of the Coulombic SE (24) by employing the general procedure proposed in Section 3.

4.3.1. *Computation of  $b'_k(\ell) \forall k \geq \eta - \ell$ .* Employing the resulting equations (16) and (17) for the case  $m = \ell$ ,  $b_0(\ell) = 1$  and  $\kappa = \frac{Z}{\eta a}$  to get

$$b'_k(\ell) = b_k(\ell) J_k(\ell), \quad (35)$$

where

$$b_k(\ell) = \frac{1}{k!} \prod_{j=1}^k \frac{(j + \ell - \eta)}{(j + 2\ell + 1)} \left( \frac{2Z}{\eta a} \right)^k \quad \forall k \geq 1;$$

$$J_k(\ell) = \sum_{j=1}^k \frac{f'_1(j - 1 + \ell)}{f_1(j - 1 + \ell)} - \sum_{j=1}^k \frac{f'_0(j + \ell)}{f_0(j + \ell)} = \sum_{j=1}^k \left( \frac{1}{j - \eta + \ell} - \frac{1}{j} - \frac{1}{j + 2\ell + 1} \right),$$

which becomes an indeterminate for  $j = \eta - \ell$ . To overcome this situation, we re-write equation (28) as

$$\begin{aligned} b_k(m) &= b_0(m) \frac{\prod_{j=1}^{\eta-\ell} (m - \eta + j) \prod_{j=\eta-\ell+1}^k (j + m - \eta)}{\prod_{j=1}^k (j + m - \ell)(j + m + \ell + 1)} \left( \frac{2Z}{\eta a} \right)^k \\ &= b_0(m) \frac{(m - \eta + 1)(m - \eta + 2) \cdots (m - \ell - 1)(m - \ell) \prod_{j=\eta-\ell+1}^{\eta-\ell} (j + m - \eta)}{\prod_{j=1}^k (j + m - \ell)(j + m + \ell + 1)} \left( \frac{2Z}{\eta a} \right)^k, \end{aligned}$$

which vanishes for  $m = \ell$ . Therefore, we re-write the foregoing equation as

$$b_k(m) = (m - \ell) C_k(m), \quad (36)$$

where

$$C_k(m) = b_0(m) \frac{(m - \eta + 1)(m - \eta + 2) \cdots (m - \ell - 1) \prod_{j=\eta-\ell+1}^k (j + m - \eta)}{\prod_{j=1}^k (j + m - \ell)(j + m + \ell + 1)} \left( \frac{2Z}{\eta a} \right)^k.$$

Differentiating the resulting equation (36) with respect to  $m$  yields

$$b'_k(m) = (m - \ell) C'_k(m) + C_k(m). \quad (37)$$

Plugging the root  $m = \ell$ ,  $b_0(\ell) = 1$  into (37) yields

$$\begin{aligned} b'_k(\ell) &= C_k(\ell) = \frac{(\ell - \eta + 1)(\ell - \eta + 2) \cdots (\ell - \ell - 2)(\ell - \ell - 1) \prod_{j=\eta-\ell+1}^k (j + m - \eta)}{\prod_{j=1}^k (j)(j + 2\ell + 1)} \left( \frac{2Z}{\eta a} \right)^k \\ &= \frac{(-1)^{\eta-\ell-1} (\eta - \ell - 1)! \prod_{j=\eta-\ell+1}^k (j + \ell - \eta)}{k! \prod_{j=1}^k (j + 2\ell + 1)} \left( \frac{2Z}{\eta a} \right)^k. \end{aligned}$$

But

$$\prod_{j=1}^k (j + 2\ell + 1) = (1 + 2\ell + 1)(2 + 2\ell + 1) \cdots (k - 1 + 2\ell + 1)(k + 2\ell + 1) = \frac{(k + 2\ell + 1)!}{(2\ell + 1)!}.$$

Also

$$\begin{aligned} \prod_{j=\eta-\ell+1}^k (\ell - \eta + j) &= (\ell - \eta + \eta - \ell + 1)(\ell - \eta + \eta - \ell + 2)(\ell - \eta + \eta - \ell + 3) \cdots (\ell - \eta + k) \\ &= 1 \cdot 2 \cdot 3 \cdots (\ell - \eta + k) = (k - \eta + \ell)!. \end{aligned}$$

Therefore

$$b'_k(\ell) = \frac{(-1)^{\eta-\ell-1} (\eta - \ell - 1)! (k - \eta + \ell)! (2\ell + 1)!}{k! (k + 2\ell + 1)!} \left( \frac{2Z}{\eta a} \right)^k \quad \forall k \geq \eta - \ell.$$

4.3.2. *Computation of  $b'_k(\ell) \forall 1 \leq k \leq \eta - \ell - 1$ . Re-writing equation (28) as*

$$\begin{aligned} b_k(m) &= \frac{b_0(m)(m - \eta + k)(m - \eta + k - 1) \cdots (m - \eta + 3)(m - \eta + 2)(m - \eta + 1) \left( \frac{2Z}{\eta a} \right)^k}{(m - \ell + k)(m - \ell + k - 1) \cdots (m - \ell + 1)(m + \ell + 1 + k)(m + \ell + 1 + k - 1) \cdots (m + \ell + 2)} \\ &= \frac{b_0(m)(m - \eta + k)!(m - \ell)!(m + \ell + 1)!}{(m - \ell + k)!(m + \ell + 1 + k)(m - \eta)!} \left( \frac{2Z}{\eta a} \right)^k. \end{aligned}$$

Setting  $m = \ell$ ,  $b_0(\ell) = 1$ , in the foregoing equation, in this case, yields

$$b'_k(\ell) = \frac{\partial}{\partial m} \frac{(m - \eta + k)!(m - \ell)!(m + \ell + 1)!}{(m - \ell + k)!(m + \ell + 1 + k)(m - \eta)!} \left( \frac{2Z}{\eta a} \right)^k \Bigg|_{m=\ell}. \quad (38)$$

The expression on the right hand side of (40) can be further simplified as shown in the following theorem.

**Theorem 4.** The coefficient

$$\frac{\partial}{\partial m} \frac{(m - \eta + k)!}{(m - \eta)!} \frac{(m - \ell)!}{(m - \ell + k)!} \frac{(m + \ell + 1)!}{(m + \ell + 1 + k)!} \Bigg|_{m=\ell}$$

simplifies to

$$\frac{(-1)^{k+1}}{k!} \left( \prod_{j=1}^k \frac{\eta - \ell - j}{2\ell + 1 + j} \right) \sum_{j=1}^k \left( \frac{1}{\eta - \ell - j} + \frac{1}{2\ell + 1 + j} + \frac{1}{j} \right). \quad (39)$$

**Proof:** Define

$$\begin{aligned} c(\eta, \ell, k) &= \frac{\partial}{\partial m} \frac{(m - \eta + k)!}{(m - \eta)!} \frac{(m - \ell)!}{(m - \ell + k)!} \frac{(m + \ell + 1)!}{(m + \ell + 1 + k)!} \Big|_{m=\ell} \\ &= \frac{\partial}{\partial m} \left( \prod_{j=1}^k \frac{m - \eta + j}{(m - \ell + j)(m + \ell + 1 + j)} \right) \Big|_{m=\ell} = \frac{\partial}{\partial m} F(\eta, \ell, k, m) \Big|_{m=\ell}, \end{aligned} \quad (40)$$

where

$$F(\eta, \ell, k, m) = \prod_{j=1}^k \frac{m - \eta + j}{(m - \ell + j)(m + \ell + 1 + j)}.$$

Define a logarithmic derivative of  $F(\eta, \ell, k, m)$  through

$$G(\eta, \ell, k, m) \equiv \frac{1}{F(\eta, \ell, k, m)} \frac{\partial}{\partial m} F(\eta, \ell, k, m) = \frac{\partial}{\partial m} (\ln F(\eta, \ell, k, m)),$$

with the advantage that products in  $F(\eta, \ell, k, m)$  become sums. We have

$$\begin{aligned} G(\eta, \ell, k, m) &= \frac{\partial}{\partial m} \ln \prod_{j=1}^k \left( \frac{m - \eta + j}{(m + \ell + 1 + j)(m - \ell + j)} \right) \\ &= \frac{\partial}{\partial m} \sum_{j=1}^k (\ln(m - \eta + j) - \ln(m + \ell + 1 + j) - \ln(m - \ell + j)) \\ &= \sum_{j=1}^k \left( \frac{1}{m - \eta + j} - \frac{1}{m + \ell + 1 + j} - \frac{1}{m - \ell + j} \right). \end{aligned}$$

Therefore (41) gives one

$$\begin{aligned} c(\eta, \ell, k) &= F(\eta, \ell, k, m) G(\eta, \ell, k, m) \Big|_{m=\ell} \\ &= \left( \prod_{j=1}^k \frac{m - \eta + j}{(m - \ell + j)(m + \ell + 1 + j)} \right) \sum_{j=1}^k \left( \frac{1}{m - \eta + j} - \frac{1}{m - \ell + j} - \frac{1}{m + \ell + 1 + j} \right) \Big|_{m=\ell} \\ &= \frac{(-1)^{k+1}}{k!} \left( \prod_{j=1}^k \frac{\eta - \ell - j}{2\ell + 1 + j} \right) \sum_{j=1}^k \left( \frac{1}{\eta - \ell - j} + \frac{1}{j} + \frac{1}{2\ell + 1 + j} \right). \end{aligned}$$

With the aid of resulting equation (40), the undergoing equation (39) yields

$$b'_k(\ell) = \frac{(-1)^{k+1}}{k!} \left( \prod_{j=1}^k \frac{\eta - \ell - j}{2\ell + 1 + j} \right) \sum_{j=1}^k \left( \frac{1}{\eta - \ell - j} + \frac{1}{2\ell + 1 + j} + \frac{1}{j} \right) \left( \frac{2Z}{\eta a} \right)^k \quad \forall 1 \leq k \leq \eta - \ell - 1. \quad (41)$$

Here, we assume  $b'_k(\ell) = 0 \forall 1 \leq k \leq 0$ .

**4.3.3. Computation of  $w_1$ .** For obtaining the second exact solution of (24), the resulting expressions for  $b'_k(\ell)$  represented by (38) and (42) and Theorem 2 suggest us to write

$$w_1 = u(r, \ell) \log r + r^\ell \sum_{k=1}^{\eta-\ell-1} b'_k(\ell) r^k + r^\ell \sum_{k=\eta-\ell}^{\infty} b'_k(\ell) r^k.$$

**4.3.4. Computation of  $C$ .** Setting  $b_0(m_2) = b_0(-\ell - 1) = 1$  into the resulting equation (28) yields

$$b_k(-\ell - 1) = \left( \frac{2Z}{\eta a} \right)^k \frac{\prod_{j=1}^k (\eta + \ell + 1 - j)}{k! \prod_{j=1}^k (2\ell + 1 - j)}.$$

In particular, setting  $k = 2\ell$  into the undergoing equation yields

$$b_{2\ell}(-\ell - 1) = \left( \frac{2Z}{\eta a} \right)^{2\ell} \frac{1}{(2\ell)!} \frac{\prod_{j=1}^{2\ell} (\eta + \ell + 1 - j)}{\prod_{j=1}^{2\ell} (2\ell + 1 - j)}. \quad (42)$$

But

$$\prod_{j=1}^{2\ell} (2\ell + 1 - j) = (2\ell)(2\ell - 1) \cdots 3 \cdot 2 \cdot 1 = (2\ell)!.$$

Also

$$\begin{aligned} \prod_{j=1}^{2\ell} (\eta + \ell + 1 - j) &= (\eta + \ell + 1 - 1)(\eta + \ell + 1 - 2) \dots (\eta + \ell + 1 - 2\ell + 1)(\eta + \ell + 1 - 2\ell) \\ &= \frac{(\eta + \ell)(\eta + \ell - 1) \dots (\eta - \ell + 2)(\eta - \ell + 1)(\eta - \ell)!}{(\eta - \ell)!} = \frac{(\eta + \ell)!}{(\eta - \ell)!}. \end{aligned}$$

Plugging the resulting expressions into (43) yields

$$b_{2\ell}(-\ell - 1) = \frac{(\eta + \ell)!}{(\eta - \ell)!(2\ell)!(2\ell)!} \left( \frac{2Z}{\eta a} \right)^{2\ell}.$$

Therefore by definition

$$\begin{aligned} C &= -\frac{f_1(m_1 - 1)b_{t-1}(m_2)}{\alpha_0 stb_0(m_1)} = -\frac{f_1(\ell - 1)b_{2\ell}(-\ell - 1)}{2\ell + 1} \\ &= -\frac{2Z}{\eta a} \frac{(\eta - \ell)b_{2\ell}(-\ell - 1)}{2\ell + 1} = -\frac{(\eta + \ell)!}{(2\ell + 1)!(2\ell)!(\eta - \ell - 1)!} \left( \frac{2Z}{\eta a} \right)^{2\ell+1}. \end{aligned} \quad (43)$$

4.3.5. *Computation of  $w_2$ .* By definition,

$$w_2 = \sum_{k=0}^{2\ell} b_k(-\ell - 1)r^{k-\ell-1} = r^{-\ell-1} \sum_{k=0}^{2\ell} \frac{\prod_{j=1}^k (\eta + \ell + 1 - j)}{k! \prod_{j=1}^k (2\ell + 1 - j)} \left( \frac{2Zr}{\eta a} \right)^k.$$

Finally, the second exact solution to Coulombic Schrödinger equation (18) is

$$\begin{aligned} S_{\eta\ell}^Z(r) &= R(r, m_2) = e^{-\frac{Zr}{\eta a}} u(r, m_2) = e^{-\frac{Zr}{\eta a}} (w_2 + Cw_1) \\ &= e^{-\frac{Zr}{\eta a}} \left[ r^{-\ell-1} \sum_{k=0}^{2\ell} \frac{1}{k!} \prod_{j=1}^k \frac{\eta + \ell + 1 - j}{2\ell + 1 - j} \left( \frac{2Zr}{\eta a} \right)^k \right. \\ &\quad - \frac{(\eta + \ell)! r^\ell}{(2\ell + 1)!(2\ell)!(\eta - \ell - 1)!} \left( \frac{2Z}{\eta a} \right)^{2\ell+1} \left\{ \left( \sum_{k=0}^{\eta-\ell-1} \frac{1}{k!} \prod_{j=1}^k \frac{(j + \ell - \eta)}{(j + 2\ell + 1)} \left( \frac{2Zr}{\eta a} \right)^k \right) \log r \right. \\ &\quad + \sum_{k=1}^{\eta-\ell-1} \frac{(-1)^{k+1}}{k!} \left( \prod_{j=1}^k \frac{\eta - \ell - j}{2\ell + 1 + j} \right) \sum_{j=1}^k \left( \frac{1}{\eta - \ell - j} + \frac{1}{j} + \frac{1}{2\ell + 1 + j} \right) \left( \frac{2Zr}{\eta a} \right)^k \\ &\quad \left. \left. + \sum_{k=\eta-\ell}^{\infty} \frac{(-1)^{\eta-\ell-1} (\eta - \ell - 1)!(k - \eta + \ell)!(2\ell + 1)!}{k!(k + 2\ell + 1)!} \left( \frac{2Zr}{\eta a} \right)^k \right\} \right]. \end{aligned}$$

We are now in a position to provide some example expressions and plots of the Coulombic radial wave functions of the second kind (and of the first kind) in the following section 5.

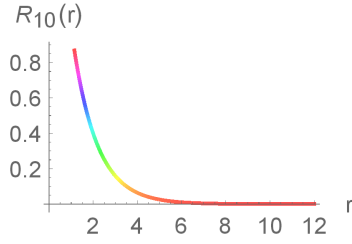
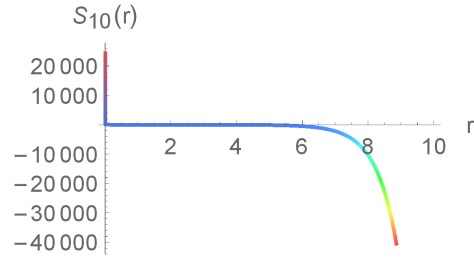
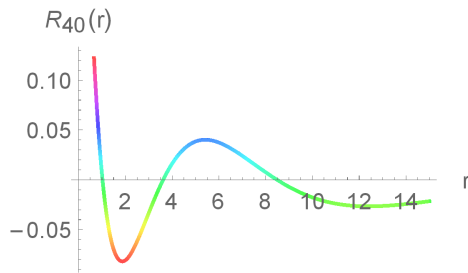
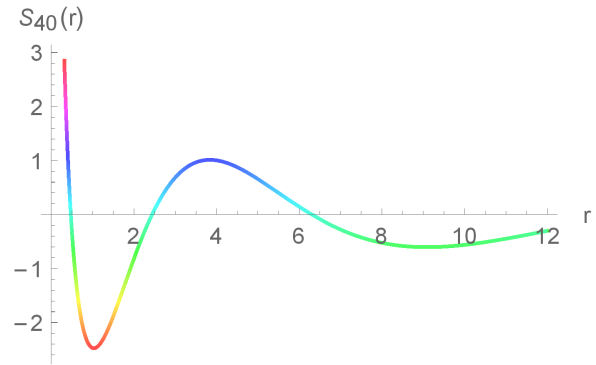
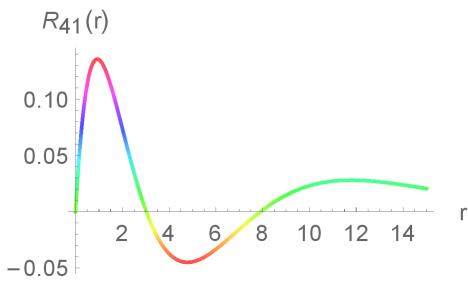
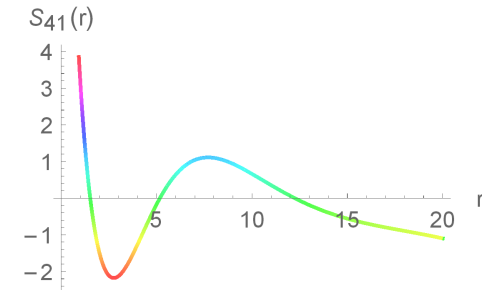
## 5. Examples of radial wave functions of second kind

**Case I.** If  $\eta = 1$ , then  $\ell = 0$ . In this case, the graphical representation of the radial wave function of the second kind (and of first kind) are represented in Figs. 1 and 2 and mathematically, employing equation (45), is

$$S_{10}^Z(r) = e^{-\frac{Zr}{a}} \left\{ \frac{1}{r} - \frac{2Z}{a} \left( \log r + \sum_{k=1}^{\infty} \frac{(k-1)!}{k!(k+1)!} \left( \frac{2Zr}{a} \right)^k \right) \right\}.$$

**Case II.** If  $\eta = 2$ , then  $\ell = 0, 1$ . In this case, the graphical representation is displayed in Figs. 3 and 4, and , mathematically, using equation (45), is

$$\begin{aligned} S_{20}^Z(r) &= e^{-\frac{Zr}{2a}} \left\{ \frac{1}{r} - \frac{2Z}{a} \left( \left( 1 - \frac{Zr}{2a} \right) \log r + \frac{5Zr}{4a} - \sum_{k=2}^{\infty} \frac{(k-2)!}{k!(k+1)!} \left( \frac{Zr}{a} \right)^k \right) \right\}, \\ S_{21}^Z(r) &= e^{-\frac{Zr}{2a}} \left\{ \frac{1}{r^2} + \frac{3Z}{2ar} + \frac{3Z^2}{2a^2} - \frac{Z^3 r}{2a^3} \left( \log r + \sum_{k=1}^{\infty} \frac{6(k-1)!}{k!(k+3)!} \left( \frac{Zr}{a} \right)^k \right) \right\}. \end{aligned}$$

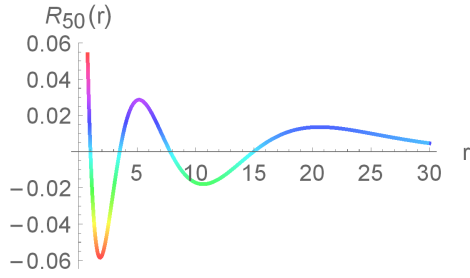
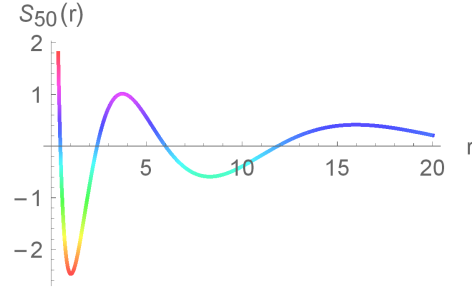
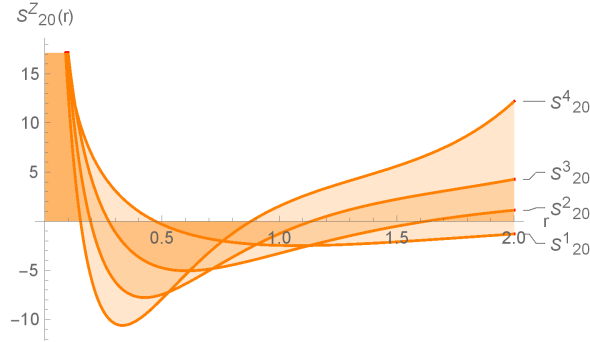
FIG. 1. Radial wave function  $R_{10}(r)$ FIG. 2. Radial wave function  $S_{10}(r)$ FIG. 3. Radial wave function  $R_{40}(r)$ FIG. 4. Radial wave function  $S_{40}(r)$ FIG. 5. Radial wave function  $R_{41}(r)$ FIG. 6. Radial wave function  $S_{41}(r)$ 

**Case III.** If  $\eta = 3$ , then  $\ell = 0, 1, 2$ , In this case, the graphical representation is displayed in Figs. 5 and 6, and mathematically,

$$S_{30}^Z(r) = e^{-\frac{Zr}{3a}} \left\{ \frac{1}{r} - \frac{2Z}{a} \left( \left( 1 - \frac{2Zr}{3a} + \frac{2Z^2r^2}{27a^2} \right) \log r + \frac{4Zr}{3a} - \frac{23Z^2r^2}{81a^2} + \sum_{k=3}^{\infty} \frac{2(k-3)!}{k!(k+1)!} \left( \frac{2Zr}{3a} \right)^k \right) \right\},$$

$$S_{31}^Z(r) = e^{-\frac{Zr}{3a}} \left\{ \frac{1}{r^2} + \frac{4Z}{3ar} + \frac{4Z^2}{3a^2} - \frac{16Z^3r}{27a^3} \left( \left( 1 - \frac{Zr}{6a} \right) \log r + \frac{3Zr}{8a} - \sum_{k=3}^{\infty} \frac{6(k-2)!}{k!(k+3)!} \left( \frac{2Zr}{3a} \right)^k \right) \right\},$$

$$S_{32}^Z(r) = e^{-\frac{Zr}{3a}} \left\{ \frac{1}{r^3} + \frac{5Z}{6ar^2} + \frac{10Z^2}{27a^2r} + \frac{10Z^3}{81a^3} + \frac{10Z^4r}{243a^4} - \frac{4Z^5r^2}{729a^5} \left( \log r + \sum_{k=1}^{\infty} \frac{5!(k-1)!}{k!(k+5)!} \left( \frac{2Zr}{3a} \right)^k \right) \right\}.$$

FIG. 7. Radial wave function  $R_{50}(r)$ FIG. 8. Radial wave function  $S_{50}(r)$ FIG. 9. Radial wave functions  $S_{\eta\ell}(r)$  with  $Z$  increases

**Case IV.** If  $\eta = 4$ , then  $\ell = 0, 1, 2, 3$ . In this case, the graphical representation is displayed in Figs. 7 and 8, and mathematically

$$S_{40}^Z(r) = e^{-\frac{Zr}{4a}} \left\{ \frac{1}{r} - \frac{2Z}{a} \left( \left( 1 - \frac{3Zr}{4a} + \frac{Z^2r^2}{8a^2} - \frac{Z^3r^3}{192a^3} \right) \log r + \frac{11Zr}{8a} - \frac{19Z^2r^2}{48a^2} + \frac{19Z^3r^3}{768a^3} - \sum_{k=4}^{\infty} \frac{6(k-4)!}{k!(k+1)!} \left( \frac{Zr}{2a} \right)^k \right) \right\},$$

$$S_{41}^Z(r) = e^{-\frac{Zr}{4a}} \left\{ \frac{1}{r^2} + \frac{5Z}{4ar} + \frac{5Z^2}{4a^2} - \frac{5Z^3r}{8a^3} \left( \left( 1 - \frac{Zr}{4a} + \frac{Z^2r^2}{80a^2} \right) \log r + \frac{7Zr}{16a} - \frac{69Z^2r^2}{1600a^2} + \sum_{k=3}^{\infty} \frac{12(k-3)!}{k!(k+3)!} \left( \frac{Zr}{2a} \right)^k \right) \right\},$$

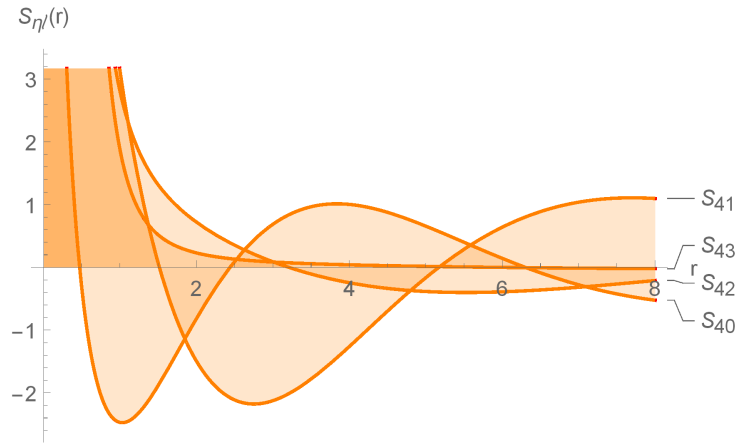
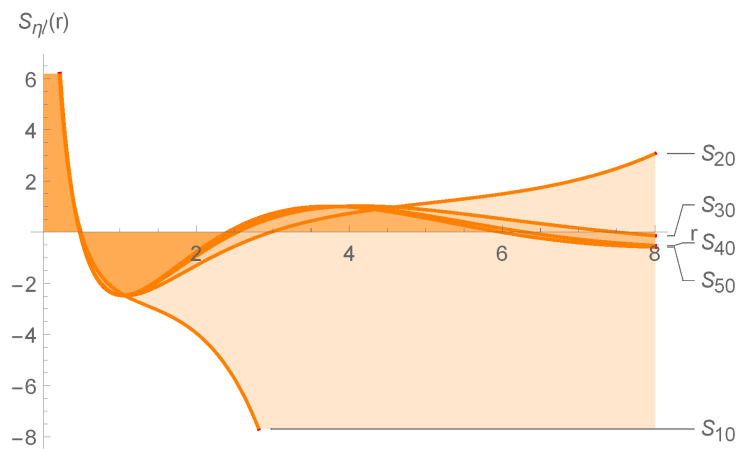
$$S_{42}^Z(r) = e^{-\frac{Zr}{4a}} \left\{ \frac{1}{r^3} + \frac{3Z}{4ar^2} + \frac{5Z^2}{16a^2r} + \frac{5Z^3}{48a^3} + \frac{5Z^4r}{128a^4} - \frac{Z^5r^2}{128a^5} \left( \left( 1 - \frac{Zr}{12a} \right) \log r + \frac{13Zr}{72a} - \sum_{k=2}^{\infty} \frac{5!(k-2)!}{k!(k+5)!} \left( \frac{Zr}{2a} \right)^k \right) \right\},$$

$$S_{43}^Z(r) = e^{-\frac{Zr}{4a}} \left\{ \frac{1}{r^4} + \frac{7Z}{12ar^3} + \frac{7Z^2}{40a^2r^2} + \frac{7Z^3}{192a^3r} + \frac{7Z^4}{1152a^4} + \frac{7Z^5r}{7680a^5} + \frac{7Z^6r^2}{46080a^6} - \frac{Z^7r^3}{92160a^7} \left( \log r + \sum_{k=1}^{\infty} \frac{7!(k-1)!}{k!(k+7)!} \left( \frac{Zr}{2a} \right)^k \right) \right\}.$$

**Case V.** If  $\eta = 5$ , then  $\ell = 0, 1, 2, 3, 4$ . In this case, we have

$$S_{50}^Z(r) = e^{-\frac{Zr}{5a}} \left\{ \frac{1}{r} - \frac{2Z}{a} \left( \left( 1 - \frac{4Zr}{3a} + \frac{4Z^2r^2}{25a^2} - \frac{4Z^3r^3}{375a^3} + \frac{2Z^4r^4}{9375a^4} \right) \log r + \frac{7Zr}{5a} - \frac{7Z^2r^2}{15a^2} + \frac{16Z^3r^3}{375a^3} - \frac{109Z^4r^4}{93750a^4} + \sum_{k=5}^{\infty} \frac{4!(k-5)!}{k!(k+1)!} \left( \frac{2Zr}{5a} \right)^k \right) \right\},$$

$$S_{51}^Z(r) = e^{-\frac{Zr}{5a}} \left\{ \frac{1}{r^2} + \frac{6Z}{5ar} + \frac{6Z^2}{5a^2} - \frac{16Z^3r}{25a^3} \left( \left( 1 - \frac{3Zr}{10a} + \frac{3Z^2r^2}{125a^2} - \frac{Z^3r^3}{1875a^3} \right) \log r + \frac{19Zr}{40a} - \frac{167Z^2r^2}{2500a^2} + \frac{257Z^2r^3}{112500a^3} - \sum_{k=4}^{\infty} \frac{36(k-4)!}{k!(k+3)!} \left( \frac{2Zr}{5a} \right)^k \right) \right\}.$$

FIG. 10. Radial wave functions  $S_{\eta\ell}(r)$  with  $\ell$  increasesFIG. 11. Radial wave functions  $S_{\eta\ell}(r)$  with  $\eta$  increases

### 5.1. Properties of the Coulombic radial solutions

As expected, Figs. 9–11 reveal that both the regular and the irregular solutions to the Coulombic radial SE spread in their radial distribution as the system energy increases from strongly negative values to values closer to zero. Also, both distributions move away from the origin as the angular momentum of the electron increases. However, the threshold and asymptotic behavior are quite different. The regular solutions have an  $r^\ell$  dependence near the origin, while the irregular solutions diverge as  $r^{-\ell-1}$ . Asymptotically, the regular solutions drop exponentially in proportion to  $r^{n-1} \exp(-r/n)$ , in natural units, while the irregular solutions grow as  $r^{-n-1} \exp(r/n)$ .

## 6. Conclusions and future scope

We have shown that a large class of second-order linear differential equations with polynomial coefficients determine two-term recursion relations which can be solved explicitly, and also yield second (irregular) solutions. The procedure is applied to find the regular and irregular (second) solutions to the Coulombic Schrödinger equation for an electron experiencing a Coulomb force, and examples are displayed. Even though second solutions are ordinarily rejected in the Coulombic case because of their unbound character, having explicit expressions for them has utility for several reasons. One is in the study of the analytic behavior of general solutions as a function of the energy and angular momentum of the electron-nucleus system (See Gaspard [16]). Another is in the study of numerical-solution techniques when three-term recurrence relations are used to solve  $2^{nd}$  order differential equations. In such cases, the second solution may invade the wanted first solution through truncation errors during iteration. Asymptotically, the regular solutions drop exponentially while the irregular solutions grow exponentially. Moreover, knowledge of the behavior of the second solution can be used to control the errors in the first. With these techniques at hand, exploration of second solutions to other important linear differential equations is possible.

## References

- [1] Geilhufe M., Achilles S., et al. Numerical Solution of the Relativistic Single-Site Scattering Problem for the Coulomb and the Mathieu Potential. *J. Phys. Condens. Matter*, 2015, **27** (43), 435202.
- [2] Newton R.G. Comment on “Penetrability of a One-Dimensional Coulomb Potential” by M. Moshinsky. *J. Phys. Math. Gen.*, 1994, **27** (13), P. 4717–4718.
- [3] Cantelaube Y.C. Solutions of the Schrödinger Equation, boundary condition at the origin, and theory of distributions. ArXiv:1203.0551, 2012.
- [4] Khelashvili A., Nadareishvili T. Delta-Like Singularity in the Radial Laplace Operator and the Status of the Radial Schrödinger Equation. *Bulletin of The Georgian National Academy of Sciences*, 2012, **6** (1), P. 69–73.
- [5] Seaton M.J. Coulomb Functions for Attractive and Repulsive Potentials and for Positive and Negative Energies. *Comput. Phys. Commun.*, 2002, **146** (2), P. 225–249.
- [6] Khalilov V.R., Mamsurov I.V. Planar Density of Vacuum Charge Induced by a Supercritical Coulomb Potential, *Phys. Lett. B*, 2017, **769**, P. 152–158.
- [7] Michel N. Precise Coulomb Wave Functions for a Wide Range of Complex  $\ell$ ,  $\eta$  and  $z$ . *Comput. Phys. Commun.*, 2007, **176** (3), P. 232–249.
- [8] Galiev V.I., Polupanov A.F. Accurate Solutions of Coupled Radial Schrödinger Equations. *J. Phys. Math. Gen.*, 1999, **32** (29), P. 5477–5492.
- [9] Schulze-Herberg A. On Finite Normal Series Solution of the Schrodinger Equation with Irregular Singularity. *Foundations of Physics Letters* 2000, **13** (1), P. 11–27.
- [10] Gersten A. Wavefunction Expansion in Terms of Spherical Bessel Functions, *J. Math. Phys.*, 1971, **12** (6), P. 924–929.
- [11] Mukhamedzhanov A.M., Irgaziev B.F., Goldberg V.Z., Orlov Yu.V., Qazi I. Bound, Virtual, and Resonance S-Matrix Poles from the Schrödinger Equation. *Phys. Rev. C*, 2010, **81** (5), 054314.
- [12] Cattapan G., Maglione E. From Bound States to Resonances: Analytic Continuation of the Wave Function. *Phys. Rev. C*, 2000, **61** (6), 067301.
- [13] Midy P., Atabek O., Oliver G. Complex Eigenenergy Spectrum of the Schrödinger Equation Using Lanczos’ Tau Method. *J. Phys. B At. Mol. Opt. Phys.*, 1993, **26** (5), P. 835–853.
- [14] Thompson I.J., Barnett A.R. Coulomb and Bessel Functions of Complex Arguments and Order. *J. Comput. Phys.*, 1986, **64** (2), P. 490–509.
- [15] Frobenius F.G. Ueber die Integration der linearian Differential gleichungen durch Reihen. *J. Reine Angew. Math.*, 1873, **76**, P. 214–235.
- [16] Gaspard D. Connection formulae between Coulomb wave functions. *J. of Math. Phys.*, 2018, **59** (11), 112104.
- [17] Toli I., Zou S. Schrödinger Equation With Coulomb Potential Admits No Exact Solutions. *Chemical Physics Letters: X*, 2019, **737**, 100021.
- [18] Messiah A. *Quantum Mechanics, Vol. I*, North-Holland Publishing Company, Amsterdam, 1967. (Translated from French by G.M. Temmer, Rutgers).
- [19] Simos T.E. Exponentially-Fitted Multiderivative Methods For The Numerical Solution of the Schrödinger Equation. *J. of Mathematical Chemistry*, 2004, **36** (1), P. 13–27.
- [20] Parke W.C., Maximon L.C. Closed-form Second Solution to the Confluent Hypergeometric Difference Equation in the Degenerate Case. *Int. J. of Difference Equations*, 2016, **11** (2), P. 203–214.
- [21] Yi-Hsin Liu, Wai-Ning Mai. Solution of The Radial Equation For Hydrogen Atom: Series Solution or Laplace Transform. *Int. J. of Mathematical Education in Science and Technology*, 1990, **21** (6), P. 913–918.

---

*Submitted 10 December 2022; revised 18 January 2023; accepted 19 January 2023*

*Information about the authors:*

*Chander Parkash* – Department Of Mathematics, Rayat Bahra University, Mohali, Punjab, 140104, India; ORCID 0000-0003-1746-5894; cchanderr@gmail.com

*William C. Parke* – Department Of Physics, The George Washington University, Washington D.C., USA; ORCID 0000-0002-3771-5371; wparke@email.gwe.edu

*Parvinder Singh* – Department of Chemistry, Rayat Bahra University, Mohali, Punjab, 140104, India; ORCID 0000-0003-3815-4534; drparvinder62@gmail.com

*Conflict of interest:* the authors declare no conflict of interest.

## A study of confined Stark effect, hydrostatic pressure and temperature on nonlinear optical properties in 1D Ga<sub>x</sub>Al<sub>1-x</sub>As/GaAs/Ga<sub>x</sub>Al<sub>1-x</sub>As quantum dots under a finite square well potential

Rohit Chaurasiya, Suman Dahiya, Rinku Sharma

Department of Applied Physics, Delhi Technological University, Shahbad Daultapur, 110042, Delhi, India

Corresponding author: Rohit Chaurasiya, rohitqc2000@gmail.com

**ABSTRACT** In the present paper, investigations of nonlinear optical rectification, absorption coefficient and refractive index in a 1D Ga<sub>x</sub>Al<sub>1-x</sub>As/GaAs/Ga<sub>x</sub>Al<sub>1-x</sub>As quantum dots under a finite square well potential using simulation software such as COMSOL Multi-Physics and Matlab have been carried out in the presence of electric field, hydrostatic pressure and temperature. Results show that the resonant peaks of ORC (optical rectification coefficient) exhibit a blue shift under increasing of the electric field, while a red shift trailed by a blue shift is displayed under increasing of hydrostatic pressure and temperature. Similar trends take place for the refractive index as well as for the absorption coefficient under changing of the electric field, temperature and hydrostatic pressure. The attained theoretical results would pave a novel opportunity in designing, optimizing and applications of nonlinear opto-electronic devices by tuning the performance of the quantum dots and controlling some of their specific properties.

**KEYWORDS** confined Stark effect, quantum dot, second harmonic generation, third harmonic generation

**FOR CITATION** Chaurasiya R., Dahiya S., Sharma R. A study of confined Stark effect, hydrostatic pressure and temperature on nonlinear optical properties in 1D Ga<sub>x</sub>Al<sub>1-x</sub>As/GaAs/Ga<sub>x</sub>Al<sub>1-x</sub>As quantum dots under a finite square well potential. *Nanosystems: Phys. Chem. Math.*, 2023, **14** (1), 44–53.

### 1. Introduction

The broad range of applications of nano-scale semiconductors has piqued the interest of scientists from various fields. It has applications in quantum computing, photonic computing, photovoltaics, biomedicine, and other fields. At nanoscales, the potential barrier can be used to confine electrons and holes inside the potential well. These quantum systems are classified into three types based on the degree of confinement. When an electron is confined in all three dimensions, it is referred to as a quantum dot. When electrons are confined in two dimensions, they form quantum wires, and when they are confined in only one dimension, they form quantum layers (quantum wells in one dimension). All of these systems cause interesting changes in the nonlinear optical properties.

The quantum confined Stark effect is a well-known phenomenon that occurs when an electric field is added to a potential well. This phenomenon has piqued researchers to investigate the effect [1–4]. Two distinct characters of behaviour have been revealed. The electric field first induces bending and tilting of the material energy band structure. This has a direct impact on lowering electron energy, resulting in a red shift. The electric field also causes excitons to polarise. The electron and hole are pushed back, reducing the Coulomb force of attraction and increasing the energy of the electron-hole pair. As a result, the demand for non-linear crystals is increasing [5]. The study of optical behaviour in the presence of the electric field provides insight into the crystal controllability. This has prompted a slew of researchers to investigate these properties, as well as the impact of the electric field [6, 7].

There were numerous studies that showed the effect of field strength, temperature, and pressure on non-linear properties such as Optical Rectification Coefficient (ORC), Absorption Coefficient (AC), and change in Refractive Index (RI) in quantum dot systems including parabolic and semi-parabolic potentials [8, 9]. Observing these changes is crucial because these external factors can be used to tune and control nanoscale devices with quantum dots. The second harmonic generation was first reported experimentally by [10]. Since then, there were a plethora of simulation studies on these properties including different structures [5, 11, 12], and different potentials such as parabolic [14], semi-parabolic [13]. To the best of our knowledge, the work done on the study of non-linear optical properties, particularly for finite square well potential was not sufficient. The effect of an external electric field, pressure and temperature on optical rectification coefficient (ORC), Absorption coefficient (AC) and Refractive Index (RI) are discussed in 1D.

The band gaps of semiconductor materials can also be determined by the material's composition. The energy band of ternary semiconductors, for example, is determined by the composition of one of the elements in the compound. Al<sub>x</sub>Ga<sub>1-x</sub>N is one of the well-established materials used for UV light emitters and detectors [15] because of its wide band gap, which may span a wide range of wavelengths in this region. These materials' band structures are also affected by temperature and pressure. These variables have a significant impact on the fundamental properties of these materials

including the optoelectronic properties. Many semiconductor devices, such as QLEDs, Lasers, and white light sources, can benefit from the application of these external influences, which can improve the band structures of the material and, hence, boost efficiency [8].

The study starts with an overview of the methods used to run the simulations and compute the nonlinear features, as well as the state's wave functions and energy values. This section is followed by the problem's theoretical formulation. Following that, we present the findings and discuss them in the next section.

## 2. Theory and method

This work considers the quantum dot system of  $\text{Ga}_x\text{Al}_{1-x}\text{As}/\text{GaAs}$ . A 3D quantum well is created by sandwiching a nano cube of GaAs in a sea of  $\text{Ga}_x\text{Al}_{1-x}\text{As}$ . It is formed as a result of GaAs having a lower barrier potential than the surrounding material, which in our case is  $\text{Ga}_x\text{Al}_{1-x}\text{As}$ . When an external electric field is applied to a quantum dot system, the electron's energy tends to decrease. As a result, the allowed frequency of the light absorption or emission decreases. Correspondingly, drastic changes in nonlinear optical properties such as coefficient of absorptions and refractive index occur. Fig. 1(b) depicts the effect of the external electric field [16],  $E = -eFx$ . The potential level tilts by a slope of  $-eF$  in its application, where  $e$  is the charge of the electron.

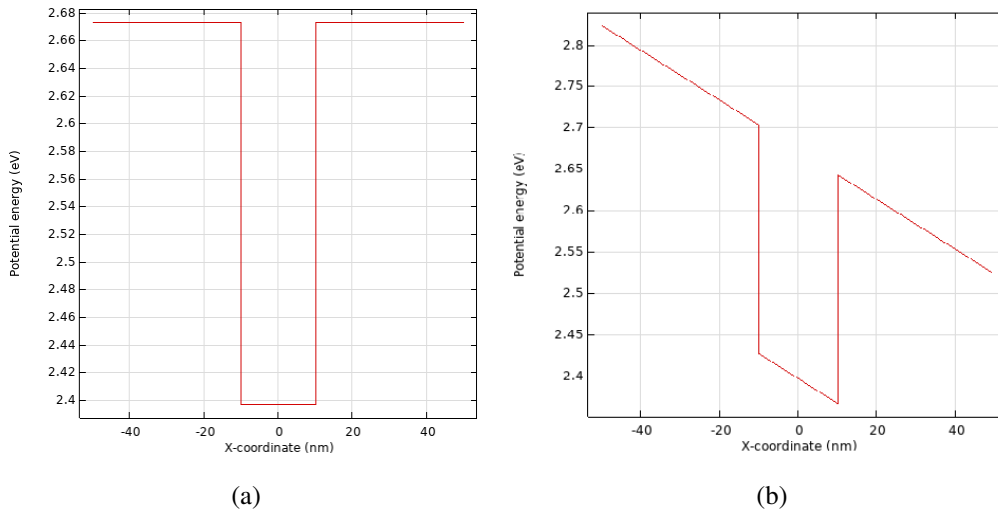


FIG. 1. Potential well of the system with the effect of a linearly varying external electric field: no electric field is applied (a); the application of the electric field (b)

### 2.1. Schrödinger equation for the system

Equation (1) gives the Schrödinger equation for the same system (considering only one dimension) in the presence of external electric field  $F$  for a single electron.

$$-\frac{\hbar^2}{2m_e^*} \frac{\partial^2 \psi}{\partial x^2} + (V_0 - eFx)\psi = E\psi, \quad (1)$$

where,

$$V_0 = \begin{cases} V_{\text{GaAs}} & -10 \text{ nm} \leq x \leq 10 \text{ nm}; \\ V_{\text{Ga}_x\text{Al}_{1-x}\text{As}} & \text{elsewhere.} \end{cases}$$

The effective mass of the electron is denoted by  $m_e^*$ . The pressure and temperature dependent effective electron mass has been calculated using the temperature and pressure dependent relation [17] for the GaAs region. It is expressed as eq. (2):

$$m_e^*(P, T) = m_e \left[ 1 + 7.51 \left( \frac{2}{E_g(P, T)} + \frac{1}{E_g(P, T) + \Delta_0} \right) \right]^{-1}. \quad (2)$$

The mass of the electron was calculated using eq. (3) for the region outside GaAs, which is the region of  $\text{Ga}_x\text{Al}_{1-x}\text{As}$ . The expression is a function of the fraction of Gallium mass in the semiconductor and the electron rest mass  $m_e$  [18]. For our investigation, the value of  $x$  has been set to zero.

$$m_e^* = (0.067 + 0.083(1 - x))m_e. \quad (3)$$

Similarly, the energy band gap for GaAs was calculated using the pressure and temperature dependence relation [19] given in eq. (4). While that for  $\text{Ga}_x\text{Al}_{1-x}\text{As}$ , eq. 5 was used.

$$E_g(P, T) = 1.519 - \frac{5.4 \times 10^{-4} T^2}{T + 204} + 0.01261P + 3.77 \times 10^{-5} P^2, \quad (4)$$

$$E_g = (1.426 + 1.247(1 - x)) \text{ eV}. \quad (5)$$

Equation (1) is a special differential equation and its solution comes in the form of Airy functions [20]. The detailed derivation for the analytical solution of eq. 1 can be found in [21]. The final form of the solution is expressed in eq. (6):

$$\psi = \begin{cases} A_1 \text{Ai}(x) + A_2 \text{Bi}(x) & -10 \text{ nm} \leq x \leq 10 \text{ nm}; \\ B_1 \text{Ai}(x) + B_2 \text{Bi}(x) & x \leq -10 \text{ nm}; \\ C_1 \text{Ai}(x) + C_2 \text{Bi}(x) & -10 \text{ nm} \leq x. \end{cases} \quad (6)$$

$A_i(x)$  and  $B_i(x)$  are the coefficients of the Airy functions. These coefficients are in integral form and henceforth, it becomes difficult to calculate exact solution and other parameter associated in the study. Due to this reason, numerical simulation was used to perform calculations.

## 2.2. Non-linear optical properties

The study takes into account non-linear properties such as absorption co-efficient and change in refractive index. This study addresses these properties by utilising a two-level system. The non-linear susceptibility is directly related to the coefficient of absorption and changes in the refractive index. Consider eq. (8) for the effective susceptibility with linear and non-linear terms.

$$\chi_{eff} = \chi^{(1)} E + \chi^{(2)} E^2 + \chi^{(3)} E^3, \quad (7)$$

$\chi^{(1)}$ ,  $\chi^{(2)}$  and  $\chi^{(3)}$  are linear, the second order, and the third order susceptibility terms that depend on the frequency of the falling radiation.  $\chi^{(2)}$  is made up of two terms: the optical rectification  $\chi^{(2)}(0)$  and the second harmonic generation  $\chi^{(2)}(2\omega)$ .

$$\chi^{(2)}(0) = \frac{4\sigma |M_{12}|^2 (M_{22} - M_{11})}{\epsilon \hbar^2} \left( \frac{\left( \omega_{12}^2 \left( 1 + \frac{\Gamma_1}{\Gamma_2} \right) + \left( w_p^2 + \frac{1}{\Gamma_2^2} \right) \right)}{\left( (\omega_{12} - \omega)^2 + \frac{1}{\Gamma_2^2} \right) \left( (\omega_{12} + \omega)^2 + \frac{1}{\Gamma_2^2} \right)} \right), \quad (8)$$

$$\chi_{2\omega}^{(2)} = \frac{\sigma}{\epsilon_0} \frac{M_{12} M_{23} M_{31}}{(\hbar\omega - E_{12} - j\hbar\Gamma_{21}) (2\hbar\omega - E_{31} - j\hbar\Gamma_{31})}. \quad (9)$$

Equations (8) and (9) were derived by using the density matrix approach [22].  $M_{ij}$  is the dipole transition element. It can be calculated by using the following expression:  $M_{fi} = -e \langle \psi_f | x | \psi_i \rangle$ , where,  $\psi_i$  and  $\psi_f$  are the initial and the final state wavefunction of the electron. The  $E_{ij}$  terms are the transition energy between  $i^{th}$  to  $j^{th}$  state. Finally,  $\sigma$  and  $\Gamma$  are the electron charge density and relaxation time, respectively.

The linear term of the coefficient of absorption is given by eq. (10). In the equation,  $\epsilon_0$  and  $\epsilon_R$  are the permittivity and the relative permittivity respectively.  $n_r$  is the relative refractive index of the material and  $I$  is the intensity of the electric field.

$$\alpha^{(1)}(\omega) = \omega \sqrt{\frac{\mu}{\epsilon_R}} \frac{|M_{21}|^2 \sigma_v \hbar \Gamma_{21}}{(E_{21} - \hbar\omega)^2 + (\hbar\Gamma_{21})^2}. \quad (10)$$

The non-linear term of AC is a function of the intensity of the incoming radiation and its frequency. It is expressed in eq. (11):

$$\alpha^{(3)}(I, \omega) = -\omega \sqrt{\frac{\mu}{\epsilon_R}} \left( \frac{I}{2\epsilon_0 n_r c} \right) \frac{|M_{21}|^2 \sigma_v \hbar \Gamma_{21}}{\left[ (E_{21} - \hbar\omega)^2 + (\hbar\Gamma_{21})^2 \right]^2} \times \left[ 4|M_{21}|^2 - \frac{|M_{22} - M_{11}|^2 [3E_{21}^2 - 4E_{21}\hbar\omega + \hbar^2(\omega^2 - \Gamma_{21}^2)]}{E_{21}^2 + (\hbar\Gamma_{21})^2} \right]. \quad (11)$$

The total coefficient of absorption can be written as the sum of linear and non-linear terms [23].

$$\alpha(I, \omega) = \alpha^{(1)}(\omega) + \alpha^{(3)}(I, \omega). \quad (12)$$

Similarly, the change in RI can be given as the sum of linear and non-linear parts as shown in eq. (13). The linear part is given by eq. (14) and the non-linear term is expressed as eq. (15):

$$\frac{\Delta n(\omega)}{n_r} = \frac{\Delta n^{(1)}(\omega)}{n_r} + \frac{\Delta n^{(3)}(\omega)}{n_r}, \quad (13)$$

$$\frac{\Delta n^{(1)}(\omega)}{n_r} = \frac{\sigma_v |M_{21}|^2}{2n_r^2 \varepsilon_0} \left[ \frac{E_{21} - \hbar\omega}{(E_{21} - \hbar\omega)^2 + (\hbar\Gamma_{21})^2} \right], \quad (14)$$

$$\frac{\Delta n^{(3)}(\omega)}{n_r} = -\frac{\mu c}{4n_r^3 \varepsilon_0} |M_{21}|^2 \left[ \frac{\sigma I}{E_{21} - \hbar\omega} (E_{21} - \hbar\omega)^2 + (\hbar\Gamma_{21})^2 \right]^2 \times \left[ 4(E_{21} - \hbar\omega) |M_{21}|^2 - \frac{(M_{22} - M_{11})^2}{(E_{21})^2 + (\hbar\Gamma_{21})^2} \left\{ (E_{21} - \hbar\omega) \times [E_{21}(E_{21} - \hbar\omega) - (\hbar\Gamma_{21})^2] - (\hbar\Gamma_{21})^2 (2E_{21} - \hbar\omega) \right\} \right]. \quad (15)$$

### 2.3. Method

To solve the Schrödinger equation in 1D, we used the finite elements method with the help of COMSOL Multiphysics. In the regions of different materials and at the boundary, suitable conditions such as mass approximation and zero probability conditions were used. The wavefunction and the eigenenergy values for eq. (1) are shown in Fig. 2. The thickness of the GaAs is set at 20 nm, with values ranging from 10 to  $-10$  nm. Using the finite element method, the numerical values of the wavefunctions were used to calculate the transition dipole matrix element. Matlab simulation software was used to perform this calculation.

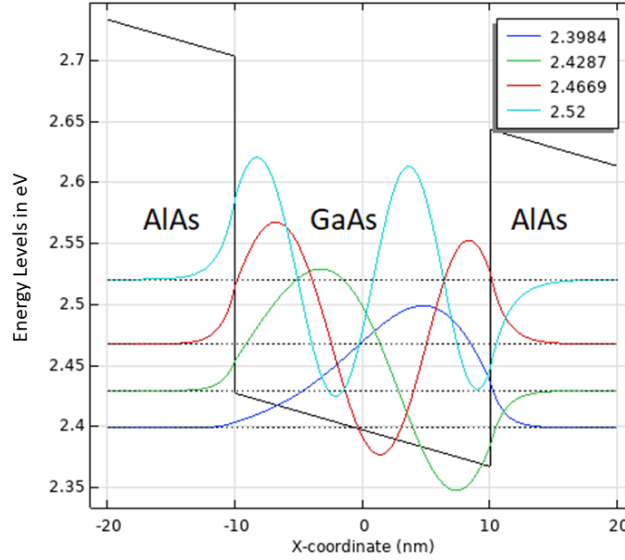


FIG. 2. Wavefunction of electron till 4<sup>th</sup> level. Here the y-axis shows the energy levels of the wavefunction

### 3. Result and discussion

This section presents the results of the simulations for varying electric fields, hydrostatic pressure and temperature strength at  $5k$  V/cm fixed intervals. Table 1, displays the list of fixed parameters as well as the values used to run the simulation. The values for relaxation time are as follows:  $\tau_{31} = \tau_{21}/2$  and  $\tau_{41} = \tau_{21}/3$ . The transition dipole matrix elements were calculated using the numerical wavefunctions obtained from the simulation. The matrix is important because all of the simulation results are related to its elements.

Parameters	Values
electron charge density ( $\sigma$ )	$2.8 \times 10^{22} \text{ m}^{-3}$
incident intensity ( $I$ )	$4 \times 10^6 \text{ W/m}^2$
relative refractive index ( $n_r$ )	3.2
relaxation time ( $\tau_{21}$ )	$0.5 \text{ ps}^{-1}$

TABLE 1. Table for Parameters and Values

Optical Rectification Coefficient or ORC, with the variation of the electric field in the interval of 25 kV/cm keeping temperature and pressure constant at 50 K and 100 kbar, respectively, for the system under consideration, is depicted in Fig. 3(a). Fig. 3(b) demonstrates energy eigenvalues for different values of the external electric field  $F$ . It can be observed from the figure that while increasing the electric field ORC peaks decrease in magnitude and shift towards higher frequencies, hence exhibiting a blue shift. As we can observe from Fig. 3(b) the increasing electric field strength leads to the increase of the energy eigenvalue, hence, an increase in the electric field lead to increase of the difference between energy levels leading to the blue shift.

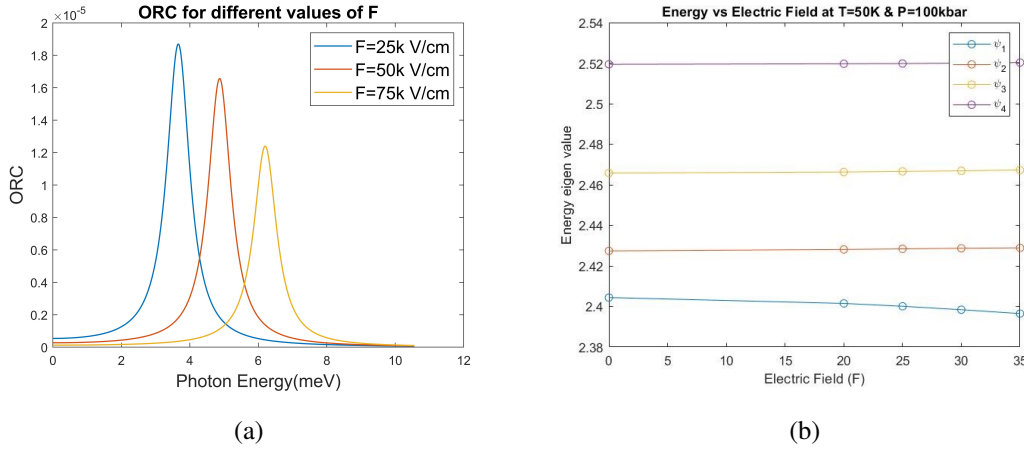


FIG. 3. (a) ORC for different values of electric field strength keeping temperature and hydrostatic pressure constant. (b) Energy eigenvalue vs electric field strength

Figure 4(a) shows a plot of ORC vs temperature at three diverse values fixing  $P = 50$  kbar, electric field strength = 25 kV/cm. Blue shift is observed with an increase in the temperature as the resonant peaks move towards higher energy domain with significant decrease in the peak height. As the transition energy goes to increase with the increase in temperature, the blue shift happens. Also, with an increase in temperature, a decrease in the effective radius of the quantum dot is observed due to an enhancement in the effective electron mass as well an increase in energy interval is observed with an increase in the temperature.

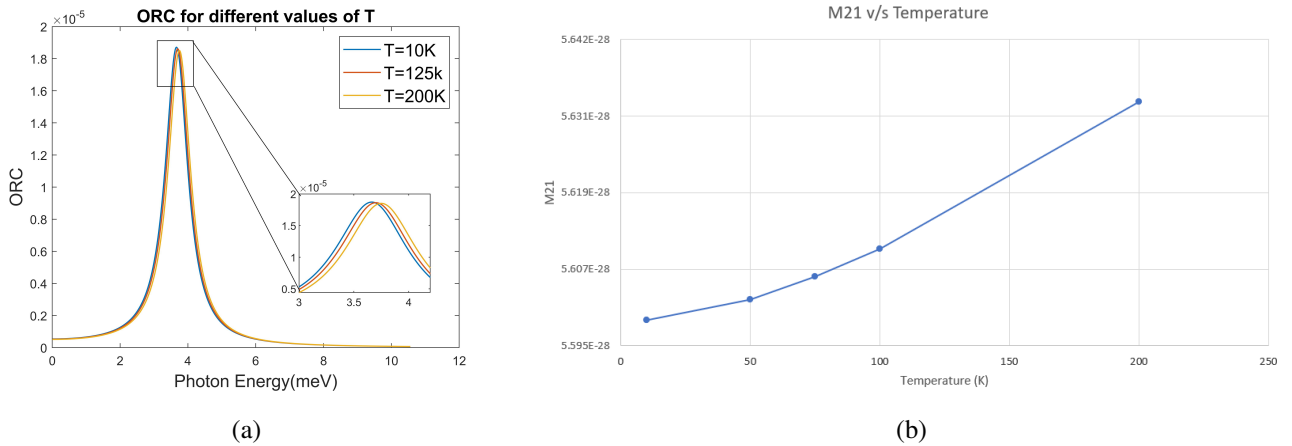
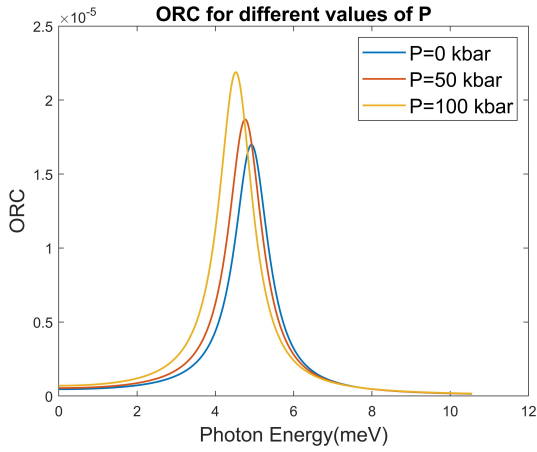


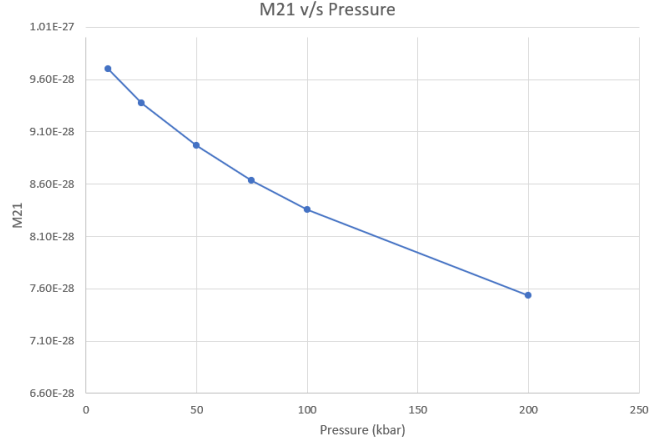
FIG. 4. (a) ORC for diverse values of temperature keeping the strength of the field and hydrostatic pressure constant. (b) matrix element vs temperature

Figure 5(a) shows a plot of ORC vs pressure at three different values fixing  $T = 50$  K, the electric field strength equals to 25 kV/cm. It is observed that with an increase in the hydrostatic pressure the red shift is observed with the movement of resonant peaks towards higher energy domain with a substantial increase in the peak heights. This is due to the weakness of the quantum confinement with the decrease in the energy interval with a rise in hydrostatic pressure.

Figure 6(a) shows the first and the third order coefficients of absorption for different values of the electric field strength while keeping the temperature and the hydrostatic pressure constant, whereas Fig. 6(b) shows the total coefficients of absorption for different values of the electric field strength while keeping the temperature and the hydrostatic pressure constant. The total coefficient of absorption was displayed for various values of the electric field strength while keeping



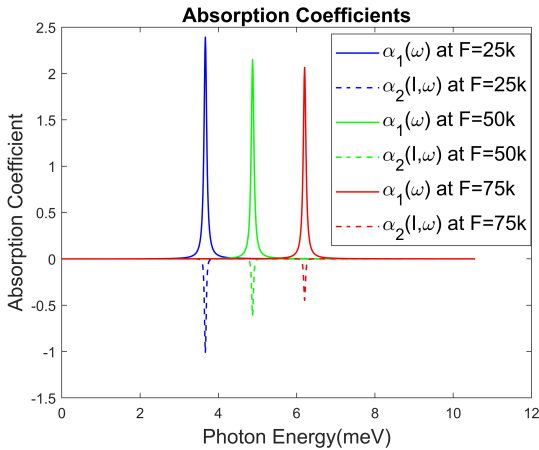
(a)



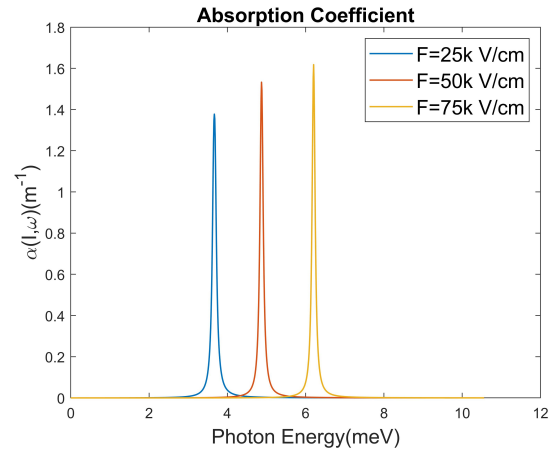
(b)

FIG. 5. (a) ORC for various values of hydrostatic pressure while maintaining constant electric field and temperature. (b) dipole transition  $M_{21}$  vs pressure

the temperature and the hydrostatic pressure constant. As can be seen in the figures, the linear coefficient of absorption decreases in amplitude as the electric field increases, while the nonlinear term remains nearly constant. As a result, this slight decrease in the linear coefficient of absorption also tries to reduce the total coefficient of absorption. It is also noticed that an increase in the electric field causes the peak positions to move towards lower photon energies, resulting in a red shift since the difference between energy levels decreases as the electric field increases.



(a)



(b)

FIG. 6. (a) 1<sup>st</sup> and 3<sup>rd</sup> order coefficient of absorption for diverse values of strength of the electric field keeping the temperature and the hydrostatic pressure constant. (b) The total coefficient of absorption for various field strength keeping temperature and hydrostatic pressure constant

In Fig. 7(a), the coefficient of absorption, for temperature values of 10, 100 and 200 K keeping the electric field and the hydrostatic pressure constant, was plotted. In Fig. 7(a), maximum values for the 1<sup>st</sup> order and the 3<sup>rd</sup> (nonlinear term) absorption coefficients were plotted while the sum of both the terms, with variation of temperature  $T$ , were plotted in Fig. 7. We can observe that the magnitude of the maximum value for the first order AC is increasing with an increase in the temperature as well as peaks are shifting towards higher energy depicting a blue shift. As shown in Fig. 7, as the temperature rises, the maximum values of the total ACs rise, demonstrating that temperature  $T$  influences intersubband optical absorption in QD. Furthermore, because the first and the third-order nonlinear ACs are diametrically opposed, the total ACs will be lowered, owing to the decrease in the effective mass of the electron with the rise in the temperature. The graphs reveal direct relationship between the peak values of the total ACs, the transition dipole element and the difference between energy levels  $E_{10}$ . The influence of the dipole matrix element  $|M_{21}|^2$  on the total ACs, on the other hand, is shown to be opposite that of the energy difference  $E_{10}$ . The second significant result depicted in the graph is the blue shift that occurs as the temperature  $T$  rises, which is due to a rise in the transition energy  $E_{10}$  as the temperature increases,

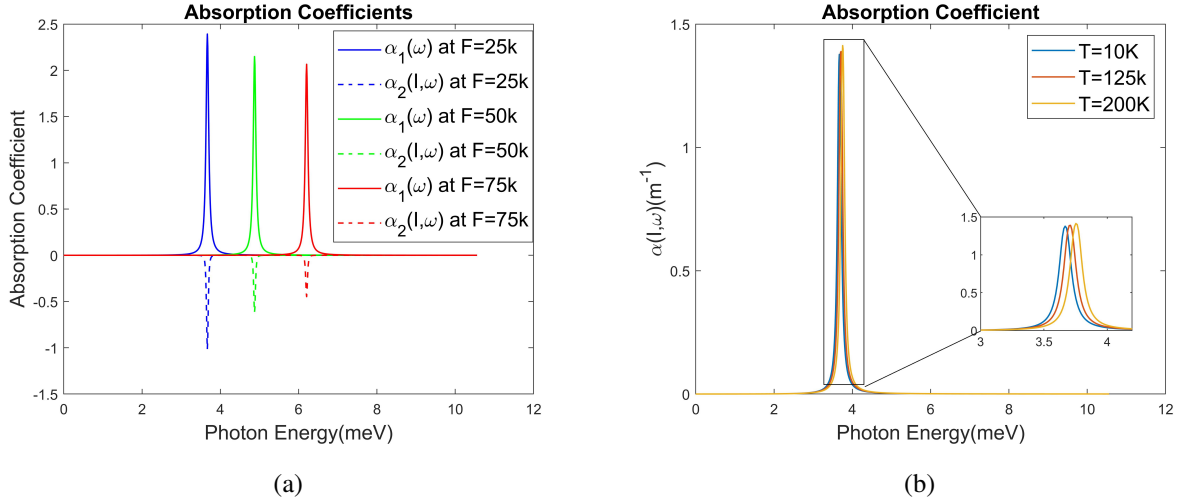


FIG. 7. (a)  $1^{st}$  and  $3^{rd}$  order coefficient of absorption for different values of temperature strength keeping the electric field and the hydrostatic pressure constant. (b) The total coefficient of absorption for different values of the temperature strength keeping the electric field and the hydrostatic pressure constant

resulting in a drop in the electron effective mass, and in an expansion of the transition energy. It happens because of the electron-photon interaction which depends on the temperature as well.

In Fig. 8(a), the coefficient of absorption for different values of the hydrostatic pressure strength keeping the electric field and the temperature constant was plotted. We can observe that the first order linear coefficient of absorption, as well as the total coefficient of absorption, show a red shift as the peaks move towards lower energies while increasing the pressure. It can also be observed that the magnitude of peaks is also diminishing with the increase in the pressure. As the linear  $\alpha_1(\omega)$ , the third-order nonlinear  $\alpha_3(\omega)$  are opposite in sign, hence the magnitude of the total coefficient of absorption is also reduced subsequently. The main rationale for this behaviour is as follows: when the hydrostatic pressure rises, so does the electron effective mass, resulting in a slight weakening of the strength of confinement. Furthermore, because the peak intensity is proportional to the dipole matrix element  $|M_{21}|^2$  and the energy difference, the energy difference grows as hydrostatic pressure rises. Additionally, because strain is directly related to the variety of energy levels, the hydrostatic pressure causes the lattice constant to change. As a result, the strain fluctuates, decrease the first excited state.

In Fig. 9(a), the refractive index for various values of the field strength keeping the temperature and the pressure constant was plotted. The 1st order linear refractive index, as well as the total refractive index, show the same behaviour

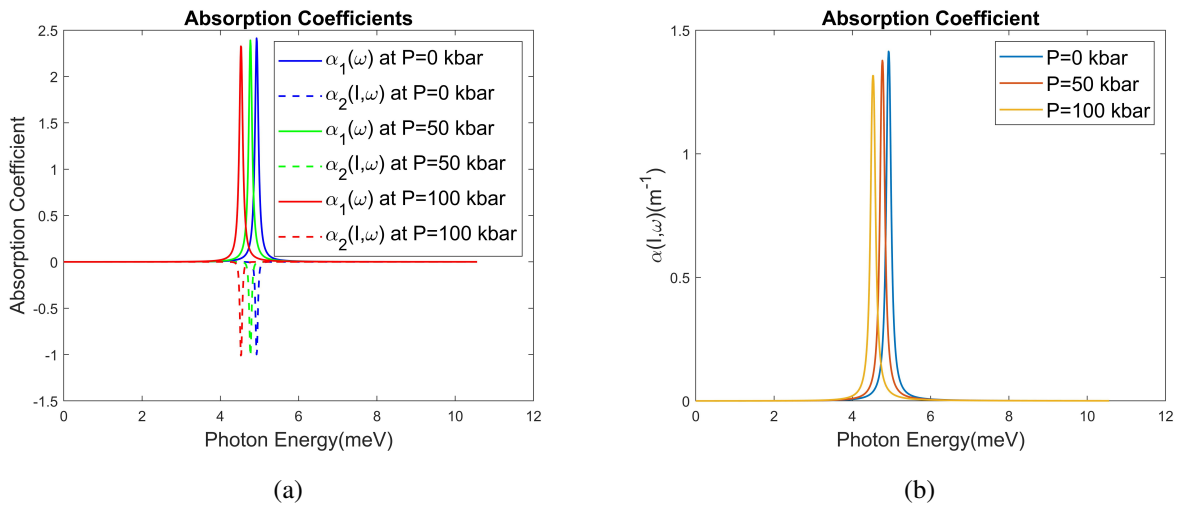


FIG. 8. (a) the  $1^{st}$  and The  $3^{rd}$  order coefficient of absorption for varied hydrostatic pressure keeping the strength of the field and the temperature constant. (b) The total coefficient of absorption for different values of the hydrostatic pressure strength keeping the electric field and the temperature constant

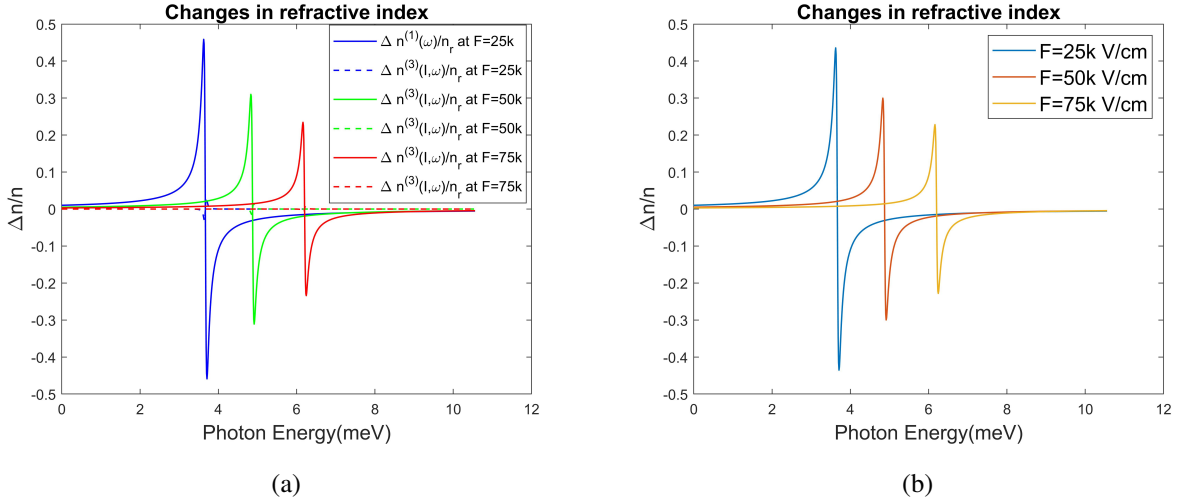


FIG. 9. (a)  $1^{st}$  and  $3^{rd}$  order refractive index for various values of electric field keeping temperature and pressure constant. (b) Total refractive index for various values of strength of the electric field keeping Temperature and Hydrostatic Pressure constant

with an increase in the electric field, as seen in Figs. 9(a) and 9(b), while the 3rd order non-linear term has no effect on the total refractive index due to its minimal contribution. It is observed that the magnitude of peaks is decreasing with an increase in the electric field while going towards a high energy state resulting in the blue shift.

In Fig. 10(a), the refractive index for various values of the temperature keeping the strength of the field and the hydrostatic pressure constant, was plotted. It can be observed from Fig. 10(b) that the 1st order linear refractive index, as well as the total refractive index, result in quite similar behaviour as we increase temperature although there is no noticeable effect in the 3rd order non-linear term hence observing a similar trend in peaks for both the 1st and the total refractive index due to neglecting the low contribution of the 3rd order non-linear term. A blue shift can be observed from the graphs as the peaks are moving towards a higher energy region with a significant increase in the peak height.

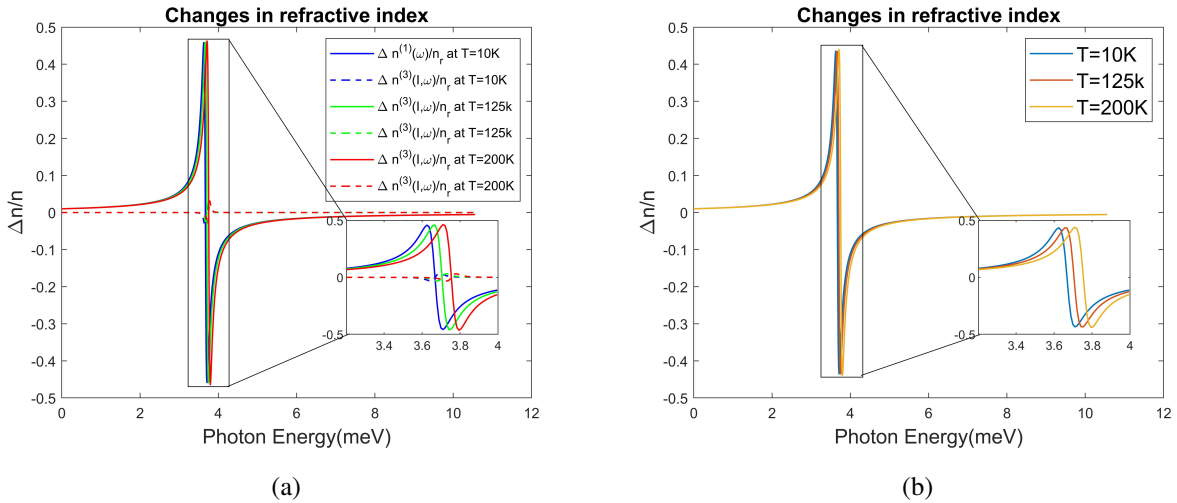


FIG. 10. (a) The  $1^{st}$  and the  $3^{rd}$  order refractive index for various temperature while maintaining the electric field and the hydrostatic pressure constant (b) The total refractive index at various temperature while the strength of the field and the hydrostatic pressure are held constant

In Fig. 11(a), the refractive index was plotted for various values of the hydrostatic pressure while maintaining the field strength and the hydrostatic pressure constant. Figs. 11(a) and 11(b) result in quite similar behaviour in both of the 1st order linear refractive index as well as the total refractive index with a significant increase in the hydrostatic pressure with no alteration although in the 3rd order non-linear term. Hence, we observe that the 1st order linear refractive index and the total refractive index are similar in magnitude as well as they exhibit the red shift with an increase in the magnitude of the peaks intensity.

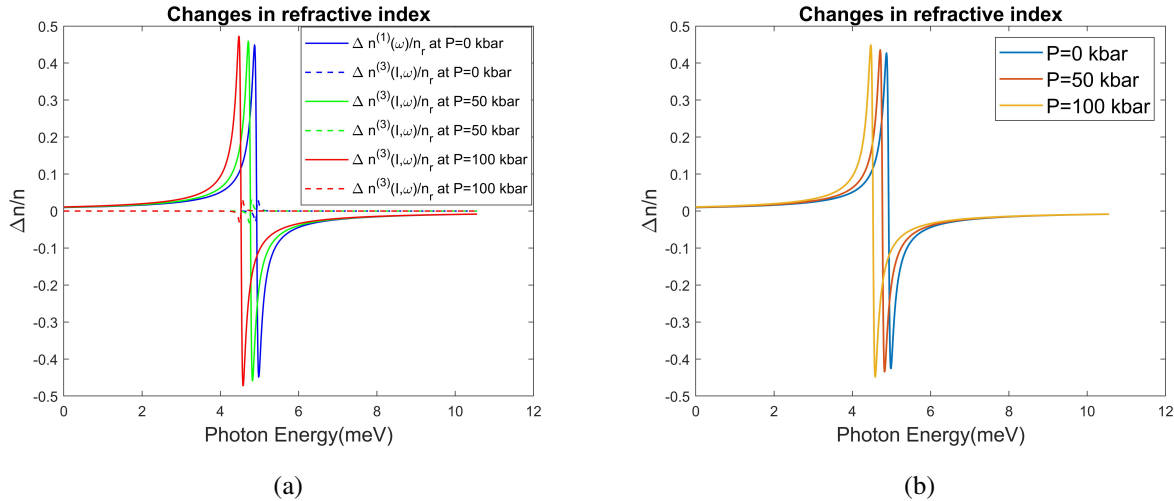


FIG. 11. (a) The 1<sup>st</sup> and the 3<sup>rd</sup> order refractive index for various hydrostatic pressure strengths while maintaining the electric field and the temperature constant (b) Total refractive index for various Hydrostatic pressure strengths while keeping the electric field and temperature constant

#### 4. Conclusion

We reported the variation of optical properties as a function of the external applied electric field, hydrostatic pressure and temperature in this study. The results show that increasing the field strength causes a red shift in all of the optical properties studied as well as a surge can be seen in the peak's intensity with an increase in the electric field. Furthermore, the simulation results show that the temperature causes a blue shift in the optical properties while hydrostatic pressure causes a redshift in the optical properties. As a result, the hydrostatic pressure  $P$ , temperature  $T$ , and applied electric field  $E$  all have a significant impact on the system's optical response.

#### References

- [1] Aderras L., et al. Stark-shift of impurity fundamental state in a lens shaped quantum dot. *Physica E: Low-dimensional Systems and Nanostructures*, 2017, **89**, P. 119–123.
- [2] Temkin H., et al.  $\text{Ge}_x\text{Si}_{1-x}$  strained-layer heterostructure bipolar transistors. *Applied Physics Letters*, 1988, **52** (13), P. 1089–1091.
- [3] Luryi S., Kastalsky A., Bean J.C. New infrared detector on a silicon chip. *IEEE Transactions on Electron Devices*, 1984, **31** (9), P. 1135–1139.
- [4] Rhee S.S., et al. Resonant tunneling through a  $\text{Si}/\text{Ge}_x\text{Si}_{1-x}/\text{Si}$  heterostructure on a GeSi buffer layer. *Applied Physics Letters*, 1988, **53** (3), P. 204–206.
- [5] Mohamed Kria Varsha, et al. Quantum Confined Stark Effect on the Linear and Non-linear Optical Properties of SiGe/Si Semi Oblate and Prolate Quantum Dots Grown in Si Wetting Layer. *Nanomaterials*, 2021, **11** (6).
- [6] Mourad Baira, et al. Intersubband optical nonlinearity of GeSn quantum dots under vertical electric field. *Micromachines*, 2019, **10** (4), 243.
- [7] Dvovyan K.G., Kazaryan E.M. Impurity states in a weakly prolate (oblate) ellipsoidal microcrystal placed in a magnetic field. *Physica Status Solidi B*, 2001, **228** (3), P. 695–703.
- [8] Suman Dahiya, Siddhartha Lahon, Rinku Sharma. Effects of temperature and hydrostatic pressure on the optical rectification associated with the excitonic system in a semi-parabolic quantum dot. *Physica E: Low-dimensional Systems and Nanostructures*, 2020, **118**, 113918.
- [9] Amal Abu Alia, Mohammad K. Elsaid, Ayham Shaer. Magnetic properties of GaAs parabolic quantum dot in the presence of donor impurity under the influence of external tilted electric and magnetic fields. *J. of Taibah University for Science*, 2019, **13** (1), P. 687–695.
- [10] Franken P.A., et al. Generation of optical harmonics. *Physical Review Letters*, 1961, **7** (4), 118.
- [11] Keyin Li, Kangxian Guo, Litao Liang. Effect of the shape of quantum dots on the refractive index changes. *Physica B: Condensed Matter*, 2016, **502**, P. 146–150.
- [12] Khaledi-Nasab A., et al. Optical rectification and second harmonic generation on quasi-realistic InAs/GaAs quantum dots: with attention to wetting layer effect. *Int. Scholarly Research Notices*, 2013 (2013).
- [13] Jin-Feng You, et al. The effect of temperature, hydrostatic pressure and magnetic field on the nonlinear optical properties of AlGaAs/GaAs semi-parabolic quantum well. *Int. J. of Modern Physics B*, 2019, **33** (27), 1950325.
- [14] Yuan Lihua, et al. Effect of a magnetic field on the energy levels of donor impurities in the ZnO parabolic quantum well. *J. of Semiconductors*, 2011, **32** (8), 082001.
- [15] Gil B. *Group III nitride semiconductor compounds: physics and applications*. Clarendon Press, 1998.
- [16] Empedocles S.A., Bawendi M.G. Quantum-confined Stark effect in single CdSe nanocrystallite quantum dots. *Science*, 1997, **278** (5346), P. 2114–2117.
- [17] Zaiping Zeng, et al. Competition effects of electric and magnetic fields on impurity binding energy in a disc-shaped quantum dot in the presence of pressure and temperature. *Science of Advanced Materials*, 2014, **6** (3), P. 586–591.
- [18] Harrison P., Valavanis A. *Quantum wells, wires and dots: theoretical and computational physics of semiconductor nanostructures*. John Wiley and Sons, 2016.
- [19] Aghoutane N., et al. Refractive index changes and optical absorption involving 1s1p excitonic transitions in quantum dot under pressure and temperature effects. *Applied Physics A*, 2019, **125** (1).

- [20] Vallee O., Soares M. *Airy functions and applications to physics*. World Scientific Publishing Company, Singapore, 2010.
- [21] Ghatak A.K., Goyal I.C., Gallawa R.L. Mean lifetime calculations of quantum well structures: a rigorous analysis. *IEEE J. of Quantum Electronics*, 1990, **26** (2), P. 305–310.
- [22] Boyd R.W. *Nonlinear optics*. Academic press, NY, 2020.
- [23] Rezaei G., Karimi M.J., Keshavarz A. Excitonic effects on the nonlinear intersub-band optical properties of a semi-parabolic one-dimensional quantum dot. *Physica E: Low-dimensional Systems and Nanostructures* 43 (1) (2010), pp. 475–481.

---

*Submitted 21 September 2022; revised 22 November 2022; accepted 23 November 2022*

*Information about the authors:*

*Rohit Chaurasiya* – Department of Applied Physics, Delhi Technological University, Shahbad Daulatpur, Main Bawana Road, Delhi, 110042, Delhi, India; rohitqc2000@gmail.com

*Suman Dahiya* – Department of Applied Physics, Delhi Technological University, Shahbad Daulatpur, Main Bawana Road, Delhi, 110042, Delhi, India; ORCID 0000-0003-4815-5354; dahiyasuman90@gmail.com

*Rinku Sharma* – Department of Applied Physics, Delhi Technological University, Shahbad Daulatpur, Main Bawana Road, Delhi, 110042, Delhi, India; ORCID 0000-0001-6812-4358; rinkusharma@dtu.ac.in

*Conflict of interest:* the authors declare no conflict of interest.

## Tunneling current of contact of fractal object with metal and superlattice

Natalia N. Konobeeva<sup>a</sup>, Mikhail B. Belonenko<sup>b</sup>

Volgograd State University, University avenue, Volgograd, Russia

<sup>a</sup>yana.nn@volsu.ru, <sup>b</sup>belonenko@volsu.ru

Corresponding author: Natalia N. Konobeeva, yana.nn@volsu.ru

PACS 73.40.Gk, 61.72.-y

**ABSTRACT** In this paper, we study the features of the electric current under conditions of the tunnel effect in fractal structures. Based on the electron dispersion law for fractal objects, an expression for finding the tunneling current is obtained. Current-voltage characteristics are constructed for the following contacts: fractal-fractal, fractal-metal, fractal-superlattice. The influence of the fractal dimension on the characteristics of the tunneling current is revealed.

**KEYWORDS** fractals, fractions, tunneling, current-voltage characteristic.

**FOR CITATION** Konobeeva N.N., Belonenko M.B. Tunneling current of contact of fractal object with metal and superlattice. *Nanosystems: Phys. Chem. Math.*, 2023, **14** (1), 54–58.

### 1. Introduction

Recently, more and more attention of researchers has been attracted by sets of fractional dimensions [1] – fractals, which allow one not only to describe physical, biological and other phenomena, but also to obtain new theoretical and practical results in various fields of human activity, including medicine [2,3], biology [4], astrophysics [5], geography [6]. Fractals also made a great contribution to the development of modern electrical engineering and electronics. As an example, we can note: a fractal antenna [7,8], a fractal capacitor [9], fractal coding [10], fractal analysis of power system failures [11], elastic electronics devices [12]. A wide range of use of fractals is possible due to their properties such as self-similarity, space filling and fractal dimension, different from the topological one.

It is also known, that elastic vibrations occur in materials with a fractal structure. In this case, the concept of localized vibrational states, called fractons, is introduced [13]. Interest in this class of quantum states of matter is increasing every year, which is associated with the search for new states of matter, which is the main direction in condensed matter physics [14–18]. Similarly, electronic states in fractal structures will be localized, by analogy with Anderson localization [19] and, accordingly, give a nontrivial contribution, for example, to the tunneling current.

Although the tunneling current measurement method itself has a number of disadvantages (the distance between the samples determines the current, the degree of “roughness” of the samples, etc.), in our opinion, it has the advantage that it allows optimizing the choice of the second sample to achieve the highest sensitivity (for example, see [20]). In this paper, fractals are considered on the basis of two-dimensional lattices, and the formalism allows generalization to the case of a higher dimension.

### 2. Basic equations

Our system is a contact of two different materials: the first of which is a fractal object, and the second is a metal, a superlattice or a fractal lattice. Thus, a metal probe, superlattice (SR) or other fractal is brought to the fractal at an angle of 90 °C. The aim of this work is to calculate the tunneling current in the considered system of two contacting materials.

The electron dispersion law for a fractal object can be written as:

$$\varepsilon_1(p_x, p_y) = V (p_x^2 + p_y^2)^{0.5\sigma}, \quad (1)$$

here  $(p_x, p_y)$  are the electron quasi-momentum components,  $V$  is the analogue of the Fermi velocity for fractals,  $\sigma$  is the dimension that is used to describe the fracton states [21]:

$$\sigma = \frac{2d_f}{d_w}, \quad (2)$$

$d_f$  is the fractal dimension of an object,  $d_w$  is the diffusion index.

The dimension of a fractal is one of its most important characteristics [22]. In the general case, there are several definitions of this quantity. In particular, fractal dimensions can be divided into two classes, which are called “metric” and “probabilistic”. The former describes only the geometry of a metric space. The latter takes into account both the geometry of the given set and the probability distribution supported by this set [23]. In this paper, we will be interested in the geometric fractals. Therefore, by fractal dimension, we mean the degree of space filling by it or a measure of the

degree of geometric irregularity of an object. Note that the fractal dimension is not an integer. For example, for the Koch curve it is  $\approx 1.26$ , for the Cesaro fractal it is about 1.78.

An important point is the choice of indicator  $\sigma$ . For the case of the simplest lattices without defects (hexagonal, square, triangular, similar three-dimensional ones),  $\sigma$  is calculated, as well as all other exponents and dimensions, analytically. Here, by defects, we mean the absence of certain bonds in the lattice. In this case, it coincides with the exponent in the electron dispersion law (1), which is also considered analytically. It is natural to assume that similar calculations can be performed for decorated gratings, which corresponds to the analogy with fracton modes.

The expression for the contact current density is given by the following formula [24]:

$$J(U) = \frac{4\pi e |T|^2}{\hbar} \int_{-\infty}^{\infty} d\varepsilon \cdot \nu_1(\varepsilon + eU) \cdot \nu_2(\varepsilon) (N_F(\varepsilon) - N_F(\varepsilon + eU)),$$

$$\nu_i(\varepsilon) = \iint_{p_x, p_y} \delta(\varepsilon - \varepsilon_i) \cdot dp_x \cdot dp_y,$$
(3)

where  $\delta(x)$  is the Dirac delta function,  $\nu_i(\varepsilon)$  is the tunneling density of states for the  $i$ -th contact;  $N_F(\varepsilon)$  is the equilibrium number of fermions with energy  $\varepsilon$ ,  $T$  is the matrix element of the tunneling operator. Here and below, we use the ‘‘rough’’ contact approximation. That is, the surface of the fractal object is perpendicular to the surface of the contact material. This limitation is not fundamental and corresponds to the conditions of the experiment. Note that, for definiteness, we will apply stress to the fractal.

Here we use the Kubo approach. Within the framework of this approach, the tunneling current is determined only by the equilibrium number of electrons and the density of states of the contacting objects. The matrix element  $T$  is determined by the properties of the contact itself, i.e. the distance between objects, the angle of inclination (if one of the objects is made in the form of a probe), etc. Note that this approach makes it possible to do without solving Schrödinger-type equations on fractals [25–28] and use only an assumption about the form of the density of states. In addition to the proposed approach, the density of states can also be obtained by directly diagonalizing the Hamiltonian, which takes into account the electron energy at the fractal node and jumps between nodes. This approach has its limitations related to the size of the fractal and the computational resources. Therefore, in this paper, we chose the assumption of the density of states.

Let us choose a fractal, a metal (4) and a superlattice (5) as the materials with which the fractal object comes into contact. The electronic spectrum for them can be written in the following form:

$$\varepsilon_2(p_x, p_y) = \frac{p_x^2 + p_y^2}{2m},$$
(4)

where  $m$  is the effective electron mass.

$$\varepsilon_2(\mathbf{p}) = \varepsilon_0 - \Delta \cdot \cos(\mathbf{k} \cdot \mathbf{p}),$$
(5)

$\varepsilon_0$  is the quantum well electron energy,  $\Delta$  is the tunneling integral determined by the overlap of the electronic wave functions in neighboring wells,  $p = (p_x, p_y)$ ,  $k$  is the superlattice reciprocal lattice vector.

Next, we calculate the tunneling density of states for all types of contact materials using the properties of the Dirac delta function:

$$\nu_1(\varepsilon) = \frac{\varepsilon^{(3-\sigma)/\sigma}}{2\pi^2 \sigma V^{4-\sigma}},$$
(6)

$$\nu_2(\varepsilon) = \frac{\sqrt{2m^3\varepsilon}}{\pi^2},$$
(7)

$$\nu_2(\varepsilon) = \frac{1}{\Delta \cdot \sqrt{1 - \left(\frac{\varepsilon_0 - \varepsilon}{\Delta}\right)^2}}.$$
(8)

Formulas (6), (7) and (8) correspond to the fractal, metal and superlattice.

### 3. Main results and discussion

For definiteness, we choose the Sierpinski carpet (Fig. 1) as a fractal object, for which the value of  $d_w$  can be calculated using the effective volume resistance [29].

Note that the fractal generator is defined by two numbers ( $a$ ,  $b$ ), where  $a$  is the size of the generator,  $b$  is the size of the holes. The fractal dimension of the carpet can be calculated as:

$$d_f = \frac{\log(a^2 - b^2)}{\log a}.$$
(9)

Note that at first glance, one can assume that the dimension is taken into account very roughly and the properties are the same for different quantum graphs. But, as shown in [29] and formula (9), the quantities  $a$  and  $b$  affect the fractal dimension. And for graphs with different geometry, the dimension also changes.

Equation (3) is solved using numerical integration.

The dependence of the tunneling current for different materials in the contact on the voltage is shown in Fig. 2.

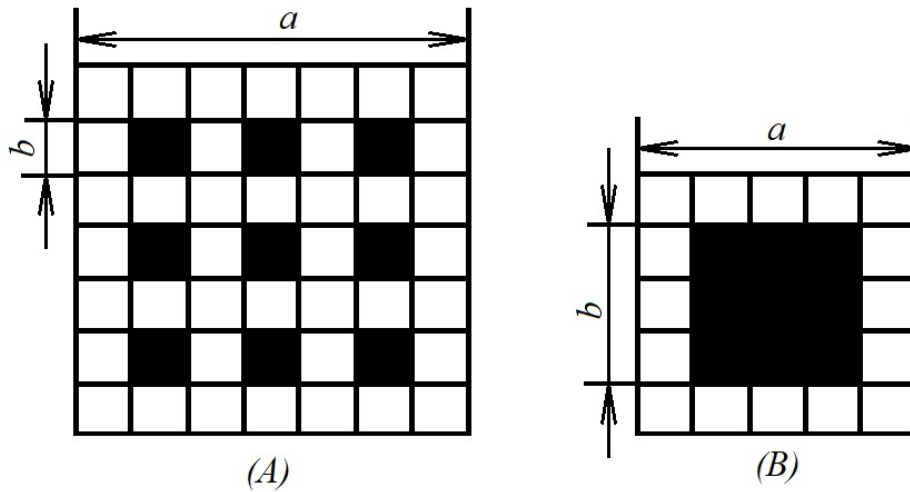


FIG. 1. Sierpinski carpet: (A) generator (7, 3); (B) generator (5,3)

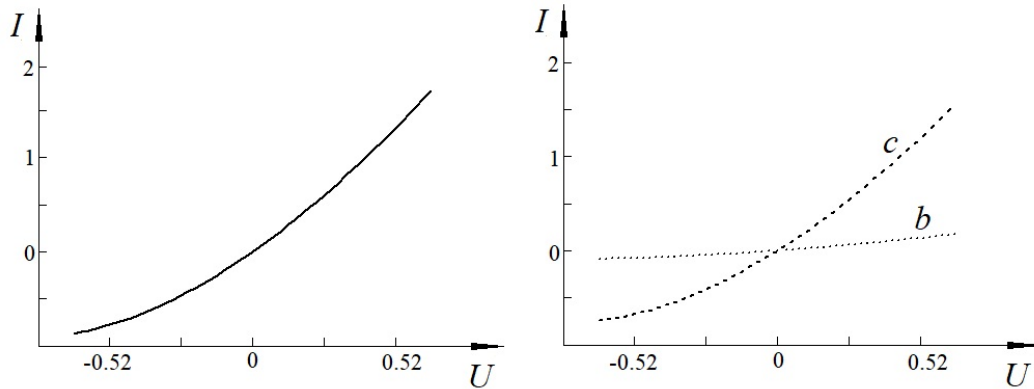


FIG. 2. Dependence of the tunneling current on voltage ( $\sigma = 1.801$ ) for the contact of the fractal Sierpinski carpet (7,3): (a) with the Sierpinski carpet fractal (5,3); (b) with metal; (c) with superlattice. The non-dimensional unit of  $I$ -axis corresponds to  $\mu\text{A}$  (for curve a), mA (for curves b-c). The non-dimensional unit of  $U$ -axis corresponds to 1 V

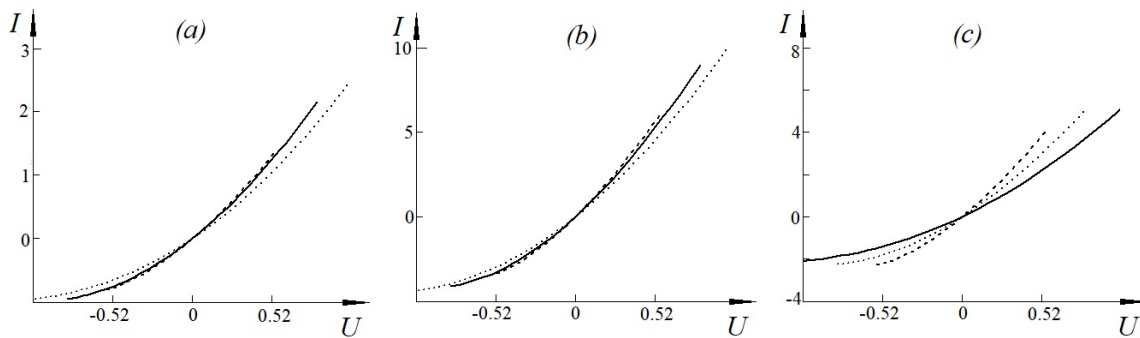


FIG. 3. Tunnel current versus voltage for different values of  $\sigma$ : (a) with Sierpinski carpet (5,3); (b) with metal; (c) with a superlattice. The solid line corresponds to  $\sigma = 1.2$ , the dotted line corresponds to  $\sigma = 1.6$ , the dashed line corresponds to  $\sigma = 1.9$ . The non-dimensional unit of  $I$ -axis corresponds to  $\mu\text{A}$  (for figure a), 0.1 mA (for figure b), mA (for figure c). The non-dimensional unit of  $U$ -axis corresponds to 1 V

Figure 2 shows the asymmetric nature of the dependence of the current on the voltage applied to the contact. This is explained by the features of the electronic structure (density of states) of the fractal object. We also note that the CVC for all three cases corresponds to the diode type. We can consider our system as a tunnel diode, since it is asymmetrical. Since on one side of the contact there is a fractal object, and on the other side there is a metal/SR/another fractal. The situation here is similar to a conventional tunnel contact, for example, a metal with a semiconductor. Fig. 2a is built separately due to the lower current value (by 3 orders of magnitude).

The influence of the dimension  $\sigma$  on the tunneling current in different contacts is shown in Fig. 3.

As can be seen from Fig. 3, the fracton dimension, and, consequently, the form of the fractal object, has a significant effect on the CVC of the tunnel contact. This is especially pronounced for the case with a superlattice in contact. We note an important practical application. By preparing a fractal from one material (for example, using a laser-based procedure [30]), it is possible to achieve different current-voltage characteristics in tunneling contacts.

#### 4. Conclusion

Here we formulate the main results:

- (1) The expression for the tunneling current density of a two-dimensional material with a fractal structure is obtained.
- (2) The current-voltage characteristics of a fractal object with a metal and a superlattice are constructed. Its asymmetric nature is found, which indicates the possibility of using fractal elements in diodes and transistors.
- (3) Possibility to control the magnitude of the tunneling current using the fractal dimension determined by the fractal structure of the material is shown.

#### References

- [1] Hausdorff F. Dimension und äußeres Maß. *Math. Ann.*, 1919, **79**, P. 157–179.
- [2] Heymans O., Fissette J., Vico P., Blacher S., Masset D., Brouers F. Is fractal geometry useful in medicine and biomedical sciences? *Med Hypotheses*, 2000, **54**(3), P. 360–6.
- [3] Uahabi K.L., Atounti M. Applications of fractals in medicine. *Annals of the University of Craiova, Mathematics and Computer Science Series*, 2015, **42**(1), P. 167–174.
- [4] Buldyrev S.V. *Fractals in Biology*. In: Meyers, R. (eds) *Encyclopedia of Complexity and Systems Science*. Springer, New York, 2009, P. 3779–3802.
- [5] Criscuoli S., Rast M.P., Ermolli I., Centrone M. On the reliability of the fractal dimension measure of solar magnetic features and on its variation with solar activity. *Astronomy and Astrophysics*, 2007, **461**(1), P. 331–338.
- [6] Husain A., Reddy J., Bisht D., Sajid M. Fractal dimension of coastline of Australia. *Scientific Reports*, 2021, **11** Article number 6304.
- [7] Abed A.T., Abu-AlShaer M.J., Jawad A.M. Fractal Antennas for Wireless Communications. In book: *Modern Printed-Circuit Antennas* Ed. H. Al-Rizzo. IntechOpen, London, 2020, 176 p.
- [8] De Nicola F., Puthiya Purayil N.S., Spirito D., Miscuglio M., Tantussi F., Tomadin A., De Angelis F., Polini M., Krahe R., Pellegrini V. Multiband plasmonic Sierpinski carpet fractal antennas. *ACS Photonics*, 2018, **5**, P. 2418.
- [9] Liu W., Wang Z., Wang G., Zeng Q., He W., Liu L., Wang X., Xi Y., Guo H., Hu C., Wang Z.L. Switched-capacitor-convertors based on fractal design for output power management of triboelectric nanogenerator. *Nature Communications*, 2020, **11** Article number 1883.
- [10] Menassel R. Optimization of fractal image compression. In book: *Fractal Analysis* Ed. R. Koprowski, IntechOpen, London, 2020, 128 p.
- [11] Tiwari A. Fractal applications in electrical and electronics engineering. *International Journal of Engineering Science and Advanced Technology*, 2012, **2**(3), P. 406–411.
- [12] Fan J.A., Yeo W.-H., Su Y., Hattori Y., Lee W., Jung S.-Y., Zhang Y., Liu Z., Cheng H., Falgout L., Bajema M., Coleman T., Gregoire D., Larsen R.J., Huang Y., Rogers J.A. Fractal design concepts for stretchable electronics. *Nature Communications*, 2014, **5**, Article number 3266.
- [13] Alexander S., Laerman C., Orbach R., Rosenberg H.M. Fracton interpretation of vibrational properties of crosslinked polymers, glasses and irradiated quartz. *Phys. Rev. B.*, 1983, **28**(8), P. 4615–4619.
- [14] Yoshida B. Exotic topological order in fractal spin liquids. *Phys. Rev. B*, 2013, **88**, P. 125122.
- [15] Vijay S., Haah J., Fu L. A new kind of topological quantum order: A dimensional hierarchy of quasiparticles built from stationary excitations. *Phys. Rev. B*, 2015, **92**, P. 235136.
- [16] Williamson D.J. Fractal symmetries: Ungauging the cubic code, *Phys. Rev. B*, 2016, **94**, P. 155128.
- [17] Ma H., Schmitz A.T., Parameswaran S.A., Hermele M., Nandkishore R.M. Topological entanglement entropy of fracton stabilizer codes. *Phys. Rev. B*, 2018, **97**, P. 125101.
- [18] Slagle K., Kim Y.B. Fracton topological order from nearest-neighbor two-spin interactions and dualities. *Phys. Rev. B*, 2017, **96**, P. 165106.
- [19] Anderson P.W. Absence of diffusion in certain random lattices, *Physical Review*, 1958, **109**(5), P. 1492–1505.
- [20] Konobeeva N.N., Belonenko M.B. Sensitivity characteristics of germanene. *Nanosystems: physics, chemistry, mathematics*, 2018, **9**(6), P. 770–774.
- [21] Zosimov V.V., Lyamshev L.M. Fractals and scaling in acoustics. *Acoustical Physics*, 1994, **40**(5), P. 627–653.
- [22] Zhikharev L.A. Fractal dimensionalities. *Geometry and Graphics*, 2018, **6**(3), P. 33–48.
- [23] Adams H., Aminian M., Farnell E., Kirby M., Peterson C., Mirth J., Neville R., Shipman P., Shonkwiler C. A fractal dimension for measures via persistent homology. In: Baas N., Carlsson G., Quick G., Szymik M., Thaulle M. (eds), *Topological Data Analysis*. Abel Symposia, vol 15. Springer, 2020.
- [24] Levitov L.S., Shitov A.V. *Green's functions. Problems with solutions*. Fizmatlit, Moscow, 2003, 392 p.
- [25] Dalrymple K., Strichartz R.S., Vinson J.P. Fractal differential equations on the Sierpinski gasket. *The Journal of Fourier Analysis and Applications*, 1999, **5**(73), P. 203–284.
- [26] Fukushima M., Shima T. On a spectral analysis for the Sierpinski gasket. *Potential Analysis*, 1992, **1**, P. 1–35.
- [27] Strichartz R.S. Analysis on Fractals. *Notices of the AMS*, **46**(10), P. 1199–1208.

- [28] Strichartz R.S. Some properties of Laplacians on fractals. *Journal of Functional Analysis*, 1999, **164**, P. 181–208.
- [29] Kim M.H., Yoon D.H., Kim I. Lower and upper bounds for the anomalous diffusion exponent on Sierpinski carpets. *J. Phys. A Math. Gen.*, 1993, **26**, P. 5655–5660.
- [30] Reinhardt H., Kroll M., Karstens S.L., Schlabach S., Hampp N.A., Tallarek U. Nanoscaled fractal superstructures via laser patterning – A versatile route to metallic hierarchical porous materials. *Adv. Mater. Interfaces*, 2020, **8**, P. 2000253.

---

*Submitted 13 November 2022; revised 30 November 2022; accepted 11 December 2022*

*Information about the authors:*

*Natalia N. Konobeeva* – Volgograd State University, University avenue, 100, Volgograd, 400062, Russia;  
ORCID 0000-0002-6043-9555; yana\_nn@volsu.ru

*Mikhail B. Belonenko* – Volgograd State University, University avenue, 100, Volgograd, 400062, Russia;  
ORCID 0000-0003-2003-3793; belonenko@volsu.ru

*Conflict of interest:* the authors declare no conflict of interest.

## Increase of signal to reference ratio for phase compensation in continuous-variable quantum key distribution systems

Fedor M. Goncharov, Boris E. Pervushin, Boris A. Nasedkin, Roman K. Goncharov, Daniil A. Yashin, Mikhail E. Gellert, Danil V. Sulimov, Polina A. Morozova, Ilya M. Filipov, Iurii A. Adam, Vladimir V. Chistiakov, Eduard O. Samsonov, Vladimir I. Egorov

ITMO University, St. Petersburg, 197101, Russia

Corresponding author: Fedor M. Goncharov, [fedor\\_goncharov@itmo.ru](mailto:fedor_goncharov@itmo.ru)

PACS 03.67.Dd, 42.30.Rx

**ABSTRACT** Continuous variables quantum key distribution (CV-QKD) systems are a promising direction for quantum communications. Coherent detection, which is the basis of CV-QKD, requires taking into consideration and compensating phase distortions. Phase compensation algorithms rely on using reference pulses for phase drift estimation and correcting signal quadratures. The ratio of the number of reference pulses to that of the signal ones, affects the accuracy of the phase compensation algorithm. On the other hand, it influences the secure key rate (SKR). The paper considers the effect of the reference to signal ratio on the SKR, and proposes a modification of the phase compensation algorithm, which allows using a smaller number of references at a pulse repetition frequency close to that of the system phase noise, which results in increasing SKR. We also propose a method for estimating the phase noise in the system for selection of the optimal signal to reference ratio.

**KEYWORDS** continuous-variable quantum key distribution, quantum communications, phase noise, phase compensation, algorithm

**ACKNOWLEDGEMENTS** The work was completed by the Leading Research Center “National Center for Quantum Internet” of ITMO University by order of JSCo Russian Railways. This research was funded by JSCo Russian Railways.

**FOR CITATION** Goncharov F.M., Pervushin B.E., Nasedkin B.A., Goncharov R.K., Yashin D.A., Gellert M.E., Sulimov D.V., Morozova P.A., Filipov I.M., Adam I.A., Chistiakov V.V., Samsonov E.O., Egorov V.I. Increase of signal to reference ratio for phase compensation in continuous-variable quantum key distribution systems. *Nanosystems: Phys. Chem. Math.*, 2023, **14** (1), 59–68.

### 1. Introduction

Since the implementation of the first quantum key distribution (QKD) protocol by Charles Bennett and Gilles Brassard in 1984, quantum communications have been actively developing. QKD is the main constituent of quantum communications, which allows two remote parties (usually referred to as Alice and Bob) to safely distribute the secure key through a quantum channel subject to any actions on the part of the eavesdropper (Eve) obeying the laws of quantum mechanics.

There are two main approaches to QKD implementation, one of them using discrete variables (DV) [1] and the other one using continuous variables (CV) [2]. The first protocols developed for QKD were those for discrete variables. However, this approach has some disadvantages, in particular, the need to use expensive single photon detectors.

Presently, CV-QKD is a promising approach, since it uses standard telecommunication equipment as part of the so-called coherent detection scheme [3] operating with a high detection frequency (of GHz order). Coherent detection approach in its turn is based on the interference of weak signal radiation and on powerful local oscillator (LO), which makes it possible to measure quadrature components of electromagnetic field carrying the encoded information. There are two main approaches to generating LO: on Alice’s side or on Bob’s side. In the former case, the signal and the LO are generated by the same laser in the sender and are jointly transmitted to the receiver using time-division multiplexing and polarization-division multiplexing. Coherent detection makes it possible to measure the quadrature of signal pulses, provided the power of the LO is much higher than the amplitude of the signal, therefore, a combination of multiplexing methods is established to separate the LO and the signal to avoid interference between them in the channel. If the LO is generated on Bob’s side (the so-called “local” LO (LLO)), then there is no need for multiplexing, the system becomes more secure, since there are no loopholes for attacks on LO [4, 5]. However, there is a problem of synchronization of two free-running lasers [6].

Interference as fundamental element of coherent detection makes it necessary to take account of the phase noise in the system and compensate it. Phase distortions in CV-QKD systems are discussed in multiple articles on quantum communications where algorithms are proposed [7] based on the alternation of signal and reference pulses, which are

used for phase compensation. Most studies [5, 8] describes systems with LLO, where phase noise is particularly strong because of two lasers used. Thus, the limiting ratio of reference pulses to signal pulses (one to one) is chosen as the most reliable option that provides the most accurate phase compensation. Nevertheless, in systems with transmitted LO (and in LLO-based systems with relatively low phase noise), the limiting ratio of reference and signal pulses may be redundant. Increasing the number of signal pulses by one reference increases secure key rate.

The paper consists of four sections: section 1 contains a review of the existing phase compensation method for protocol with Gaussian-modulated coherent states, as well as the essentials of excess phase noise model; section 2 provides a modification for the phase compensation algorithm based on two references instead of one; section 3 analyzes of the effect of the signal to reference ratio on the secure key rate; section 3 presents an experimental comparison of two phase compensation algorithms and estimates the phase noise in the system and the effect of the reference pulses frequency on the accuracy of phase compensation.

## 2. Phase compensation for CV-QKD protocol based on Gaussian-modulated coherent states

Here we review the CV-QKD protocol based on Gaussian coherent states, discuss the existing phase compensation algorithm and the standard phase compensation model.

### 2.1. Phase compensation algorithm

In the CV-QKD protocol with Gaussian [9, 10] modulation, Alice prepares numerous coherent states  $|\alpha_S\rangle = |Q_{A_S} + iP_{A_S}\rangle$  with quadratures  $Q_{A_S}$  and  $P_{A_S}$ , each of them independently and identically distributed from two random sets of variables with Gaussian distribution  $\mathcal{N}(0, V_A)$  with  $V_A$  variance centered at zero [11]. Quantum key is distributed by those quantum states, so we will call them quantum signals. The reference pulses required for phase compensation are the classical coherent states  $|\alpha_R\rangle = |Q_{A_R} + iP_{A_R}\rangle$  with the quadratures  $Q_{A_R}$  and  $P_{A_R}$ . For convenience, the zero-phase is usually chosen for the reference pulses. A LO is known to be essential to implement coherent detection. For the value at the output of the balanced detector to be proportional to the quadrature components of the field, the intensity of the LO has to be much higher than that of the reference and signal pulses [12]. Besides, the intensity of the reference pulse should also be significantly superior to the signal pulse in order to eliminate the occurrence of interference between the signal and the reference pulse during multiplexing [12]. The intensity of the reference pulses cannot be too low either, since otherwise the phase noise increases [13].

Alice sends Bob a sequence of signal and reference pulses with a certain ratio. Bob performs heterodyne detection, whereby he obtains the values of the signal quadratures  $(Q_{B_S}, P_{B_S})$  and the reference  $(Q_{B_R}, P_{B_R})$ . It is important that in the case of homodyne detection, Alice sends a pair of consecutive reference pulses, one of which introduces a delay of  $\pi/2$  before measuring. Another option is to use homodyne detection for signal pulses and heterodyne detection for reference ones. If during the time between the two reference pulses, the influence of phase noise is negligible, i.e.  $\tau \ll f_{phase}^{-1}$  (where  $\tau$  is the time interval between the two reference pulses, and  $f_{phase}$  is the characteristic frequency of phase noise in the system), the receiver can estimate the phase shift  $\hat{\theta}$  that occurs during the pulse transmission through the channel between the reference pulse and the LO [7]:

$$\hat{\theta} = \arctan\left(\frac{P_{B_R}}{Q_{B_R}}\right). \quad (1)$$

Since the intensity of the reference pulses is quite low, quantum uncertainty is also to be considered, so there is a phase error of random nature [7]:

$$\hat{\theta} = \theta + \varphi. \quad (2)$$

It is important that the variables  $\theta$  and  $\varphi$  have different physical nature, therefore they are independent. Besides the phase drift, the receiver also calculates the effective transmission of the channel  $T$ , given by:

$$T = \frac{\|(Q_{B_R}, P_{B_R})\|^2}{\|(Q_{A_R}, P_{A_R})\|^2}. \quad (3)$$

Reverse matching is often used in phase compensation protocols. Bob transmits to the sender the values of the measured quadratures of the reference pulses, using which he calculates the phase drift and the effective transmission according to formulas (1), (3). Otherwise, calculations can be performed on the recipient's side, and it is the values of  $\theta$  and  $T$  that are transmitted. Further, using the values of phase drift and effective transmission received from Bob, Alice corrects the values of her quadratures as follows [7]:

$$\begin{pmatrix} \hat{Q}_{A_S} \\ \hat{P}_{A_S} \end{pmatrix} = \sqrt{T} \begin{pmatrix} \cos \hat{\theta} & -\sin \hat{\theta} \\ \sin \hat{\theta} & \cos \hat{\theta} \end{pmatrix} \begin{pmatrix} Q_{A_S} \\ P_{A_S} \end{pmatrix}. \quad (4)$$

## 2.2. Phase noise model with phase compensation

Studies [7] and [14, 15] guarantee and prove the security of protocols containing reference pulses. The authors claim that under the standard assumption for CV-QKD, Eve can collect complete information about the reference pulses, however, this does not give her any additional information about the signal pulses. During phase compensation, there still appears to be some excess phase noise  $\xi_{phase}$ . Generally, the excess noise  $\xi_{tot}$  of the CV-QKD system is a key parameter for evaluating its performance. This can be represented by the expression [6]:

$$\xi_{tot} = \xi_{phase} + \xi_{rest}, \quad (5)$$

where  $\xi_{rest}$  includes all other sources of excess noise. As follows from [16, 17], phase noise can be represented as:

$$\xi_{phase} = V_A(V_{comp} + V_{ref}) = \xi_{comp} + \xi_{ref}, \quad (6)$$

$$V_{comp} = V_{drift} + V_{channel}. \quad (7)$$

The variance of  $V_{drift}$  occurs when using two independent lasers in the protocols with LLO and is given by the expression [16]:

$$V_{drift} = 2\pi(\Delta\nu_A + \Delta\nu_B)|t_R - t_S|, \quad (8)$$

where  $\Delta\nu_A$  and  $\Delta\nu_B$  are line widths of two free-running lasers,  $t_R$  and  $t_S$  are the time points of signal and reference pulses emission.

The  $V_{channel}$  component evaluates the change in the phase drift between the reference and the signal pulse resulting from the passage of the optical channel. The variance of  $V_{channel}$  can be defined as [16]:

$$V_{channel} = \text{var}(\theta_S - \theta_R). \quad (9)$$

Phase compensation is based on the measurement of reference pulses, and quadratures are further corrected with respect to their values. Obviously, phase shift measurement cannot be performed perfectly, thus the measured value of the phase shift  $\hat{\theta}_R$  may differ from the actual  $\theta_R$ . Therefore, the variance introduced by the inaccuracy of phase shift measurement is given as follows [7]:

$$V_{ref} = \text{var}(\theta_R - \hat{\theta}_R). \quad (10)$$

In practice, when the ratio of signal and reference pulses is one to one, the main contribution to excess phase noise is through the components  $\xi_{ref}$  and  $\xi_{drift}$ , whereas  $\xi_{drift}$  occurs only when using LLO and is crucial for the analysis of phase noise [16]. In addition, it is important to note that part of the excess phase noise can be considered trusted and irrelevant when evaluating the performance of CV-QKD system. The trusted phase noise model is given in [6].

## 3. Linear phase compensation algorithm

An important assumption of the phase compensation method discussed in the previous section was that the phase shift between the reference pulse and the following signal pulse it undergoes almost no change. This assumption has also be met with a theoretical increase in the number of signal pulses by one reference pulse: the phase drift for all signal pulses has to be almost the same. Based on this assumption, in the [6, 7] the component  $\xi_{channel}$  in the expression (6) was considered negligible. However, with an increase in the number of signal pulses between the reference ones, this assumption may not be met. In this paper we propose to modify the phase compensation algorithm so that the phase shift can be considered as linearly changing rather than constant between the reference pulses. The resulting phase compensation algorithm will be referred to as linear.

### 3.1. Linear phase compensation algorithm

A sequence consisting of a reference pulse (a pair of reference pulses for homodyne detection) and subsequent signal pulses up to the next reference pulse will be called a cycle (Fig. 1). The idea of using two reference pulses for phase compensation of one signal between them using the average value of the reference phase drift was proposed in [14] for a system with a ‘‘local’’ LO, since in such implementation phase noise can have high impact even on the interval between the neighboring pulses. Here we extend this approach to multiple signals in a cycle. Thus, linear phase compensation combines the ideas of using two reference pulses to compensate for the phase of one signal pulse, and using several signal pulses in a cycle, which allows increasing secure key rate (see section 3). The difference between the algorithms is shown in the Fig. 1.

Based on the assumption of the linear nature of the phase shift changes in the time interval between the reference pulses, the phase compensation is performed for each signal pulse in the cycle. The values of phase drift and transmission for the first and second reference pulses are calculated according to the following formulas, respectively:

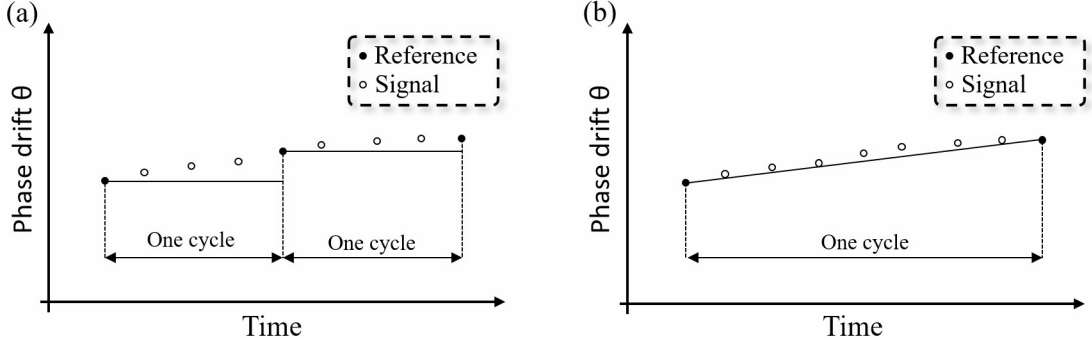


FIG. 1. Single reference pulse method (a) and linear method (b) of phase compensation

$$\hat{\theta}^{1st} = \arctan\left(\frac{P_{B_R}^{1st}}{Q_{B_R}^{1st}}\right), \quad T^{1st} = \frac{\|(Q_{B_R}^{1st}, P_{B_R}^{1st})\|^2}{\|(Q_{A_R}, P_{A_R})\|^2}; \quad (11)$$

$$\hat{\theta}^{2nd} = \arctan\left(\frac{P_{B_R}^{2nd}}{Q_{B_R}^{2nd}}\right), \quad T^{2nd} = \frac{\|(Q_{B_R}^{2nd}, P_{B_R}^{2nd})\|^2}{\|(Q_{A_R}, P_{A_R})\|^2}, \quad (12)$$

where  $Q_{B_R}^{1st}$ ,  $P_{B_R}^{1st}$  and  $Q_{B_R}^{2nd}$ ,  $P_{B_R}^{2nd}$  are the measured quadrature values of the first and the second reference pulses, correspondingly.

Next, using the values for each signal pulse in the cycle obtained from formulas (11), (12), phase drift correction and transmission are calculated:

$$\hat{\theta}_m = \frac{m(\hat{\theta}^{2nd} - \hat{\theta}^{1st})}{n_S + 1} + \hat{\theta}^{1st}, \quad (13)$$

$$T_m = \frac{m(T^{2nd} - T^{1st})}{n_S + 1} + T^{1st}, \quad (14)$$

where  $n_S$  is the number of signal pulses in the cycle. Then, similarly to the expression (4), the receiver corrects the value of each signal pulse in the cycle by using the formula:

$$\begin{pmatrix} \hat{Q}_{A_S}^m \\ \hat{P}_{A_S}^m \end{pmatrix} = \sqrt{T_m} \begin{pmatrix} \cos \hat{\theta}_m & -\sin \hat{\theta}_m \\ \sin \hat{\theta}_m & \cos \hat{\theta}_m \end{pmatrix} \begin{pmatrix} Q_{A_S}^m \\ P_{A_S}^m \end{pmatrix}. \quad (15)$$

This method provides an opportunity to increase the time interval of one cycle, thereby increasing the number of signal pulses by one reference. The experimental difference in the operation of phase compensation algorithms is presented in Section 4.1.

### 3.2. Effect of the ratio of reference and signal pulses on the accuracy of the phase compensation algorithms

The use of a linear phase compensation algorithm is aimed at increasing the number of signal pulses in the cycle. However, it is necessary to consider how an increase in the number of signal pulses affects the accuracy of the phase compensation operation, in other words, how the excess phase noise of CV-QKD system will change.

Let us return to expression (6). The accuracy of measuring the reference pulses does not appear to depend on the number of signal pulses, so  $\xi_{ref}$  will not be considered. However, the number of pulses in the cycle affects the second part of the equation (6), namely  $\xi_{comp}$ . For further discussion, it is more convenient to switch from the value of the number of signal pulses in the cycle to the frequency of sending reference pulses  $f_{ref}$ :

$$f_{ref} = \frac{f_{rep}}{n_S + n_R}, \quad (16)$$

where  $f_{rep}$  is the frequency of sending pulses (corresponds to the frequency of signals),  $n_R = 1$  for heterodyne detection of reference pulses,  $n_R = 2$  for homodyne detection.

In systems with transmitted LO, a theoretical analysis of the effect of the frequency of reference pulses on the phase noise component  $\xi_{comp}$  seems to be challenging, since in real-world operating conditions of CV-QKD systems, phase noise depends on many factors, such as temperature [18], vibrations and others. Thus, it is more reliable to determine the phase noise of a particular system experimentally before running the CV-QKD protocol. Therefore, it is possible to analyze resulting phase noise regardless of the reasons it appears. The method of determining the phase noise of the system and the assessment of the effect of reference pulses frequency on  $V_{comp}$  is discussed in the experimental part of this paper (section 4.2).

On the other hand, in a system with LLO, it is possible to analytically evaluate the component  $\xi_{drift}$ . The value  $V_{drift}$  defining  $\xi_{drift}$  is given by formula (8). Let us estimate the maximum possible value of  $V_{drift}$ , which is achieved by a signal pulse in a cycle that is as far as possible from the reference ones in the time domain. This signal pulse is the central signal in the cycle. Denote  $\Delta t = |t_R - t_S|$ . Then for the central signal in the cycle  $\Delta t$  can be obtained as follows:

$$\Delta t = \frac{n_S + 1}{2} \frac{1}{f_{rep}}. \quad (17)$$

Therefore,  $V_{drift}$  takes the following form:

$$V_{drift} = 2\pi(\Delta\nu_A + \Delta\nu_B) \frac{n_S + 1}{2f_{rep}}. \quad (18)$$

Specifically, for the case of heterodyne detection  $n_R = 1$ , (18) can be represented in terms of the frequency of reference pulses using (16):

$$V_{drift} = \frac{\pi(\Delta\nu_A + \Delta\nu_B)}{f_{ref}}. \quad (19)$$

It can be noted that for the linear phase compensation algorithm, the variance of  $V_{drift}$  is half as large as for the phase compensation discussed in [16].

#### 4. Secure key rate dependence on signal to reference ratio

The purpose of increasing the number of signal pulses in the cycle is to raise the secure key rate. This section examines the effect of the number of signal pulses in a cycle on the rate of secure key generation in the protocols of the CV-QKD. The value of the secure key rate is given in the approximation for the keys of infinite length by the expression [11]:

$$K = f_{sym} \cdot r, \quad (20)$$

where  $f_{sym}$  is the symbol rate (in units of symbols with  $^{-1}$ ), and  $r$  is the key generation rate in terms of the parcel. The above expression already contains a fraction of signal pulses relative to all pulses. To simplify the analysis of the secure key rate dependence on the ratio of signal and reference pulses, let us assume that this expression takes into account the ratio of one reference pulse to one signal pulse. Then we rewrite the expression for the secure key rate to include the change in the number of signal pulses in the cycle relative to the above:

$$K' = \varepsilon \cdot K \quad (21)$$

where  $\varepsilon = 2n_S \cdot (n_S + 1)^{-1}$  shows the change in the ratio of signal and reference pulses in the cycle relative to the one-to-one ratio.

Figure 2 reflects an increase in the secure key rate compared to that with one signal pulse from the number of signals in the cycle. Fig. 2 shows that when a ratio of about one hundred signal pulses per reference is reached, a further increase in the ratio only leads to a slight gain in the secure key rate and, perhaps, can only be reasonable if the number of reference pulses is increased by an order of magnitude.

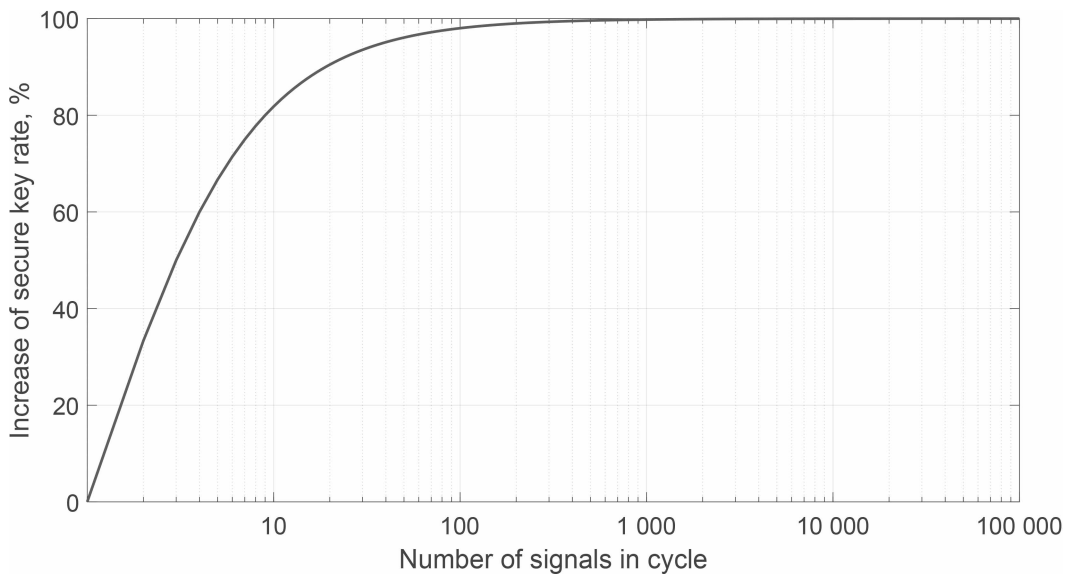


FIG. 2. Dependence of the increase of secure key rate (relative to one signal pulse in a cycle) on changing the number of reference pulses in a cycle

If the number of signals in the cycle is below one hundred, the effect of each additional signal is much more pronounced. For example, even using two reference pulses in a cycle instead of one increases secure key rate by 33 %.

## 5. Experimental setup

### 5.1. Comparison of the phase compensation algorithms efficiency

First, we compare the efficiency of phase compensation algorithm [7] and the linear algorithm for different frequencies of reference pulses. The characteristic phase noise for the experimental scheme shown in Fig. 3 is of the order of one Hz, therefore, for a more visual demonstration of the difference in the algorithms, there were used reference pulses with the power in order of 1 mW and the frequency  $f_{ref} = 4$  Hz, which is close to phase noise. For more information of the evaluation of the phase noise in the CV-QKD system, see Section 4.2. The experimental setup is a Mach-Zehnder interferometer – a simplified version of the CV-QKD system. The first amplitude modulator AM1 sets pulses with a frequency of  $f_{rep}$ , the second amplitude modulator AM2 generates reference pulses with a frequency of  $f_{ref}$ . In this experiment, all pulses are classical, which allows to ignore the phase error  $\phi$  from the expression (2), which has quantum nature. The phase of the pulses sent by Alice is set to zero, so the phase measured by the receiver corresponds to the phase shift  $\hat{\theta}$ .

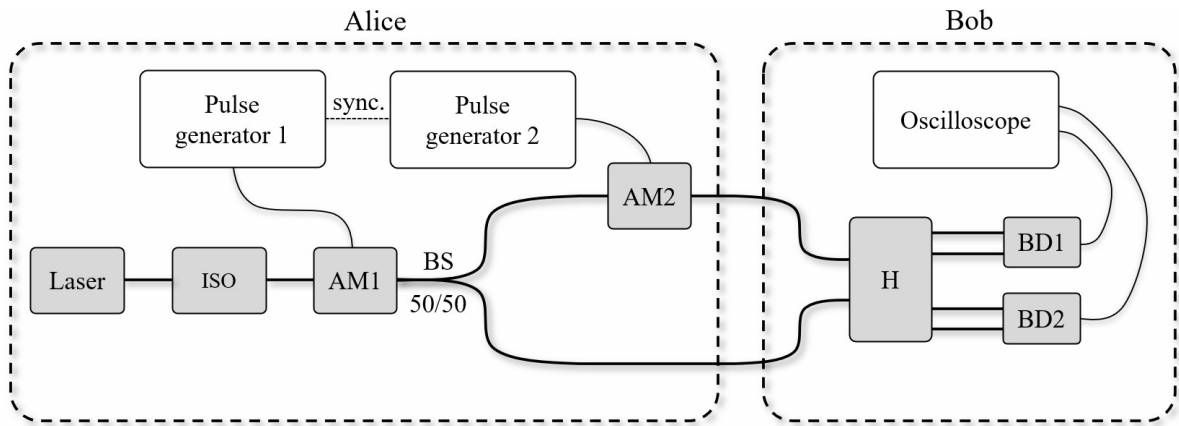


FIG. 3. Scheme of experimental setup No. 1, where ISO is optical isolator, BS is 50/50 beam splitter, AM1 and AM2 are amplitude modulators, H is 90-degree hybrid, BD1 and BD2 are balanced detectors

The graph presented in Fig. 4(a) shows the measured phase shift of the signal and reference pulses, the phase shift reconstructed by the method of a single reference pulse and the linear algorithm. With strong phase changes, the phase compensation algorithm using two reference pulses is characterized by a smaller error in the phase adjustment of signal pulses, especially in the areas of strong linear changes, for instance, in the area from 52 to 80 pulses.

The graph presented in Fig. 4(b) shows the averaged error values for each signal pulse over all cycles. The phase error for the algorithm with one reference pulse increases as it moves away from the reference pulse. For a linear phase

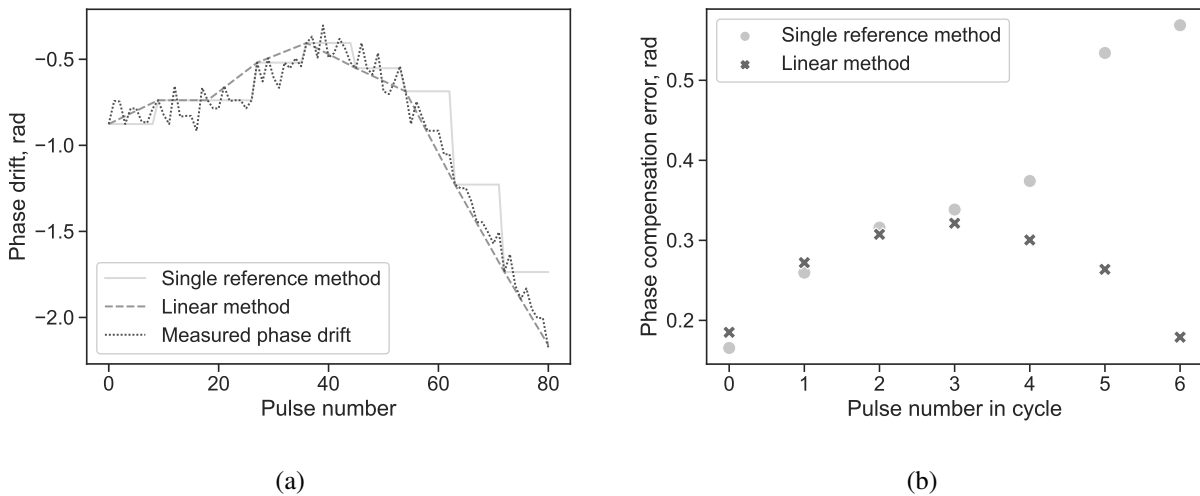


FIG. 4. (a) Phase shift of the pulses for  $f_{ref} = 4$  Hz and (b) dependence of the cycle-averaged phase compensation error on the number of the signal pulse

compensation algorithm using two reference pulses, an increase is observed first, whereas there is a decrease in the phase error after the middle signal pulse. This results from the fact that the phase of the signal pulses of the cycle second half is closer to the phase of the second reference pulse, and it is this phase that is used to a greater extent to compensate for the phase distortions of the signal pulses. The phase error in this experiment is characterized by large values due to the low frequency of pulse transmission. During the characteristic time of this experiment, the phase of the pulses relative to the LO appears to shift by significant amounts. The graph in Fig. 5(a) shows the statistics of the phase error when averaging by pulses and by cycle. When using two reference pulses, the median of the phase recovery error decreases.

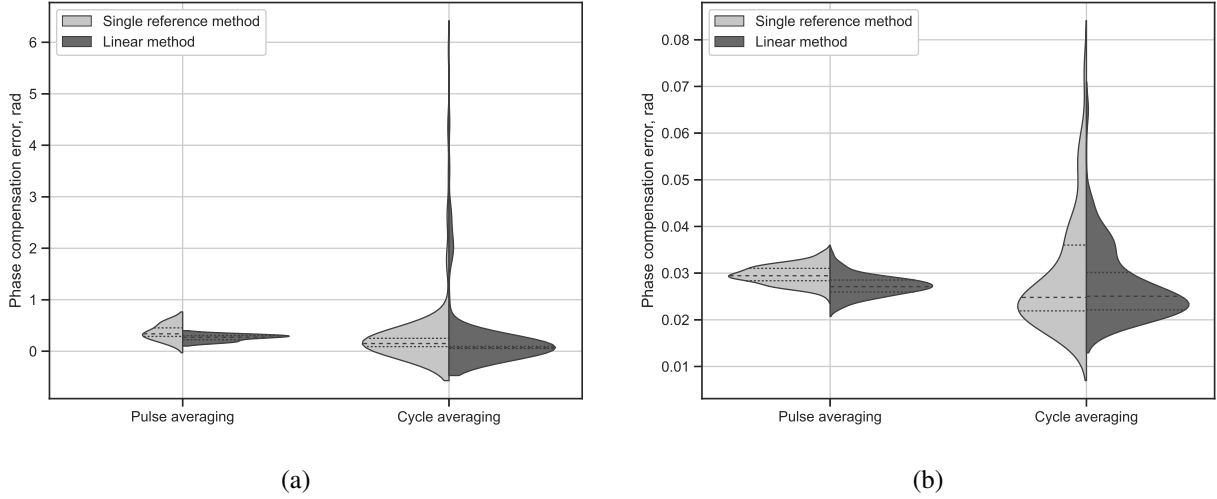


FIG. 5. Statistics of phase error when averaging by state and by cycle. When averaging over a pulse, statistics of the average phase error for each signal pulse in a cycle are built; when averaging over a cycle it is the statistics of the average error in a cycle. The strokes indicate the distribution of quantiles: 25, 50, 75 %

To analyze phase compensation with parameters close to the real parameters of a CV-QKD system, we handled measurements with a pulse frequency  $f_{rep}$  of 50 MHz, duration of 3 ns, reference pulses with a frequency  $f_{ref}$  of 500 kHz. The resulting statistics of the phase compensation performed are shown in Fig. 5(b). Since the characteristic operating time of the system determined by the frequency of sending pulses is too small compared to the characteristic phase change time, the error in phase noise compensation is relatively small. Therefore, the difference between algorithms with one and two reference pulses is insignificant either.

Summarizing, it can be concluded that with the frequency of reference pulses close to the frequency of phase noise in the system, the linear phase compensation algorithm is more effective, especially with strong phase noise in the system, which allows to increase the number of signal pulses in the cycle, and consequently, increase the speed of secure key rate. When the frequency of the reference pulses is much higher than the characteristic frequencies of the reference pulses, the difference in the operation of the algorithms is negligible.

## 5.2. Phase noise and phase compensation accuracy

This section discusses a method for estimating phase noise in the CV-QKD system and the effect of the selected frequency of reference pulses on the accuracy of the linear phase compensation algorithm.

Phase noise evaluation was evaluated before starting the CV-QKD protocol. It consists of the accumulation and analysis of phase shifts within a few seconds [19]. Let us consider phase noise on an experimental setup (Fig. 6), similar to the one used in the previous section. In this scheme, a channel is added for transmitting the LO and the signal from Alice to Bob, where the LO and the signal are multiplexed. The channel consists of 500 meters of polarization-maintaining optical fiber, thus, it allows avoiding polarization distortion.

To collect statistics, Alice sends a sequence of identical pulses with zero phase, the quadrature values of which are recorded by Bob. Next, using the formula (1), the receiver calculates the phase shift  $\hat{\theta}$ . Phase noises are low-frequency compared to the rest of the noise, therefore, for the rest of the noise not to affect further analysis, the dependence obtained of the phase shift on time was smoothed using the moving average method. The resulting graph is shown in Fig. 6(a). The amplitude spectrum of phase noise is shown in Fig. 6(b). For the experimental setup presented, the main phase noises are up to 80 Hz. Note that a phase noise could be higher in real systems with longer channels. Nevertheless, the further analysis and conclusions about results of current experimental setup are also relevant to higher phase noises.

Let us simulate the phase compensation for a different number of signal pulses in a cycle and, consequently, a different frequency of reference pulses. To do this, we will consider some of the pulses as reference ones, and the rest of the pulses

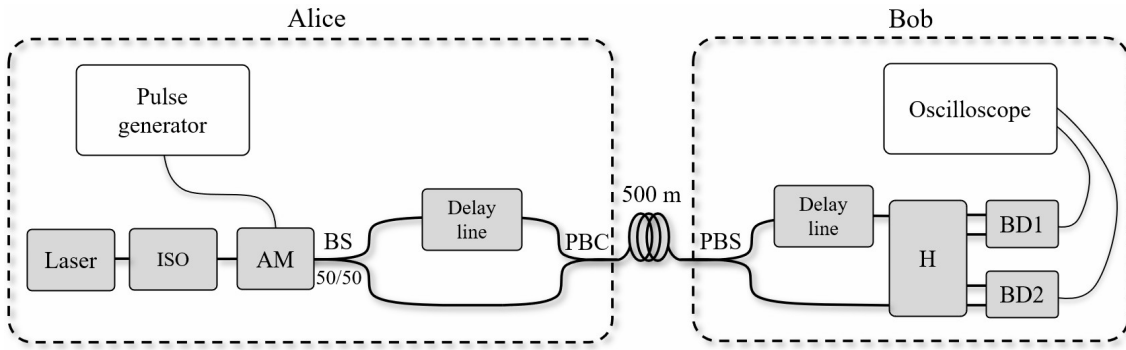


FIG. 6. Scheme of experimental setup No. 2, where ISO is optical isolator, AM is amplitude modulator, BS is beam splitter 50/50, PBS is polarization beam splitter, PBC is polarization beam combiner, H is 90-degree hybrid, BD1 and BD2 are balanced detectors

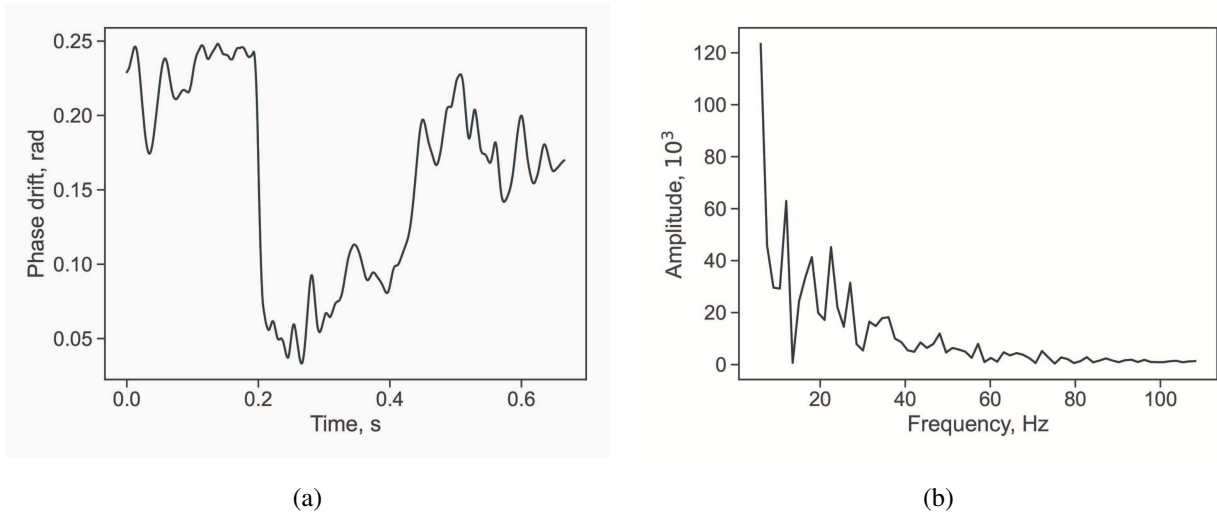


FIG. 7. (a) Phase noise versus time plot and (b) phase noise spectrum

between them as signal ones. We will estimate the accuracy of the phase compensation by the value  $V_{comp}$ , determined by formula (9). Fig. 8(a) shows the phase compensation error variance  $V_{comp}$  for reference pulse frequencies up to 150 Hz.

Comparison of this graph with the spectrum (Fig. 7(b)) shows the similarity of these dependencies. For the highest characteristic frequency of phase noise, the phase error is already relatively small (of the order of  $10^{-5}$ ). However, in

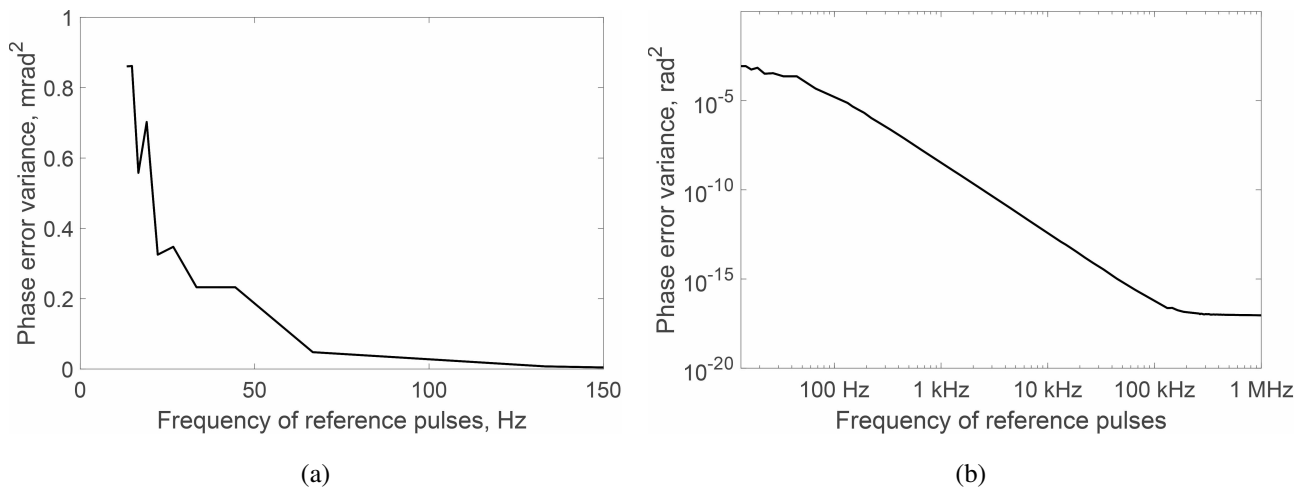


FIG. 8. Plot of phase compensation error variance  $V_{comp}$  versus reference pulse frequency  $f_{ref}$ :  $f_{ref}$  up to 150 Hz (a);  $f_{ref}$  up to 1 MHz (b)

this case, the phase noise itself is quite small due to the experimental conditions. In practice, phase noise can be much higher, however it is still limited to  $[-\pi/2, \pi/2]$ . Fig. 8(b) shows the phase compensation error for higher reference pulse frequencies, which rapidly decreases with their growth.

The optimal frequency of the reference pulses is selected based on the condition that  $V_{ref} \gg V_{comp}$ . For strong phase noise, the frequency of the reference pulses can be taken an order of magnitude or two higher than the characteristic maximum phase noise frequency  $f_{phase}$ ; for weak phase noise, phase compensation will be highly accurate even at a frequency of reference pulses comparable to the characteristic frequency of phase noise. On the other hand, the frequency of the reference pulses has to be chosen for one reference pulse to accounts for as many signal pulses as possible up to the ratio of 1:100; a further increase in the ratio gives a minuscule increase in the secure key generation rate. Summing up, for a linear phase compensation algorithm, the optimal frequency of the reference pulses at low-frequency phase noise ( $f_{phase} \ll f_{rep}$ ) can be roughly estimated as

$$10f_{phase} < f_{ref}^{optimal} < 10^{-2}f_{rep}. \quad (22)$$

With high-frequency phase noise, the left boundary of the estimate can be reduced if the phase noise is weak, otherwise the right boundary of the estimation can be changed, based on the dependence of the secure key generation rate on the number of reference pulses in the cycle (Fig. 2).

## Conclusion

We analyzed the effect of the signal to reference ratio on the secure key rate in the CV-QKD system, as well as its influence on the accuracy of the phase compensation. To increase the number of signal pulses in a cycle, we proposed a linear method of phase compensation. The experiment showed that linear phase compensation algorithm works more efficiently than conventional method, which makes it applicable to increase the number of signals in systems with strong and high-frequency phase noise. We also proposed a method for estimating phase noise in a system that provides evaluating optimal frequency of reference pulses for phase noise with the characteristic frequency of the latter much lower than that of sending reference pulses.

## References

- [1] Gleim A.V., Egorov V.I., Nazarov Yu.V., Smirnov S.V., Chistyakov V.V., Bannik O.I., Anisimov A.A., Kynev S.M., Ivanova A.E., Collins R.J., et al. Secure polarization-independent subcarrier quantum key distribution in optical fiber channel using BB84 protocol with a strong reference. *Optics express*, 2016, **24** (3), P. 2619–2633.
- [2] Goncharov R., Vorontsova I., Kirichenko D., Filipov I., Adam I., Chistiakov V., Smirnov S., Nasedkin B., Pervushin B., Kargina D., et al. The rationale for the optimal continuous-variable quantum key distribution protocol. *Optics*, 2022, **3** (4), P. 338–351.
- [3] Hirano T., Yamanaka H., Ashikaga M., Konishi T., Namiki R. Quantum cryptography using pulsed homodyne detection. *Physical review A*, 2003, **68** (4), 042331.
- [4] Jouguet P., Kunz-Jacques S., Diamanti E. Preventing calibration attacks on the local oscillator in continuous-variable quantum key distribution. *Physical Review A*, 2013, **87** (6), 062313.
- [5] Wang T., Huang P., Zhou Y., Liu W., Ma H., Wang S., Zeng G. High key rate continuous-variable quantum key distribution with a real local oscillator. *Optics express*, 2018, **26** (3), P. 2794–2806.
- [6] Shao Y., Wang H., Pi Y., Huang W., Li Y., Liu J., Yang J., Zhang Y., Xu B. Phase noise model for continuous-variable quantum key distribution using a local local oscillator. *Physical Review A*, 2021, **104** (3), 032608.
- [7] Soh D.B.S., Brif C., Coles P.J., Lütkenhaus N., Camacho R.M., Urayama J., Sarovar M. Self-referenced continuous-variable quantum key distribution protocol. *Physical Review X*, 2015, **5** (4), P. 1–15.
- [8] Ren S., Yang S., Wonfor A., White I., Pentyl R. Demonstration of high-speed and low-complexity continuous variable quantum key distribution system with local local oscillator. *Scientific Reports*, 2021, **11** (1), P. 1–13.
- [9] Weedbrook C., Lance A.M., Bowen W.P., Symul T., Ralph T.C., Ping Koy Lam. Quantum cryptography without switching. *Physical review letters*, 2004, **93** (17), 170504.
- [10] Grosshans F., Van Assche G., Wenger J., Brouri R., Cerf N.J., Grangier P. Quantum key distribution using gaussian-modulated coherent states. *Nature*, 2003, **421** (6920), P. 238–241.
- [11] Laudenbach F., Pacher C., Fung C.-H.F., Poppe A., Peev M., Schrenk B., Hentschel M., Walther P., Hübel H. Continuous-variable quantum key distribution with gaussian modulation—the theory of practical implementations. *Advanced Quantum Technologies*, 2018, **1** (1), 1800011.
- [12] Huang D., Huang P., Lin D., Wang C., Zeng G. High-speed continuous-variable quantum key distribution without sending a local oscillator. *Optics letters*, 2015, **40** (16), P. 3695–3698.
- [13] Ma X.-C., Sun S.-H., Jiang M.-S., Liang L.-M. Local oscillator fluctuation opens a loophole for eavesdropping in practical continuous-variable quantum-key-distribution systems. *Physical Review A*, 2013, **88** (2), 022339.
- [14] Zou M., Mao Y., Chen T.-Y. Phase estimation using homodyne detection for continuous variable quantum key distribution. *J. of Applied Physics*, 2019, **126** (6), 063105.
- [15] Qi B., Loughovski P., Pooser R., Grice W., Bobrek M. Generating the local oscillator “locally” in continuous-variable quantum key distribution based on coherent detection. *Physical Review X*, 2015, **5** (4), 041009.
- [16] Marie A., Alleaume R. Self-coherent phase reference sharing for continuous-variable quantum key distribution. *Physical Review A*, 2017, **95** (1), 012316.
- [17] Wang T., Huang P., Zhou Y., Liu W., Zeng G. Pilot-multiplexed continuous-variable quantum key distribution with a real local oscillator. *Physical Review A*, 2018, **97** (1), 012310.
- [18] Bartolo R.E., Tveten A.B., Dandridge A. Thermal phase noise measurements in optical fiber interferometers. *IEEE J. of Quantum Electronics*, 2012, **48** (5), P. 720–727.

- [19] Zhang L., Wang Y., Yin Z., Chen W., Yang Y., Zhang T., Huang D., Wang S., Li F., Han Z. Real-time compensation of phase drift for phase-encoded quantum key distribution systems. *Chinese Science Bulletin*, 2011, **56** (22), P. 2305–2311.

---

*Submitted 22 November 2022; revised 3 December 2022; accepted 12 December 2023*

*Information about the authors:*

*Fedor Mikhailovich Goncharov* – ITMO University, Kronverksky Pr. 49, bldg. A, Saint Petersburg, 197101, Russia; ORCID 0000-0002-7370-4450; fedor\_goncharov@itmo.ru

*Boris Evgenevich Pervushin* – ITMO University, Kronverksky Pr. 49, bldg. A, Saint Petersburg, 197101, Russia; ORCID 0000-0002-0935-2614; borispervushin@itmo.ru

*Boris Aleksandrovich Nasedkin* – ITMO University, Kronverksky Pr. 49, bldg. A, Saint Petersburg, 197101, Russia; ORCID 0000-0002-4507-8616; banasedkin@itmo.ru

*Roman Konstantinovich Goncharov* – ITMO University, Kronverksky Pr. 49, bldg. A, Saint Petersburg, 197101, Russia; ORCID 0000-0002-9081-8900; rkgoncharov@itmo.ru

*Daniil Aleksandrovich Yashin* – ITMO University, Kronverksky Pr. 49, bldg. A, Saint Petersburg, 197101, Russia; ORCID 0000-0001-5127-0578; dayashin@itmo.ru

*Mikhail Evgenevich Gellert* – ITMO University, Kronverksky Pr. 49, bldg. A, Saint Petersburg, 197101, Russia; ORCID 0000-0002-2180-7052; mihailgellert@yandex.ru

*Danil Vasilevich Sulimov* – ITMO University, Kronverksky Pr. 49, bldg. A, Saint Petersburg, 197101, Russia; ORCID 0000-0002-7964-0697; dvsulimov@itmo.ru

*Polina Alekseevna Morozova* – ITMO University, Kronverksky Pr. 49, bldg. A, Saint Petersburg, 197101, Russia; ORCID 0000-0003-3741-3506; 283021@edu.itmo.ru

*Ilya Maksimovich Filipov* – ITMO University, Kronverksky Pr. 49, bldg. A, Saint Petersburg, 197101, Russia; ORCID 0000-0003-4564-8284; imfilipov@itmo.ru

*Iurii Alexandrovich Adam* – ITMO University, Kronverksky Pr. 49, bldg. A, Saint Petersburg, 197101, Russia; ORCID 0000-0002-5040-0040; adam\_yura@mail.ru

*Vladimir Viktorovich Chistiakov* – ITMO University, Kronverksky Pr. 49, bldg. A, Saint Petersburg, 197101, Russia; ORCID 0000-0002-2414-3490; v\_chistyakov@itmo.ru

*Eduard Olegovich Samsonov* – ITMO University, Kronverksky Pr. 49, bldg. A, Saint Petersburg, 197101, Russia; ORCID 0000-0002-4349-6603; eosamsonov@itmo.ru

*Vladimir Ilyich Egorov* – ITMO University, Kronverksky Pr. 49, bldg. A, Saint Petersburg, 197101, Russia; ORCID 0000-0003-0767-0261; viegorov@itmo.ru

*Conflict of interest:* the authors declare no conflict of interest.

## Performance enhancement of triboelectric nanogenerator using iodine doped PVDF

Rohit Phogaat<sup>1</sup>, Venkatesh Yepuri<sup>2,a</sup>

<sup>1</sup>Amity Institute of Nanotechnology, Amity University Haryana, Haryana, India

<sup>2</sup>Swarnandhra College of Engineering and Technology, Seetharampuram, Narsapur, India

<sup>a</sup>venkatesh.yepuri555@gmail.com

Corresponding author: Venkatesh Yepuri, venkatesh.yepuri555@gmail.com

**ABSTRACT** Because of the rapid improvement of energy collecting technologies, unique mechanical devices have been created. As a result of the energy problems, however, researchers began to create new procedures and strategies for storing as much energy as feasible. Nanotechnology is unique, and it spurred the invention of Triboelectric Nanogenerators (TENGs), which are employed as a source of energy in wearables by transforming mechanical energy into electrical energy. This article discusses TENG, which is a triboelectric material made from Polyvinylidene fluoride (PVDF) and aluminium (Al). TENG may be made in two ways: with PVDF alone or with iodine doped PVDF, with Al staying the same in the both cases. Despite the fact that the materials are triboelectric, aluminium electrodes are utilised to attach to the materials, which are created on a plastic substrate using a thermal evaporator and taped together. The existence of PVDF was verified by the Fourier transform infrared spectroscopy (FTIR) examinations, which revealed high absorption peaks at  $723\text{ cm}^{-1}$  and  $849\text{ cm}^{-1}$ , respectively. The digital storage oscilloscope (DSO) and pico-ammeter ( $10\text{--}12\text{ m}$ ) measurements of the TENG device's output voltage and current yielded results of 25V and 8 pA, respectively. Additionally, this study reveals the power density produced and the distinctiveness of this TENG device, both of which are critical to the efficiency and applicability of TENG in a new generation of electronics.

**KEYWORDS** doping, iodine, Polyvinylidene fluoride (PVDF), Polyethylene terephthalate (PET), Triboelectric Nanogenerator (TENG).

**FOR CITATION** Rohit Phogaat, Venkatesh Yepuri Performance enhancement of triboelectric nanogenerator using iodine doped PVDF. *Nanosystems: Phys. Chem. Math.*, 2023, **14** (1), 69–73.

### 1. Introduction

The development of technology throughout many spheres of existence has enhanced man's creativity in several ways. Despite the advancements, there are still some concerns, one of which is the energy crisis, which has led to several environmental issues. The topic of renewable energy is therefore the subject of many researches. One of the most prevalent and plentiful forms of energy, mechanical energy is employed in practically all activities. With a capacity of up to  $500\text{W/m}^2$ , the Nano generator is a tool used to convert mechanical energy into electrical energy on a smaller scale. Fig. 1 demonstrates the block diagram of the triboelectric nanogenerator.

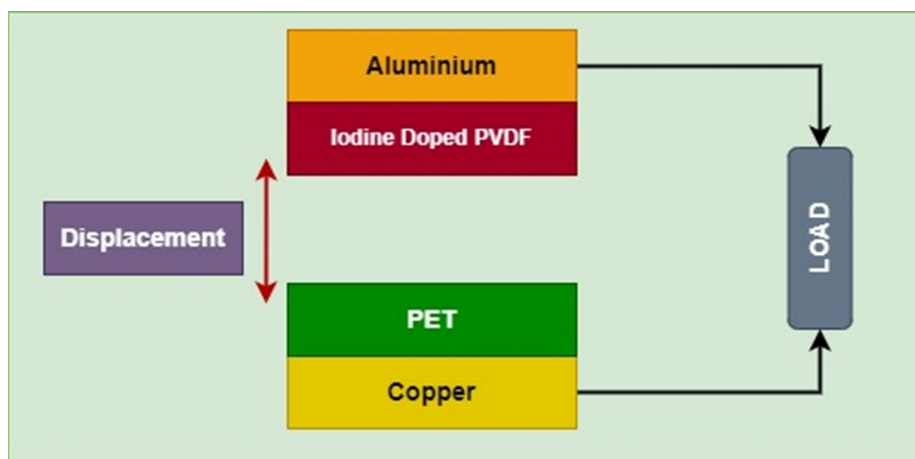


FIG. 1. Triboelectric nanogenerator setup with iodine doped PVDF and PET with aluminium and copper as electrodes

Two triboelectric materials are used in this generator, and they are brought into contact via charge transfer between their two layers. Material selection is critical in triboelectric materials. The TENG in this gadget is made up of two materials. The first is a polar material, whereas the second is non-polar. PVDF is one such non-polar material that is used, and it is recognised as the best polymer in the energy yielding sector because to its strong piezoelectric response, remarkable flexibility, and superior mechanical and ferroelectric properties [1, 2]. Aluminium (Al) is another substance that is recyclable, colourless, semi-crystalline resin, flexible, and present in its natural state. This work demonstrates the fabrication of a triboelectric Nanogenerator using PVDF and PET as triboelectric layers. Second, the focus of this study is on the layer-by-layer manufacturing of PVDF doped with iodine and PET [3,4]. Because of its charge transfer capability, iodine doped PVDF contributes significantly to higher output power when compared to other doping materials. PVDF is a semi-crystalline, high thermoplastic fluoropolymer that can withstand temperatures of up to 1500 °C and has strong mechanical, piezoelectric, and pyroelectric characteristics for increased processability. It is created by the synthesis of 1, 1-difluoroethylene ( $\text{CH}_2\text{-CF}_2$ ). This occurs in emulsion or suspension form at 10–1500 °C and 10–300 atm pressure. It is then converted into film sheets. PVDF has the property of being roughly 50% amorphous. The majority of PVDF units are connected head to tail, with only a small number of monomers attached head-to-head.

The phases  $\alpha$ ,  $\beta$ ,  $\gamma$  and  $\delta$  configurations are the four potential configurations. Because all of the dipoles are aligned in the same direction with regard to the PVDF phase, the carbon-fluorine bonds are polar and have large dipole moment. Although the melting point is low, the temperature under load during heat deflection is quite high. Low permeation is caused by the PVDF's high surface tension and high crystallinity. When exposed to heat or flame, PVDF does not burn or leak, demonstrating its excellent resistance to ultraviolet (UV) radiation. As previously said, another material is PET, thermoplastic polymer, which is well recognised for its superior mechanical, thermal, and chemical property combinations, also known as dimensional stability. PET is a widely recycled polymer. Recycled PET is transformed into fibre, textiles, and sheets for use in packaging and the production of vehicle parts. In its natural condition, it is a flexible, colourless, semi-crystalline resin with high dimensional stability, impact resistance, moistures, solvents, and alcohols. PET is employed because it promotes strength and is extremely strong and light in weight, which increases energy density. It is created from the condensation reaction of monomers acquired using any of the following techniques.

- a) Esterification between terephthalic acid and ethylene glycol.
- b) Trans-esterification between glycol and dimethyl terephthalate.

Kise et al. [5] experimented with dehydrofluorinating PVDF powder and films, and the results indicated that iodine doping increased electrical conductivity and even caused anisotropy to be seen. The linear slope may be seen in the conductivity temperature dependency. Increased iodine doping results in higher conductivities. As a dehydrofluorinated material, the doping of iodine on PVDF film doesn't show a significant improvement in conductivity [5]. Lee et al. [10] exhibited PVDF as a functional material in TENG that may also be utilised for deicing self-powered sensors. PVDF is a non-polar triboelectric material/polymer that functions as one of the layers of TENG [6]. Despite its numerous benefits, PVDF is notable for its high dipole mobility in its phase, strong formability, and flexibility. The dielectric constant increases as the charge density of the substance increases. Work functions and dielectric constants are kept as high as possible. The dielectric constant is high because PVDF belongs to the fluorine functional groups, which have a strong electron affinity, which boosts the charge accepting properties. When the TENG is pointing forward, the dipole movement increases. Garcia et al. [7] demonstrated TENG as a self-energizing impact sensor. TENG is used to transform mechanical energy from the surrounding environment into electrical energy via the triboelectric effect [7]. Because the electrical reaction from the TENG is precisely proportional to the mechanical motion, it is employed as a power activate sensor. TENG is made by sandwiching PVDF and PVP between copper electrodes, and PET is employed as the wrapping material. A drop ball test is used to measure the impact of electrical conductivity, which determined that the greater the drop height, the larger the sensor's velocity and impact energy. Madhuri et al. [8] exhibited the impacts of iodine on the structural morphology and physical characteristics of manganese phthalocyanine thin films, as the doping is done using Iodine and it is a halide group that includes ions and they are doped to modify the material's properties [8]. In terms of magnetic and electrical characteristics, semiconductor properties are changed. They alter the structure of molecular packing. Physical characteristics may also be connected. There is a shift in optical properties owing to iodine, indicating the creation of distinct polymorphs due to structural alterations. The structural characteristics of the film are also altered when the iodine doping concentration increases, resulting in a decrease in crystallinity and an increase in amorphous nature. Magnetic characteristics are also altered because they disrupt interchain reactions by reducing magnetic saturation, which disrupts molecular stack order. However, iodine improves electrical characteristics by increasing electrical conductivity.

Zhu et al. investigated the performance of grapheme films steam doped with iodine for electrochemical capacitive energy storage [9]. This study showed that iodine is an efficient p-type dopant that increased the material's electrical conductivity while also exhibiting strong cyclic stability and favourable electrochemical stability. Lee et al. described a TENG device that could self-improve the charge density and charge accumulation speed [10]. The charge density was the measure used to describe performance in prior TENGs, however, it was limited due to air breakdown. Unlike the previous devices, this device attained a maximum charge density of  $490 \text{ cm}^{-2}$ , which is double that of a standard TENG operating in air environment. This device has higher effective charge density and improved output performance, resulting in faster charge accumulation. Bahrami et al. demonstrated the improved output of TENG in PVDF by coating printer ink. PVDF

is utilised as one of the materials because of its well-known features such as ferroelectricity, piezoelectricity, and high crystallinity [11]. Since printer ink was utilised as nanofibers in PVDF by electron spin process of diverse growth rates to make PVDF PI NFs, phase is deemed to be the biggest and 88% is boosted and is noticed. These devices are well-known for being extremely efficient, self-powered gadget candidates.

Based on the research, it can be concluded that iodine doped PVDF is the most crucial factor in the device's manufacturing. Doping is a material modification technique in which one or more elements or compounds are doped with a substrate to achieve certain electrical or optical characteristics. Despite the fact that there are many different compounds, Iodine is chosen for doping because it offers few advantages in terms of ionic conductivity, charge transfer creation, high polymer charge-storing capacity, and good electrical and dielectrical characteristics.

## 2. Experimental

### 2.1. Materials and Methodology

Sigma-Aldrich provided the PVDF powder, DMF (N, N - Dimethylformamide), and acetone used to make the PVDF solution. Merck provides the PET film. Sigma-Aldrich supplies copper and aluminium adhesive tape. PVDF solution is made by dissolving PVDF powder (10 wt% PVDF) in N,N Dimethylformide and acetone in a 3:2 volume ratio and stirring well. For Iodine doped PVDF solution, 6% (w/w) Iodine (I) is mixed in 3:2 volume ratios of N, N Dimethylformide and acetone, which is made and agitated until the solution is well disseminated, and then 10% PVDF powder is added.

Triboelectric Nano generators are made in two ways: PVDF without any doping and PVDF with iodine doping. Regardless of the triboelectric materials, aluminium and copper electrodes are required, with the aluminium electrode being manufactured on a plastic substrate using a thermal evaporator. This electrode is connected to PVDF, one of the TENG materials. The PVDF solution is used to spin coat the initial dielectric layer on aluminium. The second material is PET film, which serves as a second dielectric and is bonded to a copper electrode. A spacer separates the two dielectric layers. Copper wires are used to link the electrode at the receiver's end to the load. The only common feature between the first and second TENG devices is the doping of PVDF with Iodine. One triboelectric layer is Al, while the other is a PVDF layer doped with Iodine.

The fabricated nanogenerator is characterized using the Fourier transform infrared (FTIR) spectroscopy for functional bond analysis, and the output voltage of TENG devices is measured using a Digital Storage Oscilloscope (DSO), and the current output is measured using a pico-ammeter (10–12 m) and pushing tester at constant force of 33.8 N.

## 3. Results and discussions

Figure 2 depicts the Fourier transform infrared spectroscopy analysis on the fabricated TENG. The absorption peaks identified at  $724\text{ cm}^{-1}$  and  $849.833\text{ cm}^{-1}$  correspond to  $\alpha$  crystal and  $\beta$  crystal shapes of PVDF, respectively. C–H stretching vibrational bonds were observed at  $1021\text{ cm}^{-1}$ . Furthermore, the peaks observed at  $1095\text{ cm}^{-1}$  and  $1244\text{ cm}^{-1}$  show amorphous phase of PVDF and stretching frequency of C–F bond.

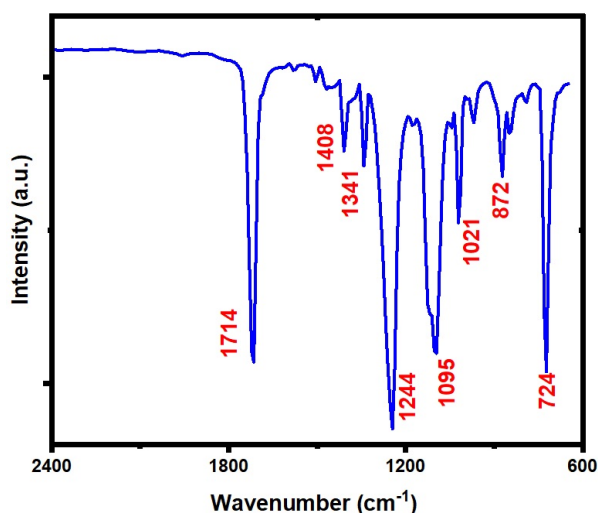


FIG. 2. FTIR spectra of the Iodine doped PVDF

A plot between resistivity and temperature of iodine doped PVDF is shown in Fig. 3a,b. The figure clearly shows that the resistivity of the constructed TENG reduces with increasing temperature with dramatical drop at  $37\text{ }^{\circ}\text{C}$ . hence, the below Fig. 3b between resistivity and temperature also suggests that the conductivity of a PVDF-based nanogenerator increases with device temperature.

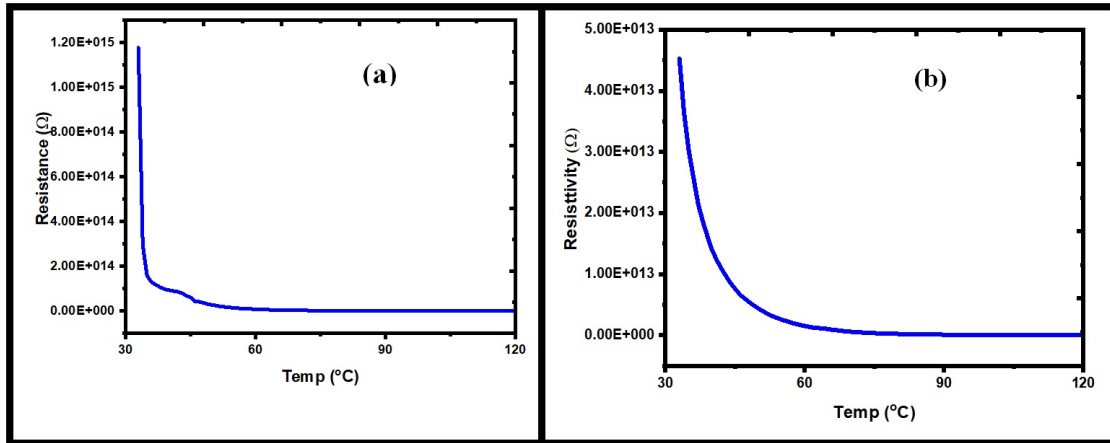


FIG. 3. The resistance (a) and resistivity (b) dependence on temperature

In this scenario, one of the triboelectric materials or layers is PVDF or iodine doped with PVDF layer, while another layer is PET. When the two layers come into contact, charges are generated on their surfaces, and when the surface separates, an electric potential is produced on the aluminium and copper electrodes. These copper and aluminium electrodes are connected to an external load. The passage of current will occur between them, resulting in a screen out of the electric field with charged surfaces created on them. A pushing tester is used to tap the surfaces back into contact. The electrode's potential difference will eventually charge, causing current to flow in the opposite direction, resulting in a continuous AC output.

Figure 4a,b depicts the open circuit voltage and current response with a force of 33.8 N on constructed TENG. The iodine-doped PVDF unit is thought to become positively charged, whereas the other component that comes into touch with PET and copper is thought to become negatively charged. When the iodine-doped sheet moves away from the TENG, an electrical potential difference develops, which forces electrons from the PVDF electrode to the copper electrode through an external circuit to offset the produced triboelectric potential. As seen in Fig. 4a this produces an alternating electrical output. Under these conditions, the TENG could produce an open circuit voltage ( $V_{oc}$ ) of around 25 V and enhanced with the force applied. The undoped TENG resulted in open circuit voltage variation between 0 to 12 V, whereas in this work, when compared to the undoped, their better findings showed that iodine doping had an impact on TENG performance in terms of conductivity and output voltage [12].

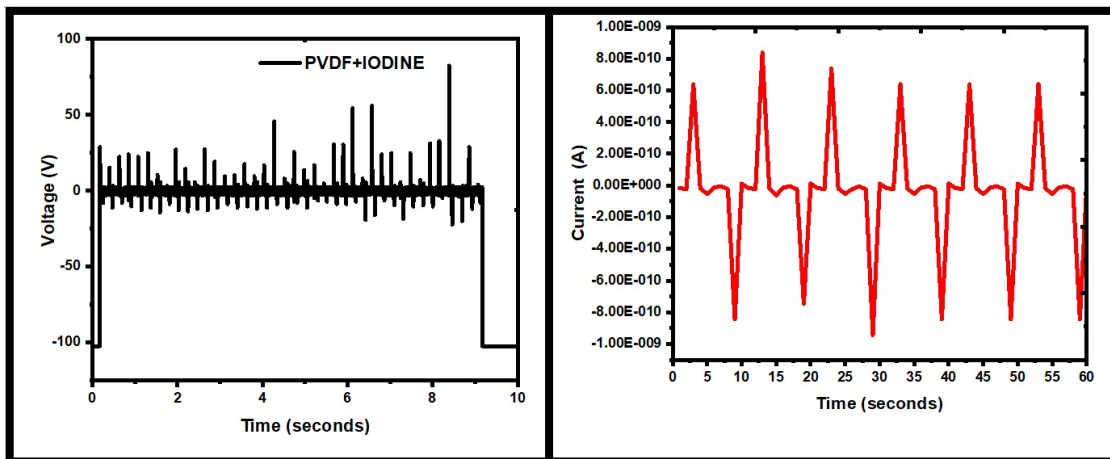


FIG. 4. Open-circuit voltage response (a) and current waveform of the TENG during press and release (b)

We also examined the TENG's current output and presented in Fig. 4b, when it was in contact with free-standing triboelectric layers constructed of iodine doped PVDF and with copper foil at a normal applied force of 33.8 N, the peak-to-peak current was approximated as 8 pA.

#### 4. Conclusions

Finally, we demonstrated an iodine doped structural TENG that captures mechanical energy from applied force using iodine doped PVDF and PET. A free-standing triboelectric layer that moves relative to the TENG surface generates the power. The thin films are fabricated on the specified substrate using the thermal evaporation process. The proposed TENG can capture mechanical energy from a force of 33.8 N and produce a peak-to-peak current of 8 pA. As a consequence, the proposed TENG shows promise as a power source for variable devices and has the potential to be developed to a wide range of other applications.

#### References

- [1] Tayyab M., Wang J., Wang J., Maksutoglu M., Yu H., Sun G., Yildiz F., Eginligil M., Huang W. Enhanced output in polyvinylidene fluoride nanofibers based triboelectric nanogenerator by using printer ink as nano-fillers. *Nano Energy*, 2020, **77**, P. 105178.
- [2] Cheng L., Xu Q., Zheng Y. A self-improving triboelectric nanogenerator with improved charge density and increased charge accumulation speed. *Nature Communications*, 2018, **9**, P. 3773.
- [3] Bazaka K., Jacob M. Effects of Iodine Doping on Optoelectronic and Chemical Properties of Polyterpenol Thin Films. *Nanomaterials*, 2017, **7**(1), P. 11.
- [4] Harold O. Lee III, Sam-Shajing Sun. Properties and mechanisms of iodine doped of P3HT and P3HT/PCBM composites. *AIMS Materials Science*, 2018, **5**(3), P. 479–493.
- [5] Kise H., Ogata H., Nakata M. *Angewandte Makromolekulare Chemie*. 1989, **168**(1), P. 205–216.
- [6] Lee J., Lee J., Baik J. The Progress of PVDF as a Functional Material for Triboelectric Nanogenerators and Self-Powered Sensors. *Micromachines*, 2018, **9**(10), P. 532.
- [7] Garcia C., Trendafilova I., De Villoria R.G., Del Rho J.S. Triboelectric nanogenerator as self-powered impact sensor. *MATEC Web of Conferences*, 2018, **148**, P. 14005.
- [8] Madhuri P.K., Santra P.K., Bertram F., John N.S. Current Mapping of Lead Phthalocyanine Thin Films in the Presence of Gaseous Dopants. *Physical Chemistry Chemical Physics*, 2019, **21**, P. 22955–22965.
- [9] Zhu Y., Ye X., Jiang H., Wang L., Zhao P., Yue Z., Jia C. Iodine-steam doped graphene films for high-performance electrochemical capacitive energy storage. *Journal of Power Sources*, 2018, **400**, P. 605–612.
- [10] Lee J., Lee J., Baik J. The Progress of PVDF as a Functional Material for Triboelectric Nanogenerators and Self-Powered Sensors. *Micromachines*, 2018, **9**(10), P. 532.
- [11] Bahrami S., Yaftian M.R., Najvak P., Dolatyari L., Shayani-Jam H., Kolev S.D. PVDF-HFP based polymer inclusion membranes containing CyphosIL 101 and Aliquat336 for the removal of Cr(VI) from sulfate solutions. *Separation and Purification Technology*, 2020, **250**, P. 117251.
- [12] Wang Y., Yang Y., Wang Z.L. Triboelectric nanogenerators as flexible power sources. *Npj Flexible Electronics*, 2017, **1**, article 10.

---

*Submitted 21 December 2022; revised 02 January 2023; accepted 03 January 2023*

*Information about the authors:*

**Rohit Phogaat** – Amity Institute of Nanotechnology, Amity University Haryana, Haryana, India-122412

**Venkatesh Yepuri** – Department of Electrical and Electronics Engineering, Swarnandhra College of Engineering and Technology, Seetharampuram, Narsapur, India-534280; ORCID 0000-0003-1544-9532; venkatesh.yepuri555@gmail.com

*Conflict of interest:* the authors declare no conflict of interest.

## Electric field effect on the light penetration depth and switching times in liquid crystal cells with nonuniform director orientation

Elena V. Aksenova<sup>1,a,b</sup>, Aleksandr A. Karetnikov<sup>1,c</sup>, Nikita A. Karetnikov<sup>2,d</sup>,  
Aleksandr P. Kovshik<sup>1,e</sup>, Anastasiya V. Svanidze<sup>1,3,f</sup>, Sergey V. Ul'yanov<sup>1,g</sup>

<sup>1</sup>Saint Petersburg State University, St. Petersburg, Russia

<sup>2</sup>ITMO University, St. Petersburg, Russia

<sup>3</sup>Ohio State University, Columbus, Ohio, USA

<sup>a</sup>[e.aksenova@spbu.ru](mailto:e.aksenova@spbu.ru), <sup>b</sup>[aksev@mail.ru](mailto:aksev@mail.ru), <sup>c</sup>[akaret@mail.ru](mailto:akaret@mail.ru), <sup>d</sup>[nkaret@mail.ru](mailto:nkaret@mail.ru),

<sup>e</sup>[Sashakovshik@yandex.ru](mailto:Sashakovshik@yandex.ru), <sup>f</sup>[avsvanidze@gmail.com](mailto:avsvanidze@gmail.com), <sup>g</sup>[s.ulyanov@spbu.ru](mailto:s.ulyanov@spbu.ru)

Corresponding author: E. V. Aksenova, [e.aksenova@spbu.ru](mailto:e.aksenova@spbu.ru)

PACS 42.70.Df, 78.20.Fm, 42.25.Lc

**ABSTRACT** The features of light refraction in liquid crystal cells with a continuously changing director distribution are studied. The theoretical description is constructed within the framework of the geometrical optics approximation. The neighborhoods of the turning points are considered, where due to the variable refractive index the ray smoothly changes the direction of propagation to the opposite one. It is shown that the applied electric field changes the nature of the extraordinary ray refraction. Electrically controlled refraction of light in cells with a planar and hybrid director orientation for incident angles exceeding the angle of total internal reflection is experimentally studied. The dependencies of the turn on and turn off times of the optical response on the applied voltage and the incident angles on the glass – liquid crystal boundary are obtained.

**KEYWORDS** refraction, liquid crystal, relaxation time, extraordinary wave, penetration depth

**ACKNOWLEDGEMENTS** A. V. Svanidze thanks for the support Saint Petersburg State University (Pure ID 28571656, IAS\_11.41.1554.2017).

**FOR CITATION** Aksenova E.V., Karetnikov A.A., Karetnikov N.A., Kovshik A.P., Svanidze A.V., Ul'yanov S.V. Electric field effect on the light penetration depth and switching times in liquid crystal cells with nonuniform director orientation. *Nanosystems: Phys. Chem. Math.*, 2023, **14** (1), 74–85.

### 1. Introduction

The wide practical application of liquid crystals (LC) explains the great interest in the study of their optical properties and behavior in external fields. This is due to the simplicity of controlling the optical properties of thin LC layers using an electric field: under the action of an electric field, the LC director is reoriented, which makes it possible to control the intensity of light passing through the LC layer. The unique electro-optical properties of LCs are used in display technology, information transmission systems and various optical devices [1–3].

The complexity of describing LC systems in external fields is due to the fact that the distribution of the director and, consequently, the optical characteristics are not constant, but vary over the thickness of the sample. The study of the trajectories of rays passing through such systems makes it possible to study the change in the local structure of an LC depending on the applied external field. The presence of a spatial helicoidal structure makes the problem of describing the transition in external fields mathematically more complex. The Fréedericksz transition in cholesteric liquid crystals (CLC) was first considered by Leslie [4]. Note that there is a significant difference between the descriptions of the Fréedericksz effect in electric and magnetic fields. The reason is that the electric field in LC is not uniform. This problem was considered in detail in [5–7].

Theoretically, the problem of the propagation of light obliquely incident on an anisotropic medium with an arbitrary direction of the optical axes was solved by various methods. Numerical methods [8–13] are intensively used. Much attention is paid to exact and approximate analytical methods [14–17], the method of interacting modes [18, 19] and methods of geometric optics [20, 21].

In this paper, cells are considered in which significant changes of the director orientation occur at distances much larger than the light wavelength. When describing the light propagation in such systems, the so-called Mougouin adiabatic regime is used. The properties of such media change smoothly on a scale of the order of the light wavelength, and it turns out to be possible to use the WKB method. Light propagates in the adiabatic regime. There are two normal waves, locally ordinary and locally extraordinary, whose polarization vectors are determined by the local directions of the optical axis and the wave vector at a given point. When an extraordinary ray is incident on an LC layer at angles greater than a

certain minimum angle, the extraordinary ray turns (reflects) inside the medium and leaves the medium [22]. Note that the turning occurs inside the cell at a certain depth of penetration, and not on the surface of the sample.

To describe the optical properties of an LC cell, it is necessary to know the distribution of the director in the volume. In this paper, we obtain this distribution using the method of direct minimization of free energy [17, 23, 24].

Associated with the director reorientation, the light transmission turn on and turn off times are one of the most important performance characteristics of liquid crystal devices. The research of the LC director reorientation dynamics at different distances from the LC layer boundary is of particular interest.

In this paper, we study the dependencies of the turn on and turn off times of the optical response on the angle of incidence of the ray on the LC layer. This makes it possible to study the dynamics of the electro-optical response for different depths of ray penetration into the layer. One of the aims of this work is to experimentally study electrically controlled refraction in LC cells by varying the thickness of the LC layer, the incident angle of light, and the applied voltage. The study of various cell geometries and comparison of their characteristics is of great interest in terms of determining the optimal cell properties for various applications.

## 2. Free energy of the liquid crystal

We consider a thin layer of liquid crystal confined between two plane-parallel plates. The area of the plates and the thickness of LC layer are assumed to be equal  $S_{\perp}$  and  $L$  respectively. Such LC cell can be placed in the external electric  $\mathbf{E}$  or magnetic  $\mathbf{H}$  field. The field is applied in a direction perpendicular to the plates. So we suppose that the director  $\mathbf{n}(\mathbf{r})$  has a homogeneous distribution in every plane parallel the plates.

Let us introduce Cartesian coordinate system in the following way. The axis  $Oz$  is along the direction which is perpendicular to the cell's plates (the electric and magnetic fields have the same direction) and the axes  $Ox$  and  $Oy$  are directed along the short and long edges of the plate respectively. The plane  $z = 0$  coincides with the lower substrate. So the director is the function of  $z$ -coordinate,  $\mathbf{n}(\mathbf{r}) = \mathbf{n}(z)$ .

The total free energy of the system includes three terms:

$$F_{tot} = F_e + F_f + F_{sf}. \quad (1)$$

The first term represents Frank free energy and describes a volume distortion [25]:

$$F_e = \frac{1}{2} \int_V [K_{11}(\text{div } \mathbf{n}(\mathbf{r}))^2 + K_{22}(\mathbf{n}(\mathbf{r}) \cdot \text{rot } \mathbf{n}(\mathbf{r}) + q_0)^2 + K_{33}(\mathbf{n}(\mathbf{r}) \times \text{rot } \mathbf{n}(\mathbf{r}))^2] dV, \quad (2)$$

where  $K_{11}, K_{22}, K_{33}$  are elastic Frank constants,  $p_0 = 2\pi/q_0$  is the pitch,  $V$  is the volume,  $V = S_{\perp}L$ .

The second component is the contribution of the external field:

$$F_f = - \int_V \frac{\mathbf{B} \cdot \mathbf{H}}{2} dV, \quad (3)$$

for magnetic field and

$$F_f = - \int_V \frac{\mathbf{D} \cdot \mathbf{E}}{8\pi} dV, \quad (4)$$

for electric field. Here  $\mathbf{B}$  is the magnetic induction,  $\mathbf{B} = (1 + 4\pi\chi_{\perp})\mathbf{H} + \chi_a(\mathbf{H} \cdot \mathbf{n})\mathbf{n}$ ,  $\chi_a = \chi_{\parallel} - \chi_{\perp}$  is the anisotropy of the magnetic susceptibility, where  $\chi_{\parallel}$  and  $\chi_{\perp}$  are the magnetic susceptibilities along and perpendicular to  $\mathbf{n}$ ;  $\mathbf{D} = \tilde{\epsilon}_{\perp}\mathbf{E} + \tilde{\epsilon}_a(\mathbf{E} \cdot \mathbf{n})\mathbf{n}$  is the electric displacement vector,  $\tilde{\epsilon}_a = \tilde{\epsilon}_{\parallel} - \tilde{\epsilon}_{\perp}$  is the anisotropy of the dielectric permittivity;  $\tilde{\epsilon}_{\parallel}, \tilde{\epsilon}_{\perp}$  are the dielectric permittivities along and perpendicular to  $\mathbf{n}$  at the electric field frequency.

The last term in Eq. (1) is the surface energy of anchoring

$$F_{sf} = \frac{S_{\perp}}{2} \sum_{j=1,2} w_j(\mathbf{n}(z_j), \mathbf{n}_{0(j)}), \quad (5)$$

where  $\mathbf{n}(z_j)$  ( $j = 1, 2$ , the terms with indexes 1 and 2 relate to up and down substrates of the cell, respectively) are directors in the planes of the plates, vectors  $\mathbf{n}_{0(j)}$  are easy orientation axes,  $w_j$  are scalar functions of two unit vectors. They take minimal values if  $\mathbf{n}(z_j) = \mathbf{n}_{0(j)}$ .

The director in every point of the cell's space can be represented by the polar  $\theta$  and the azimuthal  $\phi$  angles:  $\mathbf{n}(z) = (\sin \theta(z) \cos \phi(z), \sin \theta(z) \sin \phi(z), \cos \theta(z))$ . The angle  $\theta$  is counted from the axis  $Oz$  and the angle  $\phi$  from the axis  $Ox$ . The elastic energy (2) in these terms has the form [26]:

$$F_e = \frac{V}{2} K_{22} q_0^2 + \frac{S_{\perp}}{2} \int_0^L [A(\theta)(\theta')^2 + B(\theta)(\phi')^2 - 2C(\theta)\phi'] dz, \quad (6)$$

where

$$A(\theta) = K_{11} \sin^2 \theta + K_{33} \cos^2 \theta, \quad (7)$$

$$B(\theta) = \sin^2 \theta (K_{22} \sin^2 \theta + K_{33} \cos^2 \theta), \quad (8)$$

$$C(\theta) = q_0 K_{22} \sin^2 \theta. \quad (9)$$

The contributions of the external fields are

$$F_f = -\frac{S_{\perp}}{2} \int_0^L \frac{D_z^2}{4\pi(\tilde{\varepsilon}_{\perp} + \tilde{\varepsilon}_a \cos^2 \theta)} dz \quad (10)$$

or

$$F_f = -\frac{S_{\perp}}{2} \int_0^L \chi_a H^2 \cos^2 \theta dz. \quad (11)$$

Note that the electric field has the inhomogeneity induced by the nonuniform director distribution. For the further calculations and comparison with the experimental data it is convenient to represent the electric field contribution by the voltage  $U$ . The voltage is applied to the lower and upper plates of the LC cell.

$$U = \int_0^L E_z(z) dz = D_z \int_0^L (\tilde{\varepsilon}_{\perp} + \tilde{\varepsilon}_a \cos^2 \theta)^{-1} dz. \quad (12)$$

Then the second term can be written as

$$F_f = -\frac{S_{\perp} U^2}{8\pi \int_0^L (\tilde{\varepsilon}_{\perp} + \tilde{\varepsilon}_a \cos^2 \theta)^{-1} dz}. \quad (13)$$

For the last term the Rapini–Papoular potential is usually used

$$F_{sf} = \frac{S_{\perp}}{2} \sum_{j=1,2} (w_{\theta}^{(j)} \sin^2(\theta(z_j) - \theta_{0(j)}) + w_{\phi}^{(j)} \sin^2(\phi(z_j) - \phi_{0(j)})). \quad (14)$$

The angles  $\theta_{0(j)}$  and  $\phi_{0(j)}$  describe the vectors of the easy orientation axes  $\mathbf{n}_{0(j)}$ .

We will calculate director configuration for different LC cells by the direct minimizing the free energy. For this purpose one can use director representation within the finite elements method or the Fourier transform by the polar and the azimuthal angles.

Within this model we can also calculate a capacity  $C$  of the LC cell. It depends on the director distribution

$$C = \frac{q}{U} = \frac{S_{\perp}}{4\pi \int_0^L (\tilde{\varepsilon}_{\perp} + \tilde{\varepsilon}_a \cos^2 \theta)^{-1} dz}. \quad (15)$$

Here we suppose that  $S_{\perp} \gg L$  and the boundary effects are neglected.

### 3. Light propagation in the LC cells within the geometrical optics approximation

In this section, we consider the light propagation in the anisotropic medium within the geometrical optics approximation. Note that the dielectric permittivity tensor  $\hat{\varepsilon}$  is taken at the optical frequency and describes the medium optical properties. Further the medium is supposed to be nonmagnetic i.e. the magnetic permeability tensor is  $\mu_{\alpha\beta} = \delta_{\alpha\beta}$ . We are interested in the wave equation solution. In our problem the ray is incident to the plane  $z = 0$ . Let  $p$  is a typical scale of the director variation and its value is  $p \sim (dn/dz)^{-1}$ . We assume in the framework of geometrical optics that  $p \gg \lambda$ . So  $\Omega = p/\lambda$  is the large parameter. The presence of the large parameter makes it possible to solve the wave equation using the WKB method. We consider only the first two orders in the  $\Omega$  parameter within this method. Then the electric field of the wave can be written as [27]:

$$\mathbf{E}_{\pm}^{(j)}(\mathbf{r}) = A_{\pm}^{(j)}(\mathbf{k}_{\perp}; z, z_0) \mathbf{e}_{\pm}^{(j)}(\mathbf{k}_{\perp}, z) \exp\left(i\mathbf{k}_{\perp} \cdot \mathbf{r}_{\perp} + i \int_{z_0}^z k_{z\pm}^{(j)}(\mathbf{k}_{\perp}, z') dz'\right), \quad (16)$$

where  $(j)$  is the type of the wave ( $(o)$  is ordinary and  $(e)$  is extraordinary),  $A_{\pm}^{(j)}$  is the wave amplitude,  $z_0 = 0$ ,  $\mathbf{e}_{\pm}^{(j)}$  are the polarization vectors, the wave vector  $\mathbf{k}$  takes the form  $\mathbf{k} = (\mathbf{k}_{\perp}, k_z)$ ,  $\mathbf{k}_{\perp}$  is the two-dimensional vector, its magnitude is determined only by the incident angle  $\delta$  and the refractive index of medium  $n_{gl}$ . In the introduced coordinate system  $\mathbf{k}_{\perp} = (0, k_{\perp})$ , where  $k_{\perp} = k_0 n_{gl} \sin \delta$ . The longitudinal component of the wave vector  $k_z$  has enough complicated form. It can be derived from the eikonal equation [28]:

$$k_{z\pm}^{(o)} = \pm \sqrt{k_0^2 \varepsilon_{\perp} - k_{\perp}^2}, \quad (17)$$

$$k_{z\pm}^{(e)} = \frac{k_0}{\varepsilon_{\perp} + \varepsilon_a \cos^2 \theta} \left( \frac{k_{\perp}}{k_0} \varepsilon_a \sin \theta \cos \theta \sin \phi \pm \varepsilon_{\perp} \sqrt{D(k_{\perp}, \theta, \phi)} \right), \quad (18)$$

where

$$D(k_{\perp}, \theta, \phi) = \varepsilon_{\parallel} \left( 1 - \frac{k_{\perp}^2}{k_0^2 \varepsilon_{\perp}} + \frac{\varepsilon_a}{\varepsilon_{\perp}} \cos^2 \theta \right) + \frac{k_{\perp}^2 \varepsilon_a}{k_0^2 \varepsilon_{\perp}} \sin^2 \theta \cos^2 \phi, \quad (19)$$

$k_0 = 2\pi/\lambda$ . The expression (16) describes the four possible solutions of the wave equation. Here  $\pm$  means the propagation direction in relation to the axis  $Oz$ : along the axis or the reverse one, respectively.

In the present system, the extraordinary wave can propagate in the direction along which the refractive index decreases. In this case the effect of total internal reflection is possible i.e. the wave vector change the propagation direction gradually to the reverse one. In the certain medium point  $z = z_t$  the function

$$D(k_{\perp}, \theta(z_t), \phi(z_t)) = 0 \quad (20)$$

and then becomes less than zero. This means the appearance of the complex additive in the  $k_z^{(e)}$  expression. The wave partially reflects from the layer  $z = z_t$  and partially continues to propagate with the exponential damping. The first effect is very similar to the total internal reflection within the LC volume (the wave partially reflects from some layer inside the medium and then begins to propagate in the direction reversed to the axis  $Oz$ ).

In the differential equation theory the points satisfying Eq. (20) are called the turning points. The electric field expansion is a complex task and the WKB method is not applicable in the vicinity of these points. The turning points presence and location have an important role in the investigation of the light propagation in the LC cells [22].

The wave vectors surfaces are derived from the equations (17) and (18) for ordinary and extraordinary waves, respectively. This surface is a sphere in the ordinary wave case. So for the certain incident angle i.e. for the certain  $k_{\perp}$  the longitudinal component  $k_z^{(o)}$  does not depend on  $z$  and the wave propagates in the medium in a straight line. In the extraordinary wave case the wave vectors surface takes the oblique ellipsoid form. Its orientation is determined by the angles  $\theta(z)$  and  $\phi(z)$ . The Fig. 1 shows the cross-section of this ellipsoid by the plane formed by  $k_{\perp}$  and the axis  $Oz$  for the certain value  $z$ . The magnitude of the wave vector transverse component  $k_{\perp}$  is determined by the incident angle, the medium refractive index and the incident wave length.

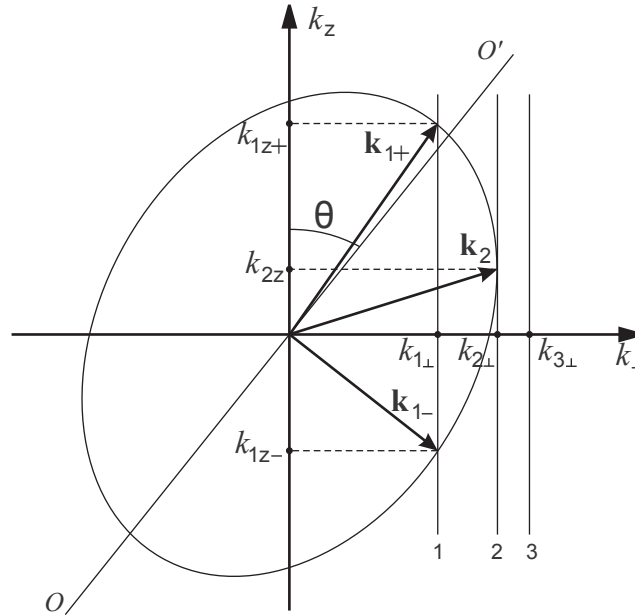


FIG. 1. The cross-section of the extraordinary wave vector surface by the plane formed by the vector  $k_{\perp}$  and the axis  $Oz$  for the certain value  $z$ . Case 1 corresponds to two solutions  $k_{1z+}$  and  $k_{1z-}$  for the  $z$ -component of the wave vector. The wave can propagate in this point of medium. Case 2 conforms to the solution degeneration,  $k_z$  takes only the value  $k_{2z}$ . If this situation takes place then in this point of the LC layer the wave has partial refraction. In case 3 the extraordinary wave vector takes complex value so the wave propagates with exponential damping in this point of the medium

If the ellipsoid cross-section and the straight line  $k_{\perp} = k_{1\perp}$  have two intersection points (i.e.  $D(k_{\perp}, \theta(z), \phi(z)) > 0$  for every value of  $z$ ) then the wave equation has two solutions for  $k_z^{(e)}$  and the extraordinary wave propagates in the whole LC cell volume. If only one value  $z_t$  corresponds to the equation (20) and  $D(k_{\perp}, \theta(z), \phi(z)) > 0$  for other values of  $z$  then the wave partially reflects from the LC layer  $z = z_t$  and partially continues to propagate in the cell. There is a

solution degeneration of  $k_z^{(e)}$  in this point  $z_t$ . On Fig. 1 the solution degeneration of  $k_z^{(e)}$  is observed in the case when the ellipsoid cross-section intersects the straight line  $k_{\perp} = k_{2\perp}$  at a single point. If there is a value  $z_t$  corresponding to  $D(k_{\perp}, \theta(z_t), \phi(z_t)) = 0$  and in this point the function  $D(k_{\perp}, \theta(z), \phi(z))$  changes the sign then the wave partially reflects from the layer  $z = z_t$  and partially continues to propagate with the exponential damping. There is a band gap in the medium. In this case the ellipsoid section and the straight line  $k_{\perp} = k_{3\perp}$  do not intersect. The presence of a few turning points and band gaps in LC cell is possible.

Since the functions  $\theta(z)$  and  $\phi(z)$  determine the ellipsoid orientation the long semi-axis changes with the parameter  $z$ . Also the external field influences the ellipsoid inclination angle.

The turning points  $z_t$  derived from Eq. (20) determine the ray penetration length in the LC layer. The director configuration and the angle of incidence of the extraordinary wave define the solution of the equation for the turning points.

#### 4. Experimental setup

The experimental cells for studying the refraction in LC layers were composed of two glass trapezoidal prisms (1) and (2) with the base size of  $52 \times 24$  mm and the height of 18 mm (Fig. 2). The inclination of the entrance faces to the base was  $68^\circ$ . Required LC layer thickness was set by Teflon spacers. The base surfaces were covered with transparent conducting electrodes. Thin polymer layers were deposited on the top of electrodes by spin coating at the prism-rotation speed of 3000 rpm. A ZhK-1466 nematic mixture (NIOPIK) with the refractive indices for the ordinary and extraordinary rays  $n^{(o)} = 1.511$  and  $n^{(e)} = 1.691$ , respectively, at  $\lambda = 632.8$  nm and temperature  $T = 20^\circ\text{C}$  was used. The mixture had positive dielectric anisotropy  $\varepsilon_a = 12.3$ ,  $\varepsilon_{\perp} = 6.9$  in the frequency range of 1–100 kHz and the elastic constants  $K_{11} = 11$  pN,  $K_{22} = 3.8$  pN and  $K_{33} = 0.99K_{11}$ . Surface planar alignment of the liquid crystal with strong anchoring was created by rubbing the polymer layers with cotton cloth.

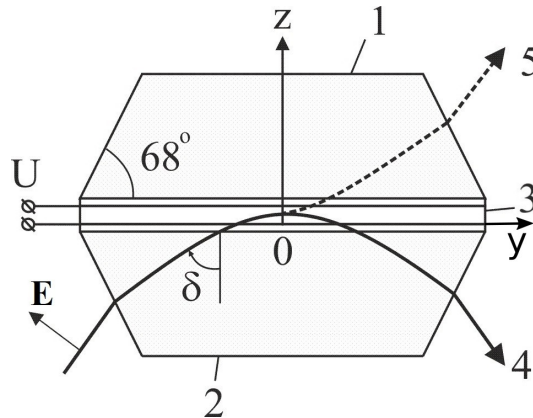


FIG. 2. Liquid crystal cell and trajectories of the extraordinary ray: (1, 2) glass prisms; (3) liquid crystal layer; (4) extraordinary ray reflected inside the liquid crystal layer; and (5) extraordinary ray transmitted through the layer

For the twisted nematic (TN) cell with the twist angle of  $90^\circ$  (cell-1) the positions of director at both surfaces were perpendicular to each other. For the super-twisted nematic (STN) cell with the twist angle of  $180^\circ$  (cell-2) the positions of director at both surfaces were the same and perpendicular to the figure plane. For cells 1 and 2 chiral dopant VICH-3 (Vilnius State University, Lithuania) was solved in nematic liquid crystal ZhK-1466. The refractive index of the prisms for these cells is  $n_{gl} = 1.7002$  for the wavelength  $\lambda = 632.8$  nm.

In the hybrid cell (cell-3) one electrode was coated with a homeotropically aligning layer obtained from a solution of chromium stearyl chloride in isopropyl alcohol while a planar orientation of director was created at the second electrode. The planar director orientation was achieved by rubbing of the polymer layer along the long axis of the prism base. The refractive index of the prisms for cell-3 is  $n_{gl} = 1.7125$  for the wavelength  $\lambda = 632.8$  nm.

The scheme of the experimental setup is shown on Fig. 3. The ray of light from a helium-neon laser with the wavelength  $\lambda = 632.8$  nm and the diameter of 1 mm was incident at the studied LC cell through the half-wave plate  $\lambda/2$ . With the half-wave plate the polarization vector of the incident ray was parallel to the director at the interface glass-LC (for cell-1 and cell-2) and was oriented orthogonally to the figure plane. For the cell-3 the polarization vector was oriented in figure plane as it shown on Fig. 2. Next, the light fell on the photodetector Ph, whose signal was recorded with the digital oscilloscope Osc (ASK-3106) and the computer. As a source of control signal, we used following voltage generator: G3-33 for cell-1, ANR-3122 for cell-2, Agilent 33522A for cell-3. The control voltage from generators was applied to the electrodes of the cells and the oscilloscope. In order to change the incident angle  $\delta$  to the liquid crystal layer, the cell was mounted on the rotary stage with the angle-reading device with the accuracy of 1 minute.

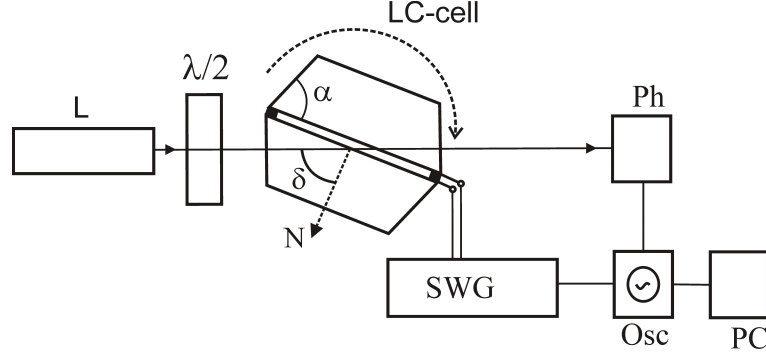


FIG. 3. Experimental setup. (L) laser; ( $\lambda/2$ ) half-wave plate; (Ph) photodetector; (SWG): voltage generator; (Osc) digital oscilloscope; (PC) computer.  $\mathbf{N}$  shows normal to the LC layer.

## 5. Experimental results

### 5.1. Twisted nematic cell (cell-1)

The first LC cell we consider is filled with the chiral LC. Its thickness  $L$  is  $8 \mu\text{m}$ . The natural LC pitch is  $p_0 = 56 \mu\text{m}$ . When the external field is absent director lies within the planes parallel to the plates. On the bottom plate (in our Cartesian coordinates this plate corresponds to the plane  $z = 0$ ) the director has direction along the axis  $Ox$  and on the top plate (plane  $z = L$ ) the director is along the axis  $Oy$ . In that case the twist angle is  $90^\circ$ . Note the pitch formed in this cell ( $p = 4L$ ) and the natural pitch are different. The surface anchoring was strong on each boundary and the director orientation coincides with the easy orientation direction  $\mathbf{n}(z_j) = \mathbf{n}^{0(j)}$ ,  $j = 1, 2$ . Strong boundary conditions give the fixed polar and azimuthal angles:

$$\theta(0) = \theta(L) = \pi/2, \quad \phi(0) = 0, \quad \phi(L) = \pi/2. \quad (21)$$

If the external field is not applied the penetration depth expression can be obtained analytically. The director has form  $\mathbf{n}(z) = (\cos qz, \sin qz, 0)$ , here  $q = \pi/2L$ . In this case, the wave vectors surface, which is ellipsoid, is not oblique i.e. its major semi-axis is perpendicular to  $Oz$ . So the wave vector is parallel to the plates in the turning point. One can find it by means of the Snell's law:

$$z_t = \frac{L}{\pi} \arccos \left( \frac{(\varepsilon_{\perp} + \varepsilon_{\parallel})n_{gl}^2 \sin^2 \delta - 2\varepsilon_{\perp}\varepsilon_{\parallel}}{\varepsilon_a n_{gl}^2 \sin^2 \delta} \right). \quad (22)$$

To obtain the turning points in the presence of external field, we should minimize the total free energy (1). For this purpose, the sample is divided into  $N$  layers along the axis  $Oz$ . We suppose the director is homogeneous in every layer and it is defined by the angles  $\theta$  and  $\phi$ . Then the framework of  $\theta_i = \theta(z_i)$ ,  $\phi_i = \phi(z_i)$ ,  $z_i = iL/N$ ,  $i = 0, 1, \dots, N$  is constructed. Now these values describe the director configuration in the volume. The total free energy can be expressed within  $\theta_i$  and  $\phi_i$ . The direct minimization of the total free energy on these parameters gives the director distribution for different values of the applied voltage. After this procedure the turning point is found by means of Eq. (20). For more convenient calculations here the incident angle is changed while the director configuration is fixed. A set of the penetration depth curves versus the incident angle is plotted for the different applied voltages (Fig. 4).

In experiment with the cell-1 the angles of the ray incidence on the layer varied within the range  $62.8^\circ$  to  $79.7^\circ$ , whereby the depth of the ray penetration into the layer varied from  $7.6$  to  $1.6 \mu\text{m}$ .

We studied the reorientation of the LC director upon switching off the electric field for different angles of light incidence on the LC layer, and hence for the penetration depths  $z_t$ . The magnitude of the control voltage was the  $U = 8 \text{ V}_{rms}$  for all the incident angles. The recovery time of the optical transmission of the cell  $\tau_{off}$  was determined using the oscillograms of the optical response on the electric field (Fig. 5).

The dependence of  $\tau_{off}$  on the depth of the ray penetration into the layer  $z_t$  for  $U = 8 \text{ V}_{rms}$  is shown in Fig. 6.

Figure 6 shows that the time  $\tau_{off}$  of the optical transmission decreases with decreasing of  $z_t$ . Qualitatively, such dependence can be explained by the fact that the recovery rate of the LC initial orientation is proportional to the magnitude of the elastic torque that affects the LC director. This elastic torque has maximum on the boundary of the LC layer, where there is a maximum orientation gradient of the director, when the electric field is off [29].

### 5.2. Super-twisted nematic cell (cell-2)

The second LC cell has thickness  $L = 18 \mu\text{m}$ . When the external field is absent director lies within the planes parallel to the plates. The director has direction along the axis  $Ox$  both on the bottom ( $z = 0$ ) and on the top ( $z = L$ ) plates. In that way the twist angle is  $180^\circ$ . The surface anchoring is strong at each boundary:

$$\theta(0) = \theta(L) = \pi/2, \quad \phi(0) = \phi(L) = 0. \quad (23)$$

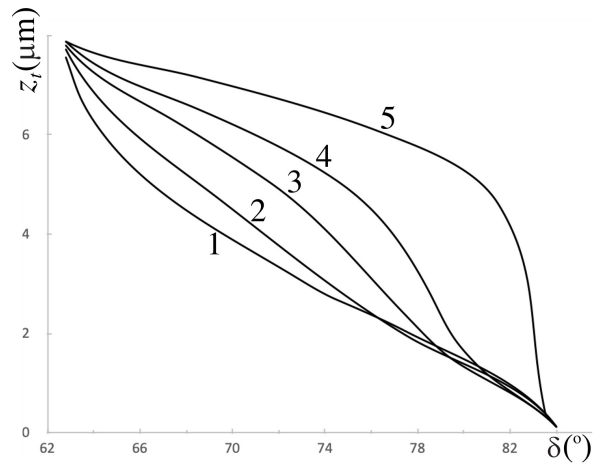


FIG. 4. Depth of the extraordinary ray penetration  $z_t$  into the TN cell as a function of the incident angle  $\delta$ . (1) no external field, (2)  $U = 1.2$  V, (3)  $U = 1.35$  V, (4)  $U = 1.5$  V, (5)  $U = 2.0$  V

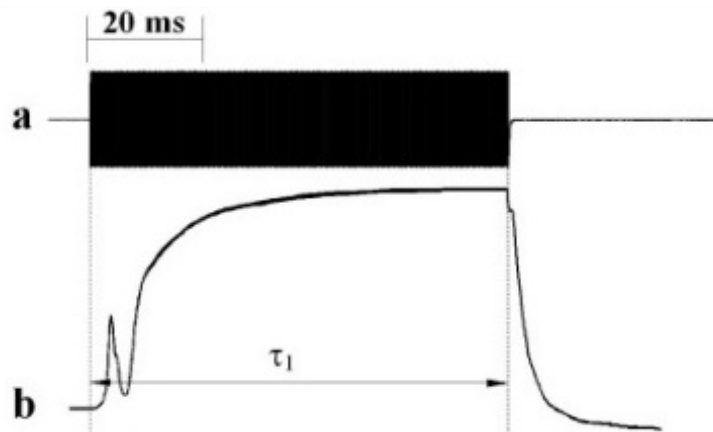


FIG. 5. Optical response of the cell-1 control voltage pulse  $U = 8.0$  V<sub>rms</sub>,  $f = 1000$  Hz. (a) control voltage, (b) optical response:  $\delta = 63.0^\circ$ ,  $z_t = 7.3$   $\mu\text{m}$ .

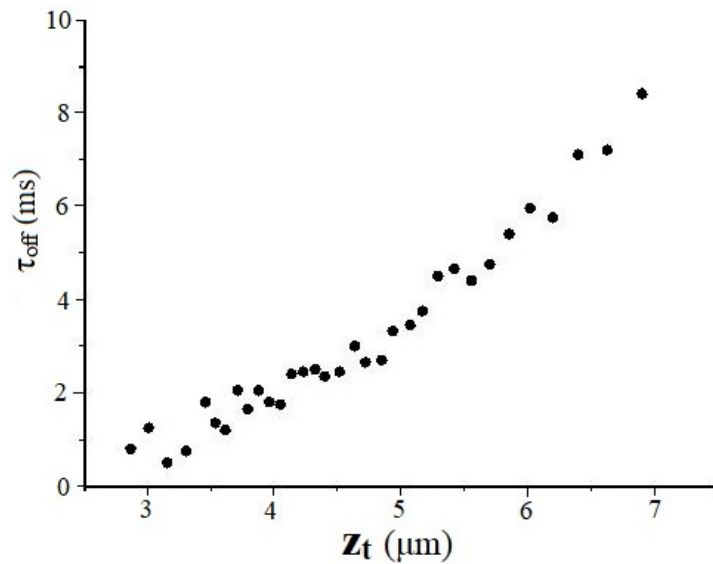


FIG. 6. Turn off time  $\tau_{off}$  for the cell-1 as a function of  $z_t$ .

The expression of the penetration depth for the cell-2 is completely analogous to the expression (22) in the absence of the external field. Here we only need to change  $L$  to  $L/2$ . This is due to the fact that the director distribution in the cell-2 at  $z < L/2$  coincides, to within a helix pitch, with the distribution of the director in the cell-1. Therefore, the penetration depth for the cell-2 in the absence of the external field is similar to the line (1) in Fig. 4 for the cell-1.

In experiment with the cell-2 [28], the angles of the ray incidence on the LC layer varied within the range  $62.8^\circ$  to  $79.7^\circ$ , whereby the depth of the ray penetration into the layer varied from  $8.7$  to  $1.7 \mu\text{m}$ .

When the control electric voltage was applied to the LC layer, the profile of the director was changed. This resulted in the violation of conditions necessary for the turn of the extraordinary ray in the layer and led to the propagation of light through the cell (see Fig. 2). The local dynamics of the director reorientation at various  $z_t$  was studied by the acquisition of the cell's optical responses. The control voltage was varied within  $3.0$  to  $6.0 V_{rms}$ . For this range of voltages the cell-2 transmits light and there is no turning points. Here and below in this section we consider the penetration depths  $z_t$  obtained for the cell-2 in the absence of the external field. Oscillograms of the optical responses of the cell-2 as the functions of the depth of the ray penetration into the LC layer at the applied voltage  $U = 5.0 V_{rms}$  are shown in Fig. 7 (for the electric field switched on) and Fig. 8 (for the electric field switched off).

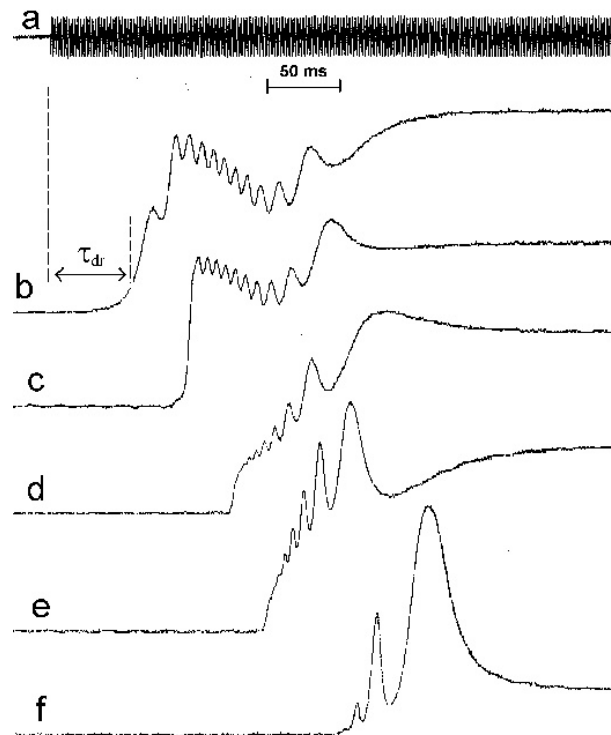


FIG. 7. Optical responses of the cell-2 after the electric field was switched on,  $U = 5.0 V_{rms}$ ,  $f = 1000$  Hz. a — control voltage pulse, b, c, d, e, f — optical responses for  $z_t = 8.7, 7.4, 5.1, 3.0, 1.7 \mu\text{m}$ .

It should be noted that the intensity variation curves for the field switched on and off undergo clearly exhibited oscillations. The intensity oscillations can be explained by the fact that the extraordinary wave passing through the cell partially reflects from the glass-LC interfaces, the reflected waves interfere, and the phase difference between them changes during reorientation of the director. Moreover, the monotonic behavior of the phase difference in the interfering waves breaks down (arrow in Fig. 8). This can be explained by the arising LC backflow [29]. The delay time  $\tau_{dr}$  of the effect optical signal rise can be readily determined from the oscillograms (Fig. 7). These times for several values of the control voltage are shown in Fig. 9.

It can be seen from Fig. 9 that at the same voltage the delay time  $\tau_{dr}$  decreases as the depth of the ray penetration  $z_t$  into the layer increases. In order to the light transmittance through the cell-2 takes place when the external field is applied to the cell, it is necessary to reorient the director in the layer  $[z_t, L - z_t]$ . This layer forms the band gap for the cell-2 in the absence of the external field. Note that director reorientation near the cell boundary is difficult due to the strong anchoring with the orienting surface [29]. Therefore, the delay time  $\tau_{dr}$  for small  $z_t$  will be longer than in the case when  $z_t$  is close to  $L/2$ . This effect is also related to the fact that, at small  $z_t$  it is necessary to reorient a sufficiently large volume inside the cell, while at  $z_t$  close to  $L/2$ , reorientation is required inside the thin layer at the center of the cell.

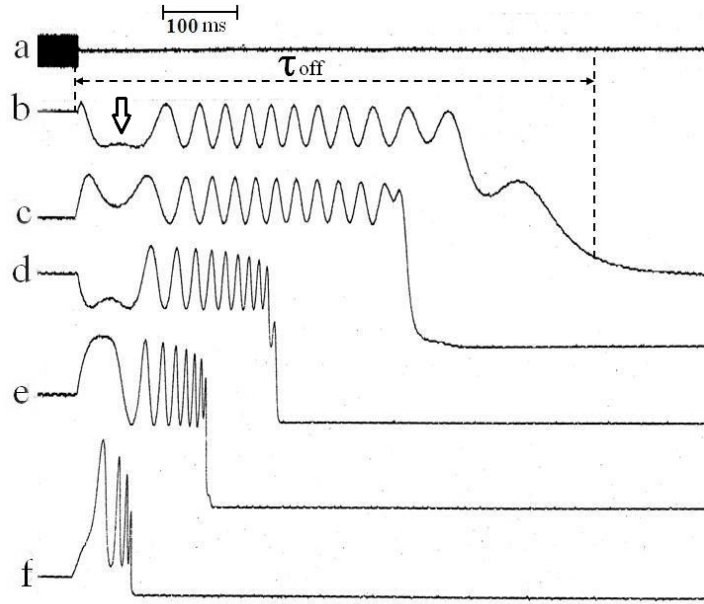


FIG. 8. Optical responses of the cell-2 after the electric field was switched off,  $U = 5.0 \text{ V}_{rms}$ ,  $f = 1000 \text{ Hz}$ . a — control voltage pulse, b, c, d, e, f — optical responses for  $z_t = 8.7, 7.4, 5.1, 3.0, 1.7 \mu\text{m}$ .

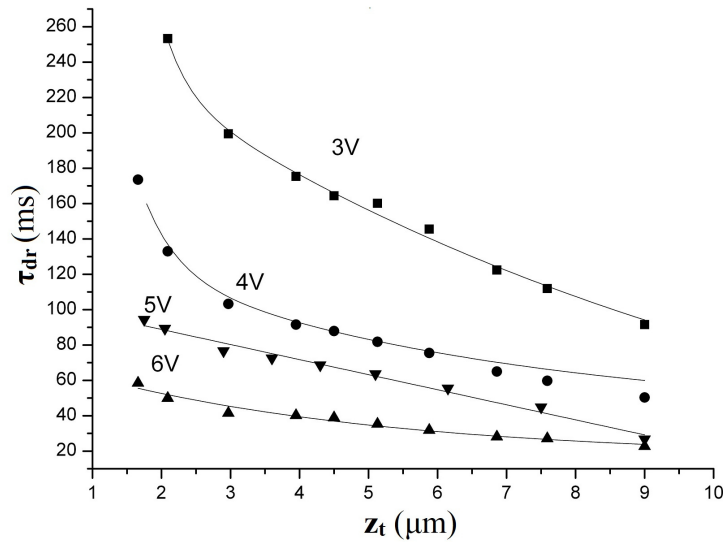


FIG. 9. Delay time of the signal rise,  $\tau_{dr}$  as a function of the penetration depth  $z_t$  for different control voltages  $U = 3.0 \text{ V}_{rms}$ ;  $U = 4.0 \text{ V}_{rms}$ ;  $U = 5.0 \text{ V}_{rms}$ ;  $U = 6.0 \text{ V}_{rms}$ . Here the penetration depths  $z_t$  were obtained for the cell-2 in the absence of the external field.

The turn off time  $\tau_{off}$  was determined from the optical responses obtained for the various depths of the ray penetration into the layer (Fig. 9). The time  $\tau_{off}$  can be interpreted as a recovery time of the initial configuration of the director. Figure 10 shows  $\tau_{off}$  as a function of the penetration depth  $z_t$ .

It can be seen from Fig. 10 that  $\tau_{off}$  decreases as  $z_t$  decreases. This dependence can be qualitatively explained by the fact that the rate of the recovery of the initial configuration is proportional to the elastic torque acting on the director [30], which is larger near the surface.

### 5.3. Hybrid liquid crystal cell (cell-3)

This LC cell is filled in with the nematic LC. Its thickness is  $L = 14 \mu\text{m}$ . On the bottom plate the director is aligned along the axis  $Oz$  and on the top plate the director is along the axis  $Oy$ . The director lies within the planes parallel to the  $yOz$  plane and the azimuthal angle  $\phi$  is fixed even in the external field presence. As before, the surface anchoring was enough strong on each boundary. So the angles on the bottom and top plates take the form

$$\theta(0) = 0, \theta(L) = \pi/2, \phi(0) = \phi(L) = \pi/2 \quad (24)$$

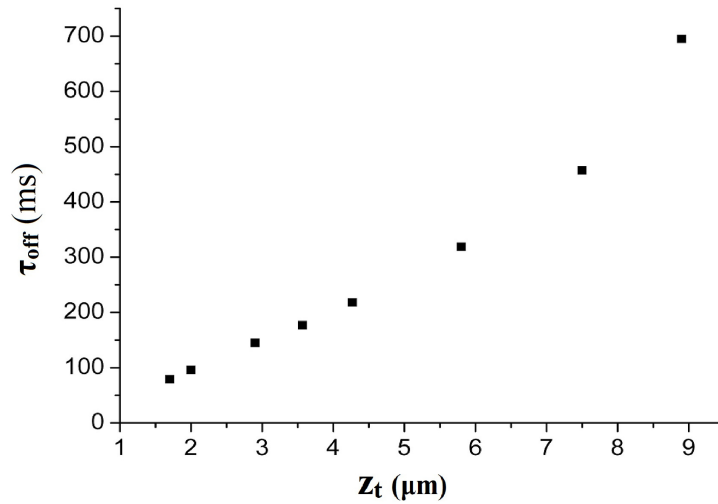


FIG. 10. Turn off time  $\tau_{off}$  as a function of the penetration depth  $z_t$  for the various incident angles  $\delta$ ,  $U = 5.0 \text{ V}_{rms}$

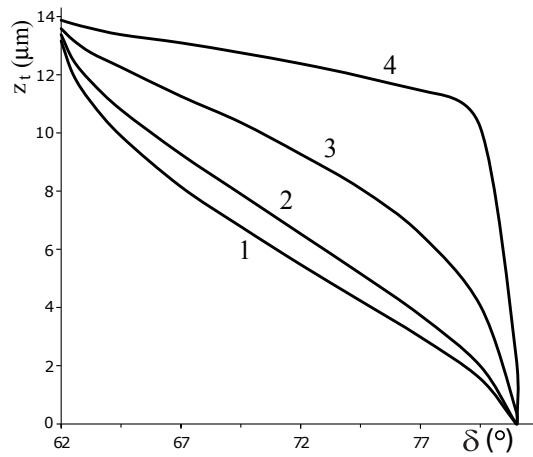


FIG. 11. Penetration depth  $z_t$  of the extraordinary ray into hybrid LC cell versus the incident angle  $\delta$ . (1) no external field, (2)  $U = 0.5 \text{ V}$ , (3)  $U = 1.0 \text{ V}$ , (4)  $U = 2.5 \text{ V}$

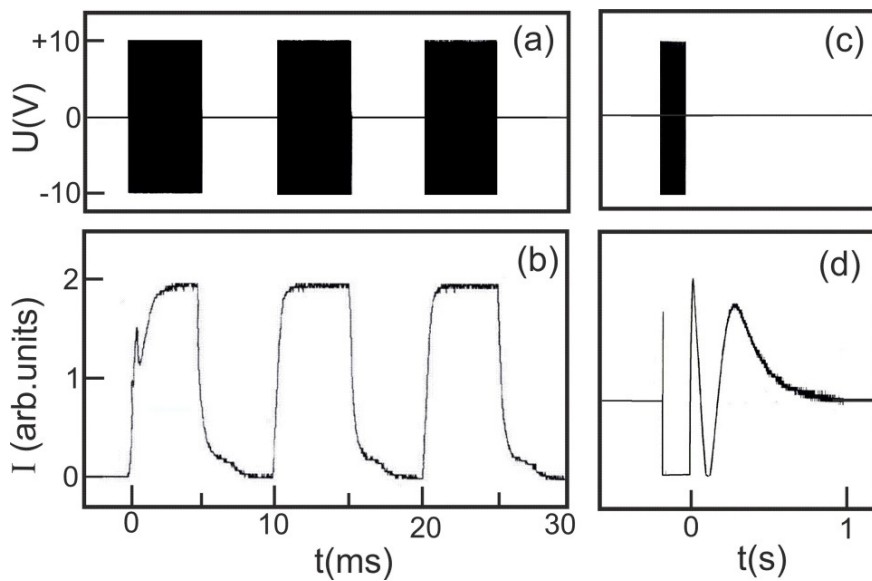


FIG. 12. Optical responses of the hybrid LC cell. (a) control voltage pulses (schematically) and (b) optical response for the incident angle  $68.0^\circ$  ( $z_t = 7.0 \mu\text{m}$ ); (c) control pulse and (d) optical response for the normal incidence of light

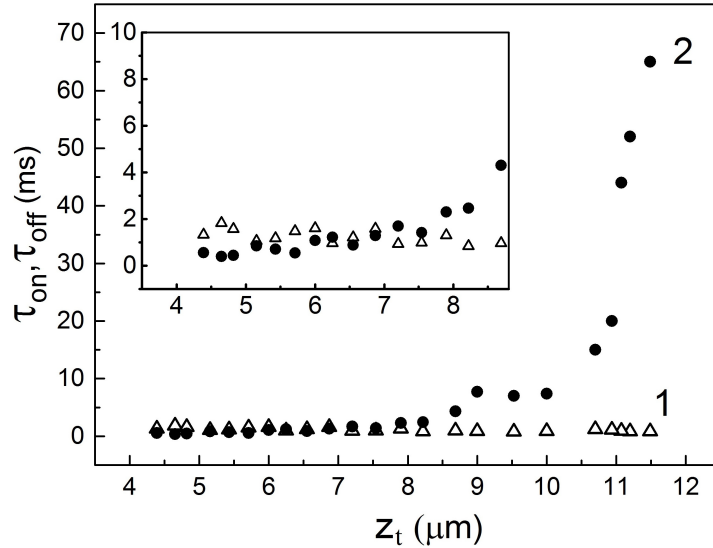


FIG. 13. (1) turn on  $\tau_{on}$  and (2) turn off  $\tau_{off}$  times for the hybrid cell-3 versus the penetration depth of the extraordinary ray into LC layer. The inset shows the same dependencies in the range of  $z_t = 4.3$ – $8.8 \mu\text{m}$

and the director is expressed as  $\mathbf{n} = (0, \sin \theta(z), \cos \theta(z))$ . In this case, when the external field is not applied, one also can derive the analytical form for the turning points:

$$z_t = \frac{L}{\pi} \arccos \frac{2n_{gl}^2 \sin^2 \delta - (\varepsilon_{\perp} + \varepsilon_{\parallel})}{\varepsilon_a}. \quad (25)$$

This equation is obtained subject to equality  $K_{11} = K_{33}$ .

For the hybrid cell-3 the penetration depth of the extraordinary ray into the LC layer versus the incident angle is shown in Fig. 11. The effect of the electric field on refraction was studied for the incident angle of light in the range of  $62.7^\circ$  to  $73.8^\circ$ .

Oscillograms of control bipolar electric pulses (meander) with a duration of 5 ms, a filling frequency of 100 kHz, and a repetition frequency of 100 Hz at the amplitude  $U = 10 \text{ V}_{rms}$  are represented in Fig. 12(a). The optical responses of the cell under study for the incident angle  $68.0^\circ$  ( $z_t = 7.0 \mu\text{m}$ ) are shown in Fig. 12(b).

The results show that the turn off time of the optical response of the cell-3 for the inclined incidence of the ray is three orders of magnitude smaller than the relaxation time of the optical response in the case of the normal incidence of the ray. It is seen in Fig. 12(d) that the total recovery time of the initial configuration of the director in the cell-3 after the termination of the electric field is about 1 s. The times  $\tau_{on}$  and  $\tau_{off}$  for the optical response were obtained for the penetration depths into LC layer from  $4.3$  to  $11.5 \mu\text{m}$  (Fig. 13).

It follows from Fig. 13 that values  $\tau_{on}$  vary in the range of 1–2 ms at the increase in the penetration depth from  $4.3$  to  $11.5 \mu\text{m}$ . In the range  $z_t = 4.3$ – $8.0 \mu\text{m}$ , the time  $\tau_{off}$  also varies from 1 to 2 ms. Apparently, small  $\tau_{off}$  values for electrically controlled refraction are related to the fast recovery of the director orientation in thin near-surface LC layers.

## 6. Conclusion

The experimental study with cell-1 and cell-2 showed that the longest recovery time corresponds to the maximum depth of the extraordinary ray penetration into the LC layer, regardless of the boundary conditions on the surfaces of the LC layer and the ray turning point in the middle of the layer (the twist angle is  $180^\circ$ ), or at the far boundary of the layer (the twist angle is  $90^\circ$ ). The revealed electro-optical properties of the hybrid cell operating on the refraction effect showed that minimal values of  $\tau_{on}$  and  $\tau_{off}$  were observed at large angles of ray incidence. The discovered electro-optical properties of a hybrid cell operating on the refraction effect can be used, for example, in promising technologies for liquid crystal displays and optical switches for planar waveguides.

The method presented in this paper for describing the optical properties of LCs can be applied to a wide class of cells. The only significant limitation imposed on the system is the condition for the applicability of geometrical optics (the WKB method).

The combined theoretical and experimental research of the light refraction in the liquid crystal cells with continuously changing orientation of director and the effect of electric field on the refraction will allow studying the process of local director reorientation at different distances from the interfaces between liquid crystals and glass.

## References

- [1] Wu Shin-Tson, Yang Deng-Ke. *Fundamentals of liquid crystal devices*. John Wiley & Sons, Chichester., 2006, 394 p.
- [2] Cai W., Shalae V. *Optical metamaterials*. Springer, New York, 2010, 200 p.
- [3] Joannopoulos J., Meade R., Winn J., Johnson S. *Photonic crystals*. Princeton University Press, Princeton, 2008, 286 p.
- [4] Leslie F.M. Distortion of twisted orientation patterns in liquid crystals by magnetic fields. *Mol. Cryst. Liq. Cryst.*, 1970, **12**(1), P. 57–72.
- [5] Berreman D.W., Heffner W.R. New bistable liquid-crystal twist cell. *J. Appl. Phys.*, 1981, **52**, P. 3032–3039.
- [6] Thurston R.N., Berreman D.W. Equilibrium and stability of liquid-crystal configurations in an electric field. *J. Appl. Phys.*, 1981, **52**(1), P. 508–509.
- [7] Hiring R., Funk W., Trebin H.R., Shmidt M., Schmiedel H. Threshold behavior and electro-optical properties of twisted nematic layer with weak anchoring in the tilt and twist angle. *J. Appl. Phys.*, 1991, **70**(8), P. 4211–4216.
- [8] Hong Qi, Wu T.X., Wu Shin-Tson. Optical wave propagation in a cholesteric liquid crystal using the finite element method. *Liq. Cryst.*, 2003, **30**(3), P. 367–375.
- [9] Berreman D.W., Scheffer T.J. Order versus temperature in cholesteric liquid crystals from reflectance spectra. *Phys.Rev. A*, 1972, **5**(3), P. 1397–1403.
- [10] Berreman D.W. Optics in stratified and anisotropic media:  $4 \times 4$ -matrix formulation. *J. Opt. Soc. Am.*, 1972, **62**, P. 502–510.
- [11] Berreman D.W. Stratified media: optics in smoothly varying anisotropic planar structures: application to liquid-crystal twist cells. *J. Opt. Soc. Am.*, 1973, **63**, P. 1374–1380.
- [12] Palto S.P. An algorithm for solving the optical problem for stratified anisotropic media. *JETP*, 2001, **92**, P. 552–560.
- [13] Gevorgyan A.H. Photonic band gaps from a stack of right- and left-hand chiral photonic crystal layers. *Phys. Rev. E*, 2012, **85**, P. 021704.
- [14] Belyakov V.A., Dmitrienko V.E. Theory of the optical properties of cholesteric liquid crystals. *Sov. Phys. Solid State*, 1974, **15**(9), P. 1811–1815.
- [15] Dmitrienko V.E., Belyakov V.A. Higher orders of the selective reflection of light by cholesteric liquid crystals. *Sov. Phys. Solid State*, 1974, **15**(12), P. 2213–2216.
- [16] Lakhtakia A., Weiglhofer W.S. Simple and exact analytic solution for oblique propagation in a cholesteric liquid crystal. *Microwave Opt. Technol.*, 1996, **12**, P. 245–248.
- [17] Val'kov A.Yu., Aksenova E.V., Romanov V.P. First-order and continuous Fréedericksz transitions in cholesteric liquid crystals. *Phys. Rev. E*, 2013, **87**, P. 022508.
- [18] Rokushima K., Yamakita J. Analysis of anisotropic dielectric gratings. *J. Opt. Soc. Am.*, 1983, **73**(7), P. 901–908.
- [19] Wang F., Lakhtakia A. Response of slanted chiral sculptured thin films to dipolar sources. *Opt. Commun.*, 2004, **235**, P. 133–151.
- [20] Avendano-Alejo M. Analysis of the refraction of the extraordinary ray in a plane-parallel uniaxial plate with an arbitrary orientation of the optical axis. *Optics Express*, 2005, **13**, P. 2549–2555.
- [21] Panasyuk G., Kelly J., Gartland E.C., Allender D.W. Geometrical optics approach in liquid crystal films with three-dimensional director variations. *Phys.Rev. E*, 2003, **67**, P. 041702.
- [22] Aksenova E.V., Karetnikov A.A., Kovshik A.P., Romanov V.P., Val'kov A.Yu. Return back of the extraordinary beam for oblique incidence in helical liquid crystals with large pitch. *Europhys. Lett.*, 2005, **69**(1), P. 68–74.
- [23] Tenishchev S.S., Kiselev A.D., Ivanov A.V., Uzdin V.M. Multiple minimum-energy paths and scenarios of unwinding transitions in chiral nematic liquid crystals. *Phys. Rev. E*, 2019, **100**, P. 062704.
- [24] Tenishchev S.S., Tambovtcev I.M., Kiselev A.D., Uzdin V.M. Hysteresis and Fréedericksz thresholds for twisted states in chiral nematic liquid crystals: Minimum-energy path approach. *Journal of Molecular Liquids*, 2021, **325**, P. 115242.
- [25] de Gennes P.-G., Prost J. *The Physics of liquid crystals*, University Press, Oxford, 1993, 616 p.
- [26] Stewart I.W. *The static and dynamic continuum theory of liquid crystals: a mathematical introduction*, *Liquid crystals book series*. Taylor & Francis, London, 2004, 360 p.
- [27] Aksenova E.V., Karetnikov A.A., Kovshik A.P., Kryukov E.V., Romanov V.P. Propagation of light through a forbidden zone in chiral media. *J. Opt. Soc. Amer. A*, 2008, **25**(3), P. 600–608.
- [28] Karetnikov A.A., Karetnikov N.A., Kovshik A.P., Ryumtsev E.I., Aksenova E.V., Kryukov E.V., Romanov V.P. Local dynamics of director reorientation under electric field in helical LC structure. *Mol. Cryst. Liq. Cryst.*, 2012, **561**(1), P. 97–106.
- [29] Blinov L.M. *Structure and properties of liquid crystals*. Springer, Dordrecht, 2011, 439 p.
- [30] Karetnikov N.A., Kovshik A.P., Karetnikov A.A., Ryumtsev E.I., Aksenova E.V., Svanidze A.V. Fast electro-optical response of a cell with a homeoplanar layer of a nematic liquid crystal. *JETP Lett.*, 2017, **106**(5), P. 313–316.

---

*Submitted 28 December 2022; revised 25 January 2023; accepted 27 January 2023*

*Information about the authors:*

*Elena V. Aksenova* – Saint Petersburg State University, Universitetskaya, 7/9, St. Petersburg, 199034, Russia;  
ORCID 0000-0002-4324-1491; e.aksenova@spbu.ru, aksev@mail.ru

*Aleksandr A. Karetnikov* – Saint Petersburg State University, Universitetskaya, 7/9, St. Petersburg, 199034, Russia;  
ORCID 0000-0002-4267-8122; akaret@mail.ru

*Nikita A. Karetnikov* – ITMO University, Kronverksky Pr. 49, bldg. A, St. Petersburg, 197101, Russia;  
ORCID 0000-0002-3262-2790; nkaret@mail.ru

*Aleksandr P. Kovshik* – Saint Petersburg State University, Universitetskaya, 7/9, St. Petersburg, 199034, Russia;  
ORCID 0000-0003-1326-2184; Sashakovshik@yandex.ru

*Anastasiya V. Svanidze* – Saint Petersburg State University, Universitetskaya, 7/9, St. Petersburg, 199034, Russia; Ohio State University, W Lane Ave, 281, Columbus, Ohio, 43210, USA; ORCID 0000-0002-8278-3429; avsvanidze@gmail.com

*Sergey V. Ul'yanov* – Saint Petersburg State University, Universitetskaya, 7/9, St. Petersburg, 199034, Russia;  
ORCID 0000-0002-6082-3733; s.ulyanov@spbu.ru

*Conflict of interest:* the authors declare no conflict of interest.

## Electrical properties of “metal-carbon film” contact

Rostyslav V. Shalayev<sup>a</sup>, Anatoliy I. Izotov<sup>b</sup>, Vladimir V. Syrotkin<sup>c</sup>

Galkin Donetsk Institute for Physics and Engineering, Donetsk, Russia

<sup>a</sup>sharos@donfti.ru, <sup>b</sup>izotov.anatoli@gmail.com, <sup>c</sup>vladir.52@mail.ru

Corresponding author: Rostyslav V. Shalayev, sharos@donfti.ru

PACS 81.15.Gh; 84.37.+q; 85.30.Hi

**ABSTRACT** Magnetron sputtering was used to obtain carbon films on of metal substrates of two types: titanium and tool chromium steel. The temperature dependence of the resistance of the films, which has a semiconductor character, has been studied. The current-voltage characteristics of the metal-carbon film contact were determined, which indicate the presence of the Schottky barrier junction.

**KEYWORDS** carbon film, magnetron sputtering, metal-semiconductor contact, Schottky barrier.

**FOR CITATION** Shalayev R.V., Izotov A.I., Syrotkin V.V. Electrical properties of “metal-carbon film” contact. *Nanosystems: Phys. Chem. Math.*, 2023, **14** (1), 86–88.

### 1. Introduction

The metal–semiconductor contact (the Schottky barrier) has attracted the attention of researchers for a long time. This is due not only to its wide and various applications, but also to the abundance of requirements for it, due to the specific conditions of use and the expanding range of semiconductor materials involved in practice. It is customary to associate the beginning of research in the field of semiconductor electronics at the end of the 19th century with the metal-semiconductor contact, and since the beginning of the 60s of the twentieth century — with a new (modern) stage in the development of microwave electronics. The foundations of the physics of contacts were laid approximately in the late 1930s and early 1940s, and by the early 1980s, thanks to the work of a number of researchers, quite complete physical ideas about the properties of contacts were formed, which were reflected in a number of monographs (see, e.g. [1–4]).

As for the involvement of new semiconductor materials in practice, carbon materials seem to be quite promising in this respect today [5–9]. It should be noted that carbon-based materials have recently been increasingly used in micro- and nanoelectronics. The traditional silicon platform does not meet many modern requirements, and more and more often researchers name carbon as its potential replacement (at least in certain niches). Due to the huge variety of allotropic forms, this material has considerable potential in many areas, but for electronics it is of particular interest.

It has long been known that its electrical properties can vary over a very wide range. Separately, it should be said about graphene, the creation of which opened up additional possibilities. This material is characterized by high carrier mobility (under normal conditions, 10 times higher than in silicon) [10, 11], ambipolar field effect, ballistic transport under normal conditions, and many other interesting properties. Prototypes of integrated circuits based on graphene have already been created, which operate at frequencies up to 10 GHz at room temperature and have an area of less than 1 mm<sup>2</sup>. In addition, we should not forget that, in addition to graphene, carbon can also form ideal one-dimensional structures. Many researchers suggest that, in combination, all of the above will make it possible in the future to realize the idea of all-carbon high-speed nanoelectronics [12].

Keeping in mind all of the above, the creation and study of the “metal-carbon film” contact seems to be a rather urgent task. In this paper, we considered some electrical properties of such a contact.

### 2. Experimental technique

Samples for the research were obtained by magnetron sputtering of graphite (purity 99.9% C) in an argon atmosphere. Carbon films were deposited on dielectric and metal substrates (titanium and tool chromium steel). The plasma was created using a planar DC magnetron with a flat cathode and an annular anode. The conditions for deposition of samples on all types of substrates were the same: the gas pressure in the chamber was 150 mTorr, the film growth time was 40 min, the substrate temperature was 350 °C, and the magnetron current was 40 mA.

The electrical properties of the obtained samples were studied in a heat chamber in the range from 20 °C to 150 °C. According to [6], the conductivity perpendicular to the film growth direction is called transverse, and along the growth direction, longitudinal. The transverse conductivity was measured by the two-probe method in films on a glass substrate (to eliminate the influence of a well-conductive metal substrate) in the voltage range from –10 V to +10 V. Phosphor bronze contacts, contact area 0.3 mm<sup>2</sup>, distance between contacts ~1 mm. The longitudinal conductivity was measured in films deposited on metal substrates. The measurements were carried out in the following structure “substrate–carbon

film–measuring contact”. A pin brass contact with an R rounding of 0.2 mm<sup>2</sup> was used. The temperature dependences of the resistance of carbon films and the current-voltage characteristics of the metal-carbon contact were obtained. The band gap of the obtained samples was estimated graphically from the temperature dependences.

### 3. Main results and discussion

The films grown show predominantly graphite-like properties: the color varies from dark gray to almost black, and the adhesion is relatively weak. The temperature dependence of the film resistance  $R$  (measurements were made perpendicular to the film growth direction) has a classical semiconductor character: a decrease in resistance with increasing temperature — ( $\frac{dR}{dT} < 0$ ). Thus, carbon films with semiconductor properties were obtained in the work as we can see.

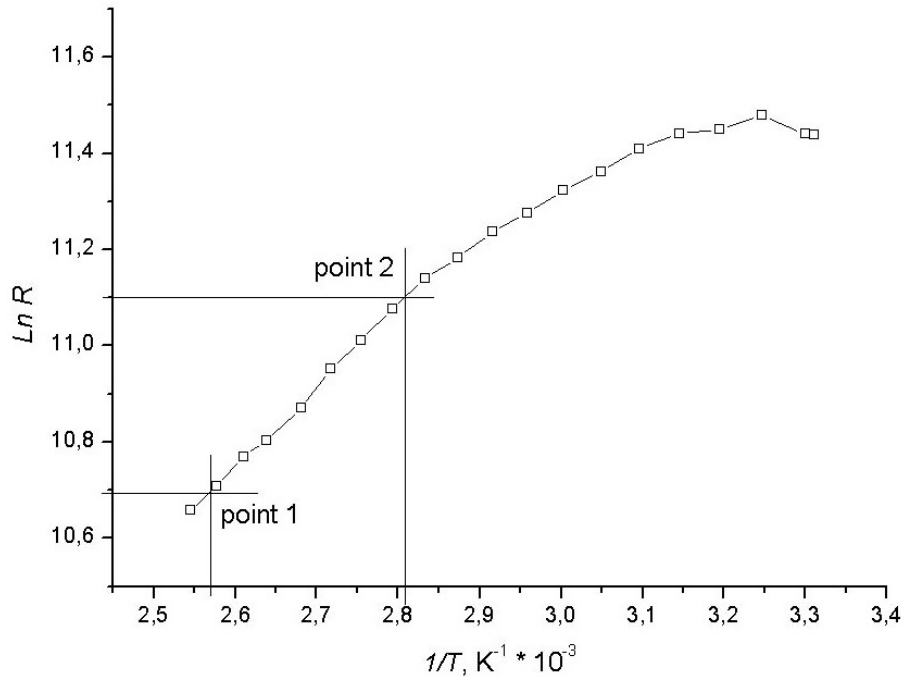


FIG. 1. Dependence  $\ln R(1/T)$  for the film on a dielectric substrate.  $R$  is measured in Ohm

Now consider this dependence in the form  $\ln R$  vs  $(1/T)$  curve shown in Fig. 1. It makes it possible to estimate the band gap (activation energy) of the resulting carbon film from the slope of the dependence graph. We chose the high-temperature section of the graph, where the conductivity of a classical semiconductor is predominantly determined by its own conductivity. Calculations carried out according to the formula:

$$\Delta E = 2k \frac{\ln R_2 - \ln R_1}{\frac{1}{T_2} - \frac{1}{T_1}},$$

where  $k$  is the Boltzmann constant and values from the abscissa/ordinate axis at point 1 and point 2 on the graph, showed that the activation energy  $\Delta E$  of the film is approximately 0.29 eV (assuming that we have an undoped or lightly doped semiconductor).

Thus, when such films are deposited on metal substrates, we obtain a “metal-semiconductor” contact, which is the subject of study in this work. Let’s consider some features of these contacts.

The current-voltage characteristics of the obtained contacts, shown in Fig. 2, are nonlinear and asymmetric, therefore, we can talk about obtaining some kind of rectifying “metal-semiconductor” contact junction (with a potential Schottky barrier). If we compare the current-voltage characteristics of contacts based on titanium (Fig. 2a) and based on steel (Fig. 2b), it can be noted that the former is characterized by a transition to the open state at lower applied voltages than the latter. Presumably, this may be due to different work functions of the metal substrate.

We have mentioned above that, at present, there are a considerable number of diodes based on the Schottky barrier, and the requirements for them vary greatly and depend on the application. The semiconductor materials most commonly used in modern diodes are silicon, silicon carbide, and gallium arsenide. Each of them has its own advantages and disadvantages. If we talk about the material used in this work, then the current-voltage characteristic demonstrates at least one of its obvious advantages compared to most other materials – a contact based on it goes into an open state at very low voltage values (tens of microvolts). This property may be of interest in many applied areas, which allows us to speak about the prospects for further research in this direction.

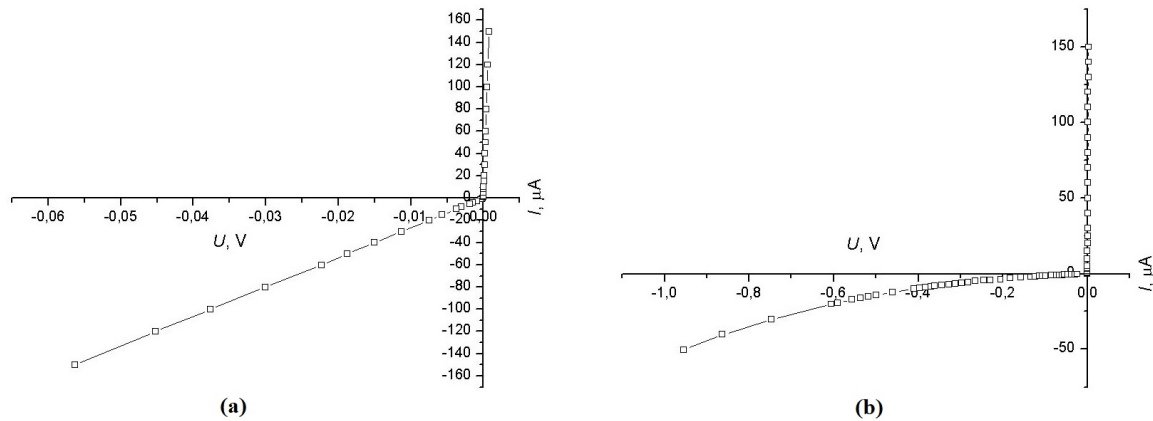


FIG. 2. Current-voltage characteristics: a) “titanium-graphite-like film” contact; b) “chromium steel-graphite-like film” contact

#### 4. Conclusion

Preliminary studies of the obtained samples allow us to suggest that graphite-like carbon films can be successfully used in rectifying metal-semiconductor junctions with the Schottky barrier. According to the current-voltage characteristics, the “metal-carbon film” contact goes into an open state at very low voltage values, thus, we can say that the proposed semiconductor material in some areas will have certain advantages over the traditional materials.

#### References

- [1] Henish H.K. *Semiconductor rectifying contacts*. Oxford, Oxford University Press, 1957, 372 p.
- [2] Striha V.I. *Theoretical foundations of the operation of a metal–semiconductor contact*. Kiev, Naukova Dumka, 1974, 264 p.
- [3] Roderic E.H. *Metal-semiconductor Contacts*. Moscow, Radio and Communications, 1982, 210 p.
- [4] Pikus G.E. *Contact Phenomena. Semiconductors in Science and Technology*. Moscow, Leningrad, Publishing House of the USSR AS, 1956, v.1, 148 p.
- [5] Vinogradov A.Ya., Grudinkin S.A., Besedina N.A., Koniakhin S.V., Rabchinskii M.K., Eidelman E.D., Golubev V.G. Structure and properties of thin graphite-like films produced by magnetron-assisted sputtering. *Semiconductors*, 2018, **52**(7), P. 914–920.
- [6] Hvostov V.V., Streletskiy O.A., Yakunin V.V., et al. Properties of carbon films with high conductivity anisotropy. *Vestn. Mosk. Univ. Ser. 3. Phys. Astron.*, 2012, **1**, P. 78–84.
- [7] Kalinin Yu.E., Kashirin M.A., Makagonov V.A., et al. Properties of amorphous carbon thin films grown by ion beam sputtering. *Technical Physics*, 2017, **62**, P. 1724–1730.
- [8] Berezin V.M., Shepvalov I.I., Lukashev V.S. Transparency factors and electrical resistance of graphite-like films on glass. *Chelyabinsk Physical and Mathematical Journal*, 2017, **2**(4), P. 483–488.
- [9] Demidov A.A., Rybalka S.B. Modern and promising semiconductor materials for microelectronics in the next decade (2020-2030). *Prikladnaya matematika & Fizika*, 2021, **53**(1), P. 53–72.
- [10] Schwierz F. Graphene transistors. *Nature Nanotechnology*, 2010, **5**, P. 487–496.
- [11] Breusing M., Ropers C., Elsaesser T. Ultrafast Carrier Dynamics in Graphite. *Phys.Rev.Lett.*, 2009, **102**(8), P. 086809.
- [12] Gubin S.P. All-carbon nanoelectronics. *Radioelectronics. Nanosystems. Information Technologies*, 2011, **3**(1), P. 47–54.

Submitted 24 January 2023; revised 02 February 2023; accepted 05 February 2023

*Information about the authors:*

Rostyslav V. Shalayev – Galkin Donetsk Institute for Physics and Engineering, R. Luxembourg str. 72, 283050, Donetsk, Russia; ORCID 0000-0003-1258-2434; sharos@donfti.ru

Anatoliy I. Izotov – Galkin Donetsk Institute for Physics and Engineering, R. Luxembourg str. 72, 283050, Donetsk, Russia; izotov.anatoli@gmail.com

Vladimir V. Syrotkin – Galkin Donetsk Institute for Physics and Engineering, R. Luxembourg str. 72, 283050, Donetsk, Russia; vladir.52@mail.ru

*Conflict of interest:* the authors declare no conflict of interest.

## Bioavailability of nanoemulsions modified with curcumin and cerium dioxide nanoparticles

Anastasiya D. Shirokikh<sup>1,a</sup>, Viktoriia A. Anikina<sup>2,b</sup>, Elizaveta A. Zamyatina<sup>2,c</sup>,  
Ekaterina V. Mishchenko<sup>1,d</sup>, Marina Y. Koroleva<sup>1,e</sup>, Vladimir K. Ivanov<sup>3,f</sup>, Nelli R. Popova<sup>2,g</sup>

<sup>1</sup>Mendeleev University of Chemical Technology, Moscow, Russia

<sup>2</sup>Institute of Theoretical and Experimental Biophysics of the Russian Academy of Sciences, Russia

<sup>3</sup>Kurnakov Institute of General and Inorganic Chemistry of the Russian Academy of Sciences, Moscow, Russia

<sup>a</sup>adshirokikh@gmail.com, <sup>b</sup>viktoriya.anikina@list.ru, <sup>c</sup>sonyoru162@gmail.com,

<sup>d</sup>mishchenkoek@list.ru, <sup>e</sup>m.yu.kor@gmail.com, <sup>f</sup>van@igic.ras.ru, <sup>g</sup>nellipopovaran@gmail.com

Corresponding author: Nelli R. Popova, nellipopovaran@gmail.com

**ABSTRACT** In this work, the physicochemical properties and biological activity of nanoemulsions prepared from paraffin oil and stabilized by nonionic surfactants as carriers of curcumin and cerium dioxide nanoparticles were studied. An analysis of the results showed that curcumin was incorporated into the oil droplets while cerium dioxide nanoparticles were adsorbed on the surface of oil droplets. The nanoemulsion droplet size did not exceed 100 nm. The absence of toxicity to mouse embryonic fibroblasts *in vitro* and after a single intraperitoneal injection to mice *in vivo* makes the nanoemulsions promising drug carriers for advanced biomedical applications.

**KEYWORDS** nanoemulsions, drug delivery, curcumin, cerium dioxide nanoparticles.

**ACKNOWLEDGEMENTS** This research has been supported by the Russian Science Foundation (project 22-63-00082).

**FOR CITATION** Shirokikh A.D., Anikina V.A., Zamyatina E.A., Mishchenko E.V., Koroleva M.Y., Ivanov V.K., Popova N.R. Bioavailability of nanoemulsions modified with curcumin and cerium dioxide nanoparticles. *Nanosystems: Phys. Chem. Math.*, 2023, **14** (1), 89–97.

### 1. Introduction

Increasing the bioavailability of a number of bioactive compounds of organic and inorganic nature is an urgent task of modern biomedicine. It is well known that some low molecular weight compounds promising for biomedical applications have poor water solubility, which potentially limits their use. Among these compounds, curcumin has a wide range of pharmacological actions, showing anti-inflammatory and antioxidant activity, antimicrobial, wound healing and anticancer properties [1, 2]. Curcumin is a poorly soluble hydrophobic polyphenolic compound of natural origin, having a limited bioavailability. In addition, it has been shown that, under certain conditions, curcumin exhibits cytotoxicity towards normal cells, inducing oxidative stress [3]. Interestingly, when curcumin is combined with cerium oxide nanoparticles (CNP), the latter leveled the toxicity of curcumin against normal cells, due to the inactivation of reactive oxygen species, while retained its action on cancer cells [4, 5]. CNP have unique physical and chemical properties being an inorganic antioxidant performing the functions of some oxidoreductases: catalase, superoxide dismutase and oxidase [6–8]. CNP possess antibacterial, radioprotective [9], regenerative [10] and wound healing properties [11]. CNP nanoemulgel with curcumin shows promise in full-thickness wound healing [12]. Thus, the current research is focused on the development of new curcumin-based formulation, including its complexes with nanoparticles, to increase their bioavailability and therapeutic effects.

To achieve this goal, nanoemulsions (NE) can be used as carrier systems for encapsulating active components, increasing their bioavailability without losing their activity. Particularly relevant is the use of NE to elaborate transdermal and oral delivery systems containing curcumin [13, 14]. NE are kinetically stable disperse systems with droplet sizes up to 100 nm based on a combination of surfactant (cosurfactant), oil and water phases [15]. NE allow the entrapment of a larger quantity of a drug in comparison to conventional topical preparations. The solubility of poorly water-soluble drugs can be increased by NE, in which drugs are dissolved in an oil droplet phase. The penetration of drugs through the diffusional barrier of the skin can also be enhanced by using NE composition [16].

In this work, we obtained NE with paraffin oil, curcumin and CNP and analyzed their properties and toxic effects in *in vitro* and *in vivo* systems.

## 2. Materials and methods

### 2.1. Preparation of CeO<sub>2</sub> nanoparticles

The aqueous sol of nanocrystalline cerium oxide stabilized by citrate ions was prepared according to the previously reported protocol [17]. 0.24 g of citric acid was dissolved in 25 ml of 0.05 M aqueous solution of cerium (III) nitrate. This solution was rapidly added to 100 ml of 3 M ammonia solution under stirring and kept for 2 h.

### 2.2. Nanoemulsion preparation

NE were prepared by low-energy phase inversion temperature method [18]. The mixture of paraffin oil, Tween 60, Span 60 and 0.15 M sodium chloride solution was heated to 95°C under stirring. As a result, a coarse W/O emulsion was produced. This W/O emulsion was quickly cooled in an ice bath under stirring (1000 rpm). Upon cooling, the phase inversion took place and O/W NE were formed. The concentration of the oil phase in NE was 25 vol.%, the surfactant mixture – 12.5 vol.%. The surfactants Tween 60 and Span 60 were taken in a molar ratio of 0.76 [19].

NE with curcumin were prepared. Curcumin (4 wt.%) was dissolved beforehand in paraffin oil, and then NE were prepared as described above (NE+curcumin).

### 2.3. Modification of curcumin nanoemulsion by cerium dioxide nanoparticles

NE with CNP were produced by mixing of the NE and CNP. Dried citrate-stabilized CNP sol was added to NE with or without curcumin under stirring at 1000 rpm (Fig. 1). Two kinds of NE were produced: NE with CNP (NE+CNP) and NE with curcumin and CNP (NE+curcumin+CNP). The concentration of CNP in both NE was 17.2 mg/ml.

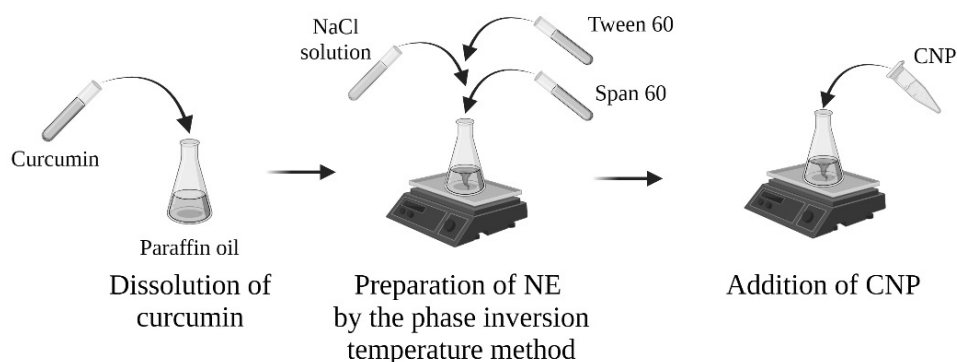


FIG. 1. Scheme of NE modification with curcumin and CNP

### 2.4. Nanoemulsion droplet size and $\zeta$ -potential analysis

The sizes of NE droplets were analyzed by dynamic light scattering technique at an angle of 173° using a helium-neon laser ( $\lambda = 633$  nm). The  $\zeta$ -potential was determined by electrophoretic light scattering method using Zetasizer Nano ZS (Malvern Instruments, United Kingdom). The measurements were carried out at 25°C. Each measurement represented an average of 15 runs (the number of runs was determined automatically by the instrument). The signals were analyzed using a single-plate multichannel correlator coupled to computer equipped with the software package Zetasizer Software for estimating the diameters by the distribution analysis model. All samples were measured at least 5 times; the average measurement error was about 5%.

### 2.5. Sedimentation stability of nanoemulsions

The sedimentation stability of NE was studied by the analysis of light transmission and backscattering of monochromatic radiation with a MultiScan MS 20 analyser (DataPhysics Instruments GmbH, Germany). The transmitted light was in the near infrared range, the light wavelength was 870 nm. Light transmission and reflection were measured depending on the height of the sample with a measurement resolution of 20  $\mu\text{m}$ . All measurements were carried out at 25°C.

### 2.6. FTIR- spectroscopy

The Fourier-transform infrared (FTIR) spectra were recorded using a Nicolet 380 (Thermo Fisher Scientific, USA) equipped with a Smart Performer single frustrated total internal reflection attachment. The samples were analyzed in the range of 900–4000  $\text{cm}^{-1}$  with a resolution of 2  $\text{cm}^{-1}$ .

### 2.7. Cell culture

The Mouse Embryonic Fibroblast (MEF) were cultured in Dulbecco's Modified Eagle's Medium (DMEM)/F12 (1:1) medium with the addition of 10% fetal bovine serum and 100 U/ml penicillin/streptomycin under 5% CO<sub>2</sub> at 37°C.

## 2.8. MTT assay

The determination of mitochondrial and cytoplasmic dehydrogenases activity in living cells was carried out using a MTT assay based on the reduction of the colorless tetrazolium salt (3-[4,5-dimethylthiazol-2-yl]-2,5-diphenyltetrazolium bromide, MTT). Briefly, different concentrations of the substances (0.0001%, 1%) were added and cells were incubated in a 96-well plate (for 24 h, 48 h and 72 h at 37°C in humid air (98%) containing 5% CO<sub>2</sub>). Three hours prior to the end of the exposure period, the supernatant was removed, and MTT (3-(4,5-dimethyl-2-thiazoly)-2,5-diphenyl-2H-tetrazolium bromide (Sigma-Aldrich, #M5655) solution in phosphate-buffered saline (0.5 mg/mL, 100 µL/well) was added to the cells for 10 min. Upon the completion of the exposure period, the supernatant was removed, and a lysis solution containing 0.1% sodium dodecyl sulfate (Sigma-Aldrich, #L3771) solution in dimethyl sulfoxide was added. Plates were shaken for 5 min, placed on a Multiskan MS Microplate Reader (Thermo Labsystems, Santa Rosa, CA, USA), and the absorbance was read colorimetrically at 570 nm. Each experiment was repeated three times, with four replications.

## 2.9. Live/Dead assay

Assessment of the viability of the cells cultured in the presence of NE was performed using a Carl Zeiss Axiovert 200 microscope. Cells were seeded into 96-well plates and stained with fluorescent dye Hoechst 33342 (absorption – 350 nm, emission – 461 nm) and a propidium iodide dye (absorption – 493, emission – 636 nm). The dyes were added to the DMEM/F12 without serum (1 µg/ml) and the plate was placed in a CO<sub>2</sub> incubator for 15 min. Microphotographs were taken after washing the cells with a phosphate-buffered saline. For each cell group, four fields in each well were examined. The number of cells (dead/live) was calculated using the ImageJ program.

## 2.10. Laboratory animals

Animal maintenance was carried out in accordance with the with Directive 2010/63/EU of the European Parliament and of the Council of the European Union on the protection of animals. The experiments were carried out on male white outbred mice (30–35 g), 8–9 weeks old. 12 animals were taken for each group to ensure the validity of the experiment. The animals were hatched and kept in the vivarium of ITEB RAS (Pushchino) by specialized personnel in accordance with the relevant requirements and documentation for the maintenance of laboratory animals. Animals were kept in polycarbonate cages with sawdust bedding, 5 animals each, at a temperature of 22 ± 2°C. Lighting mode was 12h/12h. Animals had free access to water and complete extruded feed for laboratory animals (OOO Laboratorkorm, Russia). Animals with abnormalities detected during the examination were not included in the experiment. Further, all animals were divided into 5 groups. Each animal included in the study was assigned an individual number. Animals were sacrificed after the end of the experiment by the method of cervical dislocation.

## 2.11. Acute toxicity of the nanoemulsions *in vivo*

The analysis was carried out on outbred white mice with a single intraperitoneal injection of the studied NE at a concentration of 860 mg/kg (10%) in a volume of 0.3 ml/mouse. The initial solutions of the nanoemulsions (NE, NE+CNP, NE+curcumin, NE+curcumin+CNP described above in paragraphs 2.2. and 2.3.) were diluted 10 times with a sterile injection solution (0.15 M NaCl). Control animals were intraperitoneally injected with a sterile injection solution only. All procedures with mice were carried out taking into account the international rules for working with laboratory animals and the requirements of the Commission on Biological Safety and Bioethics of the ITEB RAS (No. 25/2021 dated February 09, 2021). The acute toxicity of the nanocomposites was studied in mice using a 14-day survival test. The general condition of the animals was recorded and reflected in the primary documentation: the characteristics of their behavior, the intensity and nature of motor activity, the presence and nature of convulsions, coordination of movements, skeletal muscle tone, response to tactile, pain, sound and light stimuli, frequency and depth of respiratory movements, condition hair and skin, sensory organs, tail position, amount and consistency of fecal matter, frequency of urination and color of urine.

## 3. Results and discussion

### 3.1. Characterization of nanoemulsions

*3.1.1. Properties and structure of nanoemulsions with curcumin and cerium dioxide nanoparticles.* The size of droplets in NE depends strongly on the method of their preparation. In this work, NE were prepared by temperature phase inversion method. A coarse W/O emulsion was fabricated at elevated temperature. Then this emulsion was rapidly cooled in an ice bath that led to the phase inversion and O/W NE formation. Since the W/O emulsion was initially formed and then it was transformed into O/W one, two surfactants were used in the formulation: Span 60 with low hydrophilic–lipophilic balance (HLB) value and Tween 60 with higher HLB [15].

Our previous study has shown that the solidified shell of the mixture of Tween 60 and Span 60 is formed on the surface of oil nanodroplets at the ambient temperature. This shell provide the efficient protection from coalescence and Ostwald ripening in NE [20, 21]. Curcumin has a lipophilic nature, its molecule contains polar groups that impart amphiphilic

properties. Presumably, curcumin was located near the interface and partly embedded in a surfactant layer of oil droplets in NE.

Biomedical applications require methods for the synthesis of aggregation-resistant nanoparticles stabilized with biocompatible ligands [22–24]. In this work, we used a simple procedure for the synthesis of stable aqueous cerium dioxide sols and studied the effect of the concentration and molar ratio of the initial reagents on the size of  $\text{CeO}_2$  particles [17]. The CNP were very small; the average diameter was  $5 \pm 1$  nm (Fig. 2a). The average diameter of NE droplets without curcumin and CNP was  $55 \pm 5$  nm (Fig. 2b). Incorporating CNP in the NE led to increasing the droplet size to  $63 \pm 5$  nm. This increase in an average size indicates that CNP were adsorbed on the surface of the droplet with the formation of an outer solid shell as in the Pickering emulsions [25].

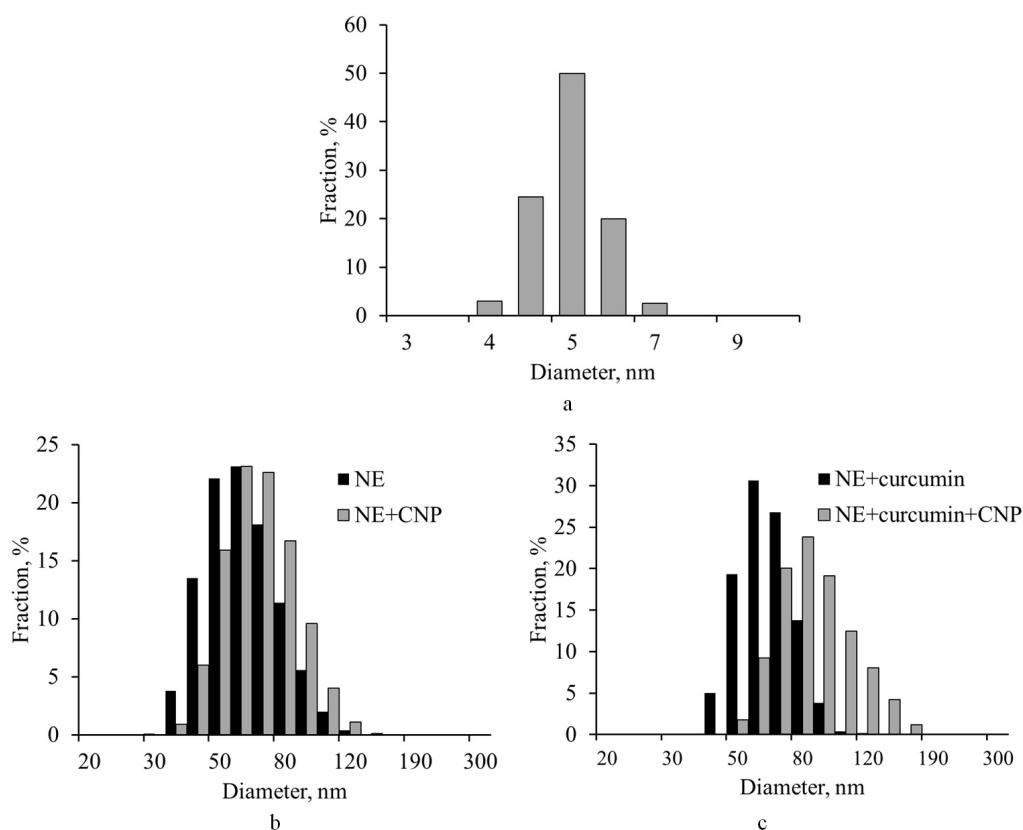


FIG. 2. Size distributions of CNP (a) and droplet size distributions in NE with CNP (b), CNP and curcumin (c)

The addition of curcumin in the lipid phase of NE gave a slight rise in the droplet size to  $58 \pm 5$  nm (Fig. 2b). Modification of the droplets with CNP led to an increase in the droplet diameter up to  $78 \pm 5$  nm, and droplet size distribution became wider. Presumably, in these NE a denser shell of CNP was formed.

CNP were highly charged,  $\zeta$ -potential was negative and equal to  $-(57 \pm 4)$  mV (Table 1). In turn, NE were stabilized with nonionic surfactants. Thus, the  $\zeta$ -potential of the oil droplets was low and did not exceed  $-(2 \pm 1)$  mV. In the presence of curcumin with amphiphilic properties,  $\zeta$ -potential of oil droplets slightly increased in absolute value.

$\zeta$ -potential of oil droplets in NE with CNP was higher in absolute value than in NE without nanoparticles. However, the charge of oil droplets with CNP was lower than the charge of individual CNP partial screening charges of nanoparticles adsorbed on the surface of oil droplets.

The potential curves were derived using the equation presented in [26]. Fig. 3 shows that the potential barrier value was rather low (less than 4 kT) in the suspension of CNP in spite of high value of  $\zeta$ -potential. In the case of interaction of oil droplet and CNP, the potential barrier was absent. These results indicate that CNP can adsorb on the surface of oil droplets with the formation of nanoparticle shell.

The proposed structure of NE droplets containing CNP is shown in Fig. 4. CNP, being absorbed on the surface of oil droplets in NE, formed a shell that prevented oil droplet flocculation. Due to the high surface charges of CNP, they were presumably located on the surface of oil drops at a small distance from each other. The effect of adsorbed nanoparticles on NE stabilization was confirmed by the long-term stability analysis of such systems. During storage for more than 30 days, all studied NE were stable and no phase separation was observed.

TABLE 1.  $\zeta$ -potentials of NE droplets with curcumin and CNP

Sample	$\zeta$ -potential, mV
NE	$-2 \pm 1$
NE+curcumin	$-7 \pm 1$
CNP	$-57 \pm 4$
NE+CNP	$-16 \pm 2$
NE+curcumin+CNP	$-38 \pm 3$

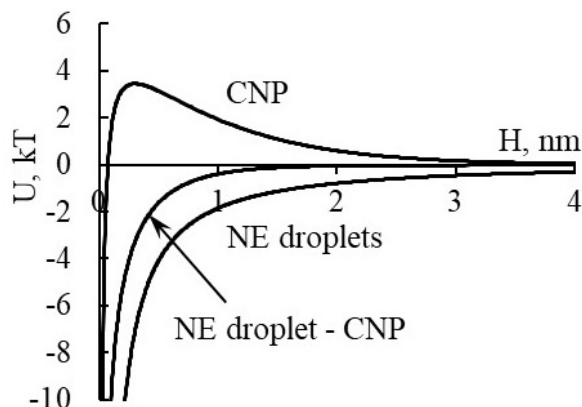


FIG. 3. Potential energy curves of oil droplets in NE, CNP and interaction of oil droplets and CNP

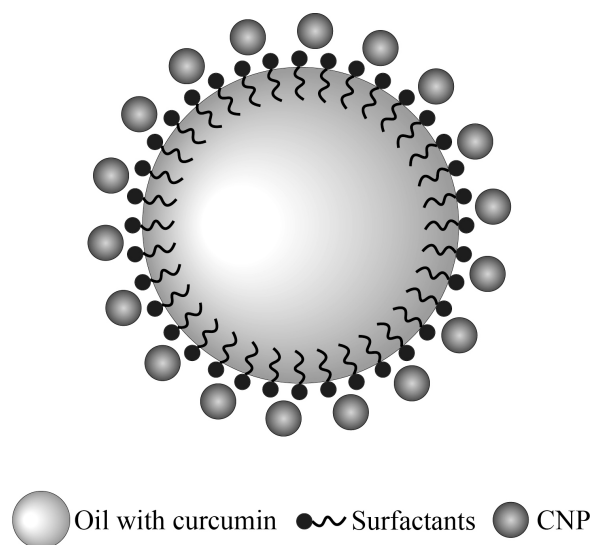


FIG. 4. Schematic representation of the structure of the NE drop with adsorbed CNP

**3.1.2. FTIR spectroscopy.** In order to confirm the incorporation of active components into the droplets and the absence of chemical interaction between them, FTIR spectroscopy study was carried out. The FTIR spectra (Fig. 5) contained the peaks corresponding to vibrations of the functional groups of the NE components. There were peaks characteristic of alkanes, which corresponded to paraffin oil at 1370 ( $-\text{CH}_3$  stretching vibrations), 1470, 2850, 2915 ( $-\text{CH}_2-$  stretches)  $\text{cm}^{-1}$ . The peaks at 950 and 2850  $\text{cm}^{-1}$  corresponded to vibrations of C-H bonds in aliphatic compounds. The peaks at 1100 and 1150  $\text{cm}^{-1}$  were characteristic of heterocycles of the furan series and C-O-C-group. The vibration of the OH-group in the FTIR spectra was observed at 3440  $\text{cm}^{-1}$ . The peaks at 1635–1700  $\text{cm}^{-1}$  corresponded to vibrations of C=O-bond. The stretching vibrations of  $-\text{C}-\text{O}$ -group, located in esters, manifested themselves as a peak at 1350  $\text{cm}^{-1}$ . All these groups were presented in both Tween 60 and Span 60. A broad peak with a maximum at 3370  $\text{cm}^{-1}$  was attributed to the aqueous phase.

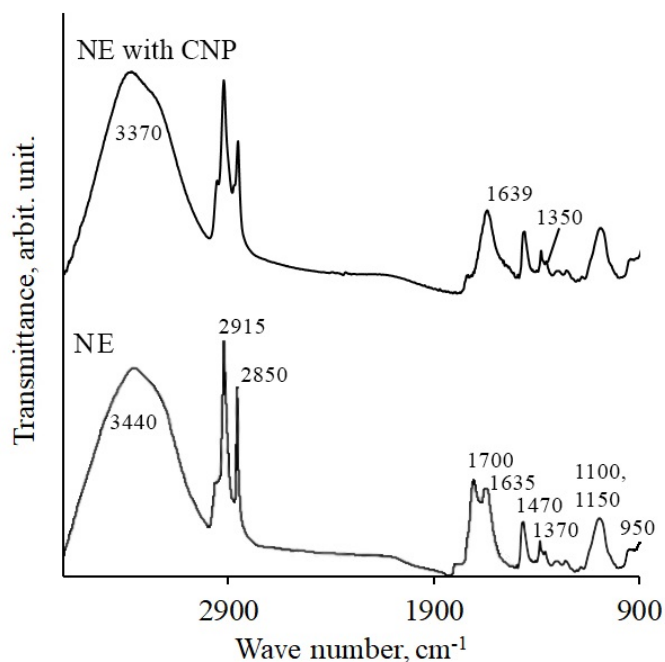


FIG. 5. FTIR spectra of NE without and with CNP

TABLE 2. Data characterizing the toxicity of NE in acute experiments on male SHK mice (intraperitoneally)

Group of animals	Dose, mg/kg	Number of animals			Lethality, %	LD <sub>50</sub> , mg/kg
		General	Deceased	Survivors		
Control	0	12	0	12	0	Not defined
NE	860	12	0	12	0	Not defined
NE+CNP	860	12	0	12	0	Not defined
NE+curcumin	860	12	0	12	0	Not defined
NE+curcumin+CNP	860	12	0	12	0	Not defined

The presence of peaks, corresponding to NE components, in the FTIR spectra confirmed their incorporation into the droplet structure without chemical alteration.

In the NE containing CNP, an increase in the intensity of the peak at  $1639\text{ cm}^{-1}$  was observed, which corresponded to their incorporation in the structure of the NE droplets.

The redox activity of cerium dioxide makes it a promising therapeutic antioxidant [27,28], but the interaction between CNP and NE components can take place in heterogeneous systems. The absence of peak shifts in the FTIR spectra of NE containing CNP indicated the absence of chemical interaction between cerium dioxide and NE components.

### 3.2. Toxicity of nanoemulsions

**3.2.1. Cytotoxicity of the nanoemulsions in vitro.** For the cytotoxicity analysis of NE, MEF was used. The metabolic activity of MEF was analyzed by the MTT test after incubation with 4 types of NE:

- 1 – NE;
- 2 – NE+CNP;
- 3 – NE+curcumin;
- 4 – NE+curcumin+CNP.

At the NE concentrations of 0.0001% and 1% after 24, 48 after 72 h incubation, any significant difference with the control group for 0.0001% NE (Fig. 6) did not reveal. Fig. 6 shows that the metabolic activity of MEF during incubation at 24 and 72 h in the presence of NE at a concentration of 1% with all experimental groups decreased by 40–90% relative to the control group without the addition of NE. In the NE+CNP group after 72 h, the metabolic activity of mouse embryonic fibroblasts increased by 30% relative to the control, which may be due to the presence of CNP in the composition of this emulsion. In the NE+curcumin group after 72 h, there was a decrease in metabolic activity by 15% relative to the control.

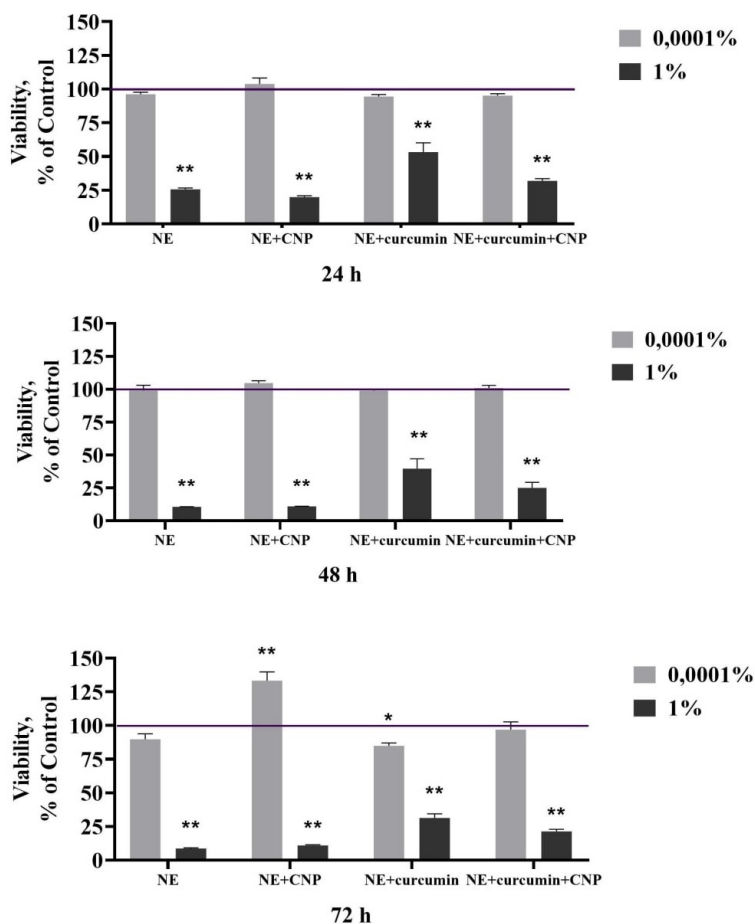


FIG. 6. Metabolic activity (as assessed by MTT assay) of MEF in the presence of NE (0.0001%, 1%) after 24, 48 and 72 h of incubation. Control group line corresponds to the cells that were not treated with. The data are presented as the mean  $\pm$ SD. \*Significant differences were assessed using the Welch *t*-test at  $0.01 < p < 0.05$  (\*),  $0.001 < p < 0.01$  (\*\*)

Most probably, this effect was due to the fact that curcumin could be partially segregated on the surface of oil droplets in the NE.

The results of cell viability analysis (Live/Dead assay) by fluorescent staining (all cells – Hoechst 33342 dye, dead cells – propidium iodide) showed that the NE upon incubation during 24, 48 and 72 h with MEF did not have a cytotoxic effect in the concentration range from 0.0001% to 1% (Fig. 7). For the studied NE in the concentration range from 0.0001% to 1%, LD<sub>50</sub> for the MEF was not detected.

In this way, the incubation of cells with NE at a concentration of 1% led to a decrease in the dehydrogenase activity of cells, which, however, did not lead to a significant increase in cell death compared to the control.

**3.2.2. Acute toxicity of the nanoemulsions in vivo.** The toxic effect of the NE was assessed by the general condition of the animals and their survival rate. The calculation of surviving and dead animals was carried out within 14 days after the administration of NE, followed by observation of surviving animals for two weeks after intraperitoneal injection. In the first 6 h, the animals were under continuous observation. During the entire observation period, the animals felt normal. Within 14 days of observation of animals, no noticeable deviations were detected in physical activity; the presence of seizures; coordination of movements, the condition of the skin, hair and color of visible mucous membranes; consumption of water and food; body weight.

The results obtained indicate that after a single intraperitoneal injection of NE at a dose of 860 mg/kg in groups of experimental animals, no death of animals was observed during 14 days of the experiment (Table 2). Thus the semi-lethal dose (LD<sub>50</sub>) could not be determined. A dose of 860 mg/kg was not toxic to mice after a single intraperitoneal injection of NE.

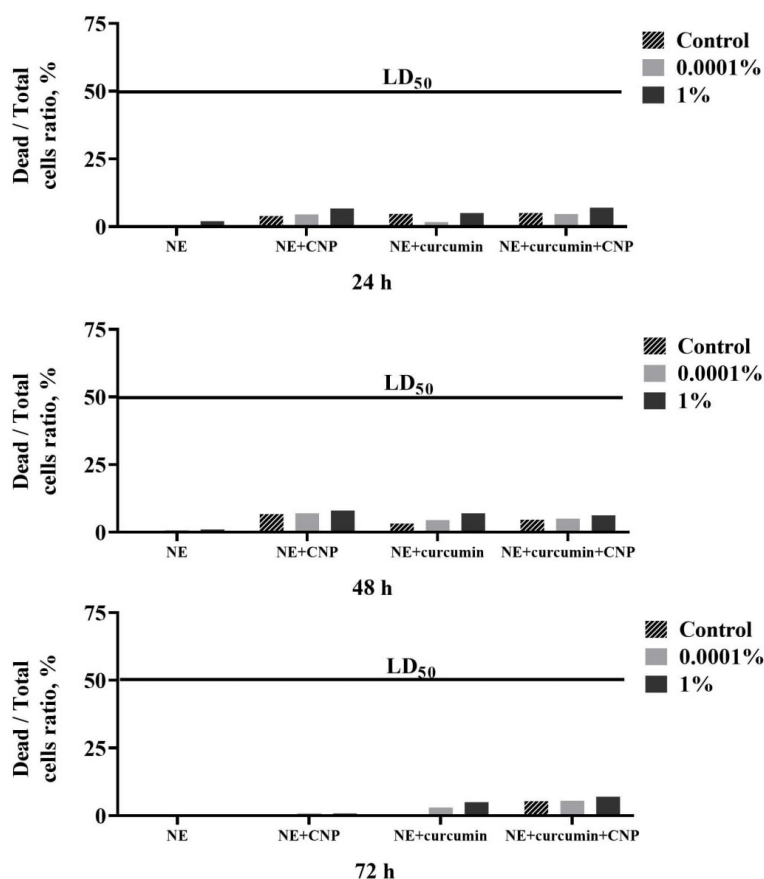


FIG. 7. Live/Dead assay for MEF after 24, 48, 72 h incubation with different concentrations of NE (0.0001%, 1%). Control group line corresponds to the cells that were not treated with. The values are indicated as a percentage of the number of dead cells to their total number

#### 4. Conclusions

In this work, NE with curcumin and cerium dioxide nanoparticles were prepared with droplet sizes less than 100 nm. The absence of a potential barrier in the interaction of oil droplets and CNP makes it possible to impart antioxidant properties to NE. The NE with curcumin and cerium dioxide nanoparticles did not show toxicity to mouse embryonic fibroblasts *in vitro* and after a single intraperitoneal injection in mice *in vivo*. Data obtained demonstrate the possibility of using NE with curcumin and cerium dioxide nanoparticles in advanced biomedical applications.

#### References

- [1] Fitzmaurice S.D., Sivamani R.K., Isseroff R.R. Antioxidant therapies for wound healing: a clinical guide to currently commercially available products. *Skin Pharmacol. Physiol.*, 2011, **24**(3), P. 113–126.
- [2] Thomas L., Zakir F., M. Mirza A., Anwer M.K., Ahmad F.J., Iqbal Z. Development of Curcumin loaded chitosan polymer based nanoemulsion gel: *in vitro*, *ex vivo* evaluation and *in vivo* wound healing studies. *Int. J. Biol. Macromol.*, 2017, **101**, P. 569–579.
- [3] Lizonova D., Hladek F., Chvila S., Balaz A., Stankova S., Stepanek F. Surface stabilization determines macrophage uptake, cytotoxicity, and bioactivity of curcumin nanocrystals. *Int. J. Pharm.*, 2022, **626**, P. 122133.
- [4] Ahsan H., Hadi S.M. Strand scission in DNA induced by curcumin in the presence of Cu (II). *Cancer letters*, 1998, **124**(1), P. 23–30.
- [5] Legonkova O.A., Korotaeva A.I., Terekhova R.P., Asanova L.Y., Shcherbakov A.B., Zholobak N.M., Baranchikov A.E., Krasnova E.V., Shekunova T.O., Ivanov V.K. Method for producing a biologically active composite based on nanocrystalline cerium dioxide and curcumin. Patent 2665378. Russia: MPK A61K 31/05. 2017134450, 2018.08.29.
- [6] Xue Y., Luan Q., Yang D., Yao X., Zhou K. Direct evidence for hydroxyl radical scavenging activity of cerium oxide nanoparticles. *J. Phys. Chem. C*, 2011, **115**, P. 4433–4438.
- [7] Yuao Wu, Hang T Ta. Different approaches to synthesising cerium oxide nanoparticles and their corresponding physical characteristics, and ROS scavenging and anti-inflammatory capabilities. *J. Mater. Chem.*, 2021, **9**(36), P. 7291–7301.
- [8] Plakhova T., Romanchuk A., Butorin S., Konyukhova A., Egorov A., Shiryayev A., Baranchikov A., Dorovatovskii P., Huthwelker T., Gerber E., Bauters S., Sozarukova M., Scheinost A., Ivanov V., Kalmykov S., Kvashnina K. Towards the surface hydroxyl species in CeO<sub>2</sub> nanoparticles. *Nanoscale*, 2019, **11**(39), P. 18142–18149.
- [9] Popova N.R., Shekunova T.O., Popov A.L., Selezneva I.I., Ivanov V.K. Cerium oxide nanoparticles provide radioprotective effects upon X-ray irradiation by modulation of gene expression. *Nanosystems: Physics, Chemistry, Mathematics*, 2019, **10**(5), P. 564–572.10.
- [10] Barker E., Shepherd J., Ortega Asencia I. The Use of Cerium Compounds as Antimicrobials for Biomedical Applications. *Molecules*, 2022, **27**(9), P. 2678.

- [11] Popov A.L., Andreeva V.V., Khohlov N.V., Kamenskikh K.A., Gavriluk V.B., Ivanov V.K. Comprehensive cytotoxicity analysis of polysaccharide hydrogel modified with cerium oxide nanoparticles for wound healing application. *Nanosystems: Physics, Chemistry, Mathematics*, 2021, **12**(3), P. 329–335.
- [12] Singh H., Bashir S.M., Purohit S.D., Bhaskar R., Rather M.A., Ali S.I., Yadav I., Makhdoomi D.M., Din Dar M.U., Gani M.A., Gupta M.K., Mishra N.C. Nanoceria laden decellularized extracellular matrix-based curcumin releasing nanoemulgel system for full-thickness wound healing. *Biomaterials Advances*, 2022, **137**, P. 212806.
- [13] Yu H., Huang Q. Improving the oral bioavailability of curcumin using novel organogel-based nanoemulsions. *Journal of agricultural and food chemistry*, 2012, **60**(21), P. 5373–5379.
- [14] Ahmad N., Ahmad R., Al-Qudaihi A., Alaseel S.E., Fita I.Z., Khalid M.S., Pottou F.H. Preparation of a novel curcumin nanoemulsion by ultrasonication and its comparative effects in wound healing and the treatment of inflammation. *RSC advances*, 2019, **9**(35), P. 20192–20206.
- [15] Solans C., Solé I. Nanoemulsions: formation by low-energy methods. *Curr. Opin. Colloid Interface Sci.*, 2012, **17**(5), P. 246–254.
- [16] Thakkar H.P., Khunt A., Dhande R.D., Patel A.A. Formulation and evaluation of Itraconazole nanoemulsion for enhanced oral bioavailability. *J. Microencapsulation*, 2015, **32**, P. 559–569.
- [17] Ivanova O.S., Shekunova T.O., Ivanov V.K., Shcherbakov A.B., Popov A.L., Davydova G.A., Selezneva I.I., Kopitsa G.P., Tret'yakov, Y.D. One-stage synthesis of ceria colloid solutions for biomedical use. *Dokl. Chem.*, 2011, **437**(2), P. 103–106.
- [18] Izquierdo P., Esquena J., Tadros Th.F., Dederen C., Garcia M. J., Azemar N., Solans C. Formation and stability of nanoemulsions prepared using the phase inversion temperature method. *Langmuir*, 2002, **18**, P. 26–30.
- [19] Koroleva M., Nagovitsina T., Yurtov E. Nanoemulsions stabilized by non-ionic surfactants: stability and degradation mechanisms. *Physical Chemistry Chemical Physics journal*, 2018, **20**(15), P. 10369–10377
- [20] Koroleva M., Nagovitsina T., Yurtov E. Properties of nanocapsules obtained from oil-in-water nanoemulsions. *Mendeleev Communications*, 2015, **25**, P. 389–390.
- [21] Mun S., McClements D.J. Influence of Interfacial Characteristics on Ostwald Ripening in Hydrocarbon Oil-in-Water Emulsions. *Langmuir*, 2006, **22**, P. 1551.
- [22] Lomanova N.A., Tomkovich M.V., Pleshakov I.V., Volkov M.P., Gusarov V.V., Danilovich D.P., Osipov A.V., Panchuk V.V., Semenov V.G. Magnetic characteristics of nanocrystalline bifeo3-based materials prepared by solution combustion synthesis. *Inorganic Materials*, 2020, **56**(12), P. 1271–1277.
- [23] Proskurina O.V., Sokolova A.N., Sirotkin A.A., Abiev R.S., Gusarov V.V. Role of hydroxide precipitation conditions in the formation of nanocrystalline BiFeO3. *Russian Journal of Inorganic Chemistry*, 2021, **66**(2), P. 163–169.
- [24] Bigall N.C., Rodio M., Avugadda S., Leal M.P., Di Corato R., Conteh J.S., Intartaglia R., Pellegrino T. Scaling Up Magnetic Nanobead Synthesis with Improved Stability for Biomedical Applications. *J. Phys. Chem. A*, 2022, **26**(51), P. 9605–9617.
- [25] Chevalier Y., Bolzinger M.A. Emulsions stabilized with solid nanoparticles: Pickering emulsions. *Colloids Surf. A*, 2013, **439**, P. 23–34.
- [26] Koroleva M., Yurtov E. Pickering emulsions stabilized with magnetite, gold, and silica nanoparticles: Mathematical modeling and experimental study. *Colloids and Surfaces A: Physicochemical and Engineering Aspects*, 2020, **601**, P. 125001.
- [27] Chen B.H., Inbaraj B.S. Various physicochemical and surface properties controlling the bioactivity of cerium oxide nanoparticles. *Critical Reviews in Biotechnology*, 2018, **38**(7), P. 1003–1024.
- [28] Celardo I., Traversa E., Ghibelli L. Cerium oxide nanoparticles: a promise for applications in therapy. *Journal of Experimental Therapeutics and Oncology*, 2011, **9**(1), P. 47–51.

---

Submitted 23 November 2022; accepted 12 December 2022

#### Information about the authors:

Anastasiya D. Shirokikh – Mendeleev University of Chemical Technology, Department of Nanomaterials and Nanotechnology, Miusskaya sq., 9, Moscow, 125047, Russia; ORCID 0000-0001-7742-7027; adshirokikh@gmail.com

Viktoriia A. Anikina – Institute of Theoretical and Experimental Biophysics of the Russian Academy of Sciences, Institutskaya str., 3, Pushchino, 142290, Russia; ORCID 0000-0002-5028-2064; viktoriya.anikina@list.ru

Elizaveta A. Zamyatina – Institute of Theoretical and Experimental Biophysics of the Russian Academy of Sciences, Institutskaya str., 3, Pushchino, 142290, Russia; ORCID 0000-0002-1275-565X; sonyoru162@gmail.com

Ekaterina V. Mishchenko – Mendeleev University of Chemical Technology, Department of Nanomaterials and Nanotechnology, Miusskaya sq., 9, Moscow, 125047, Russia; ORCID 0000-0003-4443-1569; mishchenkoek@list.ru

Marina Y. Koroleva – Mendeleev University of Chemical Technology, Department of Nanomaterials and Nanotechnology, Miusskaya sq., 9, Moscow, 125047, Russia; ORCID 0000-0002-6931-8434; m.yu.kor@gmail.com

Vladimir K. Ivanov – Kurnakov Institute of General and Inorganic Chemistry of the Russian Academy of Sciences, Leninskiy prosp., 31, Moscow, 119991, Russia; ORCID 0000-0003-2343-2140; van@igic.ras.ru

Nelli R. Popova – Institute of Theoretical and Experimental Biophysics of the Russian Academy of Sciences, Institutskaya str., 3, Pushchino, 142290, Russia; ORCID 0000-0002-0982-6349; nellipopovaran@gmail.com

*Conflict of interest:* the authors declare no conflict of interest.

## A comparative study of photocatalytic degradation of Xylenol Orange dye under natural sunlight over ZnO nanoparticles synthesized via mechanochemical and hydrothermal assistance routes

Yogeshwar D. Kaldante<sup>1,a</sup>, Manohar G. Chaskar<sup>2,b</sup>

<sup>1</sup>Department of Chemistry, PDEA's Annasaheb Waghire College, Otur, Pune, Maharashtra – 412409, India

<sup>2</sup>Department of Chemistry, PDEA's Prof. Ramkrishna More College, Akurdi, Maharashtra – 411044, India

<sup>a</sup>ydkaldante@gmail.com, <sup>b</sup>chaskarmanohar@gmail.com

Corresponding author: Yogeshwar D. Kaldante, ydkaldante@gmail.com

**ABSTRACT** Current work confers mechanochemical and hydrothermal syntheses of ZnO, its characterization and photocatalytic applications. Mechanochemical and hydrothermal assisted syntheses of ZnO involve two stages viz. formation of precursors followed by its calcination. The suitable calcination temperature for precursor materials to get ZnO was obtained by TG-DTA and FT-IR Spectroscopic study; XRD data of these samples specified hexagonal wurtzite crystallite structures of ZnO. FESEM photographs of mechanochemically and hydrothermally synthesized ZnO confirmed nanocrystalline hexagonal granular and stacked block-like particle morphologies respectively. EDX spectra of these samples support their elemental purity. The UV-DRS study was used to measure the optical band gap of ZnO samples. Optical properties of ZnO samples were also studied with room temperature PL spectra. Photocatalytic applications of aforementioned ZnO samples were investigated with Xylenol Orange as a model organic dye. The PCD efficiency of ZnO was estimated in terms of percent degradation reference to various operating factors.

**KEYWORDS** zinc oxide, Xylenol Orange, mechanochemical, hydrothermal, PCD efficiency

**ACKNOWLEDGEMENTS** Authors are exclusively grateful to PDEA's Annasaheb Waghire College, Otur for providing their continuous and valuable support, in terms of amenities like laboratories for all experimental work and library for the literature review. Authors are also thankful to PDEA's Baburaoji Gholap College, Sangvi and CIF, SPPU, Pune for giving instrumental facilities for the characterization of materials.

**FOR CITATION** Kaldante Y.D., Chaskar M.G. A comparative study of photocatalytic degradation of Xylenol Orange dye under natural sunlight over ZnO nanoparticles synthesized via mechanochemical and hydrothermal assistance routes. *Nanosystems: Phys. Chem. Math.*, 2023, **14** (1), 98–106.

### 1. Introduction

Wide range of applications of nano-sized semiconducting materials is available due to their mechanical, electrical, chemical and optical properties which can be tuned by altering their particle dimensions [1]. Metal oxides are established as promising candidates for their applications in the fields such as catalysis [2], sensing [3], energy storage and conversion [4, 5], optoelectronic devices [6], memory arrays [7], biomedical application [8] and acoustic wave devices [9]. ZnO is a key material of researcher interest because of its exceptional physico-chemical properties among semiconductor metal oxide. ZnO possess direct wide band gap (3.37 eV) with high exciton binding energy (60 meV) [1, 10]. ZnO shows strong piezoelectric, pyroelectric and optoelectronic properties [10, 11]. Eco-friendly and biocompatible nature and good thermal stability make ZnO most hopeful contestant for electronic and optoelectronic applications [11]. Nanosized ZnO materials can be gained by using various synthetic routes for instance mechanochemical [12], chemical precipitation [13], solution combustion [14], sol-gel method [15], hydrothermal synthesis [1, 10, 16], etc. Within these methods of ZnO synthesis mechanochemical and hydrothermal methods are quite suitable to control the particle size. Some advantages associated with mechanochemical method are its simplicity, low cost, eco-friendly nature and suitability for large-scale production of ZnO [17]. In addition to this, it is suitable for controlling the growth and nucleation of nanoparticles [17]. Hydrothermal method is also linked with quite a lot of advantages like low cost, large area uniform NPs production, eco-friendliness, catalyst-free growth of NPs, use of simple equipment, less hazardous [1], etc. The morphology and size of NPs can be controlled by adjusting concentration of precursors, reaction time, calcination temperature, etc. Hence, both these process are recognized to obtain the nanomaterials with diverse morphologies and particle sizes. Advanced Oxidation Processes (AOPs) are the efficient tool for the environmental technology. Within AOPs heterogeneous photocatalysis is one of the well-recognized and best substitutes for the conventional methods of water treatment [18]. Heterogeneous photocatalysis is the most efficient and economical method for the complete mineralization of organic contaminants to less and / or

non-toxic end products [19]. Midst various metal oxide photocatalysts, ZnO is extensively investigated material for its photocatalytic applications due to low cost, nontoxic nature and high photochemical reactivity [20].

In the current work, we have conferred mechanochemical and hydrothermal assisted synthesis of ZnO NPs and their thorough characterization by several techniques. The photocatalytic activities of these ZnO NPs photocatalysts were verified by means of degradation of xylenol orange dye (Fig. 1). The rate of photocatalytic degradation of xylenol orange was studied with reference to the operating factors like pH of dye solution, photocatalyst quantity, dye concentration, irradiation time, etc. The aim of the present research work is to study the effective methods of precursor preparation in the earlier stage prior to calcination during synthesis of ZnO NPs and its effect on the photocatalytic degradation of Xylenol Orange (Sulphonaphthalein) dye as a model dye. Since sulphonaphthalein dyes constitutes one of the large class of dyes used in various applications.

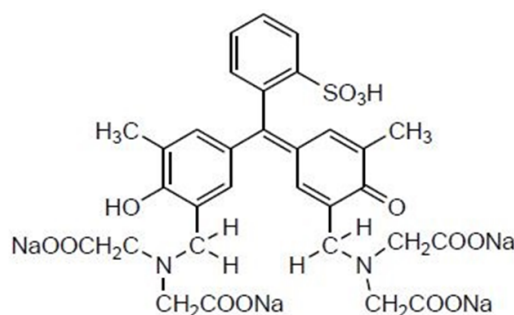


FIG. 1. Chemical structure of the Xylenol Orange dye molecule

## 2. Experimental

### 2.1. Materials

$\text{Zn}(\text{CH}_3\text{COO})_2 \cdot 2\text{H}_2\text{O}$  (assay 99.5 %),  $\text{H}_2\text{C}_2\text{O}_4 \cdot 2\text{H}_2\text{O}$  (assay 99.0 %), Xylenol Orange (assay 99.0 %), liquor  $\text{NH}_3$  (25 % w/w),  $\text{TiO}_2$  (Degussa P25) (assay 99.5 %) and additional necessary chemicals used as-received during current work were AR grade reagents acquired from S.D. Fine Chemicals Limited, India. Distilled water used to prepare all the allied experimental solutions. Wherever needed, pH of the related solutions was agreed to desired values with NaOH (0.05 M) and HCl (0.05 M).

### 2.2. Synthesis of photocatalyst

**2.2.1. Mechanochemical synthesis of ZnO.** Zinc oxide (ZnO) was gained by two step method. Initially  $\text{ZnC}_2\text{O}_4 \cdot 2\text{H}_2\text{O}$  precursor was obtained by mechanical hand grinding of a mixture of 10.975 gm of  $\text{Zn}(\text{CH}_3\text{COO})_2 \cdot 2\text{H}_2\text{O}$  with 6.93 gm of  $\text{H}_2\text{C}_2\text{O}_4 \cdot 2\text{H}_2\text{O}$  in agate mortar for about 30 minutes at room temperature. Secondly  $\text{ZnC}_2\text{O}_4 \cdot 2\text{H}_2\text{O}$  precursor was calcined at 450 °C for 4 hours in air atmosphere to give formation of ZnO powder [21–23].

**2.2.2. Hydrothermal assisted synthesis of ZnO.** Zinc Oxide (ZnO) was produced as mentioned. 10 ml liquor  $\text{NH}_3$  was added very slowly in a dropwise mode under vigorous magnetic stirring for the period of about 1 hour to the 100 ml solution of 0.5 M  $\text{Zn}(\text{CH}_3\text{COO})_2 \cdot 2\text{H}_2\text{O}$ . The pH of the reaction mixture was assured to be nearly 9 to 9.5. To ensure homogeneous phase, the resultant white suspension was furthermore stirred for another 1 hour, it was then transferred to the teflon-lined container in a hydrothermal reactor. Reactor was correctly sealed and kept at 100 °C for 4 hours under autogenous pressure. It was then naturally allow attaining room temperature. Then the resultant white residue of hydrated zinc oxide was filtered and washed with water followed by ethanol and finally dried at 100 °C and the same is calcined at 450 °C for 4 hours in air atmosphere to ensure formation of ZnO.

### 2.3. Equipments

The correct calcination temperature for the formation of ZnO from precursors in case of mechanochemical and hydrothermal assisted synthesis was gained by thermogravimetric analysis machine (Shimadzu, TG-DTG-60H) and FT-IR (PerkinElmer UATR Spectra Two) spectrometer. The XRD patterns of above mentioned ZnO samples was produced with X-ray Diffractometer (Rikagu Miniflex-600 with Cu  $K\alpha$  radiation  $\lambda\alpha = 1.5418 \text{ \AA}$ ) and the mean crystallite size ( $D$ ) was estimated from the Debye–Scherrer equation:  $D = \frac{0.90 \cdot \lambda}{\beta \cdot \cos \theta}$ , where  $\lambda$  is the wavelength ( $\lambda\alpha = 1.5418 \text{ \AA}$ ),  $\beta$  is the FWHM of the most intense peak (101) in the XRD pattern of samples and  $\theta$  is the diffraction angle [24]. The morphological depiction of ZnO samples was obtained with FE-SEM (JEOL JSM-6360A). The elemental purity of ZnO samples was studied with EDX spectra. The optical band gap of ZnO samples was gained from UV-Visible spectra and Tauc plots obtained by UV-Visible Spectrophotometer (PerkinElmer Lambda 365). The optical properties was furthermore

deliberate with room temperature PL spectra gotten with spectrofluorometer (Shimadzu, RF-5301PC) over 300 – 700 nm range with excitation source giving 320 nm wavelength. All the PCD reactions were carried out at room temperature in solar light (natural sunlight) in batch reactor during the period of November to May. Absorbance measurement with digital colorimeter (EQUIP-TRONICS EQ-353) is used to decide the percent degradation. The maiden pH of suspension was set with the help of pH meter (LABTRONICS LT-11). Lux meter (HTC LX-100) is used for determining the light intensity.

## 2.4. Photocatalytic degradation experiments

The PCD efficiency of the synthesized ZnO samples was explained by means of xylenol orange dye degradation. Entire dye solutions were prepared in distilled water with diverse primary concentrations. All experiments are executed in a batch photoreactor with glass cool trap and magnetic stirrer. Xylenol Orange (100 ml) dye solution having known original concentration at appropriate pH and at room temperature was taken with known photocatalyst quantity in a cylindrical photoreactor having 7 cm height and 5 cm diameter. The even suspension of the reaction mixture was produced with ultrasonic agitation for 5 minutes. Thereafter container was kept on magnetic stirrer under solar light irradiation. At specified time intervals supernatant solution was collected and centrifuged to settle down photocatalyst particles. Then absorbance of centrifuged supernatant solution was recorded at predetermined  $\lambda_{\max}$  value of Xylenol Orange dye solution which is used to find the percent Degradation:  $\text{Deg} = \frac{100 \cdot [A_0 - A_t]}{[A_0]}$ , where Deg is the Percent Degradation,  $A_0$  – Initial absorbance,  $A_t$  – Absorbance at time  $t$ .

## 3. Result and discussion

### 3.1. Characterization of ZnO samples

**3.1.1. Thermal gravimetric analysis.** Fig. 2 shows the TG-DTA plots for zinc oxalate dihydrate (a) produced in the mechanochemical synthesis of ZnO and zinc hydroxide / hydrated zinc oxide (b) synthesized during hydrothermal assisted synthesis of ZnO. From TG-DTA curves corresponding  $\text{ZnC}_2\text{O}_4 \cdot 2\text{H}_2\text{O}$ , two sharp endotherms (corresponding to weight losses 18.56 and 38.52 %) are presented in the temperature range from 30 to 400 °C. The first endotherm represents loss of  $2\text{H}_2\text{O}$  and second endotherm represents loss of oxalate moiety. From TG-DTA curves corresponding to  $\text{Zn}(\text{OH})_2$ , two endotherms (corresponding to weight losses 13.38 and 9.18 % ) are presented in the temperature range from 110 to 215 °C during the conversion of  $\text{Zn}(\text{OH})_2$  to ZnO which collectively associated with loss of water from  $\text{Zn}(\text{OH})_2$ . In addition to this apparent weight loss in the temperature range 340 – 410 °C in TGA, thermogram is partly contributed to the crystallization of amorphous ZnO. From these TG-DTA curves, the suitable calcination temperature for the formation of ZnO is 450 °C for 4 hours in air atmosphere in both cases.

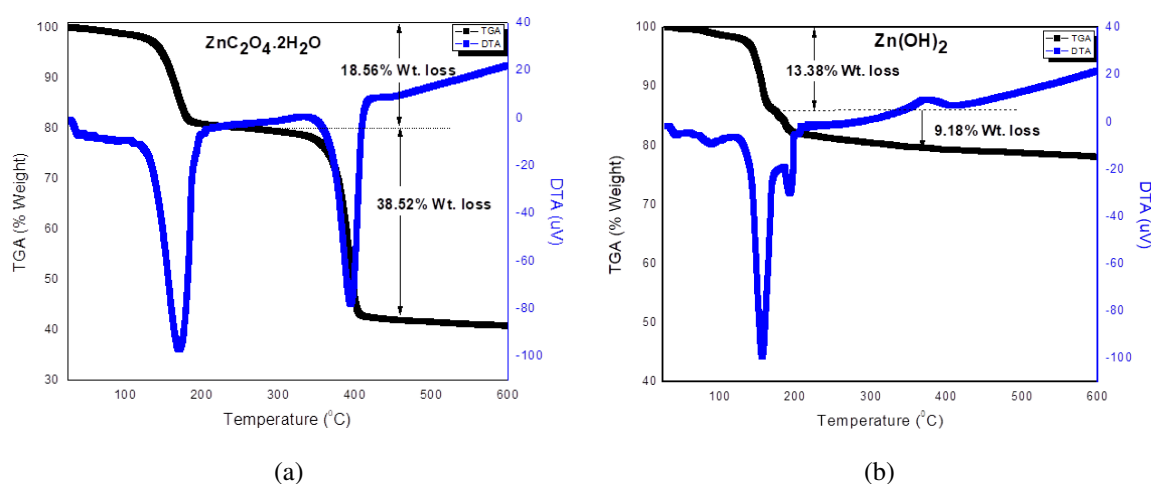


FIG. 2. TG-DTA curves of  $\text{ZnC}_2\text{O}_4 \cdot 2\text{H}_2\text{O}$  (a) and  $\text{Zn}(\text{OH})_2$  (b)

**3.1.2. FT-IR spectroscopic study.** Fig. 3 is for FT-IR spectra recorded over region 4000 – 400  $\text{cm}^{-1}$  corresponding to the mechanochemical method (a) and hydrothermal assisted method (b) of synthesis of ZnO. In case of mechanochemical and hydrothermal routes of ZnO synthesis respectively when  $\text{ZnC}_2\text{O}_4 \cdot 2\text{H}_2\text{O}$  and  $\text{Zn}(\text{OH})_2$  precursors were subjected to the calcination at 450 °C, all other bands (except those near to 450  $\text{cm}^{-1}$ ) were disappeared which were related to various symmetric and asymmetric stretching and bending vibrations in the corresponding oxalate and hydroxide precursors. This is in confirmation with the formation of pure ZnO samples [22, 25] and the same also proposed by XRD and EDS study.

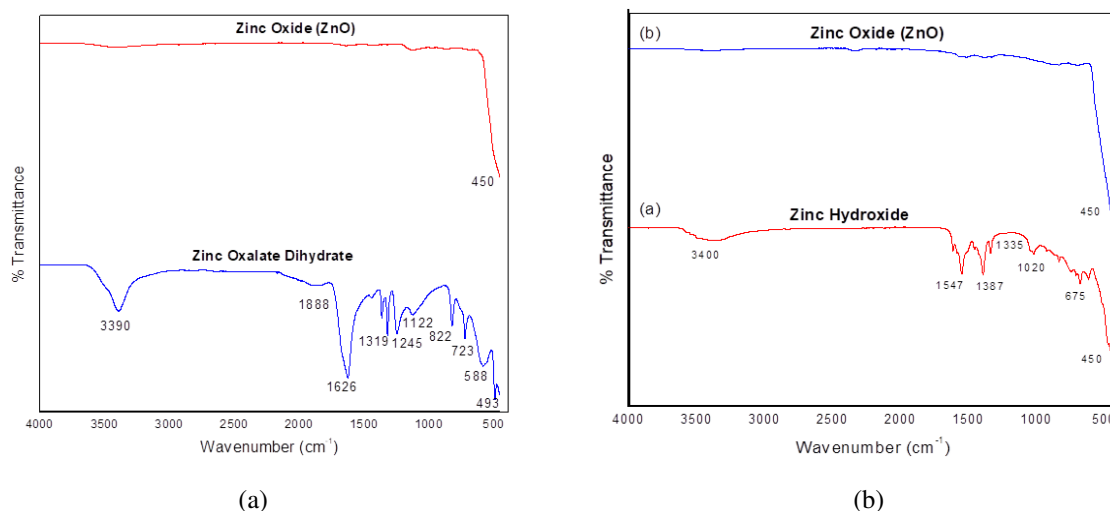


FIG. 3. FT-IR spectra of mechanochemical method (a) hydrothermal method (b)

**3.1.3. X-Ray diffraction (XRD) study.** The XRD data for mechanochemically and hydrothermally assisted synthesized ZnO samples was collected over a  $2\theta$  range of  $20^\circ - 80^\circ$  with Cu  $K\alpha$  radiation ( $\lambda = 1.5418 \text{ \AA}$ ) display series of diffraction peaks corresponds to (100), (002), (101), (102), (110), (103), (200), (112), (201), (004) and (202) crystal planes respectively (Fig. 4) and it is in accordance with JCPDS card 36-1451 for the standard wurtzite structure of ZnO [26]. The mean crystallite size gained for mechanochemically and hydrothermally synthesized ZnO samples are  $19 \pm 1.0 \text{ nm}$  and  $32 \pm 1.0 \text{ nm}$ . The lattice strains deliberated by using tangent formula [27] were found to be  $0.33 \pm 0.005$  and  $0.20 \pm 0.008$ , respectively and the specific surface areas determined by using Sauter Formula [28] were found to be  $59 \pm 0.40 \text{ m}^2/\text{g}$  and  $35 \pm 0.20 \text{ m}^2/\text{g}$  for mechanochemically and hydrothermally synthesized ZnO samples.

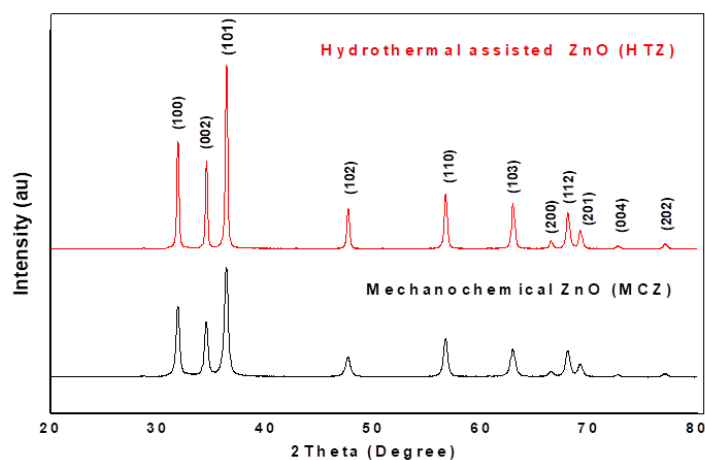


FIG. 4. XRD pattern of ZnO gained by mechanochemical (lower) and hydrothermal assisted (upper) method

**3.1.4. FE-SEM study.** Fig. 5 indicates the FESEM photographs of ZnO gained by mechanochemical (a) and hydrothermal assisted (b) method. The FESEM image of mechanochemically obtained ZnO shows formation of nearly homogeneous phase having non-agglomerated, dense particles of hexagonal morphology whereas the FE-SEM image of hydrothermal assisted obtained ZnO indicates the formation of particles having stacked hexagonal blocks like morphology. The mean particle sizes are found around 38 and 33 nm, respectively, for mechanochemically and hydrothermally obtained ZnO.

**3.1.5. EDX analysis.** Fig. 6 shows EDX spectra of ZnO samples gained by mechanochemical (a) and hydrothermal assisted (b) methods which consist of peaks corresponding to only Zn and O elements as a reflection of elemental purity of the ZnO sample. The supplementary peaks equivalent to Au, Al and C is due to their use for the preparation of conducting media to record the EDX spectra.

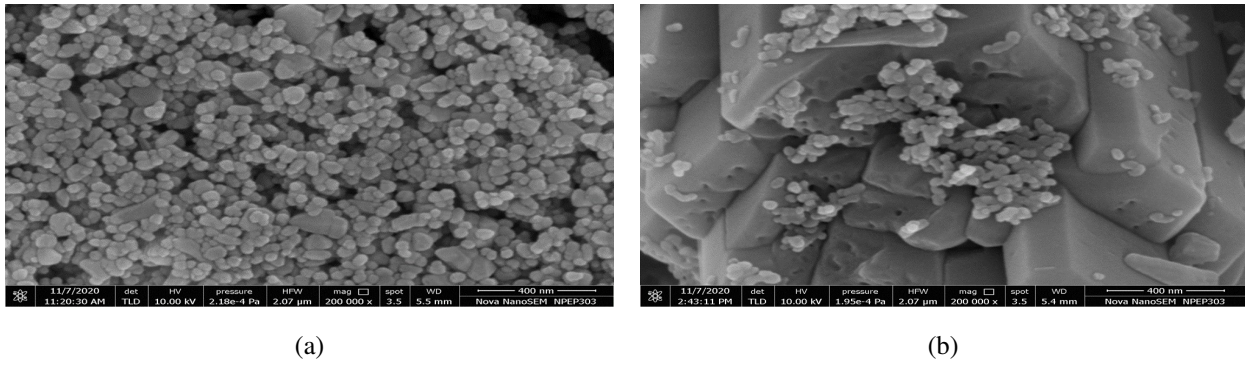


FIG. 5. FESEM photographs of ZnO gained by mechanochemical (a) and hydrothermal assisted (b) method

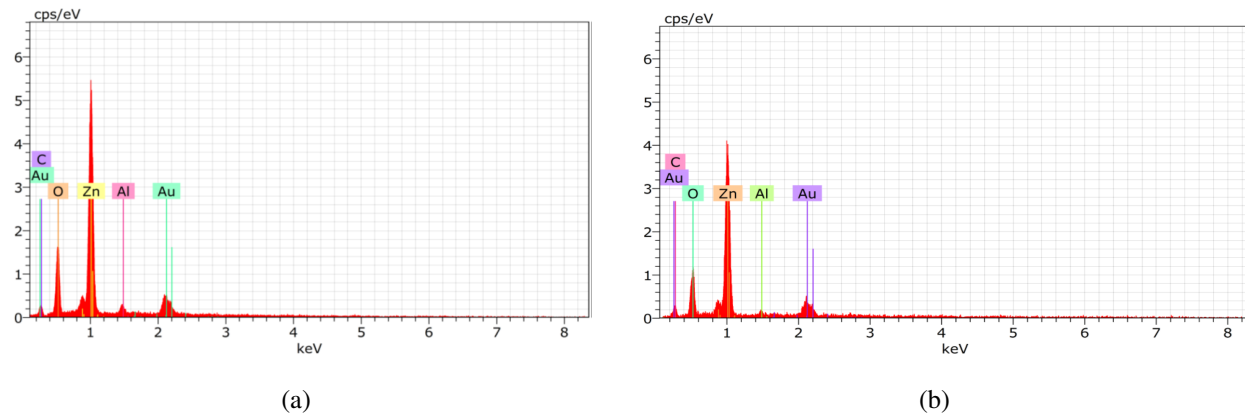


FIG. 6. EDX spectrum of ZnO gained by mechanochemical (a) and hydrothermal assisted (b) method

3.1.6. *UV-Visible spectra.* Fig. 7(a) indicates UV-visible spectrum and Fig. 7(b) indicates Tauc plot of ZnO samples. UV-Visible spectra clearly positioned optical extinction bands in the range of 375 to 420 nm. The energy band gaps obtained using UV-visible Spectra and Tauc plots for ZnO synthesized by mechanochemical and hydrothermal assisted routes were found to be 3.16 and 3.07 eV, respectively.

3.1.7. *Photoluminescence (PL) spectra.* Fig. 8 shows room temperature PL spectrum of ZnO synthesized by mechanochemical method (upper red) and hydrothermal assisted method (lower green) recorded with excitation wavelength 320 nm to investigate defect in ZnO and their optical properties as well. Both ZnO samples indicate relatively weak UV (Near Band Edge) emission peaks centered near 383 nm due to free excitonic recombination matching to the band edge emission of ZnO sample [29]. Both ZnO samples also have intense green emission bands fixed near 490 nm in PL spectrum due to radiative recombination of photogenerated holes with electrons occupying oxygen vacancies [29]. Because of faster

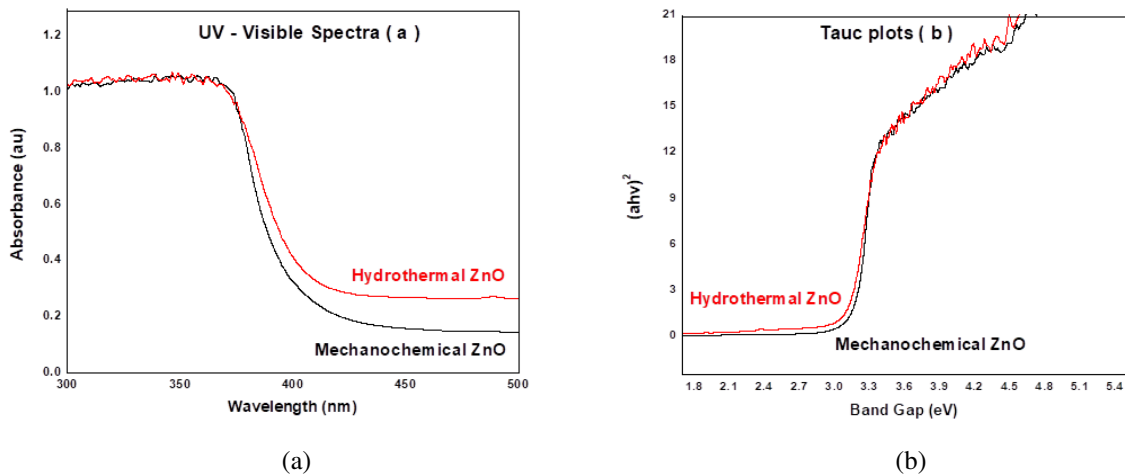


FIG. 7. UV-visible spectrum (a) and Tauc plot (b) of ZnO

recombination of photogenerated hole – electron pairs, the intensity of green emission band in case of mechanochemically synthesized ZnO is more than that of hydrothermally synthesized ZnO. Also more intensity of green emission band in case of mechanochemically synthesized ZnO is in accordance with larger number of oxygen vacancies and / or defects due to the small particle size of ZnO [30].

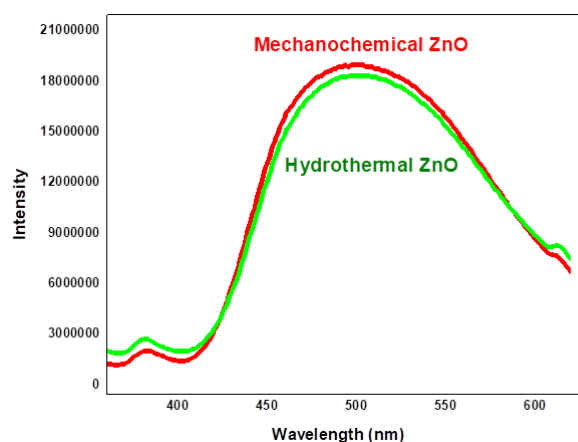


FIG. 8. Room Temperature PL spectra of ZnO samples

### 3.2. Photocatalytic activity of ZnO samples

Photocatalytic activity of mechanochemical and hydrothermal assistance synthesized ZnO nanomaterials and standard TiO<sub>2</sub> (Degussa P25) was studied with special reference to the operating parameters such as pH of dye solution, photocatalyst loading capacity, dye initial concentration, irradiation time, etc.

**3.2.1. Effect of the initial pH of Xylenol Orange dye solution.** The PCD of 100 ppm of Xylenol Orange dye over each of mechanochemically and hydrothermally synthesized ZnO and standard TiO<sub>2</sub> (Degussa P25) was deliberate at various pH from 5 to 11 with photocatalyst loading of 125 mg / 100 ml of dye solution under 6 hours of solar light irradiation (Fig. 9). The pH of the suspensions was set only prior to irradiation and set free during the course of reaction. As per fine recognized fact, slight (< 1 %) dissolution of the ZnO in acidic medium (pH 5, 6) reduces its PCD efficiency [31]. The degree of Xylenol Orange dye PCD was gradually increased with the initial pH of suspensions. Additional hydroxyl anions in alkaline medium promote photo-generation of the hydroxyl radicals (main oxidizing species) responsible for PCD [32]. Hence, PCD efficiency of ZnO samples was observed to be more at alkaline pH (9 – 11) and at pH 11 the PCD efficiency was found highest. The photocatalytic activity of hydrothermally synthesized ZnO was found quite larger than that of mechanochemically synthesized ZnO (Fig. 9).

ZnO photocatalysts obtained by both the mentioned routes show larger PCD efficiency than that of standard TiO<sub>2</sub> (Degussa P25) photocatalyst.

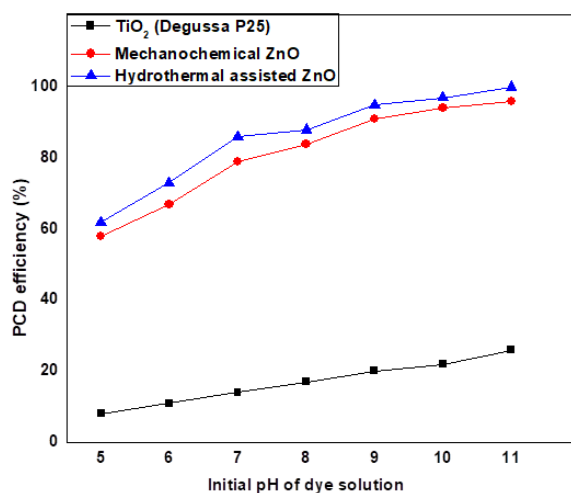


FIG. 9. Effect of the initial pH of Xylenol Orange dye solution

**3.2.2. Effect of the loading of ZnO photocatalyst.** The PCD of 100 ppm of Xylenol Orange over each of mechanochemically and hydrothermally synthesized ZnO samples and standard TiO<sub>2</sub> (Degussa P25) was deliberate at various loading amounts of photocatalyst from 50 mg / 100 ml to 175 mg / 100 ml of dye solution at pH=11 under 6 hours of solar light irradiation (Fig. 10). It was observed that, the PCD efficiency was slowly increased with ZnO loading up to particular level and acquire steadiness thereafter. The number of active sites available on the photocatalyst surface increased with its amount, hence the number of hydroxyl, and superoxide radicals also increased [22]. As a result PCD efficiency increases with ZnO loading upto 150 mg (mechanochemical) and 125 mg (hydrothermal) / 100 ml of dye solution. Beyond this limit, the PCD efficiency attains steadiness due to the availability of greater number of active species for the degradation of the same quantity of dye. Hence, 150 mg (mechanochemical) and 125 mg (hydrothermal) ZnO / 100 ml of dye solution are ample for the total degradation of Xylenol Orange within 6 hours of irradiation.

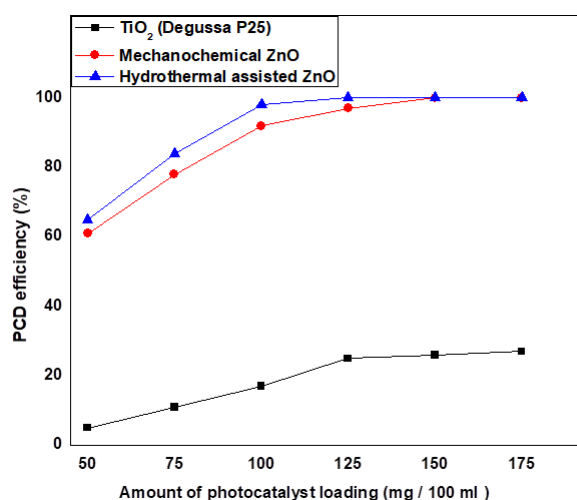


FIG. 10. Effect of the loading of ZnO photocatalyst

ZnO photocatalysts obtained by both the mentioned routes shows larger PCD efficiency than that of standard TiO<sub>2</sub> (Degussa P25) photocatalyst.

**3.2.3. Effect of the initial concentration of Xylenol Orange dye solution.** The degradation efficiency of Xylenol Orange over each of mechanochemically and hydrothermally synthesized ZnO and standard TiO<sub>2</sub> (Degussa P25) at different initial concentrations in the range 50 – 200 ppm was checked as a function of solar light irradiation time for 6 hours at the pH 11 of the suspension. The PCD efficiency is measured in terms of increase in percent degradation of Xylenol Orange and the results are shown in Fig. 11. The each of 50 and 75 ppm of Xylenol Orange was totally mineralized over 125 mg ZnO samples / 100 ml of the dye solution. For higher concentration of dye beyond 100 ppm the rate of PCD is higher in the case of hydrothermally synthesized ZnO than that of mechanochemically synthesized ZnO. As per the guess, increase in concentration of dye solutions decreases the extent of PCD over both ZnO samples. This is due to the formation of deep colored and turbid solution which generates obstacle in the path of light photons and hence reduces their absorption by the photocatalyst surface which results in the reduction of active radical species production responsible for the PCD. ZnO photocatalysts obtained by both the mentioned routes show higher PCD efficiency than that of standard TiO<sub>2</sub> (Degussa P25) photocatalyst

**3.2.4. Effect of irradiation time.** The PCD efficiency of mechanochemically and hydrothermally synthesized ZnO and standard TiO<sub>2</sub> (Degussa P25) under solar light gradually increases with increase in irradiation time (Fig. 12). 100 ml of 100 ppm Xylenol Orange dye solution was completely mineralized over 125 mg hydrothermally synthesized ZnO at the pH 11 upon 6 hours of sunlight irradiation and the rate of PCD in this case was found to be larger as compared to that of mechanochemically synthesized ZnO.

Irradiation time directly affects the PCD efficiency. Also the ZnO photocatalysts synthesized by mechanochemical and hydrothermal assisted synthesis show higher PCD efficiency as compared to that of standard TiO<sub>2</sub> (Degussa P25) photocatalyst under identical experimental conditions.

#### 4. Conclusions

In the current research, we have described the mechanochemically and hydrothermal assisted synthesis of ZnO photocatalysts. The formation of ZnO samples from the precursor materials was confirmed by FT-IR Spectroscopy, TG-DTA, EDX and XRD technique. XRD pattern of ZnO samples matches with hexagonal wurtzite structure. Calculations based on XRD data of these samples support for larger crystallite size and smaller specific surface area and lattice strain for

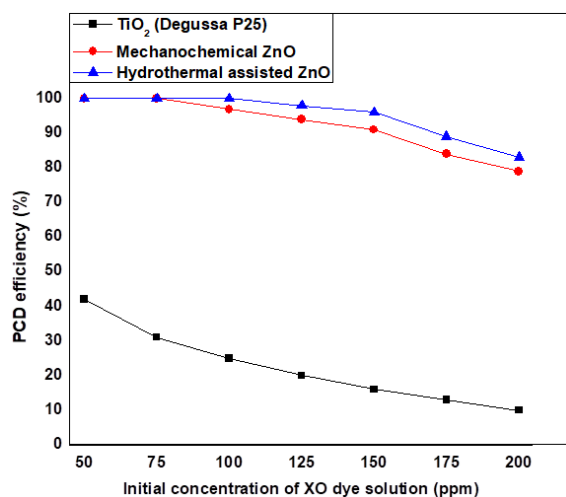


FIG. 11. Effect of the initial concentration of Xylenol Orange dye solution

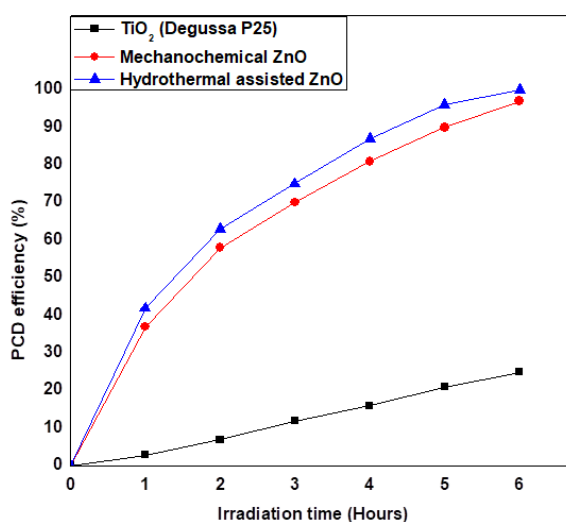


FIG. 12. Effect of irradiation time

hydrothermally synthesized ZnO sample. FE-SEM photographs indicate the formation of particles having hexagonal granular and stacked hexagonal blocks-like morphologies in case of mechanochemically and hydrothermal synthesis of ZnO samples, respectively. EDX spectra of aforementioned ZnO samples explain their elemental purity. UV-Visible and PL spectroscopies successfully explain the optical properties of ZnO nanoparticles. UV-Visible spectra gave lower bandgap energy for hydrothermally synthesized ZnO than that of mechanochemically obtained ZnO. Lower bandgap and slower recombination of photogenerated electrons and holes in case of hydrothermal ZnO may be responsible for its greater photocatalytic activity than mechanochemical ZnO. Room temperature PL spectrum of mechanochemical ZnO supports presence of more oxygen vacancies and defects which is in accordance with smaller crystallite size of the sample; but smaller photocatalytic activity of this sample may be observed due to faster recombination of photogenerated electrons and holes and large bandgap energy of this ZnO sample. The 100 ml each of 50, 75 and 100 ppm of Xylenol Orange dye solutions at pH 11 were completely mineralized over 125 mg hydrothermally obtained ZnO within 4, 5 and 6 hours of solar light irradiation, respectively. The effect of various operating factors on PCD of Xylenol Orange dye was successfully inspected.

## References

- [1] Aneesh P.M., Vanoja A.M., Jayaraj M.K. Synthesis of ZnO nanoparticles by hydrothermal method. In *Nanophotonic materials IV*, SPIE, 2007, **6639**, P. 47–55.
- [2] Hosseini-Sarvari M. Catalytic Organic Reactions on ZnO. *Current Organic Synthesis*, 2013, **10** (5), P. 697–723.
- [3] Zhu Ling, Wen Zeng. Room-temperature gas sensing of ZnO-based gas sensor: A review. *Sensors and Actuators A: Physical*, 2017, **267**, P. 242–261.
- [4] Feng Hao-peng, Lin Tang, Guang-ming Zeng, Yaoyu Zhou, Yao-cheng Deng, Xiaoya Ren, Biao Song, Chao Liang, Meng-yun Wei, Jiang-fang Yu. Core-shell nanomaterials: Applications in energy storage and conversion. *Advances in Colloid and Interface Science*, 2019, **267**, P. 26–46.

- [5] Madhu Rajesh, Vedyappan Veeramani, Shen-Ming Chen, Pitchaimani Veerakumar, Shang-Bin Liu, Nobuyoshi Miyamoto. Functional porous carbon–ZnO nanocomposites for high-performance biosensors and energy storage applications. *Physical Chemistry Chemical Physics*, 2016, **18** (24), P. 16466–16475.
- [6] Djurišić A.B., Ng A.M.C., Chen X.Y. ZnO nanostructures for optoelectronics: Material properties and device applications. *Progress in quantum electronics*, 2010, **34** (4), P. 191–259.
- [7] Liu Zi-Jheng, Jon-Yiew Gan, Tri-Rung Yew. ZnO-based one diode-one resistor device structure for crossbar memory applications. *Applied Physics Letters*, 2012, **100** (15), 153503.
- [8] Rajeshkumar S., Lakshmi T., Poonam Naik. Recent advances and biomedical applications of zinc oxide nanoparticles. *Green Synthesis, Characterization and Applications of Nanoparticles*, 2019, P. 445–457.
- [9] Xu Zhangliang, Yong J. Yuan. Implementation of guiding layers of surface acoustic wave devices: A review. *Biosensors and Bioelectronics*, 2018, **99**, P. 500–512.
- [10] Baruah Sunandan, Joydeep Dutta. Hydrothermal growth of ZnO nanostructures. *Science and technology of advanced materials*, 2009, **10** (1), 013001.
- [11] Samadi Morasae, Mohammad Zirak, Amene Naseri, Elham Khorashadizade, Alireza Z. Moshfegh. Recent progress on doped ZnO nanostructures for visible-light photocatalysis. *Thin Solid Films*, 2016, **605**, P. 2–19.
- [12] Shen Liming, Ningzhong Bao, Kazumichi Yanagisawa, Kazunari Domen, Arunava Gupta, Craig A. Grimes. Direct synthesis of ZnO nanoparticles by a solution-free mechanochemical reaction. *Nanotechnology*, 2006, **17** (20), 5117.
- [13] Khoshhesab Zahra Monsef, Mohammad Sarfaraz, Mohsen Asadi Asadabad. Preparation of ZnO nanostructures by chemical precipitation method. *Synthesis and Reactivity in Inorganic, Metal-Organic, and Nano-Metal Chemistry*, 2011, **41** (7), P. 814–819.
- [14] Khaliullin Sh M., Zhuravlev V.D., Ermakova L.V., Buldakova L.Yu., Yanchenko M.Yu., Porotnikova N.M. Solution combustion synthesis of ZnO using binary fuel (glycine+ citric acid). *Int. J. of Self-Propagating High-Temperature Synthesis*, 2019, **28** (4), P. 226–232.
- [15] Hasnidawani J.N., Azlina H.N., Norita H., Bonnia N.N., Ratim S., Ali E.S. Synthesis of ZnO nanostructures using sol-gel method. *Procedia Chemistry*, 2016, **19**, P. 211–216.
- [16] Pantelitsa G., Kolokotronis K., Simitzis J. Synthesis of ZnO nanostructures by hydrothermal method. *J. of Nano Research*, 2009, **6**, P. 157–168.
- [17] Azam Ameer, Faheem Ahmed, Nishat Arshi, Chaman M., Naqvi A.H. Low temperature synthesis of ZnO nanoparticles using mechanochemical route: A green chemistry approach. *Int. J. Theor. Appl. Sci.*, 2009, **1** (2), P. 12–14.
- [18] Tom Asha P. Nanotechnology for sustainable water treatment – A review. *Materials Today: Proceedings*, 2021, <https://doi.org/10.1016/j.matpr.2021.05.629>.
- [19] Tijani Jimoh O., Ojo O. Fatoba, Godfrey Madzivire, Leslie F. Petrik. A review of combined advanced oxidation technologies for the removal of organic pollutants from water. *Water, Air & Soil Pollution*, 2014, **225** (9), P. 1–30.
- [20] Elamin Nazar, Ammar Elsanousi. Synthesis of ZnO nanostructures and their photocatalytic activity. *J. of Applied and Industrial Sciences*, 2013, **1** (1), P. 32–35.
- [21] Kaldante Y.D., Shirsat R.N., Chaskar M.G. Photocatalytic degradation of Rose Bengal dye over mechanochemically synthesized zinc oxide under visible light irradiation. *Nanosystems: Phys. Chem. Math.*, 2021, **12** (6), P. 773–782.
- [22] Pardeshi S.K., Patil A.B. Effect of morphology and crystallite size on solar photocatalytic activity of zinc oxide synthesized by solution free mechanochemical method. *J. of Molecular Catalysis A: Chemical*, 2009, **308** (1–2), P. 32–40.
- [23] Liming Shen, Ningzhong Bao, Kazumichi Yanagisawa, Kazunari Domen, Arunava Gupta, Craig A. Grimes. Direct synthesis of ZnO nanoparticles by a solution-free mechanochemical reaction. *Nanotechnology*, 2006, **17**, P. 5117–5123.
- [24] Aparna P.U., Divya N.K., Pradyumn P.P. Structural and dielectric studies of Gd doped ZnO nanocrystals at room temperature. *J. of Materials Science and Chemical Engineering*, 2016, **4** (2), 79.
- [25] Wahab Rizwan, Young-Soon Kim, Hyung-Shik Shin. Synthesis, characterization and effect of pH variation on zinc oxide nanostructures. *Materials transactions*, 2009, **50** (8), P. 2092–2097.
- [26] Chauhan Jyotsna, Neelmani Shrivastav, Ashish Dugaya, Devendra Pandey. Synthesis and characterization of Ni and Cu doped ZnO. *J. Nanomed. Nanotechnol*, 2017, **1**, P. 26–34.
- [27] Nafees Muhammad, Wasim Liaqat, Salamat Ali, Muhammad Ahsan Shafique. Synthesis of ZnO/Al: ZnO nanomaterial: structural and band gap variation in ZnO nanomaterial by Al doping. *Applied Nanoscience*, 2013, **3** (1), P. 49–55.
- [28] Thangeeswari T., Parthipan G., Shanmugan S. Synthesize of gadolinium-doped ZnO nano particles for energy applications by enhance its optoelectronic properties. *Materials Today: Proceedings*, 2021, **34**, P. 448–452.
- [29] Jayakumar O.D., Sudarsan V., Sudakar C., Naik R., Vatsa R.K., Tyagi A.K. Green emission from ZnO nanorods: Role of defects and morphology. *Scripta Materialia*, 2010, **62** (9), P. 662–665.
- [30] Liqiang Jing, Qu Yichun, Wang Baiqi, Li Shudan, Jiang Baojiang, Yang Libin, Fu Wei, Fu Honggang, Sun Jiazhong. Review of photoluminescence performance of nano-sized semiconductor materials and its relationships with photocatalytic activity. *Solar Energy Materials and Solar Cells*, 2006, **90** (12), P. 1773–1787.
- [31] Behnajady M.A., Modirshahla N., Hamzavi R. Kinetic study on photocatalytic degradation of CI Acid Yellow 23 by ZnO photocatalyst. *J. of hazardous materials*, 2006, **133** (1-3), P. 226–232.
- [32] Muruganandham M., Swaminathan M. Solar photocatalytic degradation of a reactive azo dye in TiO<sub>2</sub>-suspension. *Solar Energy Materials and Solar Cells*, 2004, **81** (4), P. 439–457.

---

*Submitted 30 July 2022; revised 14 November 2022; accepted 27 November 2022*

#### *Information about the authors:*

*Yogeshwar D. Kaldante* – Department of Chemistry, PDEA's Annasaheb Waghire College, Otur, Pune, Maharashtra – 412409, India; ydkaldante@gmail.com

*Manohar G. Chaskar* – Department of Chemistry, PDEA's Prof. Ramkrishna More College, Akurdi, Maharashtra – 411044, India; chaskarmanohar@gmail.com

*Conflict of interest:* the authors declare no conflict of interest.

## Influence of high energy milling on titanium oxide $\text{Ti}_3\text{O}_5$ crystal structure

Albina A. Valeeva<sup>1,a</sup>, Irina B. Dorosheva<sup>2,3,b</sup>, Anna A. Sushnikova<sup>3,c</sup><sup>1</sup>Institute of Solid State Chemistry, Ural Branch of the Russian Academy of Sciences, 620108, Ekaterinburg, Russia<sup>2</sup>Ural Federal University, 620002, Ekaterinburg, Russia<sup>3</sup>Institute of Metallurgy, Ural Branch of the Russian Academy of Sciences, 620016 Ekaterinburg, Russia<sup>a</sup>anibla.v@mail.ru, <sup>b</sup>dorosheva1993@mail.ru, <sup>c</sup>sushnikova.ann@gmail.com

Corresponding author: Albina A. Valeeva, anibla.v@mail.ru

PACS 71.20.Be, 81.07.Wx, 74.62.Bf, 61.05.C-, 68.37.Hk

**ABSTRACT** The titanium oxide ( $\text{Ti}_3\text{O}_5$ ) microcrystals were synthesized by using solid-phase sintering from a mixture of titanium Ti and titanium dioxide  $\text{TiO}_2$  powders. Subsequently,  $\text{Ti}_3\text{O}_5$  nanocrystals were produced by using high-energy ball milling for 15 – 480 minutes. A full-profile analysis of the X-ray diffraction spectra of milled  $\text{Ti}_3\text{O}_5$  powders showed that high-energy milling does not lead to disordering or changing of the structure and stoichiometry, the structure remains monoclinic (sp. gr.  $C2/m$ ), and XRD reflections are broadened due to the small particle size and microdeformations. Experimental data show that increasing of the milling time leads to decreasing of the coherent scattering regions up to 26 nm, increasing of the powder volume fraction of the nanophase up to 81 %, and increasing of microdeformations value. The morphology and the surface area of milled nanopowders were examined by SEM, HRTEM and BET techniques.

**KEYWORDS** high-energy ball milling,  $\text{Ti}_3\text{O}_5$ , XRD, BET, SEM, HRTEM

**ACKNOWLEDGEMENTS** The work was carried out in accordance with the state assignment for the Institute of Solid State Chemistry of the Ural Branch of the Russian Academy of Science (No. 0397-2019-0001). Authors thanks to Gerasimov E. Yu. for HRTEM experiments.

**FOR CITATION** Valeeva A.A., Dorosheva I.B., Sushnikova A.A. Influence of high energy milling on titanium oxide  $\text{Ti}_3\text{O}_5$  crystal structure. *Nanosystems: Phys. Chem. Math.*, 2023, **14** (1), 107–111.

### 1. Introduction

The Ti–O system is attractive from both fundamental and applied points of view [1–6]. Well known due to its unique properties, titanium dioxide is the most studied material in wide areas of science and industry, ranging from memristors and capacitors to photocatalysts and photosorbents [7–10]. Nanoparticles of this material are synthesized mainly by bottom-up methods, namely, the sol-gel method, hydrothermal, anodizing, etc. [11–14]. In practical application, one of the disadvantages of this system is very wide band gap. A way to change the properties of this material is to introduce defects into the structure and  $\text{Ti}^{2+}$  and  $\text{Ti}^{3+}$  ions, which will lead to a change in the structure and properties [15–17]. Currently, a search is underway for materials that can be easily synthesized, have certain functional properties and structure, are stable during the entire period of operation under extreme conditions, and do not require additional energy supply [18]. One of the effective methods for obtaining nanoparticles is high-energy milling, which makes it possible to control the size of the resulting particles, dope the material during milling, and use various media for synthesis [19]. The milling of titanium oxides  $\text{Ti}_2\text{O}_3$  [20, 21],  $\text{TiO}_2$  (rutile) [22, 23] by means of high-energy ball milling leads to a decrease of the particle size only, the milling of ordered titanium monoxide  $\text{TiO}_y$  leads to a decrease of long-range order parameter of monoclinic  $\text{TiO}_y$  [24, 25], and phase transitions in  $\text{TiO}_2$  from anatase to the high-pressure phase  $\text{TiO}_2$  (II) occurs during milling [26, 27].

In this regard, the aim of this work is to obtain titanium oxide  $\text{Ti}_3\text{O}_5$  nanoparticles with different particle sizes by varying the duration of high-energy milling and analyze the effect of high mechanical load on the morphology, crystal structure and stability of monoclinic phase of  $\text{Ti}_3\text{O}_5$  under the intensive mechanical treatment.

### 2. Experiment

Initial microcrystals of titanium oxide  $\text{Ti}_3\text{O}_5$  with an average size of about 30  $\mu\text{m}$  were synthesized by solid-phase sintering from a mixture of titanium (Ti) and titanium dioxide ( $\text{TiO}_2$ ) powders in a vacuum of  $10^{-3}$  Pa at 1770 K.  $\text{Ti}_3\text{O}_5$  nanoparticles with different particle sizes were obtained by high-energy milling of microcrystals in a Retsch PM 200 planetary ball mill. To minimize sample contamination during milling,  $\text{ZrO}_2$  stabilized with  $\text{Y}_2\text{O}_3$  was chosen as the material for the milling bowls and balls. The optimal mass ratio of milling balls and  $\text{Ti}_3\text{O}_5$  powders, namely 10 : 1, was

chosen to effectively obtain the smallest nanoparticle size. Isopropyl alcohol was used as the milling liquid; the speed of rotation of the support disk was 500 rpm with the duration of milling 15, 30, 60, 120, 240 and 480 min.

Crystal structure studies of the initial and milled titanium oxide powders  $\text{Ti}_3\text{O}_5$  were performed in  $\text{CuK}\alpha_{1,2}$  radiation using XRD-7000 (Shimadzu, Japan) autodiffractometer. The X-ray diffraction patterns (XRD) were taken in the step-by-step scanning mode with  $\Delta(2\theta) = 0.02^\circ$  in the range of  $2\theta$  angles from  $10^\circ$  to  $140^\circ$  with high statistics. The pseudo-Voigt function was used for a full-profile description of X-ray diffraction reflections:

$$V(\theta) = c \cdot a \left[ 1 + \frac{(\theta - \theta_0)^2}{\theta_L^2} \right]^{-1} + (1 - c) \cdot a \cdot \exp \left[ -\frac{(\theta - \theta_0)^2}{2\theta_G^2} \right], \quad (1)$$

where  $c$  is the relative contribution of the Lorentz function to reflection intensity;  $\theta_L$  and  $\theta_G$  are the Lorentz and Gaussian functions parameters, respectively;  $a$  is the normalizing intensity factor;  $\theta_0$  is the maximum position of the function and reflection.

The dimensional and deformation contributions to the reflection broadening were determined by the Williamson–Hall method [28]. The reduced broadening was calculated by the formula:

$$\beta^*(2\theta) = \beta(2\theta) \frac{\cos\theta}{\lambda}.$$

The experimentally measured broadening  $\beta(2\theta)$  is a superposition of the dimensional  $\beta_s$  and deformation  $\beta_d$  broadening according to the formula:

$$\beta = \sqrt{\beta_s^2 + \beta_d^2}.$$

The size of coherent scattering regions (CSR) was determined by the formula:

$$\langle D \rangle = \frac{1}{\beta^*} \quad (2\theta = 0).$$

The morphology of the synthesized and milled powders were examined on Ultra 55 (Carl Zeiss, Germany) scanning electron microscope (SEM) under high vacuum. The working distance (WD) was 7.5 – 10 mm, the electron high tension (EHT) was 20 – 25 kV. In order to avoid excessive electrization of powder during electron microscope imaging, the examined powder was deposited on a conducting adhesive tape from carbon. The structure of the milled powders was studied by using the high-resolution transmission electron microscopy (HRTEM) on a JEM 2010 electron microscope (JEOL, Japan) with accelerating voltage of 200 kV and ultimate lattice resolution of 140 pm. Imaging was performed by means of CCD matrix of Soft Imaging System (Germany). The device was equipped with a Phoenix (EDAX, USA) energy-dispersive characteristic X-ray radiation (EDX) spectrometer with a semiconducting Si(Li)-detector with energy resolution of 130 eV. For HRTEM experiments  $\text{Ti}_3\text{O}_5$  particles were placed into alcohol and were further deposited on perforated carbon substrates (diameter of holes of about 1  $\mu\text{m}$ ) fixed on copper grids. Particles were deposited with the use of a UZD-1UCh2 ultrasonic disperser, which allowed uniform particle distribution on the substrate surface. After the grids were extracted from alcohol, the alcohol was evaporated. The specific surface area (SSA) of the powders was measured using Gemini VII 2390 (Micromeritics, USA) analyser implementing the Brunauer–Emmett–Teller (BET) method with preliminary degassing at  $120^\circ\text{C}$ .

### 3. Results and discussion

Figure 1 shows X-ray diffraction patterns of the initial and milled powders of titanium oxides  $\text{Ti}_3\text{O}_5$  for 15 to 480 min. Detailed analysis of XRD patterns of ball milled  $\text{Ti}_3\text{O}_5$  (Fig. 1) showed that the crystal structure of nanocrystal powder coincides with the crystal structure of microcrystal powder  $\text{Ti}_3\text{O}_5$ , i.e. the monoclinic structure of  $\text{Ti}_3\text{O}_5$  (sp. gr.  $C2/m$ , PDF Number: 11-217) is highly stable with respect to high-energy milling, and fragmentation does not lead to changing of crystal symmetry.

The XRD patterns of milled titanium oxide show broadening of the reflections associated with the small grain size and the microdeformations in the system due to high-energy milling. The dimensional and deformation contributions to the reflection broadening were determined by the Williamson–Hall method. The full-profile analysis of X-ray diffraction reflections showed that ball milling leads to a decrease in the coherent scattering region (CSR) from 30  $\mu\text{m}$  to 26 nm, an increase in microdeformations from 0.02 % for initial powder to 0.49 % for the milled one.

The nanofraction volume of the  $\text{Ti}_3\text{O}_5$  powders after high-energy milling at different durations showed an increase in the content of the nanosized powder phase from 1 to 81 % and decreasing of CSR with an increase in the milling time from 15 to 480 min (Table 1). Measurements of the specific surface areas of the initial  $\text{Ti}_3\text{O}_5$  powders and ball milled powder for 480 min show the significant increasing of the SSA values from 0.1 to 17  $\text{m}^2/\text{g}$ , respectively (Table 1).

Figure 2 shows SEM images of the initial and ball milled  $\text{Ti}_3\text{O}_5$  powders obtained by high-energy milling. The size of the initial microcrystals is 10 – 30  $\mu\text{m}$ . The shape of the microcrystals is complex, at higher magnification one can observe the layering of the structure, steps and terraces are visible. Analysis of SEM images showed that milling for 480 min leads to fragmentation of particles, nanocrystals with size about 25 – 50 nm are observed, nanocrystals stick to each other and form agglomerates up to 1  $\mu\text{m}$  in size.

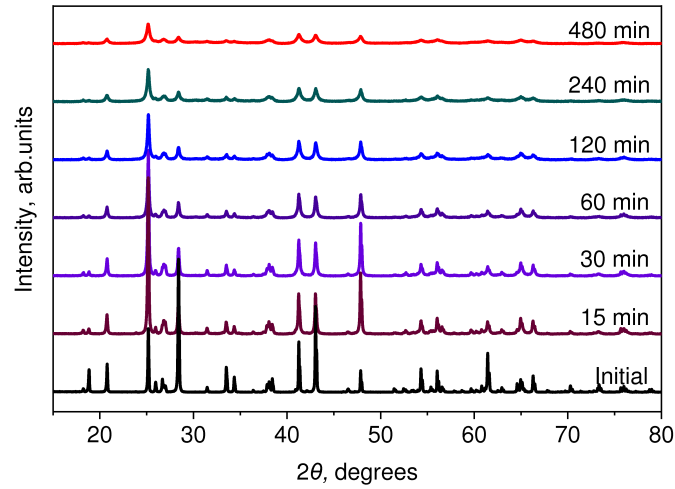
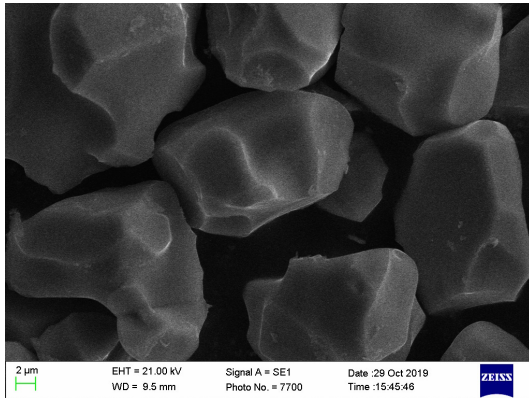


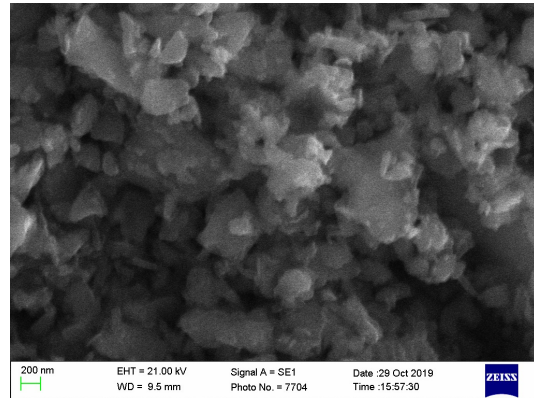
FIG. 1. X-ray diffraction patterns of the initial and milled  $Ti_3O_5$  powders for 15 – 480 minutes

TABLE 1. Characteristics of the initial and milled  $Ti_3O_5$  powders

Milling duration, min	CSR, nm	$\epsilon$ , %	Nanofraction volume, %	SSA (BET), $m^2/g$
Initial	—	0.02	—	$0.120 \pm 0.005$
15	>100	0.15	$1 \pm 0.1$	—
30	>100	0.06	$2 \pm 0.2$	
60	$100 \pm 10$	0.13	$10 \pm 1$	
120	$74 \pm 10$	0.09	$20 \pm 2$	
240	$60 \pm 10$	0.42	$53 \pm 5$	
480	$26 \pm 10$	0.49	$81 \pm 8$	$17.194 \pm 0.348$



(a)



(b)

FIG. 2. SEM images of powders: a) the initial microcrystal powder of  $Ti_3O_5$ ; b) the nanocrystal powder of  $Ti_3O_5$  after ball milling for 480 min

Figure 3 demonstrates the HRTEM micrographs of milled  $\text{Ti}_3\text{O}_5$  powders by high-energy milling. According to HRTEM data, the powder consists of lamellar particles ranging in size from 20 nm to 1  $\mu\text{m}$  (Fig. 3a). Regions with well crystallized structure are observed where the dimensions of blocks are 100 nm. In addition, a sufficiently large number of microcracks and distortions are observed. According to the EDX analysis carried out from a wide area, in addition to Ti, the powder contains zirconium Zr impurities (about 1 wt %) from the milling balls. According to the observed interplanar spacing, the phase corresponds to the  $\text{Ti}_3\text{O}_5$  phase (Fig. 3b) with monoclinic structure (sp. gr.  $C2/m$ , PDF Number: 11-217).

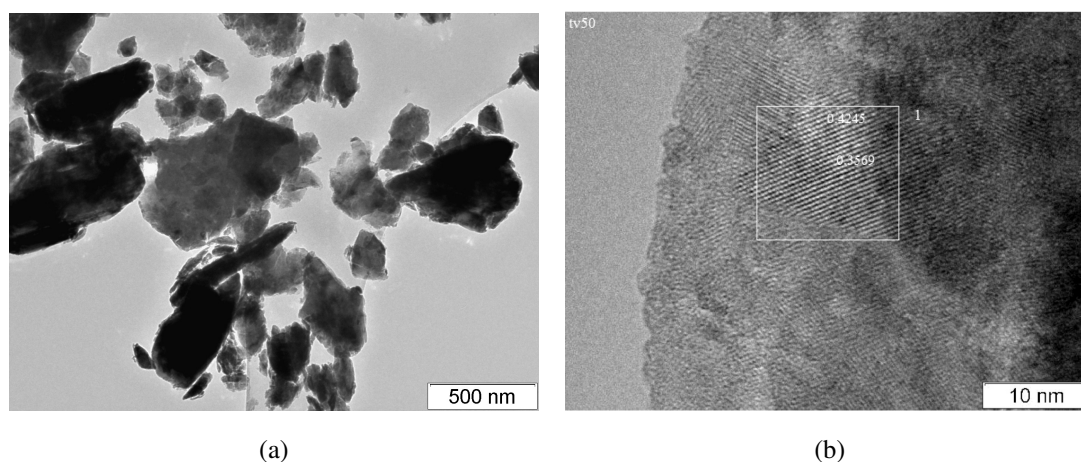


FIG. 3. HRTEM images of milled  $\text{Ti}_3\text{O}_5$  nanocrystals: a) the powder consists of plate-like particles 10 nm – 1  $\mu\text{m}$  in size; b) well crystallized structure, dimensions of blocks 100 nm, the observed interplanar spacings  $d_{hkl}$  correspond to  $\text{Ti}_3\text{O}_5$  phase (PDF 11-217)

#### 4. Conclusions

Thus, the effect of high impact loads on the crystal structure and stability of monoclinic titanium oxide  $\text{Ti}_3\text{O}_5$  during high-energy ball milling was studied by X-ray powder diffraction. A full-profile analysis of the XRD spectra of milled  $\text{Ti}_3\text{O}_5$  powders showed that high-energy ball milling does not lead to disordering or changing of stoichiometry, the structure remains monoclinic (sp. gr.  $C2/m$ ), the phase composition and oxygen content does not changed. According to XRD pattern analysis reflections of milled powders are broadened due to the small particle size and microdeformations. The Williamson-Hall method was used to analyze the dependence of the reduced broadening of reflections on the length of the scattering vector  $s$ . It was found that milling leads to a decrease in CSR from 30  $\mu\text{m}$  to 26 nm, an increase in microdeformations from 0.02 % for the initial powder to 0.49 % for the milled powder for 480 min, and the specific surface area increases from 0.1 to 17  $\text{m}^2/\text{g}$ . The nanophase volume reaches only 81 % after milling for 480 min. According to the SEM and HRTEM data, coalescence of milled nanoparticles is observed, in addition, the particles are rigidly linked to each other and form particle agglomerates. Thus, the milling conditions indicated in this work make it possible to obtain nanosized titanium oxide  $\text{Ti}_3\text{O}_5$  powder, and the monoclinic  $\text{Ti}_3\text{O}_5$  phase (sp. gr.  $C2/m$ ) is a thermodynamically stable phase.

#### References

- [1] Wang Y., Qin Y., et al. One-step synthesis and optical properties of blue titanium suboxide nanoparticles. *J. of Crystal Growth*, 2005, **282** (3–4), P. 402–406.
- [2] Valeeva A.A., Kostenko M.G. Stable  $\text{Ti}_9\text{O}_{10}$  nanophase grown from nonstoichiometric titanium monoxide  $\text{TiO}_y$  nanopowder. *Nanosystems: Phys. Chem. Math.*, 2017, **8** (6), P. 816–822.
- [3] Hauf C., Kniep R., Pfaff, G. Preparation of various titanium suboxide powders by reduction of  $\text{TiO}_2$  with silicon. *J. of Materials Science*, 1999, **34** (6), P. 1287–1292.
- [4] Valeeva A.A., Nazarova S.Z., Rempel A.A. Influence of particle size, stoichiometry, and degree of long-range order on magnetic susceptibility of titanium monoxide. *Physics of the Solid State*, 2016, **58** (4), P. 771–778.
- [5] Kostenko M.G., Valeeva A.A., Rempel A.A. Octahedral Clusters in Various Phases of Nonstoichiometric Titanium Monoxide. *Mendeleev Communications*, 2012, **22** (5), P. 245–247.
- [6] Rempel A.A., Valeeva A.A. Thermodynamics of atomic ordering in nonstoichiometric transition metal monoxides. *Mendeleev Communications*, 2010, **20** (2), P. 101–103.
- [7] Bachina A.K., Popkov V.I., et al. Synthesis, Characterization and Photocatalytic Activity of Spherulite-like  $r\text{-TiO}_2$  in Hydrogen Evolution Reaction and Methyl Violet Photodegradation. *Catalysts*, 2022, **12** (12), 1546.
- [8] Dorosheva I.B., Valeeva A.A., et al. Synthesis and Physicochemical Properties of Nanostructured  $\text{TiO}_2$  with Enhanced Photocatalytic Activity. *Inorganic Materials*, 2021, **57** (5), P. 503–510.
- [9] Valeeva A.A., Dorosheva I.B., et al. Solar photocatalysts based on titanium dioxide nanotubes for hydrogen evolution from aqueous solutions of ethanol. *Int. J. of Hydrogen Energy*, 2021, **46** (32), P. 16917–16924.

- [10] Rempel A.A., Valeeva A.A. Nanostructured titanium dioxide for medicinal chemistry. *Russian Chemical Bulletin*, 2019, **68** (12), P. 2163–2171.
- [11] Dorosheva I.B., Valeeva A.A., Rempel A.A. Sol-gel synthesis of nanosized titanium dioxide at various pH of the initial solution. *AIP Conference Proceedings*, 2017, **1886**, 020006.
- [12] Rempel A.A., Kuznetsova Y.V., et al. High Photocatalytic Activity Under Visible Light of Sandwich Structures Based on Anodic  $TiO_2/CdS$  Nanoparticles/Sol-Gel  $TiO_2$ . *Topics in Catalysis*, 2020, **63** (1–2), P. 130–138.
- [13] Popkov V.I., Bachina A.K., et al. Synthesis, morphology and electrochemical properties of spherulite titania nanocrystals. *Ceramics Int.*, 2020, **46** (14), P. 24483–24487.
- [14] Vasilevskaia A.K., Popkov V.I., Valeeva A.A., Rempel A.A. Formation of nonstoichiometric titanium oxides nanoparticles  $Ti_nO_{2n-1}$  upon heat-treatments of titanium hydroxide and anatase nanoparticles in a hydrogen flow. *Russian J. of Applied Chemistry*, 2016, **89** (8), P. 1211–1220.
- [15] Yoshimatsu K., Sakata O., Ohtomo A. Superconductivity in  $Ti_4O_7$  and  $\gamma-Ti_3O_5$  films. *Scientific Reports*, 2017, **7** (1), P. 1–7.
- [16] Yang S., Zhang L., et al. A novel carbon thermal reduction approach to prepare recorded purity  $\beta-Ti_3O_5$  compacts from titanium dioxide and phenolic resin. *J. of Alloys and Compounds*, 2021, **853**, 157360.
- [17] Tanaka K., Nasu T., et al. Structural Phase Transition between  $\gamma-Ti_3O_5$  and  $\delta-Ti_3O_5$  by Breaking of a One-Dimensionally Conducting Pathway. *Crystal Growth & Design*, 2014, **15** (2), P. 653–657.
- [18] Rempel A.A., Valeeva A.A., Vokhmintsev A.S., Weinstein I.A. Titanium dioxide nanotubes: Synthesis, structure, properties and applications. *Russian Chemical Reviews*, 2021, **90** (11), P. 1397–1414.
- [19] Valeeva A.A., Rempel A.A., et al. Nonstoichiometry, structure and properties of nanocrystalline oxides, carbides and sulfides. *Russian Chemical Reviews*, 2021, **90** (51), P. 601–626.
- [20] Valeeva A.A., Nazarova S.Z., Rempel A.A. Nanosize effect on phase transformations of titanium oxide  $Ti_2O_3$ . *J. of Alloys and Compounds*, 2019, **817**, 153215.
- [21] Valeeva A.A., Nazarova S.Z., et al. Effects of high mechanical treatment and long-term annealing on crystal structure and thermal stability of  $Ti_2O_3$  nanocrystals. *RSC Advances*, 2020, **10** (43), P. 25717–25720.
- [22] Indris S., Amade R., et al. Preparation by High-Energy Milling, Characterization, and Catalytic Properties of Nanocrystalline  $TiO_2$ . *The J. of Physical Chemistry B*, 2005, **109** (49), P. 23274–23278.
- [23] Melchakova O.V., Pechishcheva N.V., Korobitsyna A.D. Mechanically activated rutile and its sorption properties with regard to gallium and germanium. *Tsvetnye Metally*, 2019, **1**, P. 32–39.
- [24] Valeeva A.A., Schröttner H., Rempel A.A. Fragmentation of disordered titanium monoxide of stoichiometric composition  $TiO$ . *Russian Chemical Bulletin*, 2014, **63** (12), P. 2729–2732.
- [25] Valeeva A.A., Nazarova S.Z., Rempel A.A. Size effect on magnetic susceptibility of titanium monoxide nanocrystals. *Physica Status Solidi B*, 2016, **253** (2), P. 392–396.
- [26] Uzunova-Bujnova M., Dimitrov D., et al. Effect of the mechanoactivation on the structure, sorption and photocatalytic properties of titanium dioxide. *Materials Chemistry and Physics*, 2008, **110** (2–3), P. 291–298.
- [27] Ordinatsev D.P., Pechishcheva N.V., et al. Nanosized Titania for Removing Cr(VI) and As(III) from Aqueous Solutions. *Russian J. of Physical Chemistry A*, 2022, **96** (11), P. 2408–2416.
- [28] Hall W.H. X-Ray Line Broadening in Metals. *Proceedings of the Physical Society*, 1949, **62**, P. 741–743.

---

Submitted 5 October 2022; accepted 24 October 2022

#### Information about the authors:

**Albina A. Valeeva** – Institute of Solid State Chemistry, Ural Branch of the Russian Academy of Sciences, 620108, Ekaterinburg, Russia; ORCID 0000-0003-1656-732X; anibla\_v@mail.ru

**Irina B. Dorosheva** – Ural Federal University, 620002, Ekaterinburg, Russia; Institute of Metallurgy, Ural Branch of the Russian Academy of Sciences, 620016 Ekaterinburg, Russia; ORCID 0000-0001-9229-6758; dorosheva1993@mail.ru

**Anna A. Sushnikova** – Institute of Metallurgy, Ural Branch of the Russian Academy of Sciences, 620016 Ekaterinburg, Russia; ORCID 0000-0002-7604-5673; sushnikova.ann@gmail.com

**Conflict of interest:** the authors declare no conflict of interest.

## Synthesis and thermal behavior of $\text{KCe}_2(\text{PO}_4)_3$ , a new full-member in the $\text{A}^I\text{M}_2^{\text{IV}}(\text{PO}_4)_3$ family

Taisiya O. Kozlova<sup>1,a</sup>, Darya N. Vasilyeva<sup>1,2,b</sup>, Daniil A. Kozlov<sup>1,3,c</sup>, Mariia A. Teplonogova<sup>1,3,d</sup>, Alexander E. Baranchikov<sup>1,e</sup>, Nikolay P. Simonenko<sup>1,f</sup>, Vladimir K. Ivanov<sup>1,g</sup>

<sup>1</sup>Kurnakov Institute of General and Inorganic Chemistry of the Russian Academy of Sciences, Moscow, Russia

<sup>2</sup>National Research University Higher School of Economics, Moscow, Russia

<sup>3</sup>Lomonosov Moscow State University, Moscow, Russia

<sup>a</sup>taisia.shekunova@yandex.ru, <sup>b</sup>dnvasileva\_1@edu.hse.ru, <sup>c</sup>kozlov@inorg.chem.msu.ru,

<sup>d</sup>m.teplonogova@gmail.com, <sup>e</sup>a.baranchikov@yandex.ru, <sup>f</sup>n.simonenko@mail.ru, <sup>g</sup>van@igic.ras.ru

Corresponding author: T. O. Kozlova, taisia.shekunova@yandex.ru

PACS 65.40.-b; 61.50.-f; 61.66.Fn

**ABSTRACT** Hydrothermal treatment of nanoscale amorphous ceric phosphate gel in KOH aqueous solutions was found to result in a new  $\text{KCe}_2(\text{PO}_4)_3$  phase. The refinement of the  $\text{KCe}_2(\text{PO}_4)_3$  structure showed that it was isostructural to recently reported  $(\text{NH}_4)\text{Ce}_2(\text{PO}_4)_3$ . For the  $\text{KCe}_2(\text{PO}_4)_3$  phase, the unit cell parameters (sp. gr.  $C2/c$ ) were  $a = 17.3781(3)$  Å,  $b = 6.7287(1)$  Å,  $c = 7.9711(2)$  Å,  $\beta = 102.351(1)^\circ$ ,  $V = 910.53(4)$  Å<sup>3</sup>,  $Z = 4$ . The thermal decomposition of  $\text{KCe}_2(\text{PO}_4)_3$  at 800 °C resulted in the mixture of crystalline  $\text{CePO}_4$  and  $\text{KPO}_3$ .

**KEYWORDS** cerium, potassium, polyphosphate, channel, hydrothermal

**ACKNOWLEDGEMENTS** This work was supported by Russian Science Foundation (Grant no. 21-73-00294, <https://rscf.ru/en/project/21-73-00294/>) using the equipment of the JRC PMR IGIC RAS. The authors thank Dr. A. V. Gavrikov for FT-IR spectroscopy studies.

**FOR CITATION** Kozlova T.O., Vasilyeva D.N., Kozlov D.A., Teplonogova M.A., Baranchikov A.E., Simonenko N.P., Ivanov V.K. Synthesis and thermal behavior of  $\text{KCe}_2(\text{PO}_4)_3$ , a new full-member in the  $\text{A}^I\text{M}_2^{\text{IV}}(\text{PO}_4)_3$  family. *Nanosystems: Phys. Chem. Math.*, 2023, **14** (1), 112–119.

### 1. Introduction

A wide variety of crystalline phosphates of tetravalent metals is mainly represented by double salts [1]. Considerable structural diversity is characteristic of  $\text{A}^I\text{M}_2^{\text{IV}}(\text{PO}_4)_3$  compounds, which usually belong to the “ $\text{NaZr}_2(\text{PO}_4)_3$ ” (NASICON) or “ $\text{NaTh}_2(\text{PO}_4)_3$ ” structural types [2]. The structure of these double phosphates includes a metal-phosphate three-dimensional framework and is characterized by high thermal and chemical stability. Their structural features provide the ability for ion exchange and prospects for their application as matrices for radioactive elements immobilization [3–6], as well as for design of luminescent materials [7–9].

Interestingly, in comparison with actinide phosphates, only 13 crystal structures of ceric phosphates have been reliably characterized until present [10] despite the rich coordination chemistry of Ce(IV) [11] and more than a century of research in ceric phosphates [12]. The lack of information on double cerium(IV) phosphates is primarily due to the high tendency of Ce(IV) to reduce to the trivalent state in the phosphate matrix and form cerium(III) phosphate, which is characterized by extremely high thermodynamic stability [13]. Note that for the compounds having  $\text{A}^I\text{M}_2^{\text{IV}}(\text{PO}_4)_3$  (where  $\text{M} = \text{Ce}^{\text{IV}}$ ) composition, only the  $\text{NH}_4\text{Ce}_2(\text{PO}_4)_3$  phosphate isostructural to  $\text{NH}_4\text{Th}_2(\text{PO}_4)_3$  was reliably characterised [14]. Taking in mind the proximity of the potassium and ammonium ionic radii (1.51 Å [15] and 1.54 Å [16], CN = 8, respectively), the existence of  $\text{KCe}_2(\text{PO}_4)_3$  being an isostructural analog of  $\text{NH}_4\text{Ce}_2(\text{PO}_4)_3$  is anticipated. This assumption is also based on the recently reported pairs of isostructural compounds  $\text{NH}_4\text{Th}_2(\text{PO}_4)_3$  [17] –  $\text{KTh}_2(\text{PO}_4)_3$  [18], and  $\text{K}_2\text{Ce}(\text{PO}_4)_2$  [19] –  $\text{K}_2\text{Th}(\text{PO}_4)_2$  [20].

Thus, this work was aimed at the synthesis of  $\text{KCe}_2(\text{PO}_4)_3$  double cerium(IV)-potassium phosphate. The synthesis strategy was based on the hydrothermal treatment of nanoscale ceric phosphate gels. Their chemical composition can easily be adjusted by electrolyte switching and their fibrous (~ 20 nm) structure makes them highly reactive and prone to crystallisation in aqueous media under relatively mild conditions. This strategy was successfully implemented recently to synthesize new crystalline cerium(IV) phosphates, including  $\text{NH}_4\text{Ce}_2(\text{PO}_4)_3$  [14, 21, 22].

## 2. Experimental Section

The following materials were used as received, without further purification:  $\text{Ce}(\text{NO}_3)_3 \cdot 6\text{H}_2\text{O}$  (pure grade, Lanhit Russia), potassium hydroxide (pure grade, Sigma Aldrich), phosphoric acid (85 wt.% aq,  $\rho = 1.689 \text{ g/cm}^3$ , extra-pure grade, Komponent-Reaktiv Russia), aqueous ammonia (25 wt.%, extra-pure grade, Khimmed Russia), isopropanol (extra-pure grade, Khimmed Russia), distilled water.

First, ceric phosphate solution was synthesized according to the procedure reported earlier [21]. Briefly, nanocrystalline (4 – 5 nm) cerium dioxide (0.100 g) obtained by precipitation from  $\text{Ce}(\text{NO}_3)_3 \cdot 6\text{H}_2\text{O}$  aqueous solution [23] was dissolved in concentrated phosphoric acid (5 ml) at 80 °C. The calculated molar ratio of Ce:P in the solution was 1:126. To the cooled solution, 35 ml of 1 M potassium hydroxide aqueous solution was added under vigorous stirring. The resulting gel-like precipitate (~ 40 mL) was placed in 100 ml Teflon autoclave and subjected to hydrothermal treatment at 180 °C for 24 h. After cooling the autoclave, a precipitate was repeatedly washed using distilled water and dried at 60 °C in air.

Powder X-ray diffraction (PXRD) patterns were acquired using a D/MAX 2500 PC (Rigaku, Japan) powder diffractometer with a rotating anode in the reflection geometry (Bragg-Brentano) with  $\text{Cu K}\alpha_{1,2}$  radiation and a graphite monochromator. PXRD patterns were collected in the 5 – 100 ° $2\theta$  range with a 0.01 ° step. The identification of the diffraction peaks was carried out using the ICDD database (PDF2, release 2020). PXRD pattern refinement was performed using Rietveld method using the MAUD software [24]. Structure refinement and quantitative phase analysis were carried out using structures of monazite (sp. gr.  $P12_1/n1$ ,  $a = 6.788 \text{ \AA}$ ,  $b = 7.0163 \text{ \AA}$ ,  $c = 6.465 \text{ \AA}$ ,  $\beta = 103.43^\circ$ ,  $V = 299.486 \text{ \AA}^3$ ,  $Z = 4$ ) [25] and  $\text{KPO}_3$  (sp. gr.  $P12_1/a1$ ,  $a = 14.02 \text{ \AA}$ ,  $b = 4.54 \text{ \AA}$ ,  $c = 10.28 \text{ \AA}$ ,  $\beta = 101.5^\circ$ ,  $V = 641.194 \text{ \AA}^3$ ,  $Z = 8$ ) [26] taken from Crystallography Open Database [27].

Scanning electron microscopy (SEM) images were obtained using an Amber GMH (Tescan, Czech Republic) microscope operated at an accelerating voltage of 5 kV using a secondary electron (Everhart–Thornley) and backscattered electron (Low Energy BSE) detectors. Energy-dispersive X-ray spectroscopy (EDS) was performed using an Ultim Max (Oxford Instruments, UK) detector at an accelerating voltage of 20 kV.

The Fourier transform infrared (FT-IR) spectra of the samples were recorded using a Bruker ALPHA spectrometer in the range of 400 – 4000  $\text{cm}^{-1}$  in attenuated total reflectance mode.

## 3. Results and discussion

According to powder X-ray diffraction data, hydrothermal treatment of ceric phosphate gel resulted in the formation of a crystalline product with a diffraction pattern similar to  $\text{NH}_4\text{Ce}_2(\text{PO}_4)_3$  phase (monoclinic, sp. gr.  $C2/c$ ,  $a = 17.4719(4) \text{ \AA}$ ,  $b = 6.76928(14) \text{ \AA}$ ,  $c = 7.99286(14) \text{ \AA}$ ,  $\beta = 102.873(1)^\circ$ ,  $V = 921.57(4) \text{ \AA}^3$ ,  $Z = 4$ ) [14]. According to EDS analysis, the average K:Ce:P atomic ratio was close to 1:2:3, which corresponds to the nominal composition of  $\text{KCe}_2(\text{PO}_4)_3$ . PXRD pattern of the obtained sample showed that it is contained an admixture of  $\text{CePO}_4$  with monazite structure (PDF2 [00-032-199]), so further refinement of the structure was carried out taking into account the two-phase composition of the powder. Crystal structure refinement by the Rietveld method was performed using the MAUD software. Experimental and calculated PXRD patterns are shown in Fig. 1. Despite the fact that the measured diffraction pattern corresponded well to the calculated one, the refinement was characterized by rather large R-factor values ( $R_p = 0.087$ ,  $R_{wp} = 0.13$ ), which may be caused by unaccounted structural deviations or the presence of water molecules in the channels of cerium(IV)-potassium phosphate structure. The  $\text{KCe}_2(\text{PO}_4)_3$  phase, similarly to its ammonium analogue, crystallizes in a monoclinic crystal system (sp. gr.  $C2/c$ ,  $a = 17.3781(3) \text{ \AA}$ ,  $b = 6.7287(1) \text{ \AA}$ ,  $c = 7.9711(2) \text{ \AA}$ ,  $\beta = 102.351(1)^\circ$ ,  $V = 910.53(4) \text{ \AA}^3$ ,  $Z = 4$ ).

The structure of the resulting cerium(IV)-potassium phosphate is shown in Fig. 2. The coordination number of cerium in this structure was 9, Ce is surrounded by oxygen atoms of phosphate groups, while the potassium cations are arranged in channels along the  $c$  axis. Note that the  $\text{CePO}_4$  content in the initial sample determined by quantitative phase analysis is rather small and amounts to  $3.1 \pm 0.1 \text{ wt. \%}$ . The formation of cerium(III) phosphate upon hydrothermal treatment of ceric phosphate gels is rather unusual. This fact along with the similar report [21] can contribute to one of the most disputable topics of the chemistry of nanocrystalline ceria, namely its oxygen non-stoichiometry [28–30]. The possibility of the partial reduction of Ce(IV) during hydrothermal synthesis of crystalline cerium(IV) phosphates, as well as monazite structure formation under hydrothermal conditions, have been also discussed recently [31–34] but the exact mechanisms were not analyzed in detail and require further studies.

The newly synthesized double ceric phosphate  $\text{KCe}_2(\text{PO}_4)_3$  complements the family of isostructural compounds having the composition of  $\text{A}^I\text{M}_2^{\text{IV}}(\text{PO}_4)_3$  ( $\text{A}^I = \text{Li, Na, K, NH}_4$ ,  $\text{M}^{\text{IV}} = \text{Th, U}$ ) [17, 18, 35–37]. Note that the synthesis of the “ $\text{KCe}_2(\text{PO}_4)_3$ ” with a monazite structure was recently announced [38]. However, this announcement is doubtful due to the absence of the structural data. Moreover, at the temperatures (above 600 °C) used to synthesize this compound [38], cerium(IV) is extremely prone to reduction to trivalent state [34, 39, 40]. Similarly, the previously reported synthesis of  $\text{BaCe}(\text{PO}_4)_2$  [38] was further argued [41].

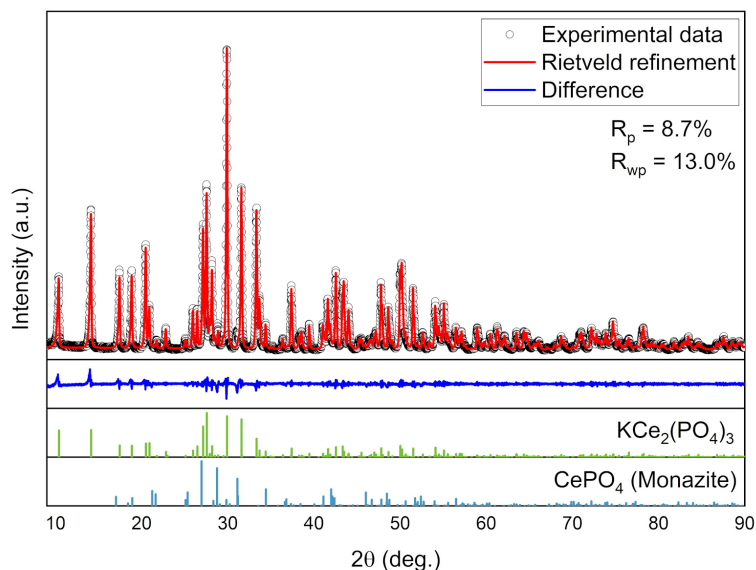


FIG. 1. Rietveld plot for the powder obtained upon hydrothermal treatment of ceric phosphate gel (observed, calculated and difference PXRD profiles along with Bragg peak positions)

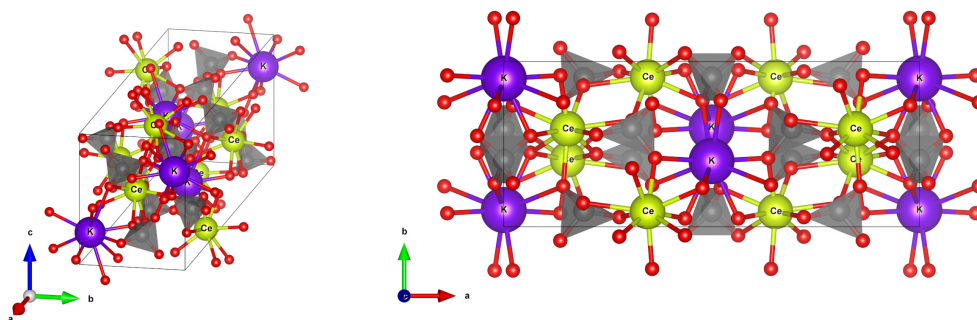


FIG. 2. Crystal structure of  $\text{KCe}_2(\text{PO}_4)_3$ . Yellow spheres denote Ce atoms, K atoms are shown in violet, O atoms are presented as red spheres, P atoms are located in  $\text{PO}_4$  tetrahedra (shown in gray)

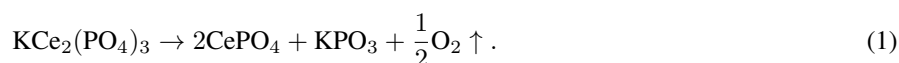
The comparison of thermal behavior of isostructural  $\text{NH}_4\text{Ce}_2(\text{PO}_4)_3$  and  $\text{KCe}_2(\text{PO}_4)_3$  compounds is quite interesting since the formation of single-phase cerium(III) orthophosphate with monazite structure during  $\text{NH}_4\text{Ce}_2(\text{PO}_4)_3$  thermolysis was previously observed [14]. On the other hand, the thermolysis of  $\text{K}_2\text{Ce}(\text{PO}_4)_2$  cerium(IV)-potassium phosphate above  $850^\circ\text{C}$  resulted in the formation of  $\text{K}_3\text{Ce}(\text{PO}_4)_2$  cerium(III)-potassium phosphate as well as of  $\text{CePO}_4$  [19].

According to the thermal analysis, the thermolysis of  $\text{KCe}_2(\text{PO}_4)_3$  (with an admixture of *ca.*  $3.1 \pm 0.1$  wt. %  $\text{CePO}_4$ ) proceeds in two main stages (Fig. 3). The first stage begins at  $\sim 220^\circ\text{C}$  and ends at  $540^\circ\text{C}$  and is apparently associated with the release of water (probably presented in the channels of the  $\text{KCe}_2(\text{PO}_4)_3$  structure) as well as oxygen [10, 42]. The second stage begins at about  $600^\circ\text{C}$  and corresponds to the release of oxygen due to the reduction of cerium(IV) to cerium(III).

To clarify the processes occurring at each stage of thermal decomposition of  $\text{KCe}_2(\text{PO}_4)_3$  and to estimate the composition of the thermolysis products, the synthesized  $\text{KCe}_2(\text{PO}_4)_3$  (with  $3.1 \pm 0.1$  wt. %  $\text{CePO}_4$  admixture) was annealed at either  $580^\circ\text{C}$  or  $800^\circ\text{C}$  in a muffle furnace for 2 h in air (the heating rate was  $5^\circ\text{C}/\text{min}$ ).

Quantitative phase analysis of PXRD data showed that the heating at  $580^\circ\text{C}$  did not change dramatically the phase composition of the powder. Like the bare sample, it contained  $\text{KCe}_2(\text{PO}_4)_3$  as the major component and an admixture of  $\text{CePO}_4$  ( $23 \pm 5$  wt. %). The reduction of cerium(IV) to cerium(III) at high temperatures is characteristic of tetravalent cerium phosphates and has been repeatedly observed recently [14, 19, 43, 44].

According to PXRD, the thermal treatment of  $\text{KCe}_2(\text{PO}_4)_3$  at  $800^\circ\text{C}$  resulted in its complete decomposition and the formation of  $\text{CePO}_4$  and potassium polyphosphate  $\text{KPO}_3$  (PDF2 35-819). According to quantitative phase analysis, the content of  $\text{KPO}_3$  in the product was  $21.0 \pm 1.2$  wt. % ( $34.6 \pm 2.0$  mol. %), which agreed well with the anticipated molar ratio  $\text{CePO}_4:\text{KPO}_3 = 2:1$ . Thus, the thermolysis of  $\text{KCe}_2(\text{PO}_4)_3$  in air can be described by the following reaction scheme:



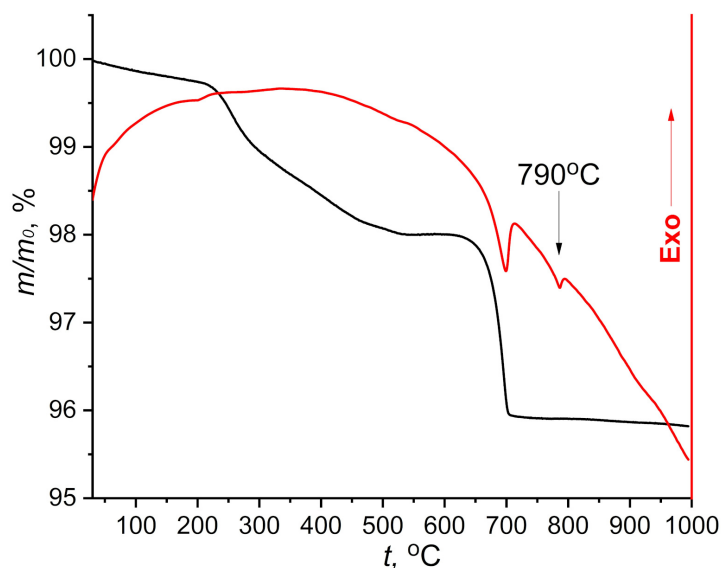


FIG. 3. Thermal decomposition curve of  $\text{KCe}_2(\text{PO}_4)_3$  (with  $3.1 \pm 0.1$  wt. %  $\text{CePO}_4$  admixture) in air

In accordance with equation (1), the total weight loss for the  $\text{KCe}_2(\text{PO}_4)_3$  phase should be *ca.* 2.5 wt. %, whereas the experimentally measured weight loss was much greater ( $\sim 4$  wt. %). Such a difference can be due to the presence of water molecules in the structure of  $\text{KCe}_2(\text{PO}_4)_3$  which were not accounted during the structural analysis. These  $\text{H}_2\text{O}$  molecules can be trapped in the  $\text{KCe}_2(\text{PO}_4)_3$  structural channels and release from the phase at temperatures up to  $540^\circ\text{C}$ . Our estimates of the water content resulted in the chemical composition of  $\text{KCe}_2(\text{PO}_4)_3 \cdot 0.4\text{H}_2\text{O}$ . Most probable, the water content can vary in a certain range and the exact chemical composition of  $\text{KCe}_2(\text{PO}_4)_3 \cdot x\text{H}_2\text{O}$  needs further refinement.

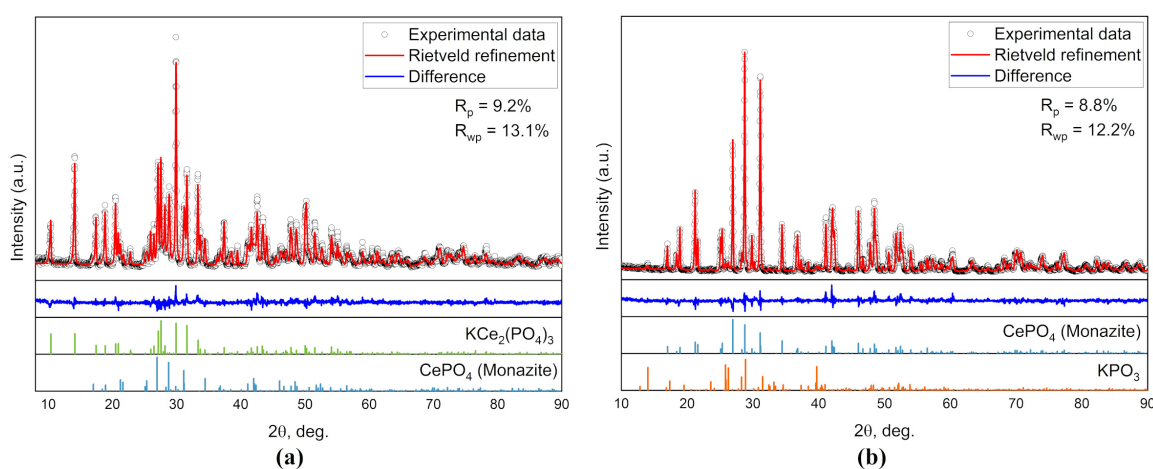


FIG. 4. Rietveld plots for the samples obtained after the thermal treatment of  $\text{KCe}_2(\text{PO}_4)_3$  (with  $3.1 \pm 0.1$  wt. %  $\text{CePO}_4$  admixture) sample at  $580^\circ\text{C}$  (a) or  $800^\circ\text{C}$  (b) (observed, calculated and difference PXRD profiles along with Bragg peaks positions for  $\text{CePO}_4$  and  $\text{KPO}_3$ )

Figure 5 shows the IR spectra of the bare  $\text{KCe}_2(\text{PO}_4)_3$  sample (with  $3.1 \pm 0.1$  wt. %  $\text{CePO}_4$  admixture) and the samples obtained after its thermal treatment at  $580^\circ\text{C}$  or  $800^\circ\text{C}$ . The IR spectra for the samples before and after the thermal treatment at  $580^\circ\text{C}$  are almost identical and coincide well with the IR spectrum of the  $\text{NH}_4\text{Ce}_2(\text{PO}_4)_3$  phase [14]. In the regions of  $1100 - 900\text{ cm}^{-1}$  and  $650 - 440\text{ cm}^{-1}$  the characteristic absorption bands are observed, which are related to the stretching and bending vibrations of phosphate anions, respectively [33, 45].

In the infrared spectrum of the powder obtained at  $800^\circ\text{C}$ , extra absorption bands are presented at  $1280\text{ cm}^{-1}$ ,  $865\text{ cm}^{-1}$ ,  $760\text{ cm}^{-1}$ ,  $680\text{ cm}^{-1}$ , and  $490\text{ cm}^{-1}$  which correspond to polyphosphate moieties [46–49]. Thus, IR data agree well with the XRD results and confirm the formation of potassium polyphosphate  $\text{KPO}_3$  upon the thermolysis of cerium(IV)-potassium phosphate  $\text{KCe}_2(\text{PO}_4)_3$ .

According to scanning electron microscopy, the  $\text{KCe}_2(\text{PO}_4)_3$  phase is represented by  $200\text{ nm}$  particles having the shape of truncated octahedrons. Thermal treatment at  $580^\circ\text{C}$  does not significantly change the size of the particles, but after the treatment at  $800^\circ\text{C}$ , large crystals up to several tens of micrometers in size are observed along with the relatively

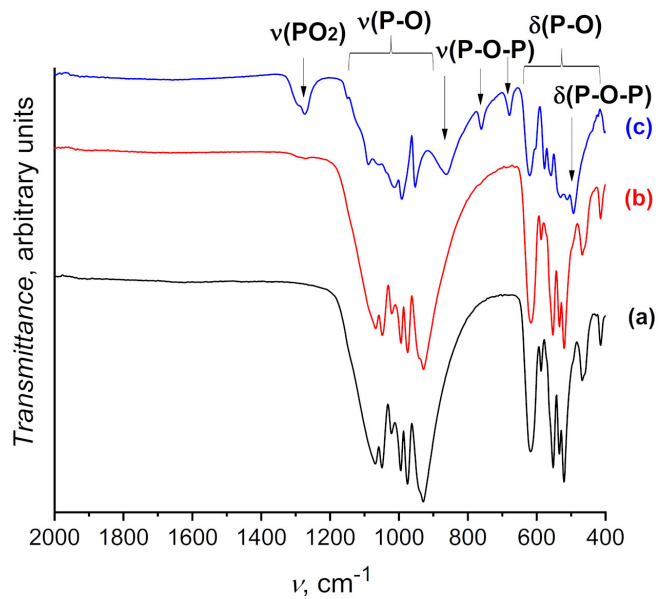


FIG. 5. IR spectra for the samples obtained after the thermolysis of  $\text{KCe}_2(\text{PO}_4)_3$  (with  $3.1 \pm 0.1$  wt. %  $\text{CePO}_4$  admixture) (a) at  $580^\circ\text{C}$  (b) or  $800^\circ\text{C}$  (c)

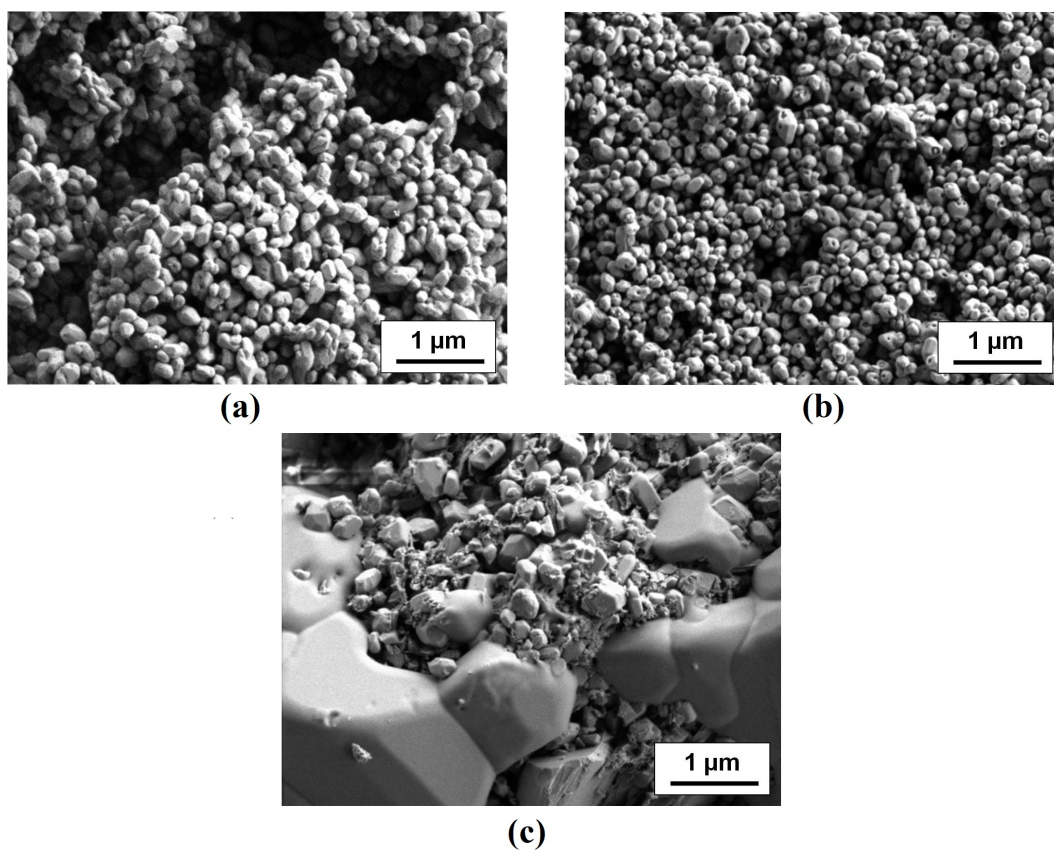


FIG. 6. SEM images for the samples obtained by thermolysis of the bare cerium(IV)-potassium phosphate (a) at  $580^\circ\text{C}$  (b) or  $800^\circ\text{C}$  (c)

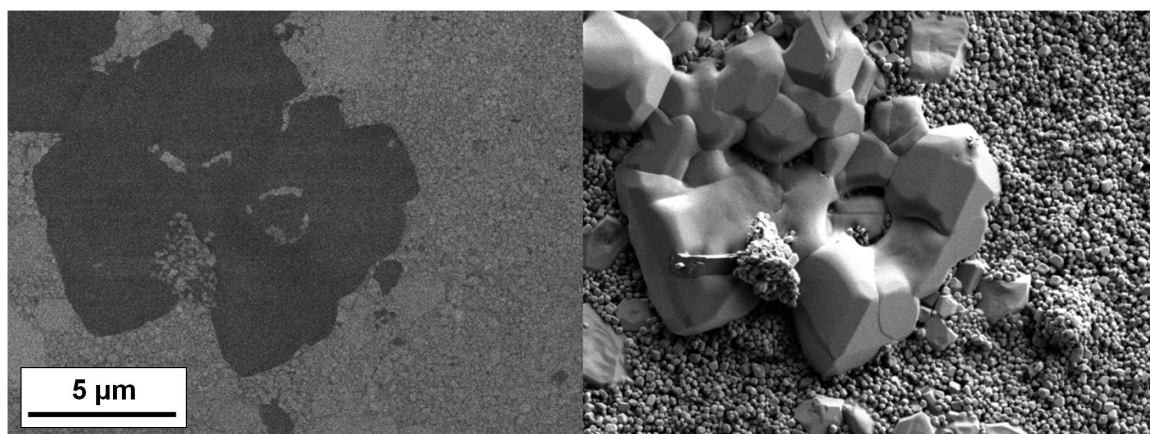


FIG. 7. SEM images for the sample obtained by thermolysis of the bare cerium(IV)-potassium phosphate at 800 °C: backscattered electron detection mode (left), secondary electrons detection mode (right)

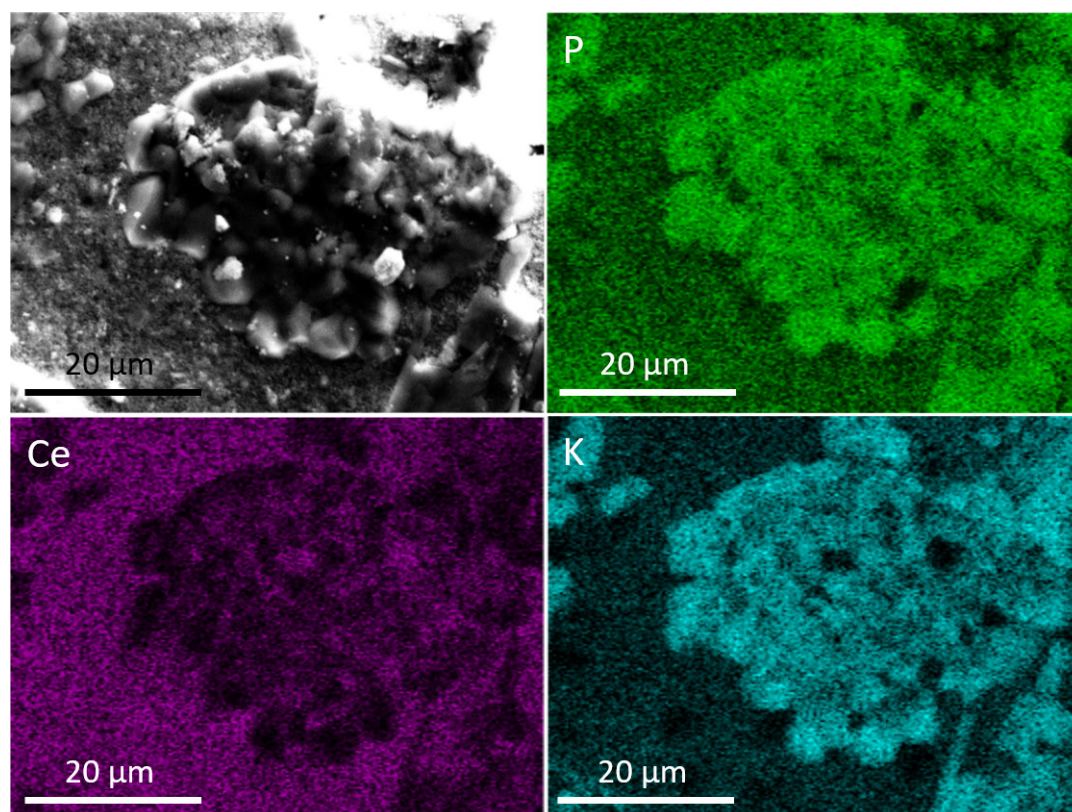


FIG. 8. SEM image and the corresponding EDS distribution maps of P, Ce and K for the sample obtained by thermolysis of the bare cerium(IV)-potassium phosphate at 800 °C

small particles (Fig. 6). The images taken in the backscattered electron detection mode (Fig. 7) show that these large crystals have a lower average atomic weight than the smaller crystals. Thus, it can be assumed that small and large crystals correspond to  $CePO_4$  and  $KPO_3$  phases, respectively (Fig. 6,7).

Large size of  $KPO_3$  crystals is most probably related to their growth from melt which can form upon heating and thermolysis of  $KCe_2(PO_4)_3$ . In the  $CePO_4$ - $KPO_3$ - $Ce(PO_3)_3$  system [50], the  $CePO_4$ - $KPO_3$  quasi-binary section corresponds to an eutectic type system with an eutectic point of 790 °C (85 wt. %  $KPO_3$ ). Note, the eutectic point agrees the position of the endothermic effect in the differential scanning calorimetry data for the bare cerium(IV)-potassium phosphate (Fig. 3). Thus, upon its heating to 800 °C, the liquid  $KPO_3$ -rich phase forms and, upon the subsequent cooling of the two-phase liquid-solid system, the crystallization of potassium polyphosphate occurs. Cerium(III) orthophosphate is anticipated to possess low solubility in the phosphate melt and the size of  $CePO_4$  crystals does not change significantly.

The EDS results corroborate the above considerations and indicate that the large aggregates dominantly contain potassium and phosphorus (Fig. 8).

#### 4. Conclusions

In this paper, nanoscale amorphous ceric phosphate was used as a convenient starting material for the hydrothermal synthesis of crystalline ceric phosphates. We have demonstrated that the hydrothermal treatment of the gels obtained by mixing of the ceric phosphate solution and 1 M potassium hydroxide aqueous solution results in the formation of the previously unknown cerium(IV)-potassium phosphate,  $\text{KCe}_2(\text{PO}_4)_3$ .  $\text{KCe}_2(\text{PO}_4)_3$  was found to be isostructural to  $\text{NH}_4\text{Ce}_2(\text{PO}_4)_3$ , and belongs to the  $A^I\text{M}_2^{IV}(\text{PO}_4)_3$  ( $A^I = \text{Li, Na, K, NH}_4$ ,  $\text{M}^{IV} = \text{Th, U}$ ) family. Thermal analysis data indicated that double ceric phosphate  $\text{KCe}_2(\text{PO}_4)_3$  decomposes through two stages with the formation of the mixture of  $\text{CePO}_4$  and  $\text{KPO}_3$  at 800 °C.

#### References

- [1] Pet'kov V.I. Complex phosphates formed by metal cations in oxidation states I and IV. *Russ. Chem. Rev.*, 2012, **81**, P. 606–637.
- [2] Locoock A.J. Crystal chemistry of actinide phosphates and arsenates. *Struct. Chem. Inorg. Actin. Compd.*, Elsevier, Amsterdam, 2007, P. 217–278.
- [3] Dacheux N., Clavier N., Robisson A.C., Terra O., Audubert F., Lartigue J.É., Guy C. Immobilisation of actinides in phosphate matrices. *Comptes Rendus Chim.*, 2004, **7**, P. 1141–1152.
- [4] Neumeier S., Arinicheva Y., Ji Y., Heuser, Julia M. Kowalski P.M., Kegler P., Schlenz H., Bosbach D., Deissmann G. New insights into phosphate based materials for the immobilisation of actinides. *Radiochim. Acta.*, 2017, **105**, P. 961–984.
- [5] Orlova A.I., Kitaev D.B., Volkov Yu.F., Pet'kov V.I., Kurazhkovskaya V.S., Spiridonova M.L. Double phosphates of Ce(IV) and some mono- and bivalent elements. *Radiochemistry*, 2001, **43**, P. 225–228.
- [6] Achary S.N., Bevara S., Tyagi A.K. Recent progress on synthesis and structural aspects of rare-earth phosphates. *Coord. Chem. Rev.*, 2017, **340**, P. 266–297.
- [7] Asabina E., Sedov V., Pet'kov V., Deyneko D., Kovalsky A. Synthesis, structure and luminescence properties of the europium-containing NASICON type phosphates. *J. Sol-Gel Sci. Technol.*, 2023.
- [8] Krutyak N., Spassky D., Deyneko D.V., Antropov A., Morozov V.A., Lazoryak B.I., Nagirnyi V. NASICON-type  $\text{Na}_{3.6}\text{Lu}_{1.8-x}(\text{PO}_4)_3 \cdot x\text{Eu}^{3+}$  phosphors: Structure and luminescence. *Dalt. Trans.*, 2022, **51**, P. 11840–11850.
- [9] Kozlova T.O., Popov A.L., Kolesnik I.V., Kolmanovich D.D., Baranchikov A.E., Shcherbakov A.B., Ivanov V.K. Amorphous and crystalline cerium(IV) phosphates: Biocompatible ROS-scavenging sunscreens. *J. Mater. Chem. B.*, 2022, **10**, P. 1775–1785.
- [10] Kozlova T.O., Baranchikov A.E., Ivanov V.K. Cerium(IV) orthophosphates (Review). *Russ. J. Inorg. Chem.*, 2021, **66**, P. 1761–1778.
- [11] So Y.M., Leung W.H. Recent advances in the coordination chemistry of cerium(IV) complexes. *Coord. Chem. Rev.*, 2017, **340**, P. 172–197.
- [12] Hartley W.N. Contributions to the chemistry of cerium compounds. *J. Chem. Soc. Trans.*, 1882, **41**, P. 202–209.
- [13] Sroor F.M.A., Edelmannand F.T. Tetravalent chemistry: Inorganic. *Rare Earth Elem. Fundam. Appl.*, John Wiley & Sons Ltd, Chichester, 2012, P. 313–320.
- [14] Shekunova T.O., Istomin S.Y., Mironov A.V., Baranchikov A.E., Yapryntsev A.D., Galstyan A.A., Simonenko N.P., Gippius A.A., Zhurenko S.V., Shatalova T.B., Skogareva L.S., Ivanov V.K. Crystallization pathways of cerium(IV) phosphates under hydrothermal conditions: A search for new phases with a tunnel structure. *Eur. J. Inorg. Chem.*, 2019, **27**, P. 3242–3248.
- [15] Shannon R.D., Prewitt C.T. Effective ionic radii in oxides and fluorides. *Acta Crystallogr. Sect. B Struct. Crystallogr. Cryst. Chem.*, 1969, **25**, P. 925–946.
- [16] Sidey V. On the effective ionic radii for ammonium. *Acta Crystallogr. Sect. B Struct. Sci. Cryst. Eng. Mater.*, 2016, **72**, P. 626–633.
- [17] Salvadó M.A., Pertierra P., Bortun A.I., Trobajo C., García J.R. Phosphorous acid and urea: Valuable sources of phosphorus and nitrogen in the hydrothermal synthesis of ammonium-thorium phosphates. *Inorg. Chem.*, 2008, **47**, P. 7207–7210.
- [18] Matkovic B., Prodic B., Sljukic M. The crystal structure of potassium dithorium trisphosphate,  $\text{KTh}_2(\text{PO}_4)_3$ . *Croat. Chem. Acta.*, 1968, **40**, P. 147.
- [19] Bevara S., Achary S.N., Patwe S.J., Sinha A.K., Tyagi A.K. Preparation and crystal structure of  $\text{K}_2\text{Ce}(\text{PO}_4)_2$ : A new complex phosphate of Ce(IV) having structure with one-dimensional channels. *Dalt. Trans.*, 2016, **45**, P. 980–991.
- [20] Yu N., Klepov V.V., Schlenz H., Bosbach D., Kowalski P.M., Li Y., Alekseev E.V. Cation-dependent structural evolution in  $\text{A}_2\text{Th}(\text{T}^V\text{O}_4)_2$  ( $A = \text{Li, Na, K, Rb, Cs}$ ;  $\text{T} = \text{P and As}$ ) series. *Cryst. Growth Des.*, 2017, **17**, P. 1339–1346.
- [21] Shekunova T.O., Baranchikov A.E., Ivanova O.S., Skogareva L.S., Simonenko N.P., Karavanova Yu. A., Lebedev V.A., Borilo L.P., Ivanov V.K. Cerous phosphate gels: Synthesis, thermal decomposition and hydrothermal crystallization paths. *J. Non. Cryst. Solids.*, 2016, **447**, P. 183–189.
- [22] Kozlova T.O., Mironov A.V., Istomin S.Y., Birihevskaya K.V., Gippius A.A., Zhurenko S.V., Shatalova T.B., Baranchikov A.E., Ivanov V.K. Meet the cerium(IV) phosphate sisters:  $\text{Ce}^{IV}(\text{OH})\text{PO}_4$  and  $\text{Ce}_2^{IV}\text{O}(\text{PO}_4)_2$ . *Chem. – A Eur. J.*, 2020, **26**, P. 12188–12193.
- [23] Kolesnik I.V., Shcherbakov A.B., Kozlova T.O., Kozlov D.A., Ivanov V.K. Comparative analysis of sun protection characteristics of nanocrystalline cerium dioxide. *Russ. J. Inorg. Chem.*, 2020, **65**, P. 960–966.
- [24] Lutterotti L. Total pattern fitting for the combined size–strain–stress–texture determination in thin film diffraction. *Nucl. Instruments Methods Phys. Res. Sect. B Beam Interact. with Mater. Atoms.*, 2010, **268**, P. 334–340.
- [25] Ni Y., Hughes J.M., Mariano A.N. Crystal chemistry of the monazite and xenotime structures. *Am. Mineral.*, 1995, **80**, P. 21–26.
- [26] Jost K.H., Schulze H.J. Zur phasentransformation des kaliumpolyphosphates  $(\text{KPO}_3)_x$ . *Acta Crystallogr. Sect. B Struct. Crystallogr. Cryst. Chem.*, 1969, **25**, P. 1110–1118.
- [27] Graulis S., Chateigner D., Downs R.T., Yokochi A.F.T., Quirós M., Lutterotti L., Manakova E., Butkus J., Moeck P., Le Bail A. Crystallography Open Database – An open-access collection of crystal structures. *J. Appl. Crystallogr.*, 2009, **42**, P. 726–729.
- [28] Shcherbakov A.B., Zholobak N.M., Ivanov V.K. Biological, biomedical and pharmaceutical applications of cerium oxide. *Cerium Oxide (CeO<sub>2</sub>): Synthesis, Properties and Applications*, 2020, Elsevier, Amsterdam, P. 279–358.
- [29] Plakhova T.V., Romanchuk A.Y., Yakunin S.N., Dumas T., Demir S., Wang S., Minasian S.G., Shuh D.K., Tylliszczak T., Shiryayev A.A., Egorov A.V., Ivanov V.K., Kalmykov S.N. Solubility of Nanocrystalline Cerium Dioxide: Experimental Data and Thermodynamic Modeling. *J. Phys. Chem. C*, 2016, **120**(39), P. 22615–22626.
- [30] Baranchikov A.E., Polezhaeva O.S., Ivanov V.K., Tretyakov Y.D. Lattice expansion and oxygen non-stoichiometry of nanocrystalline ceria. *Cryst EngComm*, 2010, **12**(11), P. 3531–3533.

- [31] Enikeeva M.O., Proskurina O.V., Danilovich D.P., Gusarov V.V. Formation of nanocrystals based on equimolar mixture of lanthanum and yttrium orthophosphates under microwave-assisted hydrothermal synthesis. *Nanosyst.: Phys. Chem. Math.*, 2020, **11**(6), P. 705–715.
- [32] Kozlova T.O., Vasil'eva D.N., Kozlov D.A., Teplonogova M.A., Birichevskaya K.V., Baranchikov A.E., Gavrikov A.V., Ivanov V.K. On the chemical stability of  $Ce^{IV}(PO_4)(HPO_4)_{0.5}(H_2O)_{0.5}$  in alkaline media. *Russ. J. Inorg. Chem.*, 2022, **67**, P. 1901–1907.
- [33] Skogareva L.S., Shekunova T.O., Baranchikov A.E., Yapryntsev A.D., Sadovnikov A.A., Ryumin M.A., Minaeva N.A., Ivanov V.K. Synthesis of cerium orthophosphates with monazite and rhabdophane structure from phosphoric acid solutions in the presence of hydrogen peroxide. *Russ. J. Inorg. Chem.*, 2016, **61**, P. 1219–1224.
- [34] Brandel V., Clavier N., Dacheux N. Synthesis and characterization of uranium (IV) phosphate-hydrogenphosphate hydrate and cerium (IV) phosphate-hydrogenphosphate hydrate. *J. Solid State Chem.*, 2005, **178**, P. 1054–1063.
- [35] Topić M., Napijalo M., Popović S., Zeljić Z. Temperature Dependence of Some Properties of  $NaTh_2(PO_4)_3$  Ferroelectric Crystals. *Phys. stat. sol.*, 1972, **11**, P. 787–790.
- [36] Guesdon A., Provost J., Ravcau B. New thorium and uranium monophosphates in the  $KTh_2(PO_4)_3$  family: Structure and cationic non-stoichiometry. *J. Mater. Chem.*, 1999, **9**, P. 2583–2587.
- [37] Brandel V., Dacheux N. Chemistry of tetravalent actinide phosphates – Part II. *J. Solid State Chem.*, 2004, **177**, P. 4755–4767.
- [38] Orlova A.I., Kitaev D.B., Kazantsev N.G., Samoilov S.G. Double phosphates of Ce (IV) and some mono- and divalent elements: synthesis and crystal structure. *Radiochemistry*, 2002, **44**, P. 326–331.
- [39] Bregiroux D., Terra O., Audubert F., Dacheux N., Serin V., Podor R., Bernache-Assollant D. Solid-state synthesis of monazite-type compounds containing tetravalent elements. *Inorg. Chem.*, 2007, **46**, P. 10372–10382.
- [40] Bamberger C.E., Begun G.M., Brynestad J., Land J.F. Simultaneous precipitation of phosphates of Bi (III) and Ce(IV) or Ce (III). Characterization of precipitates and their ignition products. *Radiochim. Acta.*, 1982, **31**, P. 57–64.
- [41] Popa K., Bregiroux D., Konings R.J.M., Gouder T., Popa A.F., Geisler T., Raison P.E. The chemistry of the phosphates of barium and tetravalent cations in the 1:1 stoichiometry. *J. Solid State Chem.*, 2007, **180**, P. 2346–2355.
- [42] Kozlova T.O., Baranchikov A.E., Birichevskaya K.V., Kozlov D., Simonenko N.P., Gavrikov A.V., Teplonogova M.A., Ivanov V.K. On the thermal decomposition of cerium(IV) hydrogen phosphate  $Ce(PO_4)(HPO_4)_{0.5}(H_2O)_{0.5}$ . *Russ. J. Inorg. Chem.*, 2021, **66**, P. 1624–1632.
- [43] Dacheux N., Podor R., Brandel V., Genet M. Investigations of systems  $ThO_2-MO_2-P_2O_5$  (M = U, Ce, Zr, Pu). Solid solutions of thorium-uranium (IV) and thorium-plutonium (IV) phosphate-diphosphates. *J. Nucl. Mater.*, 1998, **252**, P. 179–186.
- [44] Bevara S., Mishra K.K., Patwe S.J., Ravindran T.R., Gupta M.K., Mittal R.K., P.S. Ram, Sinha A.K., Achary S.N., Tyagi A.K. Phase transformation, vibrational and electronic properties of  $K_2Ce(PO_4)_2$ : A combined experimental and theoretical study. *Inorg. Chem.*, 2017, **56**, P. 3335–3348.
- [45] Clavier N., Mesbah A., Szenknect S., Dacheux N. Monazite, rhabdophane, xenotime & churchite: Vibrational spectroscopy of gadolinium phosphate polymorphs. *Spectrochim. Acta – Part A Mol. Biomol. Spectrosc.*, 2008, **205**, P. 85–94.
- [46] Jerroudi M., Bih L., Azrou M., Manoun B., Saadouni I., Lazor P. Investigation of novel low melting phosphate glasses inside the  $Na_2O-K_2O-ZnO-P_2O_5$  system. *J. Inorg. Organomet. Polym. Mater.*, 2020, **30**, P. 532–542.
- [47] Nassar A.M., El Oker M.M., Radwan S.N., Nabhan E. Effect of MO (CuO, ZnO, and CdO) on the compaction of sodium meta phosphate sealing glass. *Curr. Sci. Int.*, 2013, **2**, P. 1–7.
- [48] Nabhan E., Abd-Allah W.M., Ezz-El-Din F.M. Optical study of gamma irradiated sodium metaphosphate glasses containing divalent metal oxide MO (ZnO or CdO). *Results Phys.*, 2017, **7**, P. 119–125.
- [49] Ghoneim N.A., Abdelghany A.M., Abo-Naf S.M., Moustafa F.A., Elbadry Kh.M. Spectroscopic studies of lithium phosphate, lead phosphate and zinc phosphate glasses containing  $TiO_2$ : Effect of gamma irradiation. *J. Mol. Struct.*, 2013, **1035**, P. 209–217.
- [50] Szczygiel I. The system  $CePO_4-KPO_3-Ce(PO_3)_3$ . *Thermochim. Acta.*, 2003, **402**, P. 153–158.

---

Submitted 28 November 2022; revised 27 December 2022; accepted 28 December 2022

#### Information about the authors:

T. O. Kozlova – Kurnakov Institute of General and Inorganic Chemistry of the Russian Academy of Sciences, Leninsky prospect, 31, Moscow, 119991, Russia; ORCID 0000-0002-9757-9148; taisia.shekunova@yandex.ru

D. N. Vasilyeva – Kurnakov Institute of General and Inorganic Chemistry of the Russian Academy of Sciences, Leninsky prospect, 31, Moscow, 119991, Russia; National Research University Higher School of Economics, Moscow, Myasnit-skaya str., 20, 101000, Russia; dnavasileva\_1@edu.hse.ru

D. A. Kozlov – Kurnakov Institute of General and Inorganic Chemistry of the Russian Academy of Sciences, Leninsky prospect, 31, Moscow, 119991, Russia; Lomonosov Moscow State University, Leninskie Gory 1, Moscow, 119991, Russia; ORCID 0000-0003-0620-8016; kozlov@inorg.chem.msu.ru

M. A. Teplonogova – Kurnakov Institute of General and Inorganic Chemistry of the Russian Academy of Sciences, Leninsky prospect, 31, Moscow, 119991, Russia; Lomonosov Moscow State University, Leninskie Gory 1, Moscow, 119991, Russia; ORCID 0000-0002-4820-8498; m.teplonogova@gmail.com

A. E. Baranchikov – Kurnakov Institute of General and Inorganic Chemistry of the Russian Academy of Sciences, Leninsky prospect, 31, Moscow, 119991, Russia; ORCID 0000-0002-2378-7446; a.baranchikov@yandex.ru

N. P. Simonenko – Kurnakov Institute of General and Inorganic Chemistry of the Russian Academy of Sciences, Leninsky prospect, 31, Moscow, 119991, Russia; ORCID 0000-0002-4209-6034; n.simonenko@mail.ru

V. K. Ivanov – Kurnakov Institute of General and Inorganic Chemistry of the Russian Academy of Sciences, Leninsky prospect, 31, Moscow, 119991, Russia; ORCID 0000-0003-2343-2140; van@igic.ras.ru

Conflict of interest: the authors declare no conflict of interest.

## Influence of using different types of microreactors on the formation of nanocrystalline BiFeO<sub>3</sub>

Olga V. Proskurina<sup>1,2,a</sup>, Rufat Sh. Abiev<sup>1,2,b</sup>, Vladimir N. Nevedomskiy<sup>1,c</sup>

<sup>1</sup>Ioffe Institute, St. Petersburg, Russia

<sup>2</sup>St. Petersburg State Institute of Technology, St. Petersburg, Russia

<sup>a</sup>proskurinaov@mail.ru, <sup>b</sup>abiev.rufat@gmail.com, <sup>c</sup>nevedom@mail.ioffe.ru

Corresponding author: Olga V. Proskurina, proskurinaov@mail.ru

**ABSTRACT** The influence of the coprecipitation of bismuth and iron hydroxides in microreactors of various types on the formation of nanocrystalline bismuth orthoferrite during the heat treatment of the deposit was described. Free impinging-jets microreactor, microreactor with submerged jets, microreactor with intensively swirling flows were used. It was revealed that nanocrystalline bismuth orthoferrite with the smallest weighted average crystallite size of 12 nm is formed when a microreactor with tangentially swirling flows of reagent solutions is used for coprecipitation of hydroxides. The minimum size of BiFeO<sub>3</sub> crystallites according to transmission electron microscopy data is determined as 3–4 nm.

**KEYWORDS** free impinging-jets microreactor, microreactor with submerged jets, microreactor with intensively swirling flows, nanocrystals, bismuth ferrite.

**ACKNOWLEDGEMENTS** X-ray diffraction studies were performed employing the equipment of the Engineering Center of the St. Petersburg State Institute of Technology. TEM characterization was performed using equipment owned by the Federal Joint Research Center “Material science and characterization in advanced technology”. The authors are grateful to V. V. Gusarov for his attention to the work. The research was supported by the Russian Science Foundation Grant 20-63-47016.

**FOR CITATION** Proskurina O.V., Abiev R.Sh., Nevedomskiy V.N. Influence of using different types of microreactors on the formation of nanocrystalline BiFeO<sub>3</sub>. *Nanosystems: Phys. Chem. Math.*, 2023, **14** (1), 120–126.

### 1. Introduction

The morphology, size and structure of nanoparticles, the presence and amount of impurity phases in a nanopowder can significantly affect the mechanical and functional properties of the materials obtained from them [1–3], including the magnetic, electrical, photocatalytic properties of bismuth orthoferrite [4–11]. These reasons stimulate the development of methods for synthesis of bismuth orthoferrite nanopowders, which would provide their morphological characteristics, dispersed and phase composition, necessary to obtain materials with needed properties.

There are several methods for synthesis of bismuth orthoferrite nanoparticles, for example, solution combustion [12–20], hydrothermal synthesis [21–27], and solid phase synthesis [28–35]. However, obtaining single-phase nanocrystalline powders based on bismuth orthoferrite still causes difficulties [28, 36–40]. One of the ways to obtain oxide nanoparticles with a given composition and size is the use of microreactors [41, 42].

For example, the synthesis of nanocrystals of complex oxides using free impinging-jets microreactors demonstrated promising results [43–47]. Free impinging-jets microreactors make it possible to dissipate a large amount of energy in very small volumes [48]. This, under certain flow regimes of free impinging-jets of reagent solutions, leads to the formation of reaction zones with sizes of the order of hundreds of nanometers with localization of the initial components in them in a given stoichiometry [49]. Such self-organization of spatially separated nanoreactors makes it possible to count on the possibility of forming nanoparticles of a given composition and size [50].

When a free impinging-jets microreactor is used to obtain precursors for the following synthesis of bismuth orthoferrite, as shown in [51–53], the formation of by-products that differ in composition from the stoichiometry of the target phase is almost completely excluded. Comparison of various apparatuses for coprecipitation of precursors were considered in [51], in particular, a microreactor with submerged jets. By use of different types of microreactors, the authors of [51] obtained predominantly single-crystal BiFeO<sub>3</sub> nanoparticles with a narrow size distribution and small average sizes of crystallites and particles. At the same time, these sizes are not always close to the minimum possible sizes of bismuth orthoferrite crystals [54].

Thus, it is important to determine the types of microreactors and synthesis modes for obtaining single-phase nanopowders based on bismuth orthoferrite with the smallest possible crystal sizes. This work is aimed at solving this problem.

## 2. Experimental

The crystalline hydrates of bismuth and iron (III) nitrates were used as starting reagents. Bismuth nitrate  $\text{Bi}(\text{NO}_3)_3 \cdot 5\text{H}_2\text{O}$  was dissolved in 70 mL of 4M  $\text{HNO}_3$  with stirring for 10 minutes and heating to 70 °C. An equimolar amount of iron nitrate  $\text{Fe}(\text{NO}_3)_3 \cdot 9\text{H}_2\text{O}$  was added with stirring to the obtained solution of bismuth nitrate. Salt weights were calculated for the preparation of 3 g of bismuth ferrite. After stirring for 10 minutes, 130 mL of distilled water was added and stirred for another 20 minutes. Separately, 1 l of 4M NaOH solution was prepared. The obtained solutions were used for the coprecipitation of bismuth and iron(III) hydroxides in various types of microreactors. Coprecipitation was carried out at a temperature of about 22 °C and atmospheric pressure.

The design of the microreactor with submerged jets used for intensive mixing of the solutions of the reagents (Fig. 1a) is described in [51]. The reactor was filled with NaOH solution to a level that was kept constant by means of a hydraulic lock. After that, the solutions of nitrates and alkali were fed by means of Heidolph Pumpdrive 5201 peristaltic pumps simultaneously through two nozzles located on opposite walls of the reactor at an angle of 180 degrees to each other. A solution of bismuth and iron nitrates was supplied through one nozzle, 0.52 mm in diameter, and a solution of NaOH was supplied through another nozzle, 0.47 mm in diameter. The flow rate of both solutions was 150 mL/min. The superficial velocity of the jets at the outlet of the nozzles was 15.3 m/s for the salt mixture solution and 16.7 m/s for the alkali solution. When the pumps were started, the nitrate solution was “injected” into the reactor filled with NaOH, and metal hydroxides immediately precipitated. In essence, this method is a variant of intensive reverse precipitation. The particles of co-precipitated hydroxides formed during the chemical reaction were removed through the hydraulic lock hosepipe into a receiving tank.

A free impinging-jets microreactor (Fig. 1b) described in [52, 53] was also used to mix the reagents. A solution of bismuth and iron nitrates was fed into the jet microreactor through one of the nozzles with a diameter of 0.44 mm, and a solution of sodium hydroxide was supplied through the second nozzle with a diameter of 0.46 mm. The solutions were delivered as thin jets at a fixed flow rate of 250 mL/min, colliding at a mean velocity of about 23 m/s in a vertical plane at an angle of about 72 °. The mutual arrangement of the nozzles and the flow rate were set in such a way that the collision of the jets resulted in the formation of a liquid sheet with an average thickness of 10–15  $\mu\text{m}$  [55], in which there was contact and mixing of solutions of the initial components (Fig. 1b). The coprecipitation of bismuth and iron hydroxides in a jet microreactor was carried out for 5–10 ms.

A microreactor with intensively swirling flows (Fig. 1c) makes it possible to concentrate a large amount of kinetic energy in a relatively small volume (about 0.35 mL), which leads to the creation of a high level of specific energy dissipation rate (about 2–35 kW/kg), which, in turn, causes high local values of longitudinal and shear deformation of fluid elements and contributes to the intensification of the micromixing process [56, 57]. The flow rates of each solution at the preliminary stage of the experiment were set at 0.5, 1.0, 2.0, and 3.0 L/min. In this case, nitrate solutions were fed into one of the tangential nozzles, and the precipitant solution was fed into the axial nozzle (Fig. 1c). Since no significant effect of solution flow rates in the range of 0.5–3.0 L/min on the size of crystallites was found (the sizes varied from  $14 \pm 5$  nm for 0.5 L/min to  $12 \pm 5$  nm for 3.0 L/min), then further all studies were carried out for a sample obtained at a flow rate of 3.0 L/min. This result is important from the point of view of crystallite size stability, since it guarantees the production of particles with an average crystallite size in a narrow range, from 12 to 14 nm, with a relatively wide change in solution flow rates, from 0.5 L/min to 3.0 L/min.

As a result of mixing solutions in microreactors, a suspension of co-precipitated bismuth and iron hydroxides was obtained, which was then washed with distilled water from alkali using centrifugation and intermediate dispersion using an ultrasonic bath in order to better wash the precipitates from alkali residues. The washed samples were dried at 70 °C for a day.

The samples were designated as follows: *N1* – obtained using a microreactor with submerged jets, *N2* – using a free impinging-jets microreactor, *N3* – using a microreactor with intensively swirling flows. The samples were heated in a tubular furnace in a platinum crucible at a temperature of 490 °C in the “annealing-hardening” mode for 1 minute.

Powders were characterized by several methods. X-ray diffraction patterns were taken on a Rigaku SmartLab 3 (Rigaku Corporation, Japan) powder diffractometer ( $\text{CuK}\alpha$  radiation) in the angle range  $2\theta = 20\text{--}60^\circ$  with a step of  $0.01^\circ$  and a speed of  $0.1^\circ/\text{min}$ . The phase analysis of the samples was determined using the ICSD PDF-2 database. The average crystallite size was determined using the SmartLab Studio II software package from Rigaku. The size distribution of crystallites was determined by the method of fundamental parameters in the approximation of a lognormal distribution model using the SmartLab Studio II software package for reflection 012.

The elemental composition of the samples was determined using a Tescan Vega 3 SBH scanning electron microscope (Tescan, Czech Republic) with an energy dispersive X-ray spectroscopy (EDX) Oxford Instruments INCA x-act X-ray microanalysis attachment (Oxford Instruments, Oxford, UK).

Transmission electron microscopy (TEM) studies with the determination of microdiffraction of the samples were performed using a JEOL JEM-2100F microscope (JEOL Ltd., Akishima, Tokyo, Japan) at an accelerating voltage of 200 kV. Samples for research were prepared by preliminary dispersion of the initial powder in ethyl alcohol in an ultrasonic bath for 15 minutes, followed by deposition on a supporting film.

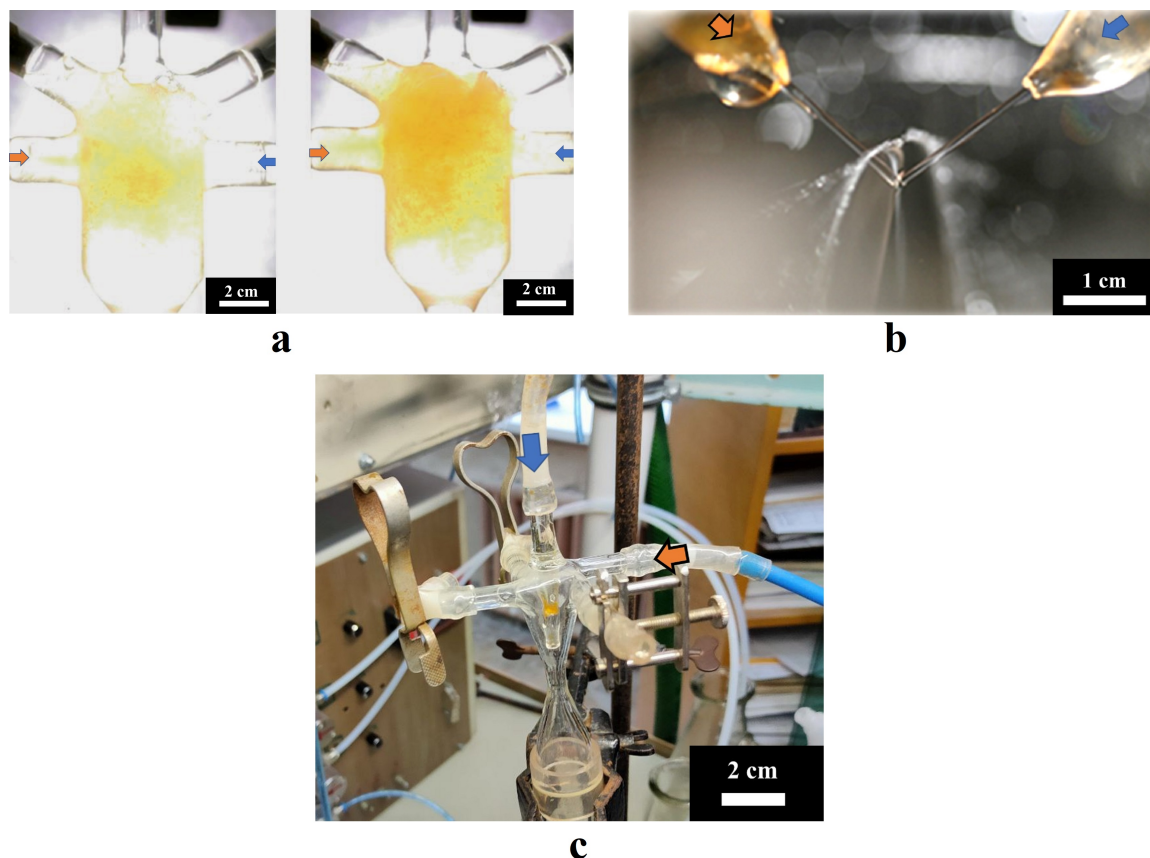


FIG. 1. Microreactors for co-precipitation of bismuth and iron hydroxides: a) with submerged jets; b) free impinging-jets; c) with intensively swirling flows

### 3. Results and discussion

The data of X-ray spectral microanalysis of all samples showed that the ratio of Bi:Fe elements in the samples, within the error limits, corresponds to the ratio specified during synthesis, with respect to the stoichiometry of  $\text{BiFeO}_3$ .

The X-ray diffraction data for the heat-treated samples are shown in Fig. 2. Diffractograms for all three samples before heat treatment, i.e. bismuth and iron hydroxides coprecipitated using different microreactors have the same X-ray

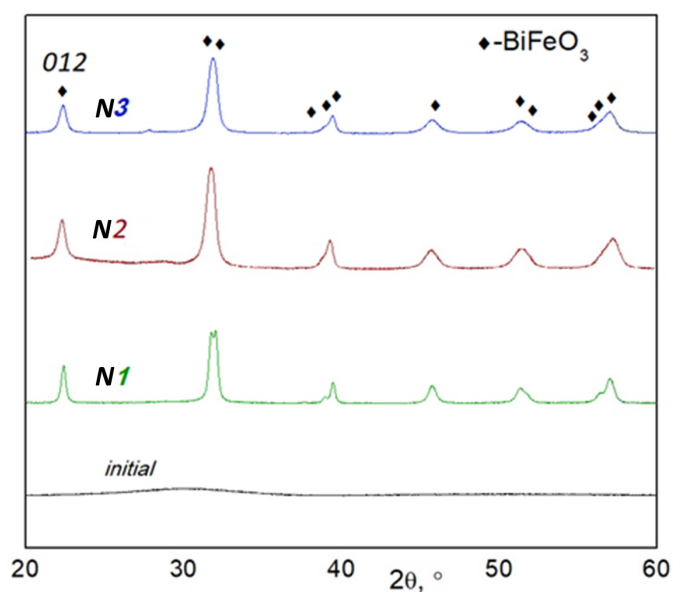


FIG. 2. X-ray diffraction patterns of samples after heat treatment ( $490\text{ }^{\circ}\text{C}$ , 1 min) –  $N1$ ,  $N2$ ,  $N3$ , and before heat treatment – “initial”

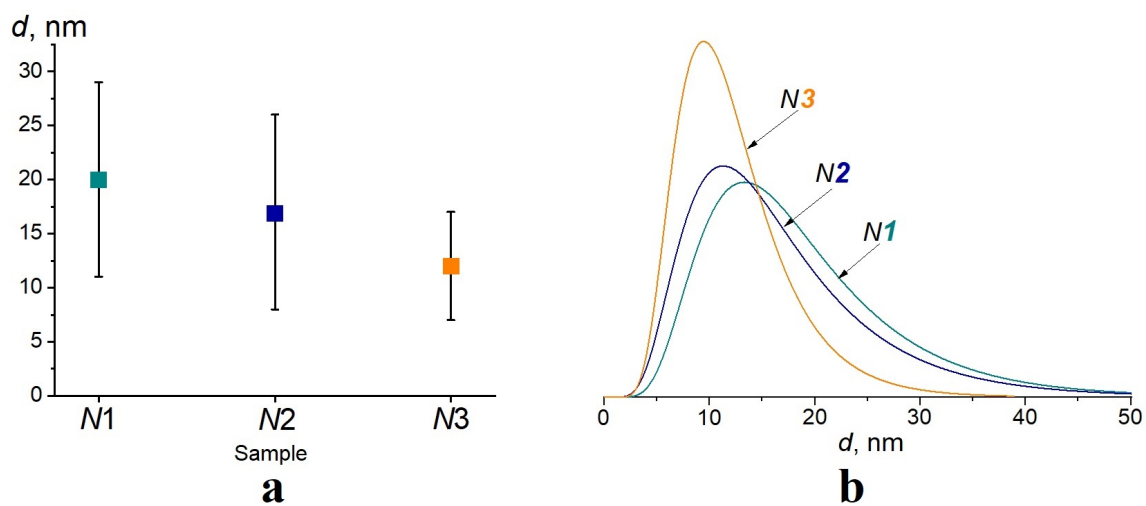


FIG. 3. Average sizes of bismuth orthoferrite crystallites in samples  $N1$ ,  $N2$ ,  $N3$  after heat treatment – a); size distribution of crystallites according to the 012 reflection in samples  $N1$ ,  $N2$ ,  $N3$  – b)

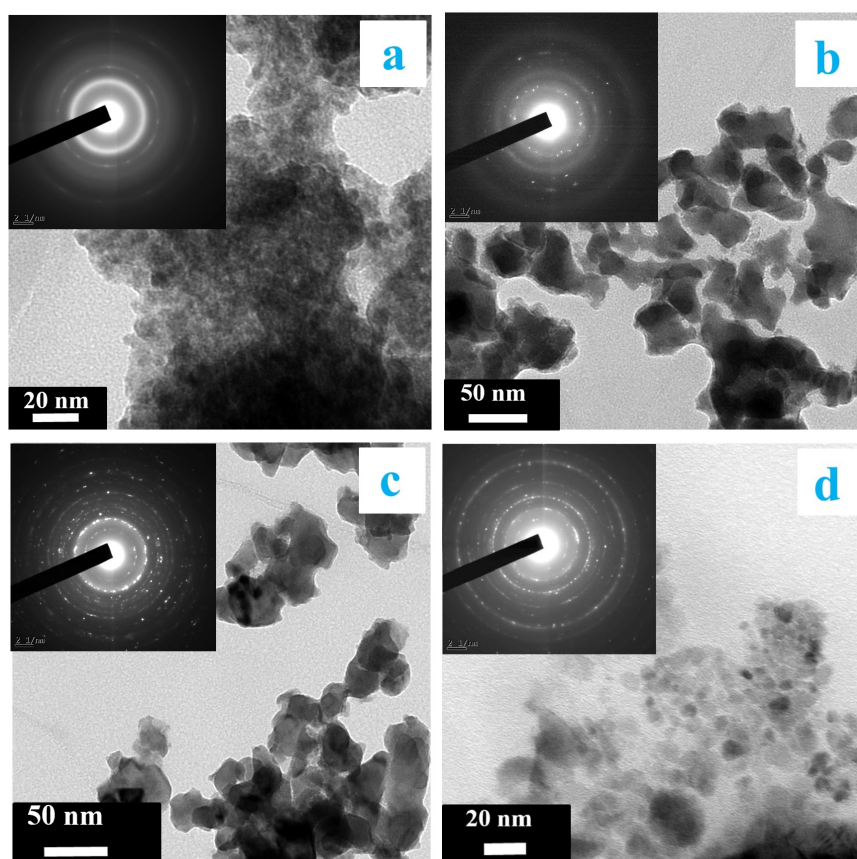


FIG. 4. TEM micrographs: sample “initial” before heat treatment (a); samples after heat treatment:  $N1$  (b),  $N2$  (c),  $N3$  (d)

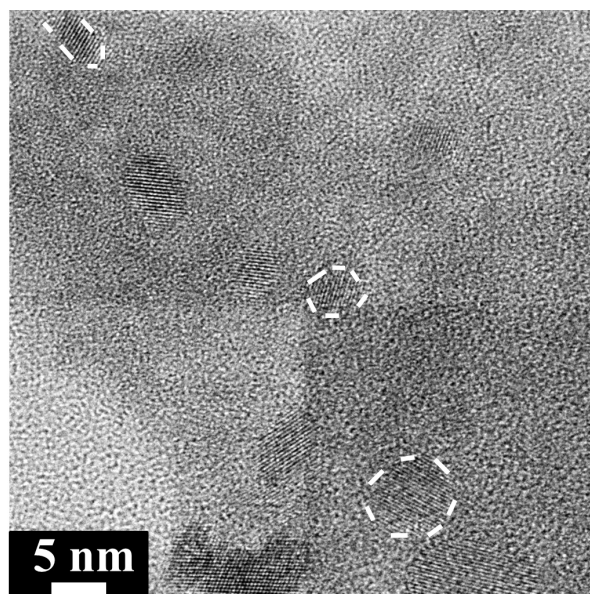


FIG. 5. TEM micrograph of sample *N3*. As an example, three  $\text{BiFeO}_3$  nanocrystals are highlighted in the image

amorphous appearance and are shown in Fig. 2 under the name “initial”. All reflections in the diffraction patterns of samples *N1*, *N2*, and *N3* correspond to the bismuth orthoferrite phase.

Figure 3 shows the average crystallite sizes of the samples (Fig. 3a), as well as the size distributions of crystallites (Fig. 3b), determined from the 012 reflection.

Sample *N3* has the smallest average crystallite size, about 12 nm. The average size of crystallites for sample *N1* is about 19 nm, for sample *N2*, is about 17 nm. The volumetric size distribution of crystallites for sample *N3*, obtained using a microreactor with intensively swirling flows, is narrower ( $\sigma = 5$  nm) than that for samples *N1* and *N2* ( $\sigma = 9$  nm), obtained using microreactors with free impinging-jets and submerged jets.

A micrograph of the *N2* sample before heat treatment, obtained with a transmission electron microscope, is shown in Fig. 4a. This sample is X-ray amorphous particles collected in aggregates. Pictures of samples *N1*, *N2*, *N3* after heat treatment are shown in Figs. 4b, 4c, 4d, respectively. The electron microdiffraction data confirm the polycrystalline nature of the samples, as well as the presence of some X-ray amorphous phase.

Figure 5 shows a micrograph of sample *N3*, which shows the crystallites of bismuth orthoferrite formed in the amorphous phase. The minimum size of  $\text{BiFeO}_3$  crystallites from transmission electron microscopy data can be estimated as approximately 3–4 nm.

The formation of nanocrystalline bismuth orthoferrite can be explained within the framework of the mechanism of self-organization of spatial restrictions on the growth of particles [50] arising in Kolmogorov-scale vortices in various types of microreactors. In this case, Kolmogorov vortices act as nanoreactors, in which, in this case, nanoparticles of bismuth and iron hydroxides are formed, which are precursors for the synthesis of  $\text{BiFeO}_3$  during their dehydration.

For the synthesis of nanoparticles with the smallest possible sizes under the conditions of the formation of such spatial restrictions, it is important to organize a large contact surface of the reagents and quickly remove the products of interaction from the reaction zone, which is facilitated by the use of microreactor technique.

#### 4. Conclusion

The presented data allow us to conclude that the use of various types of microreactors makes it possible to obtain a nanocrystalline single-phase powder based on bismuth orthoferrite. The smallest average size of  $\text{BiFeO}_3$  crystallites (about 12 nm) was observed in the sample obtained using a microreactor with intensively swirling flows with a reagent flow rate of 3.0 L/min. From the point of view of the stability of the obtained nanocrystalline  $\text{BiFeO}_3$  samples, this result is positive, since under production conditions it guarantees the production of nanocrystalline  $\text{BiFeO}_3$  with an average crystallite size of  $12 \pm 5$  nm within a wide range of the solutions flow rates, from 0.5 L/min to 3.0 L/min.

#### References

- [1] Kushwaha A.K., John M., Misra M., Menezes P.L. Nanocrystalline Materials: Synthesis, Characterization, Properties, and Applications. *Crystals*, 2021, **11**(11), P. 1317.
- [2] Wongkaew N., Simsek M., Griesche C., Baeumner A.J. Functional Nanomaterials and Nanostructures Enhancing Electrochemical Biosensors and Lab-on-a-Chip Performances: Recent Progress, Applications, and Future Perspective. *Chemical Reviews*, 2019, **119**(1), P. 120–194.

- [3] Gupta D., Varghese B.S., Suresh M., Panwar C., Gupta T.K. Nanoarchitectonics: functional nanomaterials and nanostructures – a review. *Journal of Nanoparticle Research*, 2022, **24**, P. 196.
- [4] Lomanova N.A., Panchuk V.V., Semenov V.G., Pleshakov I.V., Volkov M.P., Gusarov V.V. Bismuth orthoferrite nanocrystals: magnetic characteristics and size effects. *Ferroelectrics*, 2020, **569**(1), P. 240–250.
- [5] Wang N., Luo X., Han L., Zhang Z., Zhang R., Olin H., Yang Y. Structure, Performance, and Application of BiFeO<sub>3</sub> Nanomaterials. *Nano-Micro Letters*, 2020, **12**, P. 81.
- [6] Aishwarya K., Hannah Jeniffer I., Maruthasalamoorthy S., Nirmala R., Punithavelan N., Navamathavan R. Review State of the Art of the Multifunctional Bismuth Ferrite: Synthesis Method and Applications. *ECS Journal of Solid State Science and Technology*, 2022, **11**(4), P. 043010.
- [7] Kim S., Nam H., Calisir I. Lead-Free BiFeO<sub>3</sub>-Based Piezoelectrics: A Review of Controversial Issues and Current Research State. *Materials*, 2022, **15**(13), P. 4388.
- [8] Gao T., Chen Z., Huang Q., Niu F., Huang X., Qin L., Huang Y. A review: preparation of bismuth ferrite nanoparticles and its applications in visible-light induced photocatalyses. *Reviews on Advanced Materials Science*, 2015, **40**(2), P. 97–109.
- [9] Irfan S., Zhuanghao Z., Li F., Chen Y.-X., Liang G.-X., Luo J.-T., Ping F. Critical review: Bismuth ferrite as an emerging visible light active nanostructured photocatalyst. *Journal of Materials Research and Technology*, 2019, **8**(6), P. 6375–6389.
- [10] Chien S.-W. C., Ng D.-Q., Kumar D., Lam S.-M., Jaffari Z.H. Investigating the effects of various synthesis routes on morphological, optical, photoelectrochemical and photocatalytic properties of single-phase perovskite BiFeO<sub>3</sub>. *Journal of Physics and Chemistry of Solids*, 2022, **160**, P. 110342.
- [11] Egorysheva A.V., Kraev A.S., Gajtko O.M., Baranchikov A.E., Agafonov A.V., Ivanov V.K. Electrorheological Fluids Based on Bismuth Ferrites BiFeO<sub>3</sub> and Bi<sub>2</sub>Fe<sub>4</sub>O<sub>9</sub>. *Russian Journal of Inorganic Chemistry*, 2020, **65**(8), P. 1253–1263.
- [12] Lomanova N.A., Tomkovich M.V., Sokolov V.V., Gusarov V.V. Special Features of Formation of Nanocrystalline BiFeO<sub>3</sub> via the Glycine-Nitrate Combustion Method. *Russian Journal of General Chemistry*, 2016, **86**(10), P. 2256–2262.
- [13] Lomanova N.A., Tomkovich M.V., Sokolov V.V., Ugolokov V.L., Panchuk V.V., Semenov V.G., Pleshakov I.V., Volkov M.P., Gusarov V.V. Thermal and magnetic behavior of BiFeO<sub>3</sub> nanoparticles prepared by glycine-nitrate combustion. *Journal of Nanoparticle Research*, 2018, **20**, P. 17.
- [14] Lomanova N.A., Tomkovich M.V., Danilovich D.P., Osipov A.V., Panchuk V.V., Semenov V.G., Pleshakov I.V., Volkov M.P., Gusarov V.V. Magnetic Characteristics of Nanocrystalline BiFeO<sub>3</sub>-Based Materials Prepared by Solution Combustion Synthesis. *Inorganic Materials*, 2020, **56**(12), P. 1271–1277.
- [15] Verma R., Chauhan A., Neha, Batoo K.M., Kumar R., Hadhi M., Raslan E.H. Effect of calcination temperature on structural and morphological properties of bismuth ferrite nanoparticles. *Ceramics International*, 2021, **47**(3), P. 3680–3691.
- [16] Mhamad S.A., Ali A.A., Mohtar S.S., Aziz F., Aziz M., Jaafar J., Yusof N., Salleh W.N.W., Ismail A.F., Chandren S. Synthesis of bismuth ferrite by sol-gel auto combustion method: Impact of citric acid concentration on its physicochemical properties. *Materials Chemistry and Physics*, 2022, **282**, P. 125983.
- [17] Asefi N., Masoudpanah S.M., Hasheminasari M. Photocatalytic performances of BiFeO<sub>3</sub> powders synthesized by solution combustion method: The role of mixed fuels. *Materials Chemistry and Physics*, 2019, **228**, P. 168–174.
- [18] Parvathy N.S., Govindaraj R. Atomic scale insights on the growth nanoparticles of BiFeO<sub>3</sub> nanoparticles. *Scientific Reports*, 2022, **12**, P. 4758.
- [19] Alikhanov N.M.-R., Rabadanov M.Kh., Orudzhev F.F., Gadzhimagomedov S.Kh., Emirov R.M., Sadykov S.A., Kallaev S.N., Ramazanov S.M., Abdulvakhidov K.G., Sobola D. Size-dependent structural parameters, optical, and magnetic properties of facile synthesized pure-phase BiFeO<sub>3</sub>. *Journal of Materials Science: Materials in Electronics*, 2021, **32**, P. 13323–13335.
- [20] Ortiz-Quirionez J.-L., Pal U., Villanueva M.S. Effects of Oxidizing/Reducing Agent Ratio on Phase Purity, Crystallinity, and Magnetic Behavior of Solution-Combustion-Grown BiFeO<sub>3</sub> Submicroparticles. *Inorganic Chemistry*, 2018, **57**(10), P. 6152–6160.
- [21] Proskurina O.V., Tomkovich M.V., Bachina A.K., Sokolov V.V., Danilovich D.P., Panchuk V.V., Semenov V.G., Gusarov V.V. Formation of Nanocrystalline BiFeO<sub>3</sub> under Hydrothermal Conditions. *Russian Journal of General Chemistry*, 2017, **87**(11), P. 2507–2515.
- [22] Rouhani Z., Karimi-Sabet J., Mehdipourghazi M., Hadi A., Dastbaz A. Response surface optimization of hydrothermal synthesis of Bismuth ferrite nanoparticles under supercritical water conditions: Application for photocatalytic degradation of Tetracycline. *Environmental Nanotechnology, Monitoring & Management*, 2019, **11**, P. 100198.
- [23] Wang Z.-B., Aldabahi A., Ahamad T., Alshehri S.M., Feng P.X. Preparation of BiFeO<sub>3</sub> and its photoelectric performance as photoanode of DSSC. *Ceramics International*, 2021, **47**(19), P. 27565–27570.
- [24] Duan Q., Kong F., Han X., Jiang Y., Liu T., Chang Y., Zhou L., Qin G., Zhang X. Synthesis and characterization of morphology-controllable BiFeO<sub>3</sub> particles with efficient photocatalytic activity. *Materials Research Bulletin*, 2019, **112**, P. 104–108.
- [25] Xu Y., Gao Y., Xing H., Zhang J. Room temperature spontaneous exchange bias in BiFeO<sub>3</sub> micro/nano powders synthesized by hydrothermal method. *Ceramics International*, 2018, **44**(14), P. 17459–17463.
- [26] Huang J., Tan G., Yang W., Zhang L., Ren H., Xia A. Microwave hydrothermal synthesis of BiFeO<sub>3</sub>: Impact of different surfactants on the morphology and photocatalytic properties. *Materials Science in Semiconductor Processing*, 2014, **25**, P. 84–88.
- [27] da Cruz Severo E., Dotto G.L., Silvestri S., dos Santos Nunes I., da Silveira Salla J., Martinez-de la Cruz A., da Boit Martinello K., Foletto E.L. Improved catalytic activity of EDTA-modified BiFeO<sub>3</sub> powders for remarkable degradation of procion red by heterogeneous photo-Fenton process. *Journal of Environmental Chemical Engineering*, 2020, **8**(4), P. 103853.
- [28] Morozov M.I., Lomanova N.A., Gusarov V.V. Specific features of BiFeO<sub>3</sub> formation in a mixture of bismuth(III) and iron(III) oxides. *Russian Journal of General Chemistry*, 2003, **73**, P. 1676–1683.
- [29] Lomanova N.A., Gusarov V.V. Influence of synthesis temperature on BiFeO<sub>3</sub> nanoparticles formation. *Nanosystems: Physics, Chemistry, Mathematics*, 2013, **4**(5), P. 696–705.
- [30] Tuluk A., Brouwer H., van der Zwaag S. Controlling the Oxygen Defects Concentration in a Pure BiFeO<sub>3</sub> Bulk Ceramic. *Materials*, 2022, **15**, P. 6509.
- [31] Rojac T., Bencan A., Malic B., Tutuncu G., Jones J.L., Daniels J.E., Damjanovic D. BiFeO<sub>3</sub> Ceramics: Processing, Electrical, and Electromechanical Properties. *Journal of the American Ceramic Society*, 2014, **97**(7), P. 1993–2011.
- [32] Yao Y., Ploss B., Mak C.L., Wong K.H. Pyroelectric properties of BiFeO<sub>3</sub> ceramics prepared by a modified solid-state-reaction method. *Applied Physics A*, 2010, **99**, P. 211–216.
- [33] Han H., Lee J.H., Jang H.M. Low-Temperature Solid-State Synthesis of High-Purity BiFeO<sub>3</sub> Ceramic for Ferroic Thin-Film Deposition. *Inorganic Chemistry*, 2017, **56**(19), P. 11911–11916.
- [34] Carranza-Celis D., Cardona-Rodríguez A., Narváez J., Moscoso-Londono O., Muraca D., Knobel M., Ornelas-Soto N., Reiber A., Ramírez J.G. Control of Multiferroic properties in BiFeO<sub>3</sub> nanoparticles. *Scientific Reports*, 2019, **9**, P. 3182.
- [35] Gil-González E., Perejón A., Sónchez-Jiménez P.E., Sayagués M.J., Raj R., Pérez-Maqueada L.A. Phase-pure BiFeO<sub>3</sub> produced by reaction flash-sintering of Bi<sub>2</sub>O<sub>3</sub> and Fe<sub>2</sub>O<sub>3</sub>. *Journal of Materials Chemistry A*, 2018, **6**(13), P. 5356–5366.

- [36] Selbach S.M., Einarsrud M.-A., Grande T. On the Thermodynamic Stability of BiFeO<sub>3</sub>. *Chemistry of Materials*, 2009, **21**(1), P. 169–173.
- [37] Perdomo C.P.F., Suarez A.V., Gunnewiek R.F.K., Kiminami R.H.G.A. Low temperature synthesis of high purity nanoscaled BiFeO<sub>3</sub> by a fast polymer solution method and their ferromagnetic behavior. *Journal of Alloys and Compounds*, 2020, **849**, P. 156564.
- [38] Silva J., Reyes A., Esparza H., Camacho H., Fuentes L. BiFeO<sub>3</sub>: A Review on Synthesis, Doping and Crystal Structure. *Integrated Ferroelectrics*, 2011, **126**(1), P. 47–59.
- [39] Denisov V.M., Belousova N.V., Zhereb V.P., Denisova L.T., Skorikov V.M. Oxide Compounds of Bi<sub>2</sub>O<sub>3</sub>–Fe<sub>2</sub>O<sub>3</sub> System I. The Obtaining and Phase Equilibriums. *Journal of Siberian Federal University. Chemistry*, 2012, **5**(2), P. 146–167.
- [40] Pikula T., Szumiata T., Siedliska K., Mitsiuk V.I., Panek R., Kowalczyk M., Jartych E. The Influence of Annealing Temperature on the Structure and Magnetic Properties of Nanocrystalline BiFeO<sub>3</sub> Prepared by Sol–Gel Method. *Metallurgical and Materials Transactions A*, 2022, **53**, P. 470–483.
- [41] Stankiewicz A.I., Moulijn J.A. Process intensification: Transforming chemical engineering. *Chemical Engineering Progress*, 2000, **96**(1), P. 22–34.
- [42] Abiev R.Sh., Almyasheva O.V., Popkov V.I., Proskurina O.V. Microreactor synthesis of nanosized particles: The role of micromixing, aggregation, and separation processes in heterogeneous nucleation. *Chemical Engineering Research and Design*, 2022, **178**, P. 73–94.
- [43] Marchisio D.L., Rivautella L., Barresi A.A. Design and Scale-Up of Chemical Reactors for Nanoparticle Precipitation. *AIChE Journal*, 2006, **52**(5), P. 1877–1887.
- [44] Kumar R.D.V., Prasad B.L.V., Kulkarni A.A. Impinging Jet Micromixer for Flow Synthesis of Nanocrystalline MgO: Role of Mixing/Impingement Zone. *Industrial Engineering Chemistry Research*, 2013, **52**(49), P. 17376–17382.
- [45] Abiev R.Sh., Almyasheva O.V., Gusarov V.V., Izotova S.G. Method of producing nanopowder of cobalt ferrite and microreactor to this end. RF Patent 2625981, Bull. N 20, 20.07.2017. <https://patents.google.com/patent/RU2625981C1/en>.
- [46] Abiev R.S., Almyasheva O.V., Izotova S.G., Gusarov V.V. Synthesis of cobalt ferrite nanoparticles by means of confined impinging-jets reactors. *Journal Chemical Technology and Applications*, 2017, **1**(1), P. 7–13.
- [47] Abiev R.S. Impinging-Jets Micromixers and Microreactors: State of the Art and Prospects for Use in the Chemical Technology of Nanomaterials (Review). *Theoretical Foundations of Chemical Engineering*, 2020, **54**(6), P. 1131–1147.
- [48] Johnson B.K., Prud'homme R.K. Chemical Processing and Micromixing in Confined Impinging Jets. *AIChE Journal*, 2003, **49**(9), P. 2264–2282.
- [49] Bałdyga J., Jasińska M., Orciuch W. Barium Sulphate Agglomeration in a Pipe – An Experimental Study and CFD Modeling. *Chemical Engineering & Technology*, 2003, **26**(3), P. 334–340.
- [50] Almyasheva O.V., Popkov V.I., Proskurina O.V., Gusarov V.V. Phase formation under conditions of self-organization of particle growth restrictions in the reaction system. *Nanosystems: Physics, Chemistry, Mathematics*, 2022, **13**(2), P. 164–180.
- [51] Proskurina O.V., Sokolova A.N., Sirotkin A.A., Abiev R.Sh., Gusarov V.V. Role of Hydroxide Precipitation Conditions in the Formation of Nanocrystalline BiFeO<sub>3</sub>. *Russian Journal of Inorganic Chemistry*, 2021, **66**(2), P. 163–169.
- [52] Proskurina O.V., Nogovitsin I.V., Il'ina T.S., Danilovich D.P., Abiev R.Sh., Gusarov V.V. Formation of BiFeO<sub>3</sub> Nanoparticles Using Impinging Jets Microreactor. *Russian Journal of General Chemistry*, 2018, **88**(10), P. 2139–2143.
- [53] Proskurina O.V., Abiev R.S., Danilovich D.P., Panchuk V.V., Semenov V.G., Nevedomskiy V.N., Gusarov V.V. Formation of nanocrystalline BiFeO<sub>3</sub> during heat treatment of hydroxides co-precipitated in an impinging-jets microreactor. *Chemical Engineering and Processing – Process Intensification*, 2019, **143**, P. 107598.
- [54] Almyasheva O.V., Lomanova N.A., Popkov V.I., Proskurina O.V., Tugova E.A., Gusarov V.V. The minimal size of oxide nanocrystals: phenomenological thermodynamic vs crystal-chemical approaches. *Nanosystems: Physics, Chemistry, Mathematics*, 2019, **10**(4), P. 428–437.
- [55] Abiev R.S., Sirotkin A.A. Effect of Hydrodynamic Conditions on Micromixing in Impinging-Jets Microreactors. *Theoretical Foundations of Chemical Engineering*, 2022, **56**(1), P. 9–22.
- [56] Abiev R.Sh., Makusheva I.V. Effect of Macro- and Micromixing on Processes Involved in Solution Synthesis of Oxide Particles in Microreactors with Intensively Swirling Flows. *Theoretical Foundations of Chemical Engineering*, 2022, **56**(2), P. 141–151.
- [57] Abiev R.Sh., Makusheva I.V. Energy Dissipation Rate and Micromixing in a Two-Step Micro-Reactor with Intensively Swirled Flows. *Micromachines*, 2022, **13**(11), P. 1859.

---

Submitted 27 September 2022; revised 10 October 2022; accepted 30 October 2022

#### Information about the authors:

*Olga V. Proskurina* – Ioffe Institute, 194021 St. Petersburg, Russia; St. Petersburg State Institute of Technology, 190013 St. Petersburg, Russia; ORCID 0000-0002-2807-375X; proskurinaov@mail.ru

*Rufat Sh. Abiev* – Ioffe Institute, 194021 St. Petersburg, Russia; St. Petersburg State Institute of Technology, 190013 St. Petersburg, Russia; ORCID 0000-0003-3571-5770; abiev.rufat@gmail.com

*Vladimir N. Nevedomskiy* – Ioffe Institute, 194021 St. Petersburg, Russia; ORCID 0000-0002-7661-9155; nevedom@mail.ioffe.ru

*Conflict of interest:* the authors declare no conflict of interest.

## Time of transition processes in a CdS-CIGS structural solar cells in the short-wave part of the absorption spectrum at different loading resistances

Rustam R. Kabulov<sup>1,a</sup>, Farrux A. Akbarov<sup>2,1,b</sup>, Anvar A. Alimov<sup>2,c</sup>

<sup>1</sup>Physical – Technical Institute Academy of Sciences of the Republic of Uzbekistan, Tashkent, Uzbekistan

<sup>2</sup>Tashkent State Technical University named after Islam Karimov, Tashkent, Uzbekistan

<sup>a</sup>krr1982@bk.ru, <sup>b</sup>farrux1927@mail.ru, <sup>c</sup>alimovanvar62@gmail.com

Corresponding author: F. A. Akbarov, farrux1927@mail.ru

**ABSTRACT** The work is devoted to the study of the influence of solar radiation in the short-wave part of the absorption spectrum at different loading resistances on the lifetime ( $\tau$ ) of minority photogenerated charge carriers ( $\Delta n$ ) of a thin-film solar cell based on Cu(In,Ga)Se<sub>2</sub>. It was found that with an increase in the generated photocurrent and the magnitude of the load resistance the lifetime of minority photogenerated charge carriers of a thin-film solar cell based on Cu(In,Ga)Se<sub>2</sub> increases. The obtained experimental results are interpreted by the charge exchange of defect states, which capture the injected and photogenerated electrons, as a result of which they cease to be active recombination centers.

**KEYWORDS** CIGS, solar cell, monochromatic radiation, absorption coefficient, lifetime, photogenerated charge carriers, minority charge carriers.

**ACKNOWLEDGEMENTS** The authors express their gratitude to the management, employees of the Physical-technical Institute Academy of Science of the Republic of Uzbekistan for technical assistance in performing experimental research, discussing the results of these scientific studies and writing an article, and also express their gratitude to the employees of the Tashkent State Technical University who took an active part in discussing the results of our scientific research.

**FOR CITATION** Kabulov R.R., Akbarov F.A., Alimov A.A. Time of transition processes in a CdS-CIGS structural solar cells in the short-wave part of the absorption spectrum at different loading resistances. *Nanosystems: Phys. Chem. Math.*, 2023, **14** (1), 127–131.

### 1. Introduction

One of the important parameters that determine the efficiency of photosensitive structures is the lifetime ( $\tau$ ) of minority photogenerated charge carriers ( $\Delta n$ ). In real solar cells and photodetectors, due to the complexity of the structure design, since in the process of creating a photoactive CIGS layer, due to the mutual diffusion of chemical elements from the CdS and CIGS layers, a layer that is inhomogeneous in respect to chemical composition is formed at the CdS/CIGS heterojunction boundary in the photoactive layer. In the photovoltaic mode, the photovoltage on the load resistance is connected in the direct direction to the p-n junction, it changes both the size of the space charge region and the distribution of the internal potential. In this regard, it was interesting to establish the effect of the load resistance on the lifetime of nonequilibrium charge carriers when illuminated with short-wavelength solar radiation, which is mainly absorbed near the heterojunction ( $\lambda_1 \approx 450$  nm,  $h\nu_1 \approx 2.76$  eV and  $\lambda_2 \approx 520$  nm,  $h\nu_2 \approx 2.40$  eV).

Studying the relaxation characteristics of photosensitive structures, such as photocurrent decay ( $J_{ph}$ ), under illumination with discontinuous monochromatic light, will allow one to estimate the value of  $\tau$  and establish the mechanism of photogeneration of nonequilibrium photogenerated charge carriers and the processes of their recombination under illumination. It is known that the magnitude of the photocurrent depends on the concentration of photogenerated charge carriers  $-\Delta n$  [1]. The time characteristic  $\Delta n$  is determined by relation (1) [1]:

$$\frac{d(\Delta n)}{dt} = -\frac{\Delta n}{\tau}, \quad (1)$$

where,  $\tau$  is the lifetime of photogenerated charge carriers. The solution to equation (1) has the form (2),

$$\Delta n = \Delta n(0) \cdot \exp(-t/\tau), \quad (2)$$

where  $\Delta n(0)$  is the stationary maximum value of photogenerated charge carriers. For the experimental determination of  $\tau$ , it is necessary to plot the time dependence of the photocurrent value on a logarithmic scale ( $\ln(J_{ph})$  on  $t$ ), where the slope of the obtained straight line gives one the value of  $\tau$  for  $\Delta n$  in the photoelectric converter.

## 2. Experimental details

To study the effect of the resistance value of the external load ( $R_{load}$ ) on  $\tau \Delta n$  under illumination with monochromatic radiation of the short-wavelength absorption spectrum ( $\lambda_1 = 450$  nm,  $h\nu_1 \approx 2.76$  eV and  $\lambda_2 = 520$  nm,  $h\nu_2 \approx 2.40$  eV), a heterostructural solar cell was created with a photosensitive region of polycrystalline indium gallium-copper selenide (Cu(In,Ga)Se<sub>2</sub> – CIGS),  $E_g \approx 1.30 \pm 0.03$  eV,  $T = 300$  K) [2]. Since thin-film CIGS solar cells are widely used in the creation of photovoltaic structures for various purposes [3], these studies are important.

In the process of creating photoconverters with the CdS/CIGS structure, due to the mutual diffusion of chemical elements from the CdS and CIGS layers, at the interface of the CdS/CIGS heterojunction in the photoactive CIGS layer, layers that are inhomogeneous in chemical composition are formed, which can lead to the formation of defect states. Defect states reduce the lifetime of photogenerated nonequilibrium carriers. In photovoltaic mode, the voltage across the load resistor ( $U_L$ ) is connected in the forward direction to the p-n junction.  $U_L$  changes the size of the space charge region and the distribution of the internal potential of the structure. In this regard, it was interesting to establish the effect of the load resistance on the lifetime of nonequilibrium charge carriers when illuminated with short-wavelength solar radiation, which is mainly absorbed near the heterojunction ( $\lambda_1 \approx 450$  nm,  $h\nu_1 \approx 2.76$  eV and  $\lambda_2 \approx 520$  nm,  $h\nu_2 \approx 2.40$  eV). Since, under illumination with  $\lambda_1$  ( $h\nu_1 \approx 2.76$  eV) due to partial absorption of quanta in the CdS layer, the number of quanta generating electron-hole pairs in the photoactive CIGS layer is less than under illumination with  $\lambda_2$ ,  $h\nu_2 \approx 2.40$  eV, as a result, the photocurrent is of little value.

For research, photosensitive SnO<sub>2</sub>/n-CdS/p-CIGS/Mo heterojunction structures were fabricated, in which n-CdS layers ( $E_g = 2.44$  eV,  $T = 300$  K) were used as the front buffer layer, which were deposited on the p layer. -CIGS by vacuum thermal spraying from the original source of CdS. The SnO<sub>2</sub> layers served as a frontal transparent conducting layer and were created by DC ion magnetron sputtering of a tin target in an argon and oxygen atmosphere [3, 4]. As mentioned above, the base material for the solar cell was p-type polycrystalline CIGS films grown by the method of simultaneous thermal evaporation in vacuum from initial sources of Cu, In, Ga, and Se on the surface of molybdenum (Mo) [5]. The rear electrical contact was Mo<sub>0.5</sub>  $\mu$ m thick, which was deposited by DC magnetron ion sputtering in an argon atmosphere from a Mo target onto the surface of a glass substrate 1 mm thick. The upper collecting electrical contact for collecting photogenerated nonequilibrium electrons was created from metallic silver (Ag) and indium (In), which was deposited on the surface of the SnO<sub>2</sub> layer by vacuum thermal spraying in the form of a comb.

Figure 1 shows the design of the created SnO<sub>2</sub>-n-CdS/p-CIGS-Mo structural solar cell and the dimensions of the layers. The photocurrent generation process proceeds as follows: electromagnetic radiation quanta, passing through layers of transparently conducting SnO<sub>2</sub> and an n-CdS buffer layer, enter the photoactive region of CIGS, where nonequilibrium electron-hole pairs are absorbed and generated. In the case of  $\lambda_2 \approx 520$  nm ( $h\nu_2 \approx 2.40$  eV), the photocurrent is  $\approx 30\%$  higher than in the case of  $\lambda_1 \approx 450$  nm ( $h\nu_1 \approx 2.76$  eV) ( $J_{sc.green}/J_{sc.blue} \approx 1.3$ ). This is due to the fact that when quanta with  $\lambda_1 \approx 450$  nm ( $h\nu_1 \approx 2.76$  eV) are absorbed by the n-CdS layer ( $E_g = 2.44$  eV), fewer  $\lambda_1$  quanta participate in the photogeneration of nonequilibrium carriers into the photoactive CIGS layer. Accordingly, the total number of generated non-equilibrium electron-hole pairs into the photoactive CIGS layer will be less. The front In/Ag metal contact and the back Mo serve as electrical collecting electrodes.

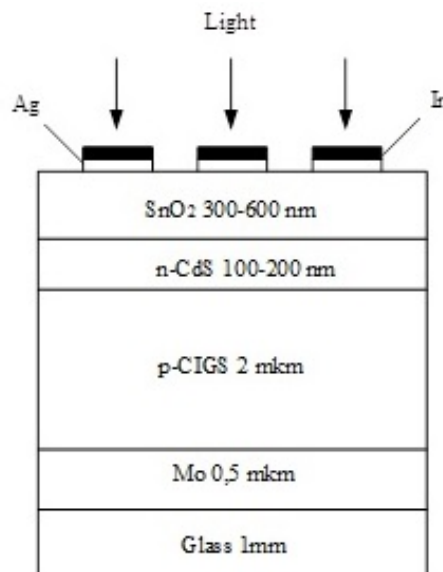


FIG. 1. Construction of the created SnO<sub>2</sub>-n-CdS/p-CIGS-Mo structural solar cell

Figure 2 shows a schematic diagram of the installation for determining time of life for the photogeneration of nonequilibrium carriers –  $\tau$  into the photoactive CIGS layer. The load resistance  $R_{load}$  and digital storage oscillograph (DO) connected in parallel with the SnO<sub>2</sub>-n-CdS/p-CIGS-Mo structural solar cell.

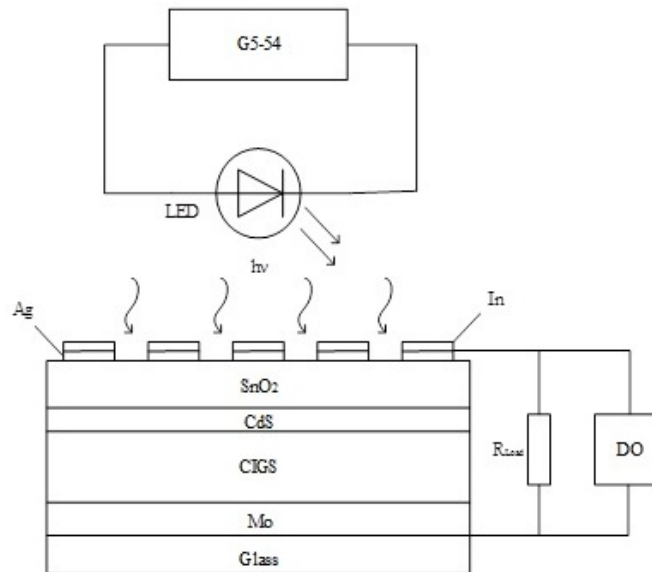


FIG. 2. Schematic diagram of the installation for determining  $\tau$

As a source of modulating electromagnetic radiation, we used light emitting diodes (LED) of green and blue radiation with a power of  $\sim 40$  mW. A voltage of 4 V, duration of 200  $\mu$ s, and frequency of 1 kHz was applied to the LEDs from the G5-54 rectangular pulse generator. From the load resistance  $R_{load}$ , the alternating signal was fed to the input of the RIGOL 1102E digital storage oscillograph (DO).

### 3. Results and discussions

Figure 3 shows the results of relaxation curves of photogenerated currents, built on a logarithmic scale, recorded from load resistances of various values (from 800 Ohm to 100 kOhm and open circuit voltage ( $R_{load} \approx 1$  MOhm)) with a DO under illumination with light  $\lambda_2 \approx 520$  nm. Plotting the relaxation values of the photocurrent on a logarithmic scale shows that the experimental curves, in accordance with relation (2), can be described by a single exponent. From which it follows that one recombination center is involved in the relaxation process.

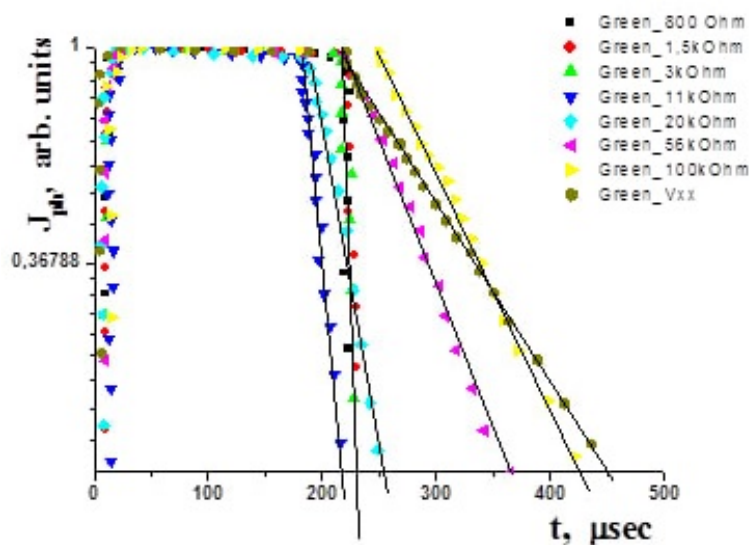


FIG. 3. Relaxation curves of photogenerated currents ( $J_{ph}$ ), built on a logarithmic scale, taken from load resistances of various sizes (from 800 Ohm to 100 kOhm and no-load voltage ( $R_{load} \approx 1$  M $\Omega$ )) on a digital oscilloscope under illumination with radiation  $\lambda_2 \approx 520$  nm (green)

Figure 4 shows the experimental results of the dependence of  $\tau \Delta n$  on  $R_{load}$ , determined in the SnO<sub>2</sub>-n-CdS/p-CIGS-Mo structural solar cell, under illumination by monochromatic radiation of the blue and green spectrum with maxima at wavelengths  $\lambda_1 \approx 450$  nm and  $\lambda_2 \approx 520$  nm.

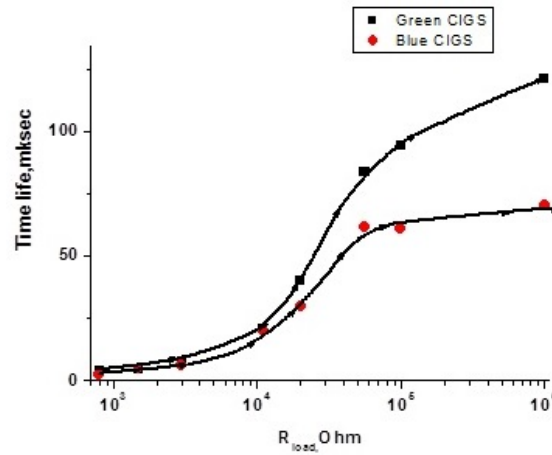


FIG. 4. Dependences of the lifetime  $\Delta n$  on  $R_{load}$  in the CdS-CIGS structure under illumination by monochromatic electromagnetic radiation with  $\lambda_2 \approx 520$  nm (green) and  $\lambda_1 \approx 450$  nm (blue)

From the experimental results presented in Fig. 4, it follows that  $\tau \Delta n$  in the range of  $R_{load} = 800\text{--}1000$  Ohm, in the CdS-CIGS heterostructure, has relatively high values  $\tau \Delta n$  when the heterostructure illuminated with green light ( $\lambda_2 \approx 520$  nm) than the blue light ( $\lambda_1 \approx 450$  nm). Electromagnetic quanta with  $\lambda_2 \approx 520$  nm ( $h\nu_2 \approx 2.40$  eV) are weakly absorbed in the n-CdS layer ( $E_g = 2.44$  eV), and are mainly absorbed in the Space Charge Region (SCR) area of the p-CIGS layer and partially in the quasineutral part, where absorption coefficient is high ( $\sim 10^5$  sm<sup>-1</sup>). As a result, nonequilibrium charge carriers are mainly photogenerated in the photoactive region of p-CIGS. Electromagnetic quanta with  $\lambda_1 \approx 450$  nm ( $h\nu_1 \approx 2.76$  eV) are absorbed in the n-CdS layer, absorbed in the SCR of the heterojunction, as well as in the p-CIGS photoactive layer. Since at  $\lambda_1 \approx 450$  nm ( $h\nu_1 \approx 2.76$  eV) relatively few quanta reach the photoactive quasineutral region of the p-CIGS layer, fewer non-equilibrium charge carriers are generated and a small value of the short-circuit current is obtained in relation to the case of  $\lambda_2 \approx 520$  nm ( $h\nu_2 \approx 2.40$  eV) ( $J_{sc.green}/J_{sc.blue} \approx 1.3$ ).

Due to the difference in the lattice constants of the CdS and CIGS layers, surface states ( $N_{ss}$ ) are formed at the heterojunction boundary, which will act as recombination centers for  $\Delta n$ . Concentration  $N_{ss} \sim d^{-2}$  [6, 7], where  $d$  is the distance between dislocations formed due to the mismatch of the crystal lattices of the contacting materials (3),

$$d = \frac{a_{CIGS} a_{CdS}}{a_{CIGS} - a_{CdS}}. \quad (3)$$

Taking into account the lattice constant of CdS and CIGS [8], the values of  $d \approx 315$  Å and  $N_{ss} = 1.96 \cdot 10^{10}$  sm<sup>-2</sup> were calculated. Also, in the volume of the photoactive part of the p-CIGS layer, there are crystal lattice defects and uncontrollable impurities, which play the role of recombination centers ( $N_{rs}$ ) for nonequilibrium photogenerated charge carriers. If the photogeneration of charge carriers mainly occur near recombination states, this leads to a decrease in  $\tau \Delta n$ . However, under certain conditions, when these recombination centers can be neutralized, and they cease to play the role of recombination centers for  $\Delta n$  [9, 10]. The recharge of recombination centers [9, 10], due to the capture of the injected charge carrier can lead to the reactivation of these centers.

As mentioned above, in the n-CdS/p-CIGS heterostructure,  $\tau \Delta n$  has relatively high values when its illuminated with light with  $\lambda_2 \approx 520$  nm than at  $\lambda_1 \approx 450$  nm in the range of  $R_{load} = 800\text{--}10^6$  Ohm. This is due to the fact that under illumination with light with  $\lambda_2 \approx 520$  nm, a large value of the short-circuit current ( $J_{sc}$ ) is generated in the heterostructure in relation to the case of  $\lambda_1 \approx 450$  nm ( $J_{sc.green}/J_{sc.blue} \approx 1, 3$ ). As a result, more voltage  $U_{load}$  falls on  $R_{load}$ . Voltage  $U_{load}$  is connected in the forward direction to the photodiode, and a relatively large dark injection current through the diode. The recombination centers, capturing the injected electrons, are recharged and cease to be active recombination centers. In the case of illumination with light with  $\lambda_2 \approx 520$  nm, there are more photogenerated electrons, and more  $N_{rs}$  centers are inactive, which should lead to an increase in  $\tau \Delta n$ .

It can be seen from Fig. 4 that  $\tau \Delta n$  both for the case of illumination with  $\lambda_1 \approx 450$  nm and for the case of illumination with  $\lambda_2 \approx 520$  nm grows to a value of  $R_{load} = 50$  kOhm and further with an increase in  $R_{load}$  the growth of  $\tau \Delta n$  slows down. This is due to the fact that with an increase in  $R_{load}$ , the effective current through  $R_{load}$  and the heterostructure decreases, which leads to a partial recharge of  $N_{rs}$  centers, as a result of which, some of the  $N_{rs}$  centers again become recombination active.

#### 4. Conclusion

The study of the influence of the load value and the power of monochromatic radiation in the short-wavelength part of the electromagnetic radiation spectrum showed that the lifetime of non-equilibrium carriers increases with an increase in the load resistance and illumination intensity, that is, either with an increase in the injection current and photogenerated carriers. The lifetime of nonequilibrium carriers decreases with an increase in the absorption coefficient of radiation, which is absorbed more near the heterojunction. The observed effect is associated with a decrease in recombination centers in the photoactive part of the heterojunction as a result of the recharging of defect states in the p-CIGS layer.

#### References

- [1] Sze S.M. and Kwok K.Ng. *Physics of Semiconductor Devices*. New Jersey, John Wiley and Sons, Inc., 2007, p. 763.
- [2] Kobulov R.R., Matchanov N.A., Ataboev O.K., Akbarov F.A. Solar cells based on Cu(In, Ga)Se<sub>2</sub>. *Applied Solar Energy*, 2019, **55**(2), p. 83–90.
- [3] Photovoltaic Report, Freiburg: Fraunhofer Institute for Solar Energy System, 2019. [www.ise.fraunhofer.de](http://www.ise.fraunhofer.de).
- [4] Mirsagatov Sh.A., Kabulov R.R., and Makhmudov M.A. Injection photodiode based on an n-CdS/p-CdTe heterostructure. *Semiconductors*, 2013, **47**, P. 825–830.
- [5] Ataboev O.K., Terukov E.I., Matchanov N.A. Heterojunction thin-film solar cell based on single-crystalline silicon. *Euroasian Journal of Semiconductors Science and Engineering*, 2020, **2**, P. 62–65.
- [6] Kobulov R.R., Matchanov N.A., Ataboev O.K. Morphological and photoelectrical characteristics of the polycrystalline SnO<sub>2</sub>-CdS/Cu(In,Ga)Se<sub>2</sub>-Ag thin film. *Applied Solar Energy*, 2018, **54**(2), P. 91–94.
- [7] Brus V.V., Ilashchuk M.I., Khomyak V.V., Kovalyuk Z.D., Maryanchuk P.D., Ulyanytsky K.S. Electrical properties of anisotype n-CdZnO/p-CdTe heterojunctions. *Semiconductors*, 2012, **46**, P. 1152.
- [8] Kobulov R.R., Makhmudov M.A., Gerasimenko S.Y., Ataboev O.K. Investigation of composition and current transport mechanism in polycrystalline thin film ultra violet Au-Zn<sub>x</sub>Cd<sub>1-x</sub>S-Mo-structure with narrow spectrum of photosensitivity. *Applied Solar Energy*, 2017, **53**(2), P. 123–125.
- [9] Kabulov R.R. Features of the buffer layer Zn<sub>x</sub>Cd<sub>1-x</sub>S for use in thin-film solar cells. *Applied Solar Energy*, 2020, **56**(5), P. 383–387.
- [10] Leiderman A.Yu., Kashaev M.M. Lifetime specifics of nonequilibrium carriers in photoelectric cells based on gallium arsenide obtained via the Czochralski method. *Applied Solar Energy*, 2013, **49**(4), P. 244–247.
- [11] Kobulov R.R., Maxmudov M.A., Gerasimenko S.Yu. Fabrication and investigation of ultraviolet Au-Zn<sub>x</sub>Cd<sub>1-x</sub>S-Mo-structures. *Applied Solar Energy*, 2017, **53**(1), P. 10–12.

---

*Submitted 20 October 2021; revised 27 July 2022, 13 December 2022; accepted 1 February 2023*

#### Information about the authors:

*R. R. Kabulov* – Physical-Technical Institute Academy of Sciences of the Republic of Uzbekistan, 2 “B”, Ch. Aytmatov str., Tashkent, 100084, Uzbekistan; ORCID 0000-0003-3157-9038; [krr1982@bk.ru](mailto:krr1982@bk.ru)

*F. A. Akbarov* – Physical-Technical Institute Academy of Sciences of the Republic of Uzbekistan, 2 “B”, Ch. Aytmatov str., Tashkent, 100084, Uzbekistan; Tashkent State Technical University named after Islam Karimov, 2A, University str. Tashkent, 100095, Uzbekistan; ORCID 0000-0003-0045-9201; [farrux1927@mail.ru](mailto:farrux1927@mail.ru)

*A. A. Alimov* – Tashkent State Technical University named after Islam Karimov, 2A, University str. Tashkent, 100095, Uzbekistan; ORCID 0000-0002-0048-3175; [alimovanvar62@gmail.com](mailto:alimovanvar62@gmail.com)

*Conflict of interest:* the authors declare no conflict of interest.

## Plasma-chemical synthesis of nanocrystalline “core-shell” structures TiN–Mo–Co

Yuliya A. Avdeeva<sup>1,a</sup>, Irina V. Luzhkova<sup>1,b</sup>, Aidar M. Murzakaev<sup>2,c</sup>, Alexey N. Ermakov<sup>1,d</sup><sup>1</sup>Institute of Solid State Chemistry, Ural Branch, Russian Academy of Sciences, Ekaterinburg, Russia<sup>2</sup>Institute of Electrophysics, Ural Branch, Russian Academy of Sciences, Ekaterinburg, Russia<sup>a</sup>y-avdeeva@list.ru, <sup>b</sup>key703@yandex.ru, <sup>c</sup>aidar@iep.uran.ru, <sup>d</sup>ermakovihim@yandex.ru

Corresponding author: Yuliya A. Avdeeva, y-avdeeva@list.ru

PACS 61.46.+w, 61.46.-w, 61.66.Fn

**ABSTRACT** In this work, the possibilities of formation of nanocrystalline powders based on titanium nitride with participation of Mo and Co under conditions of plasma-chemical synthesis have been studied. Synthesis was performed according to the plasma recondensation scheme using low-temperature nitrogen plasma. All the obtained highly dispersed powders were certified by X-ray diffraction and scanning electron microscopy. The characteristics of the disperse composition of the recondensed TiN–Mo–Co products were determined by the calculation based on the pycnometric density and specific surface area data.

The possibility of formation of a “core-shell” structure was confirmed using chemical methods by etching ultra- and nanodispersed powders in solutions of dilute HCl to remove the cobalt shell and concentrated hydrogen peroxide H<sub>2</sub>O<sub>2</sub> to neutralize metallic Mo.

Based on the information about “quasi-equilibrium state” of the products of plasma-chemical synthesis in a low-temperature gas plasma, a chemical model for the formation of nanocrystalline particles is proposed.

**KEYWORDS** core-shell structure, titanium nitride, plasma-chemical synthesis, temperature barrier, phase formation

**ACKNOWLEDGEMENTS** The authors are grateful to Dr. E. K. Dobrinsky, Ph. D., leading researcher of SSC RF JSC “GNIChTEOS” for help in carrying out the plasma-chemical synthesis. The work was carried out in accordance with the state assignment for the Institute of Solid State Chemistry of the Ural Branch of the Russian Academy of Sciences (theme No 0397-2019-0003 “New functional materials for promising technologies: synthesis, properties, spectroscopy and computer simulation”).

**FOR CITATION** Avdeeva Yu.A., Luzhkova I.V., Murzakaev A.M., Ermakov A.N. Plasma-chemical synthesis of nanocrystalline “core-shell” structures TiN–Mo–Co. *Nanosystems: Phys. Chem. Math.*, 2023, **14** (1), 132–141.

### 1. Introduction

Compounds based on titanium nitride are widely used as refractory bases for tool and structural materials, as well as decorative coatings that are resistant to aggressive chemical environments. Of particular interest to researchers is the nanocrystalline state of titanium nitride, formed under the conditions of various methods of extreme exposure, which have high productivity. Such methods include mechanical dispersion performed in high-speed attritors [1], detonation synthesis [2], plasma-chemical synthesis in low-temperature gas (including nitrogen) plasma [3], electrical explosion of a conductor in a controlled gas atmosphere [4], etc.

In the present work, an attempt was made to form a core-shell structure of TiN–Mo–Co under the conditions of plasma-chemical synthesis according to the plasma recondensation scheme. Recondensation is based on the effect of crystallization of evaporated mechanical mixtures in an intensely swirling nitrogen flow in a quenching chamber, followed by separation of the synthesis products into fractions. The products are separated in a vortex-type cyclone and a fabric bag filter.

As previous studies show, the use of plasma-chemical synthesis for the recondensation of microcrystalline materials, such as titanium nickelide [5] or mechanical mixtures based on TiC [6], VC, VN [7] with metallic nickel, allows the formation of “core-shell” structures. A refractory compound based on elements of IV-VIA subgroups of the Periodic Table acts as the core, and the peripheral shell is presented in the form of Ni of cubic modification. It should be noted that under such extreme conditions, during recondensation in a tangential flow of nitrogen at a rate of 10<sup>5</sup> °C/s, processes occur that cannot be carried out at lower crystallization rates. One of these processes is deposition of metallic nickel on ultra- and nanodispersed particles of titanium and vanadium nitrides. There is information in the literature [8] that the contact angles of wetting of complete nitride compounds of IV-VIA subgroup elements with nickel melts exceed 90°, meaning their complete non-wettability. At the same time, according to [8], highly defective titanium and vanadium nitrides (~TiN<sub>0.7</sub>) are characterized by wetting. Thus, under conditions of plasma recondensation, a layer of metallic

nickel can be formed either due to strong nonstoichiometric nature of the core of the refractory base, or in the presence of an interface layer, the phase composition of which should include elements contained both in the grain and on its periphery. Indeed, the X-ray diffraction experiments revealed the presence of highly deformed, according to [9], titanium-nickel nitride  $Ti_{0.7}Ni_{0.3}N$  [10] and presumably its analogue  $V_{0.7}Ni_{0.3}N$ , information about which is not available in X-ray databases. The presence of detected complex intermetallic compounds is in good agreement with the theory of B. Chalmers [11], corrected for the nanocrystalline state in [12].

## 2. Methods

Plasma-chemical synthesis (Saratov, branch of SSC RF JSC “GNIChTEOS”) in low-temperature (4000 – 6000 °C) nitrogen plasma with subsequent recondensation in a tangential flow of nitrogen gas is proposed as the main method for the synthesis of ultra- and nanodispersed “core-shell” TiN–Mo–Co structures. The cooling rate in this case can reach the values of  $10^5$  °C/s. The description of the synthesis procedure itself and its technological parameters are given in [3] and Table 1. It is also indicated that at the final stage encapsulation of ultradispersed and nanocrystalline synthesis products in organic vapors is envisaged, which makes it possible to reduce the chemical activity and pyrophoricity of the resulting powders, especially in a highly dispersed state.

TABLE 1. Technical parameters of plasma-chemical installation

Precursor mixture consumption, g/h	200
Plasma torch power, kW	25
Current strength, A	100 – 110
Voltage, V	200 – 220
Plasma flow rate, m/s	60 – 100
Total nitrogen consumption in the plasma reactor, nm <sup>3</sup> /h	25 – 30
Out of the total nitrogen consumption for plasma formation, nm <sup>3</sup> /h	6
Out of the total nitrogen consumption for stabilization and hardening, nm <sup>3</sup> /h	19 – 16

All the obtained ultrafine and nanocrystalline powders TiC–Mo–Co were studied by X-ray diffraction (X-ray diffractometer Shimadzu XRD 7000,  $CuK\alpha$ -cathode) and scanning electron microscopy (Scanning electron microscope JEOL JSM 9390, W-cathode) taking into account energy dispersive analysis data (analyzer JEM-2300). The phase composition and crystallographic characteristics were refined using the WinXPOW and PowderCell 2.3 software products oriented to the use of the ICDD and ISCD databases.

Additionally, to obtain the information about the physical characteristics (density, specific surface area, porosity and calculated average particle size), studies were carried out on a helium pycnometer (AccuPyc II 1340 V1.09) and a specific surface analyzer using the BET method (Gemini VII 2390 V1.03 (V1.03 t)). The calculation of the average particle size was carried out according to formula (1):

$$d_{av} = \frac{6}{S_{sp}\rho}, \quad (1)$$

where  $d_{av}$  is the average particle diameter,  $S_{sp}$  is the specific surface area determined by the BET method,  $\rho$  is the pycnometric density of the powder fraction determined on a helium pycnometer.

According to the results of high-resolution transmission electron microscopy on electron microscopy images, direct measurements of nanocrystalline particles were carried out using the software product MEASURER (own development of the Institute of Solid State Chemistry, UB RAS). Based on the results of measurements of the widths and heights of individual particles, a sample was formed. It was used to determine the particle diameters in accordance with the Pythagorean formula. Further, using the ORIGIN software, the average particle size was determined and a histogram of the size distribution was constructed, described by the lognormal law. The measurement accuracy and the error value were up to 0.1 nm, taking into account the significant sample size and the nanocrystalline state of the plasma-chemical powder.

## 3. Results and discussion

The results of the X-ray studies of recondensed nanocrystalline powders are presented in Table 2.

According to the results of X-ray diffraction, it can be seen (Table 2) that all ultrafine and nanocrystalline powders in the TiN–Mo–Co system are multiphase. The phase composition is characterized by the presence of refractory compounds based on titanium and molybdenum; individual metallic Mo and Co are also presented. Thus, all singly and doubly recondensed fractions from the cyclone and the filter contain refractory interstitial phases based on titanium nitride with

TABLE 2. Physicochemical properties of powder fractions recondensed from TiN–Mo–Co mechanical mixture taking into account etching in boiling HCl

No	Fraction	Phase composition, wt. %, $a, b, c, (\pm 0.0001 \text{ \AA})$	$\rho, \text{g/cm}^3$	$S_{\text{sp}}, \text{m}^2/\text{g}$	$d_{\text{av}}, \mu\text{m}$
1	1TiN–Mo–Co (cyclone)	Co (Fm-3m), (26.93 %), $a = 3.5440$ ; Ti <sub>1-n</sub> Mo <sub>n</sub> C <sub>x</sub> N <sub>y</sub> (Fm-3m), (43.89 %), $a = 4.2419$ ; Mo (Im-3m), (4.79 %), $a = 3.1463$ ; Mo <sub>0.42</sub> C <sub>0.58</sub> (Pnnm), (14.06 %), $a = 5.1367$ , $b = 4.7997, c = 2.9722$ ; TiO <sub>2</sub> (P42/mnm), (10.33 %), $a = 4.5845, c = 2.9615$	5.6365	3.0301	0.351
2	1TiN–Mo–Co (filter)	Co (Fm-3m), (49.87 %), $a = 3.5469$ ; Ti <sub>1-n</sub> Mo <sub>n</sub> C <sub>x</sub> N <sub>y</sub> (Fm-3m), (8.96 %), $a = 4.2444$ ; Mo (Im-3m), (1.37 %), $a = 3.1479$ ; Mo <sub>0.42</sub> C <sub>0.58</sub> (Pnnm), (8.69 %), $a = 5.1380, b = 4.8040$ , $c = 2.9713$ ; TiO <sub>2</sub> (P42/mnm), (31.12 %), $a = 4.5897, c = 2.9586$	5.7776	9.3973	0.110
3	2TiN–Mo–Co (cyclone)	Co (Fm-3m), (33.08 %), $a = 3.5473$ ; Ti <sub>1-n</sub> Mo <sub>n</sub> C <sub>x</sub> N <sub>y</sub> (Fm-3m), (44.01 %), $a = 4.2463$ ; Mo (Im-3m), (4.63 %), $a = 3.1495$ ; Mo <sub>0.42</sub> C <sub>0.58</sub> (Pnnm), (8.13 %), $a = 5.1028, b = 4.7763$ , $c = 2.9910$ ; TiO <sub>2</sub> (P42/mnm), (10.16 %), $a = 4.5937, c = 2.9570$	5.8973	3.9784	0.255
4	2TiN–Mo–Co (filter)	Co (Fm-3m), (41,54 %), $a = 3.5474$ ; Ti <sub>1-n</sub> Mo <sub>n</sub> C <sub>x</sub> N <sub>y</sub> (Fm-3m), (14.71 %), $a = 4.2463$ ; Mo (Im-3m), (2.97 %), $a = 3.1492$ ; Mo <sub>0.42</sub> C <sub>0.58</sub> (Pnnm), (17.34 %), $a = 5.1466$ , $b = 4.7906, c = 2.9770$ ; TiO <sub>2</sub> (P42/mnm), (10.33 %), $a = 4.5883, c = 2.9668$	5.7617	10.0729	0.103
Etching in boiling HCl (1 hour)					
5	1TiN–Mo–Co (cyclone)	Mo (Im-3m), (5.31 %), $a = 3.1470$ ; TiC <sub>x</sub> O <sub>z</sub> (Fm-3m), (72.47 %), $a = 4.2423$ TiO <sub>2</sub> (P42/mnm), (22.22 %), $a = 4.5901, c = 2.9598$	4.8937	2.5772	0.475
6	1TiN–Mo–Co (filter)	Mo <sub>0.42</sub> C <sub>0.58</sub> (Pnnm), (2.43 %), $a = 5.1566, b = 4.8321$ , $c = 2.9690$ ; Mo (Im-3m), (2.38 %), $a = 3.1444$ ; TiN <sub>x</sub> O <sub>z</sub> (Fm-3m), (23.95 %), $a = 4.2361$ ; TiO <sub>2</sub> (P42/mnm), (71.23 %), $a = 4.5944, c = 2.9600$	4.5530	21.6385	0.060
7	2TiN–Mo–Co (cyclone)	Mo (Im-3m), (9.41 %), $a = 3.1492$ ; TiC <sub>x</sub> O <sub>z</sub> (Fm-3m), (74.53 %), $a = 4.2456$ ; TiO <sub>2</sub> (P42/mnm), (16.06 %), $a = 4.5901, c = 2.9565$	5.2179	4.3632	0.263
8	2TiN–Mo–Co (filter)	Mo <sub>0.42</sub> C <sub>0.58</sub> (Pnnm), (2.12 %), $a = 5.1562, b = 4.8321$ , $c = 2.9654$ ; Mo (Im-3m), (5.63 %), $a = 3.1443$ ; TiC <sub>x</sub> N <sub>y</sub> (Fm-3m), (28.31 %), $a = 4.2463$ ; TiO <sub>2</sub> (P42/mnm), (63.94 %), $a = 4.5937, c = 2.9565$	4.1689	17.8331	0.080

carbon  $\text{TiC}_x\text{N}_y$  ( $x + y < 1$ ) (sp. gr. Fm-3m), in agreement with the data of [13]. The percentage of  $\text{TiC}_x\text{N}_y$  ( $x + y < 1$ ), according to semi-quantitative analysis, sharply decreases from the cyclone to the filter (Table 2, Nos. 1–4). All the recondensed powder materials contain metallic Mo of the cubic modification (sp. gr. Im-3m), the content of which decreases from the cyclone to the filter for both recondensation options. Besides, the core-shell structures contain highly defective molybdenum carbide  $\text{Mo}_{0.42}\text{C}_{0.58}$  (sp. gr. Pnm) described by Novotny et al. in [14]. Its quantitative indicators increase from the corresponding fractions from the cyclone to the filter, which is also reflected in Table 2, Nos. 1–4. The formation of  $\text{Mo}_{0.42}\text{C}_{0.58}$  carbide is due to the fact that the proposed study is part of an extensive scientific work aimed at obtaining highly dispersed “core-shell” structures, where titanium carbides and nitrides are considered as cores, including those alloyed with molybdenum in the metal sublattice. At the same time, it should be noted that the plasma-chemical installation was not cleaned when the charge materials with the carbide component were changed to those with the nitride component. Under these conditions, the formation of highly defective molybdenum carbide  $\text{Mo}_{0.42}\text{C}_{0.58}$  (sp. gr. Pnm) and titanium carbonitrides  $\text{TiC}_x\text{N}_y$  (sp. gr. Fm-3m) enriched in nitrogen in the nonmetallic sublattice is quite natural. The metal phase component of all TiN–Mo–Co nanocrystalline “core-shell” structures is also supplemented by the presence of cubic cobalt (sp. gr. Fm-3m), the quantitative content of which also increases from the cyclone to the filter (Table 2, Nos. 1–4). Additionally, it should be noted that the composition of nanocrystalline powders includes titanium-cobalt nitride  $\text{Ti}_{0.7}\text{Co}_{0.3}\text{N}$  of hexagonal modification (sp. gr. P-6m2), which was first described in [15, 16]. Under the conditions of plasma-chemical synthesis, which refer to extreme methods of influencing crystalline substances, during recrystallization in a tangential flow of gaseous nitrogen at a speed of  $10^5$  °C/s, this phase is in a highly deformed state, in accordance with [9]. This state is characterized by a forced preferential orientation along the (101) plane, which is one of the most intense orientations in the P-6m2 space group. The forced orientation of the  $\text{Ti}_{0.7}\text{Co}_{0.3}\text{N}$  phase does not allow one to refine the unit cell parameters and determine its quantity.

$\text{TiO}_2$  is included in the composition to reduce the pyrophoricity of ultra- and nanodispersed powders of plasma-chemical synthesis. Its amount increases significantly after single recondensation, and changes little if at all after double processing (Table 2, Nos. 1–4).

For a more accurate determination of the phase composition of the “core-shell” structures, chemical etching was carried out in a boiling solution of dilute (1:1) HCl for 1 hour. According to the results of X-ray phase analysis (Table 2, Nos. 5–8), metallic cobalt and highly defective  $\text{Mo}_{0.42}\text{C}_{0.58}$  in the fractions from the cyclone (Table 2, Nos. 5–7) were completely dissolved during boiling. It was also noted that during boiling in acid, the unit cell parameters of  $\text{TiC}_x\text{N}_y$  ( $x + y < 1$ ) slightly changed, but in accordance with [13], the chemical composition did not undergo any significant changes. Thus, the refractory ceramic base of all “core-shell” structures is represented by titanium nitride with nitrogen positions partially replaced by carbon in the non-metallic sublattice, while the sum  $x + y$  is less than 1. Since the ratio of phase components changed, the amount of metallic Mo (sp. gr. Im-3m) and  $\text{TiO}_2$  (sp. gr. P42/mnm) of the rutile modification increased in the etched samples. On the other hand, as is known from [17], metallic molybdenum does not dissolve in dilute HCl, and an increase in the amount of  $\text{TiO}_2$  can be associated with partial acidification of nanosized titanium carbonitride  $\text{TiC}_x\text{N}_y$  ( $x + y < 1$ ) during boiling.

Based on the data of X-ray phase analysis (Table 2) of TiN–Mo–Co powders, by comparing the conditions for their production using plasma-chemical technology with some physicochemical laws of the formation of refractory compounds and the conditions for their wetting with metallic media, it is possible to carry out physicochemical modeling of the processes of formation of “core-shell” structures. The chemical model is based on refractory titanium compounds coated with molybdenum and cobalt metal phases and takes into account the formation of highly defective carbide  $\text{Mo}_{0.42}\text{C}_{0.58}$  and complexly substituted metastable nitride  $\text{Ti}_{0.7}\text{Co}_{0.3}\text{N}$  [5] (Fig. 1).

Since the working temperature of the evaporation processes in the plasma-chemical reactor is 4000 – 6000 °C, and the crystallization rate in a tangential flow of nitrogen gas in the hardening chamber is  $10^5$  °C/s, the formation of “core-shell” structures can be modeled only as a function of temperature variation throughout the quenching chamber. Thus, the quenching chamber can be separated by temperature barriers corresponding to crystallization temperatures of the phase components, determined and refined according to the data of X-ray phase analysis. In accordance with [12, 18, 19], a low-temperature gas plasma can be considered as “quasi-equilibrium”. The formation conditions can also be considered “quasi-equilibrium” because the Arrhenius law is observed. In this case, the sequence of formation of nanocrystalline layers of TiN–Mo–Co “core-shell” structures can be determined based on the evaporation and crystallization temperatures of the phase components determined by X-ray diffraction, as well as  $\Delta G(T)$  dependencies for refractory compounds that are part of highly dispersed powders. For all phase components, with the exception of highly defective molybdenum carbide  $\text{Mo}_{0.42}\text{C}_{0.58}$  and metastable complex nitride  $\text{Ti}_{0.7}\text{Co}_{0.3}\text{N}$ , the evaporation and crystallization temperatures are presented in Table 3, and  $\Delta G(T)$  dependences in Fig. 2.

The temperature of 4000 °C can be considered as the first temperature barrier of the “core-shell” structure formation model (Fig. 1), since this temperature is the minimum when plasma-chemical synthesis is carried out in low-temperature nitrogen plasma (4000 – 6000 °C) with subsequent recondensation. On passing this temperature, in accordance with [5], Mo and Ti are presented simultaneously in the gaseous and liquid state, while C and Co are in the gaseous form, and TiN is in the liquid form. As the second temperature barrier, corresponding to the melting temperature of titanium nitride TiN (2930 °C [20]), is approached, it can be assumed that titanium carbonitride, in which the nitrogen content significantly

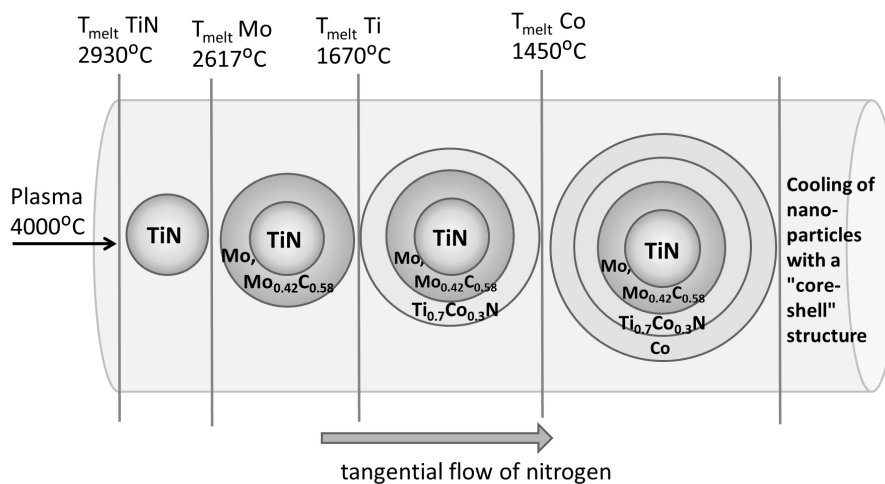


FIG. 1. Chemical mechanism of formation of TiN–Mo–Co “core-shell” structures

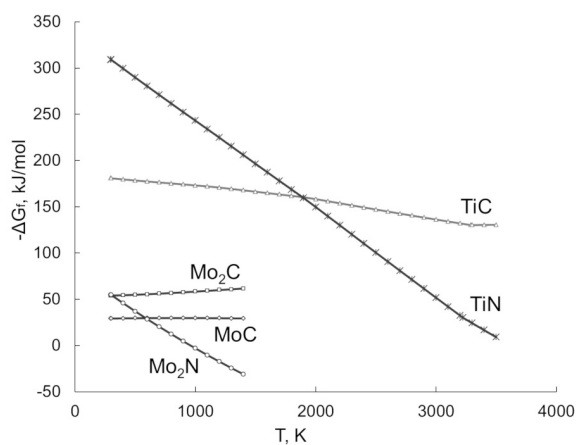
FIG. 2.  $-\Delta G_f(T)$  dependences for  $\text{Mo}_2\text{N}$ ,  $\text{MoC}$ ,  $\text{Mo}_2\text{C}$ ,  $\text{TiN}$  and  $\text{TiC}$  compounds

TABLE 3. Boiling and melting points of phase components in the TiN–Mo–Co system

Component	$T_{\text{melt}}, ^\circ\text{C}$	$T_{\text{boil}}, ^\circ\text{C}$
TiN	2930	—
TiC	3300	4300
Mo	2617	4885
Ti	1670	3287
MoC	2700	—
MoN	1750	
Co	1485	2870

exceeds the carbon content (Table 2, Nos. 1–4), crystallizes. At the same time, etching in HCl promotes a change in the lattice parameters of titanium carbide-nitride compounds for the corresponding fractions. So, for example, for singly recondensed fractions from the cyclone, the unit cell parameter increases from 4.2419 to 4.2423 Å (Table 2, Nos. 1,5), and that from the filter decreases from 4.2444 to 4.2361 Å (Table 2, Nos. 2,6). Under conditions of double recondensation, analogous parameters for the fractions from the cyclone, taking into account etching, decrease slightly from 4.2463 to 4.2456 Å (Table 2, Nos. 3,7), while for the fractions from the filter they do not change and are equal to 4.2463 Å (Table 2, Nos. 4,8).

Based on the patterns of formation of solid solutions used in the plasma-chemical synthesis of elements, it can be said that after a single recondensation (Table 2, Nos. 1, 2), a fraction is concentrated in the cyclone, in which the refractory phase based on titanium nitride is saturated with carbon. In the fraction from the filter, molybdenum is presented in the metal sublattice of carbonitride with the formation of a  $Ti_{1-n}Mo_nC_xN_y$  solid solution. Under the conditions of double recondensation (Table 2, Nos. 3,4), as mentioned above, no changes in the unit cell parameters of the refractory base of the “core-shell” structures are observed and their phase composition, in accordance with [13], can be described by the formula  $TiC_{0.12}N_{0.77}$ . Boiling in a hydrochloric acid solution, in addition to the dissolution of cobalt, which is the surface layer in all core-shell structures, can also contribute to the oxidation of the refractory base of all ultra- and nanodispersed powder fractions under study. In accordance with [13], after a single recondensation, titanium oxycarbide  $TiC_{0.21}O_{0.8}$  was recorded in the fraction from the cyclone (Table 2, No. 5), and titanium oxynitride  $TiN_{0.52}O_{0.34}$  – in the fraction from the filter (Table 2, No. 6). Etching of doubly recondensed powders, according to the results of X-ray phase analysis, contributed to the formation of titanium oxycarbide  $TiC_{0.21}O_{0.8}$  [13] (Table 2, No. 7) in the cyclone. In the fraction from the filter, as expected, it was not possible to fix phases of the composition Ti–C–O and Ti–N–O (Table 2, No. 8) due to their complete oxidation to  $TiO_2$  of the rutile modification, the content of which reaches 63.94 wt. %, and the refractory base is represented by titanium carbonitride having the composition  $TiC_{0.12}N_{0.77}$  [13].

The third temperature barrier can start from the crystallization temperature of metallic molybdenum, which is 2617 °C [8]; at this temperature, Mo crystallizes in a cubic bcc cell. Highly defective molybdenum carbide  $Mo_{0.42}C_{0.58}$  of the orthorhombic modification crystallizes as an additional phase. Its formation is due to the presence of free carbon in the recondensable system, which is presented in the described temperature range. In accordance with Fig. 2, combining the data from [21], MoN is formed at  $\Delta G(T)$  values close to 0, which is virtually impossible in the presented core-shell structures due to the extremely high cooling rate in a gaseous medium and the crystallization temperature of MoN (1750 °C [8]) compared with Mo.

The fourth temperature barrier corresponds to the formation temperature (1670 °C [8]) of a complex nitride containing Ti, Co, and N in its composition in accordance with [15]. In particular, at the onset of this temperature regime, in the process of chemical interaction, from the residual amounts of titanium that did not have time to react with nitrogen earlier, a metastable phase in the form of a complexly substituted nitride  $Ti_{0.7}Co_{0.3}N$  is formed in a complex with molten Co [15]. This phase, as described earlier in [9], is in a highly deformed state due to the use of an extreme synthesis technique, which includes plasma-chemical synthesis in low-temperature nitrogen plasma. The forced orientation of  $Ti_{0.7}Co_{0.3}N$  along the (101) direction ensures positive wettability of the nanocrystalline “core-shell” structures by metallic cobalt when passing the final fifth temperature barrier, the temperature of which specifies the crystallization of metallic cobalt (1450 °C [8]).

The described chemical model (Fig. 1) for the formation of nanocrystalline particles involving titanium nitride, metallic molybdenum, and cobalt is well confirmed by high-resolution transmission electron microscopy data. In particular, Fig. 3(a,b) show electron microscopic images illustrating the dispersity of the studied nanocrystalline fraction, and Fig. 2(c) demonstrates a size distribution histogram of the measured particles, on the basis of which it was found that, according to the results of measurements of 8598 particles, the average size was  $34.64 \pm 0.18$  nm, which is much less than the calculated data given in Table 2, No. 4.

The “core-shell” structure is visualized in Fig. 4, where it is clearly seen that the coating of the core is continuous and has a uniform thickness. Fig. 3(b) shows a FFT pattern with a banded contrast with an interplanar spacing of 0.25 nm corresponding to the (111) plane of cubic TiN (sp. gr. Fm-3m). In addition, the plane of rutile (110)  $TiO_2$  (sp. gr. P42/mnm) was determined in section 2 of Fig. 4(a, c) with an interplanar spacing of 0.33 nm.

Further, Fig. 5(a) shows a nanocrystalline particle with a core-shell structure. The core of the presented particle is characterized by moire contrast, the presence of which indicates the diffracting planes of the crystal lattice, which overlap and can have different interplanar spacing and orientation. Fig. 5(c) shows the FFT-transformation of region 1 of the core (Fig. 5(b)), where the interplanar distances of 0.25 and 0.21 nm were determined, which correspond to the (011) and (120) planes of highly defective carbide  $Mo_{0.42}C_{0.58}$  of the orthorhombic modification (sp. gr. Pnmm). Additionally,  $Ti_{0.7}Co_{0.3}N$  nitride, to which the (001) plane with an interplanar spacing of 0.29 nm belongs, was determined in section 1 (Fig. 5(b,c)). Using the Fourier transform of the shell (Fig. 5(d)), which corresponds to the banded contrast in region 2 (Fig. 5(b)), the interplanar spacing was determined to be 0.24 nm, corresponding to the (212) plane of metallic Co (sp. gr. P63mc).

Possible deviations of the values of interplanar distances of highly defective molybdenum carbide from the data of the ICDD and ICSD file cabinets are due to the fact that the powders studied in the work were obtained under extreme

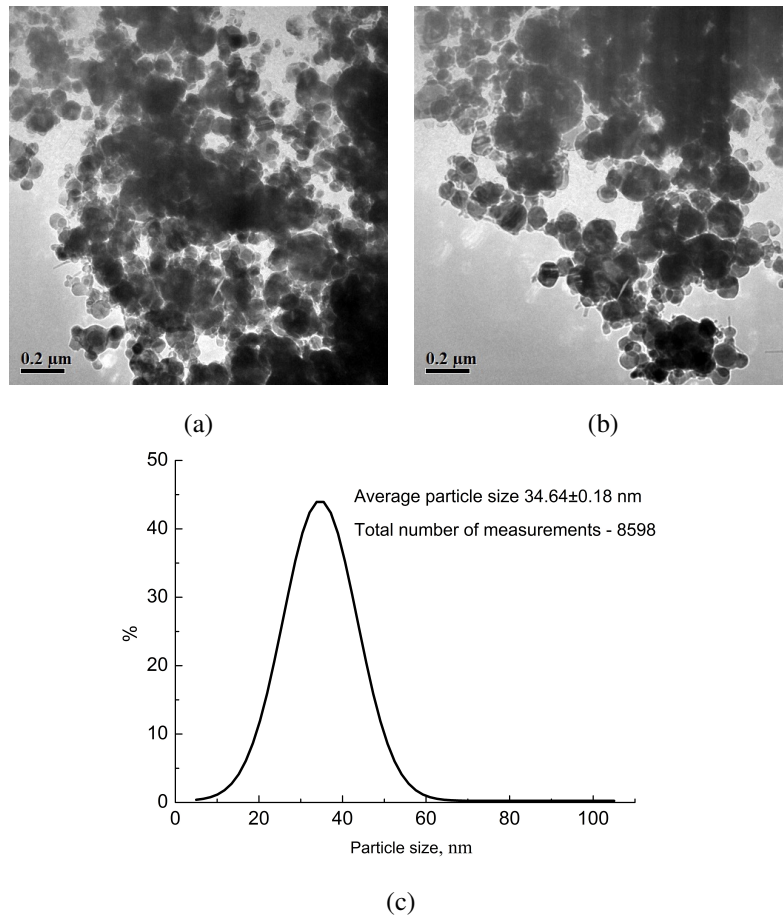


FIG. 3. Electron microscopic images of sections of TiN–Mo–Co fractions (a, b) and a histogram of particle size distribution (c)

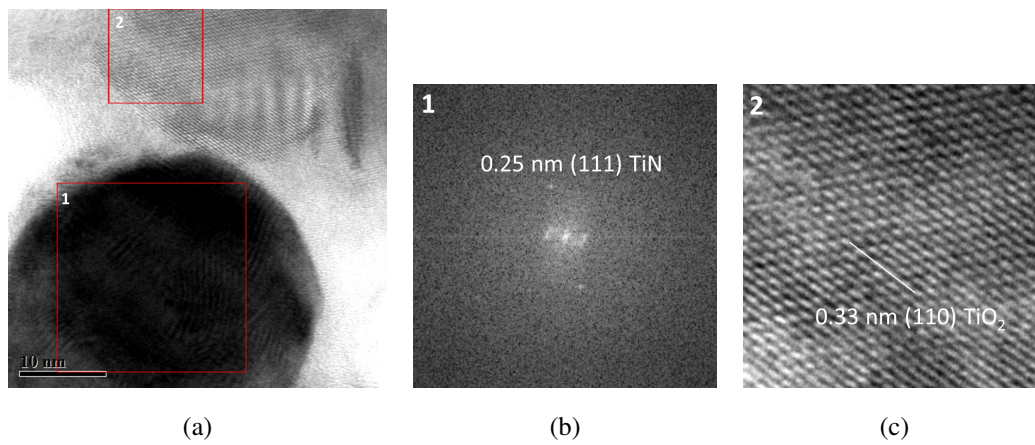


FIG. 4. Electron microscopic image of a section of the TiN–Mo–Co fraction (a), the Fourier transform of section 1 (b), enlarged image of section 2 (c)

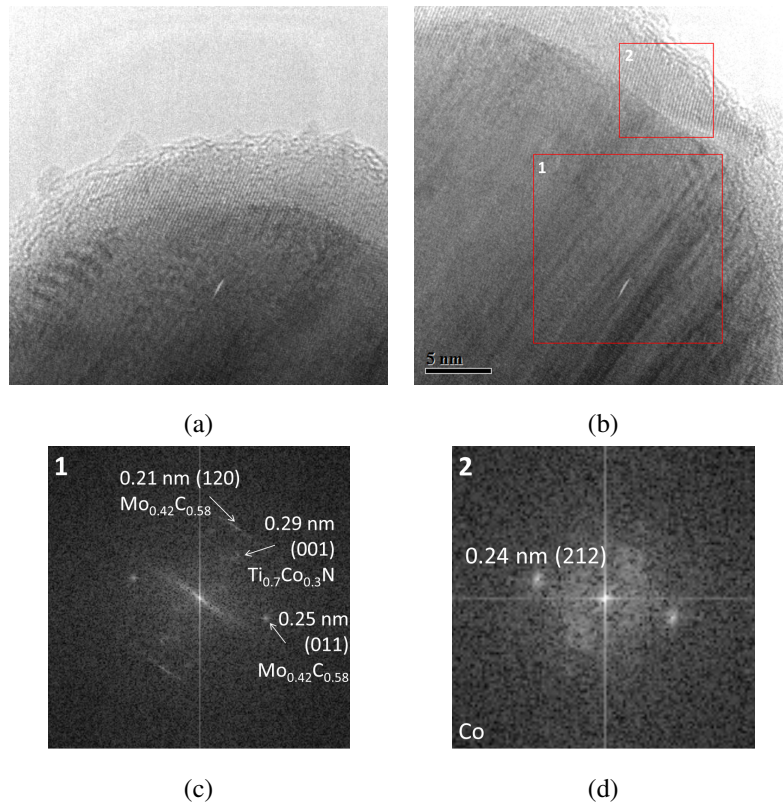


FIG. 5. HR TEM image of a TiN–Mo–Co particle (a, b), the Fourier transforms of sections 1 (c) and 2 (d)

conditions of plasma-chemical synthesis. This, in turn, creates microdeformations in the crystal lattice of  $\text{Mo}_{0.42}\text{C}_{0.58}$  and contributes to its distortion.

From the results of plasma-chemical synthesis and X-ray diffraction of the obtained products it can be said that the formation of rutile  $\text{TiO}_2$  is due to forced acidification in storage devices of separators aimed to reduce the pyrophoricity of highly dispersed TiN–Mo–Co fractions. At the same time, the HR TEM results show that some of the nanocrystalline particles with the “core-shell” structure are almost completely oxidized to  $\text{TiO}_2$ . However, in some cases, as shown in Fig. 6, carbon planes are registered (Fig. 6(b)). The Fast Fourier transform of section 1 presented in Fig. 6(a, b) illustrates the presence of  $\text{TiO}_2$  (sp. gr. Pbcn) at interplanar distances of 0.34 and 0.41 nm, which corresponds to the (111) and (020) planes. Carbon of the hexagonal modification (space group P63/mmc) was visualized on the Fourier transform (Fig. 6(c)) with an interplanar spacing of 0.33 nm, which corresponds to the (002) plane.

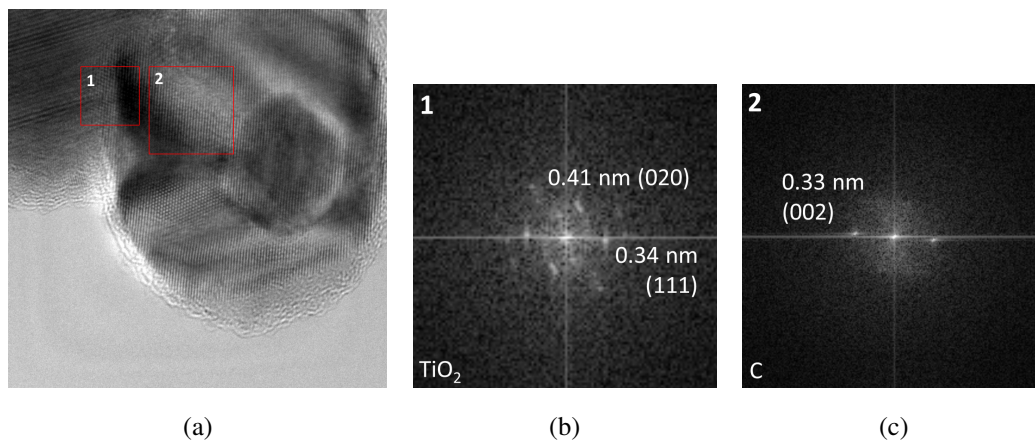


FIG. 6. HR TEM image of a TiN–Mo–Co particle (a), the Fourier transforms of sections 1 (b) and 2 (c)

In accordance with the theory of heterogeneous nucleation by Chalmers B. [11], the metallic component of Co is located on the surface of “core-shell” particles. Based on the analysis of the above electron microscopic images of TiC–Mo–Co nanoparticles, we can say that the cobalt shell (Figs. 5(d), 7(c)) is a pseudo-amorphous coating on the particle surface.

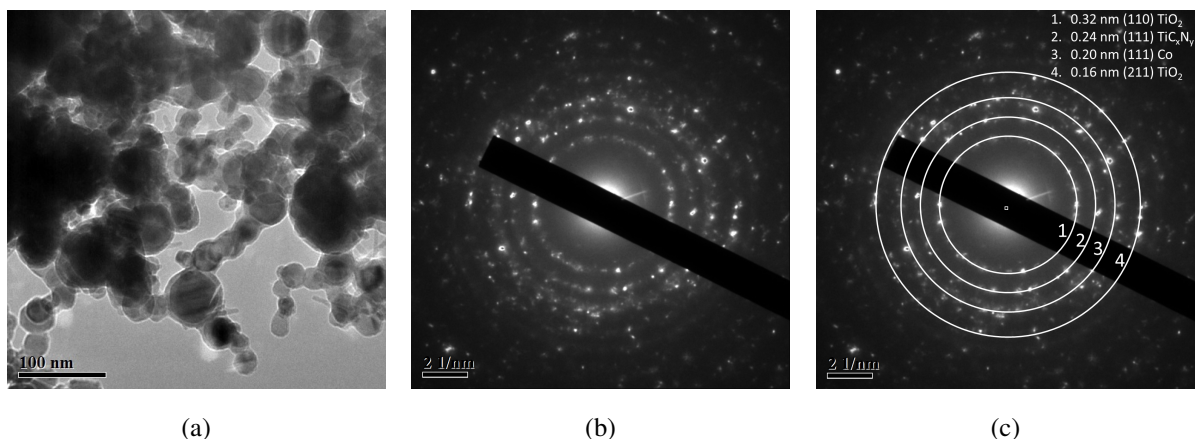


FIG. 7. Electron diffraction pattern (b, c) of the area (a) of TiN–Mo–Co fractio

To unambiguously confirm the presence of all X-ray diffraction-defined phase components, electron diffraction studies were carried out on a polycrystalline sample (Fig. 7). During the identification of electron diffraction projections, the presence of the following phase components was confirmed: the rutile modification of  $\text{TiO}_2$  (sp. gr. P42/mmm) was determined from interplanar distances of 0.32 and 0.16 nm, which corresponds to the (110) and (211) planes; the cubic titanium carbonitride  $\text{TiC}_x\text{N}_y$  (sp. gr. Fm-3m) enriched with nitrogen in the non-metallic sublattice was fixed at an interplanar distance of 0.24 nm, which corresponds to the (111) plane. Metallic Co of the cubic modification (sp. gr. Fm-3m) was determined by the interplanar spacing of 0.20 nm, which corresponds to the (111) plane.

#### 4. Conclusions

Ultrafine and nanocrystalline powders TiN–Mo–Co have been obtained by plasma-chemical synthesis in low-temperature nitrogen plasma from a mechanical mixture based on titanium nitride TiN with the participation of metallic molybdenum and cobalt.

The resulting powders were studied by X-ray diffraction and high-resolution transmission electron microscopy. It was established that under the conditions of plasma-chemical synthesis, ultrafine and nanocrystalline powder fractions are formed, which include titanium nitrides and carbonitrides, cobalt, molybdenum and its highly defective carbide  $\text{Mo}_{0.42}\text{C}_{0.58}$  of the orthorhombic modification, as well as titanium oxide  $\text{TiO}_2$  of the rutile modification.

In some cases, HR TEM images show the presence of free carbon of hexagonal modification (sp. gr. P63/mmc), and nanocrystalline grains are core-shell structures. Refractory titanium compounds act as the core, and metallic molybdenum and cobalt as the shell.

#### References

- [1] Vereshchagin M.N., Goranskij G.G., Kiriluk S.I., Agunovich I.V. Investigation of processes of structure and phase formation of blend powders on the basis of waste of hard tungsten-containing alloys at their mechano-synthesis and high-speed mechanical dispersing for production of powder compositions. *Lit'yo i Metallurgiya (Foundry Production and Metallurgy)*, 2012, **1** (84), P. 110–114.
- [2] Langenderfer M.J., Fahrenholtz W.G., Chertopalov S., Zhou Y., Mochalin V.N., Johnson C.E. Detonation synthesis of silicon carbide nanoparticles. *Ceram. Int.*, 2020, **46** (5), P. 6951–6954.
- [3] Storozhenko P.A., Guseinov Sh.L., Malashin S.I. Nanodispersed powders: synthesis methods and practical applications. *Nanotech. in Russia*, 2009, **4**, P. 262–274.
- [4] Lerner M.I., Glazkova E.A., Lozhkomoev A.S., Svarovskay N.V., Bakina O.V., Pervikov A.V., Psakhie S.G. Synthesis of Al nanoparticles and Al/AlN composite nanoparticles by electrical explosion of aluminum wires in argon and nitrogen. *Powder Technol.*, 2016, **295**, P. 307–314.
- [5] Avdeeva Y.A., Luzhkova I.V., Ermakov A.N. Mechanism of formation of nanocrystalline particles with core-shell structure based on titanium oxynitrides with nickel in the process of plasma-chemical synthesis of TiNi in a low-temperature nitrogen plasma. *Nanosystems: Phys. Chem. Math.*, 2022, **13** (2), P. 212–219.
- [6] Luzhkova I.V., Ermakov A.N., Grigorov I.G., Zainulin Yu.G., Dobrinskii E.K., Malashin S.I. Plasmachemical processing of titanium carbide and nickelide in a low-temperature nitrogen plasma. *Russ. Metall.*, 2013, **2013**, P. 11–13.
- [7] Luzhkova I.V., Ermakov A.N., Murzakaev A.M., Grigorov I.G., Zainulin Yu.G., Dobrinsky E.K., Malashin S.I. Plasma treatment with nickel of vanadium carbide and nitride. *Nanotech. in Russia*, 2014, **9**, P. 667–673.
- [8] Kosolapova T.Ya. *Handbook of high temperature compounds: properties, production, applications*. CRC Press, New York, Washington, Philadelphia, London, 1990, 958 p.
- [9] Fultz B., Howe J.M. *Transmission electron microscopy and diffractometry of materials*, 3rd ed. Springer, Berlin, Heidelberg, 2008, 758 p.
- [10] Ermakov A.N., Luzhkova I.V., Avdeeva Yu.A., Murzakaev A.M., Zainulin Yu.G., Dobrinsky E.K. Formation of complex titanium-nickel nitride  $\text{Ti}_{0.7}\text{Ni}_{0.3}\text{N}$  in the “core-shell” structure of TiN – Ni. *Int. J. Refract. Met. Hard Mater.*, 2019, **84**, 104996.
- [11] Chalmers B. *Principles of solidification*. John Wiley and Sons, Springer, New York, Dordrecht, Heidelberg, London, 1964, 319 p.
- [12] Zhukov M.F., Chersky I.N., Cherepanov A.N., Konovalov N.A., Saburov V.P., Pavlenko N.A., Galevsky G.V., Andrianova O.A., Krushenko G.G. *Strengthening of metallic polymer and elastomer materials with ultradispersed powders obtained by plasma-chemical synthesis*. Nauka, Siberian publishing company of RAS, Novosibirsk, 1999, 307 p. (In Russian)

- [13] Shveikin G.P., Alyamovsky S.I., Zainulin Yu.G., Gusev A.I., Gubanov V.A., Kurmaev E.Z. *Variable composition compounds and their solid solutions*. UNTs AN SSSR, Sverdlovsk, 1984, 292 p. (In Russian)
- [14] Schuster J.C., Nowotny H. Molybden- und Molybden-Wolfram-Carbide im Temperaturbereich von 600 – 1600 °C. *Monatshefte für Chemie*, 1979, **110**, P. 321–332.
- [15] Schönberg N. The Tungsten Carbide and Nickel Arsenide Structures. *Acta Metallica*, 1954, **2**, P. 427–432.
- [16] Bhaskar, U.K., Pradhan S.K. Microstructural evolution of nanostructured Ti<sub>0.7</sub>Ni<sub>0.3</sub>N prepared by reactive ball-milling. *Mater. Res. Bull.*, 2013, **48**, P. 3129–3135.
- [17] Knunyants I.L. *Chemical encyclopedia*: in 5 v. Soviet encyclopedia, Moscow, 1992, **3**, 125 p., 639 p. (In Russian)
- [18] Polak L. Elementary chemical processes and kinetics in a non-equilibrium and quasi-equilibrium plasma. *Pure Appl. Chem.*, 1974, **39** (3), P. 307–342.
- [19] Borodin V.I. Low-temperature plasma in metal production processes. *Lecture and report materials of the Workshop: Methods and technique of the experimental study of ordered structures self-organization processes in plasma dust formations and the School of young scientists: Topical problems of applications of physics of low-temperature plasma*, 2003, 10 p. (In Russian)
- [20] Krzhizhanovsky R.E., Stern Z.Yu. *Thermophysical properties of non-metallic materials (carbides)*. Handbook, Energiya, Leningrad, 1976, 120 p. (In Russian)
- [21] Barin I. *Thermochemical data of pure substances*. Third edition. VCH, Weinheim, New York, Basel, Cambridge, Tokyo, 1995. 2003 p.

---

*Submitted 20 September 2022; revised 28 November 2022; accepted 5 December 2022*

*Information about the authors:*

*Yuliya A. Avdeeva* – Institute of Solid State Chemistry, Ural Branch, Russian Academy of Sciences Pervomaiskaya Street, 91, Ekaterinburg, 620990, Russia; ORCID 0000-0002-1470-0476; y-avdeeva@list.ru

*Irina V. Luzhkova* – Institute of Solid State Chemistry, Ural Branch, Russian Academy of Sciences Pervomaiskaya Street, 91, Ekaterinburg, 620990, Russia; ORCID 0000-0001-9123-5371; key703@yandex.ru

*Aidar M. Murzakaev* – Institute of Electrophysics, Ural Branch, Russian Academy of Sciences Amundsen Street, 106 Ekaterinburg, 620216, Russia; ORCID 0000-0003-4440-427X; aidar@iep.uran.ru

*Alexey N. Ermakov* – Institute of Solid State Chemistry, Ural Branch, Russian Academy of Sciences Pervomaiskaya Street, 91, Ekaterinburg, 620990, Russia; ORCID 0000-0002-2746-5292; ermakovihim@yandex.ru

*Conflict of interest:* the authors declare no conflict of interest.

## Correction to the paper “Synthesis and magnetic properties of cobalt ferrite nanoparticles formed under hydro and solvothermal condition”

Boris V. Vasil'ev<sup>1,2,a</sup>, Ruslan Yu. Smyslov<sup>1,b</sup>, Demid A. Kirilenko<sup>3,4,c</sup>, Alexander N. Bugrov<sup>1,2,d</sup>

<sup>1</sup>Institute of Macromolecular Compounds RAS, St. Petersburg, Russia

<sup>2</sup>St. Petersburg Electrotechnical University “LETI”, St. Petersburg, Russia

<sup>3</sup>Ioffe Institute RAS, St. Petersburg, Russia

<sup>4</sup>ITMO University, St. Petersburg, Russia

<sup>a</sup>boris8152@gmail.com, <sup>b</sup>urs@macro.ru, <sup>c</sup>demid.kirilenko@mail.ioffe.ru, <sup>d</sup>alexander.n.bugrov@gmail.com

Corresponding author: Boris V. Vasil'ev, boris8152@gmail.com

PACS 75.20.-g; 75.75.+a

**ABSTRACT** This paper is a corrigendum related to the article Vasil'ev B.V., Smyslov R.Yu., Kirilenko D.A., Bugrov A.N. Synthesis and magnetic properties of cobalt ferrite nanoparticles formed under hydro and solvothermal condition. *Nanosystems: Phys. Chem. Math.*, 2021, **12** (4), P. 492–504, <http://nanojournal.ifmo.ru/en/articles-2/volume12/12-4/chemistry/paper11/>

**KEYWORDS** single-domain cobalt ferrite, ferrimagnetic nanocrystals, size-controlled synthesis, stoichiometry, Rietveld refinement, coercive field, saturation magnetization, squareness

**FOR CITATION** Vasil'ev B.V., Smyslov R.Yu., Kirilenko D.A., Bugrov A.N. Correction to the paper “Synthesis and magnetic properties of cobalt ferrite nanoparticles formed under hydro and solvothermal condition”. *Nanosystems: Phys. Chem. Math.*, 2023, **14** (1), 142–143.

In the paper [1], Fig. 3 contains a graphic misprint. The correct part (b) in this figure is given below.

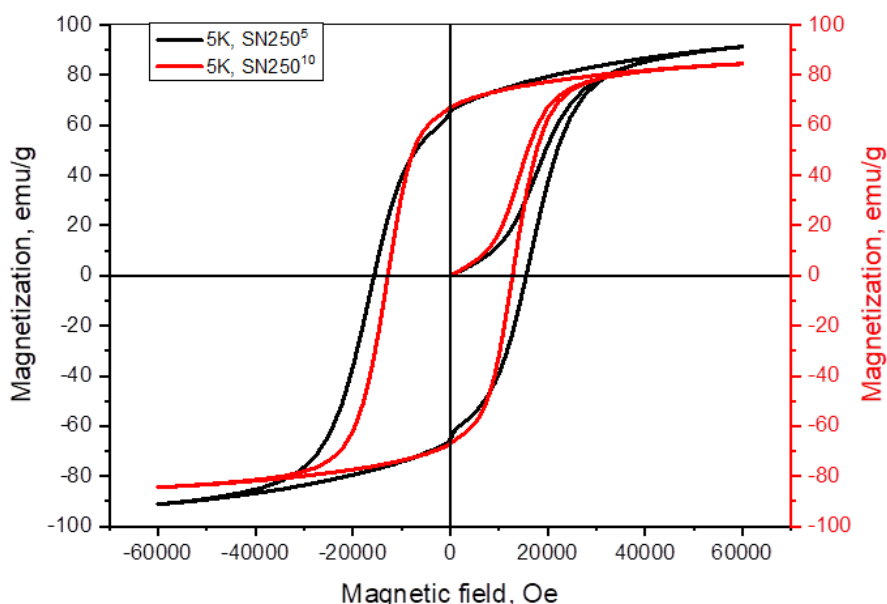


FIG. 1. The low-temperature magnetic hysteresis (M–H) loops for  $\text{Co}_x\text{Fe}_{3-x}\text{O}_4$  nanoparticles synthesized under solvo- (a,b) and hydrothermal conditions (c)

In connection with the correction of Fig. 3(b) [1], it is necessary to correct a paragraph on p. 497. Now it should read like this:

Studies of the synthesized cobalt ferrite nanoparticles using SQUID magnetometry showed that their magnetization curves have hysteresis loops regardless of the type of precursor used, as well as the chosen conditions of hydrolysis and dehydration (Fig. 3, Table 3). It should also be noted that “constricted” hysteresis loops were recorded for cobalt ferrite nanoparticles obtained under hydrothermal conditions or in an organic solvent at temperatures of 150 and 200 °C (Fig. 3), which are typical for a mixture of soft and hard magnetic materials [1, 29, 30]. In this case, such a “necking” in the central part of the M–H loop can be explained by a small amount of superparamagnetic single-domain particles in ferrimagnetic  $\text{Co}_x\text{Fe}_{3-x}\text{O}_4$  nanocrystals.

In Table 3 on Page 502 [1], the row titled “SN250<sup>5</sup>” should be now written as:

SN250 <sup>5</sup>	0.72	65.7	91	15700	0.09	7	77	245	—	0	65	0
--------------------	------	------	----	-------	------	---	----	-----	---	---	----	---

In ACKNOWLEDGMENTS, some information was omitted by the authors. Therefore, the correct version of the acknowledgments is given below.

### Acknowledgments

X-ray diffraction experiments were performed on the Engineering Center equipment of the St. Petersburg State Technological Institute (Technical University). TEM studies were carried out in the Federal Joint Research Center “Material science and characterization in advanced technology” funded by the Ministry of Education and Science of the Russian Federation. We appreciate Evgeniy V. Shevchenko from the Centre for Diagnostics of Functional Materials for Medicine, Pharmacology and Nanoelectronics (SPbU Research Park) for finding the discrepancy in the data obtained by measuring the magnetic characteristics of the ferrites by SQUID magnetometry. We give special thanks to Alexandr S. Sakhatskiy from the latter Research Park for measuring our systems using a SQUID magnetometer, as well as Ilya S. Kritchenkov from St. Petersburg State University for helping with this measuring.

### References

- [1] Vasil'ev B.V., Smyslov R.Yu., Kirilenko D.A., Bugrov A.N. Synthesis and magnetic properties of cobalt ferrite nanoparticles formed under hydro and solvothermal condition. *Nanosystems: Phys. Chem. Math.*, 2021, **12** (4), P. 492–504.

---

*Submitted 6 February 2023; accepted 7 February 2023*

### Information about the authors:

*Boris V. Vasil'ev* – Institute of Macromolecular Compounds RAS, Bolshoy pr. 31, 199004 Saint Petersburg, Russia; Saint Petersburg Electrotechnical University “LETI”, ul. Professora Popova 5, 197022 Saint Petersburg, Russia; ORCID 0000-0002-9315-7087; boris8152@gmail.com

*Ruslan Yu. Smyslov* – Institute of Macromolecular Compounds RAS, Bolshoy pr. 31, 199004 Saint Petersburg, Russia; ORCID 0000-0003-3633-4347; urs@macro.ru

*Demid A. Kirilenko* – Ioffe Institute RAS, Politekhnicheskaya ul. 26, 194021 Saint Petersburg, Russia; ITMO University, Kronverskii avenue 49, 197101 Saint Petersburg, Russia; ORCID 0000-0002-1571-209X; demid.kirilenko@mail.ioffe.ru

*Alexander N. Bugrov* – Institute of Macromolecular Compounds RAS, Bolshoy pr. 31, 199004 Saint Petersburg, Russia; Saint Petersburg Electrotechnical University “LETI”, ul. Professora Popova 5, 197022 Saint Petersburg, Russia; ORCID 0000-0003-1052-4919; alexander.n.bugrov@gmail.com

*Conflict of interest:* the authors declare no conflict of interest.



# NANOSYSTEMS:

**PHYSICS, CHEMISTRY, MATHEMATICS**

## INFORMATION FOR AUTHORS

The journal publishes research articles and reviews, and also short scientific papers (letters) which are unpublished and have not been accepted for publication in other magazines. Articles should be submitted in English. All articles are reviewed, then if necessary come back to the author to completion.

The journal is indexed in Web of Science Core Collection (Emerging Sources Citation Index), Chemical Abstract Service of the American Chemical Society, Zentralblatt MATH and in Russian Scientific Citation Index.

### Author should submit the following materials:

1. Article file in English, containing article title, the initials and the surname of the authors, Institute (University), postal address, the electronic address, the summary, keywords, MSC or PACS index, article text, the list of references.
2. Files with illustrations, files with tables.
3. The covering letter in English containing the article information (article name, MSC or PACS index, keywords, the summary, the literature) and about all authors (the surname, names, the full name of places of work, the mailing address with the postal code, contact phone number with a city code, the electronic address).
4. The expert judgement on possibility of publication of the article in open press (for authors from Russia).

Authors can submit a paper and the corresponding files to the following addresses: nanojournal.ifmo@gmail.com, popov1955@gmail.com.

### Text requirements

Articles should be prepared with using of text editors MS Word or LaTeX (preferable). It is necessary to submit source file (LaTeX) and a pdf copy. In the name of files the English alphabet is used. The recommended size of short communications (letters) is 4-6 pages, research articles– 6-15 pages, reviews – 30 pages.

#### Recommendations for text in MS Word:

Formulas should be written using Math Type. Figures and tables with captions should be inserted in the text. Additionally, authors present separate files for all figures and Word files of tables.

**Recommendations for text in LaTeX:**

Please, use standard LaTeX without macros and additional style files. The list of references should be included in the main LaTeX file. Source LaTeX file of the paper with the corresponding pdf file and files of figures should be submitted.

References in the article text are given in square brackets. The list of references should be prepared in accordance with the following samples:

- [1] Surname N. *Book Title*. Nauka Publishing House, Saint Petersburg, 2000, 281 pp.
- [2] Surname N., Surname N. Paper title. *Journal Name*, 2010, 1 (5), P. 17-23.
- [3] Surname N., Surname N. Lecture title. In: Abstracts/Proceedings of the Conference, Place and Date, 2000, P. 17-23.
- [4] Surname N., Surname N. Paper title, 2000, URL: <http://books.ifmo.ru/ntv>.
- [5] Surname N., Surname N. Patent Name. Patent No. 11111, 2010, Bul. No. 33, 5 pp.
- [6] Surname N., Surname N. Thesis Title. Thesis for full doctor degree in math. and physics, Saint Petersburg, 2000, 105 pp.

**Requirements to illustrations**

Illustrations should be submitted as separate black-and-white files. Formats of files – jpeg, eps, tiff.



# ***NANOSYSTEMS:***

***PHYSICS, CHEMISTRY, MATHEMATICS***

**Журнал зарегистрирован**

Федеральной службой по надзору в сфере связи, информационных технологий и массовых коммуникаций

(свидетельство ПИ № ФС 77 - 49048 от 22.03.2012 г.)

ISSN 2220-8054

**Учредитель:** федеральное государственное автономное образовательное учреждение высшего образования

«Национальный исследовательский университет ИТМО»

**Издатель:** федеральное государственное автономное образовательное учреждение высшего образования

«Национальный исследовательский университет ИТМО»

**Отпечатано** в Учреждении «Университетские телекоммуникации»

Адрес: 197101, Санкт-Петербург, Кронверкский пр., 49

**Подписка на журнал НФХМ**

На второе полугодие 2023 года подписка осуществляется через

ОАО «АРЗИ», подписной индекс Э57385